INTERMEDIATE-DEPTH EARTHQUAKES, SLAB STRESS STATE AND UPPER MANTLE STRUCTURE BENEATH THE NORTH CENTRAL ANDES

Abhash Kumar

A dissertation submitted to the faculty at the University of North Carolina at Chapel Hill in partial fulfillment of the requirements for the degree of Doctor of Philosophy in the Department of Geological Sciences.

Chapel Hill
2015

Approved by:

Drew Coleman

Lara Wagner

Jonathan Lees

Kevin Stewart

Gordana Vlahovic

ABSTRACT

Abhash Kumar: Intermediate-depth earthquakes, slab stress state and upper mantle structure beneath the north central Andes
(Under the direction of Drew Coleman)

Flat slab subduction in Peru and the Central Andean Plateau of southern Peru, Bolivia and northwestern Argentina are the two intriguing geologic features along the western margin of South America. Flat slab subduction has often been causally linked to wide host of geological observations including the cessation of arc volcanism, inboard thick-skinned deformation of the overriding plate, ignimbrite volcanism, and the evolution of high plateaus. Yet several questions continue to exist on both the requirements for its formation and the consequences of its existence. For the purpose of this dissertation, I define "flat slab subduction" as subduction zones where the downgoing slab subducts normally (~30° dip) to a depth of ~100 km and then abruptly bends to travel horizontally for several hundred kilometers before resuming its descent. Understanding the mechanisms responsible for the formation of existing flat slabs will help us understand if they can be scaled up to match predictions for paleo-flat slabs. There are a number of proposed contributing factors to the formation of flat slab subduction, including ridge subduction, rapid overriding plate velocity and trenchward motion of a thick cratonic root. In this dissertation I investigate the role of Nazca ridge subduction on the formation of Peruvian flat slab in Chapter 1 and Chapter 2.

Previous studies of the geometry of the subducted Nazca plate in central and southern Peru have had to rely on primarily teleseismic data or local data collected from small seismic network. In Chapter 1 I determined the geometry of the subducting Nazca slab beneath central

and southern Peru using data from the three recently deployed local seismic networks. I determined new contours of the slab geometry between 9° and 18°S using 508 relocated hypocenters and constraints from teleseismic surface wave tomography. This region offers a unique opportunity to study the link between ridge buoyancy and occurrence of the flat slab in general because of the unique ridge geometry relative to the convergence direction of the plates. My results show that the shallowest portion of the southern Peruvian flat slab is either at or just south of the subducted Nazca Ridge and events deepens to the north in the region of previously proposed flat or even shallower slab geometries. The fact that the shallowest portion of the Nazca plate is straddling the ridge and events deepen along strike and away from the ridge has important implications for the ridge buoyancy hypothesis. My relocated hypocenters also indicate an absence of seismicity along the projected location of the subducting Nazca Ridge, which is likely due to an absence of mantle hydrous phases beneath the overthickened crust of the Nazca Ridge. This provides an important insight for the genesis of intermediate depth seismicity.

The distribution of earthquake hypocenters as determined in Chapter 1 indicates strong along-strike variability in the slab geometry, from flat slab subduction north of 15 °S, to uniform normal subduction south of 15 °S. In Chapter 2 I obtained high quality focal mechanisms for intermediate depth events to investigate how the slab is deforming along strike. South of the Nazca Ridge, my results suggest uniform extension in the slab down dip of the ridge. Down dip tension is consistent with a highly deformed slab, but no tearing between the normally dipping plate and the flat slab along the Nazca Ridge. North of the Nazca Ridge, the T-axes are largely ridge-parallel in map view, but with a distinct downward dip that is not parallel to the slab. These steeply dipping T-axes differ from the expected stress pattern for a fully supported flat slab and indicate that the flat slab north of the ridge may not stable.

South of the Peruvian flat slab, the Central Andean Plateau (i.e. Altiplano-Puna plateau) is the second largest tectonically active orogen along the western margin of South America. This plateau has influenced both local and far field lithospheric deformation, global sediment flux, atmospheric circulation and climate since the early Miocene. Significant geologic and geophysical efforts have been made to constrain the tectonomorphic evolution of the central Andean plateau, yet the role of surface and deep lithospheric processes in the evolution of the plateau is unclear. Existing theories predict two contrasting models of rapid and recent versus slow and steady uplift for the temporal evolution of the Central Andean Plateau. One possible discriminating factor between these two theories is seismic evidence for the presence or absence of mantle lithosphere. In Chapter 3 I investigate the current state of lithospheric structure below the northern Altiplano, northernmost portion of the Central Andean Plateau, in southern Peru and northern Bolivia. My results indicate an absence of a high velocity lower crust beneath the northern Altiplano, suggesting a weak lower crust of felsic composition or the loss of a high velocity mafic lower crust due to delamination. The upper mantle under the northern Altiplano is heterogeneous, consistent with piecemeal delamination. My tomography results for the lower crust and upper mantle beneath the northern Altiplano are in better agreement with the slow and steady uplift model.

I dedicate my thesis work to my loving family. A remarkable feeling of thankfulness to my loving parents, Nawindra Kumar Mishra and Savita Mishra whose words of encouragement and appreciation ring in my ears. My sisters Nibha and Pratibha always supported me and are very special. My nephew Valentino and my niece Palak have been great source of joy.

I dedicate this work and give exceptional thanks to my elder brother and my best friend Santosh Kumar for being there for me throughout the entire doctorate program. You have been my biggest support ever.

I remarkably dedicate this thesis to my loving wife Priyanka and my four-month-old adorable daughter Laavanya for their unconditional support.

ACKNOWLEDGEMENTS

I would like to thank, first and foremost my research advisor Lara Wagner for her support, inspiration, giving me opportunity to work on CAUGHT and PULSE project, and her significant contribution to the ideas presented in this dissertation. My dissertation would not have been possible without financial support through the Department of Geological Sciences, University of North Carolina at Chapel Hill, and grants awarded to my research adviser through the National Science Foundation.

I would like to thank the rest of my committee members for their countless hours of reading, encouraging remarks and scientific guidance.

This dissertation work was strongly encouraged from the exchange of ideas from many people within and outside of the University of North Carolina, and I would like extend special thanks to Sanja Knezevic Antonijevic, C. Berk Biryol, Jesse Hill, Keehoon Kim, Daniel Bowman, Kevin M. Ward, and Linda M. Warren.

Special thanks goes to Deborah Harris and Liz Steadman for the administrative support.

TABLE OF CONTENTS

LIST OF TABLES

LIST OF FIGURES

Chapter 1: Geometry of the subducting Nazca plate in the Peruvian flat slab region of central and southern Peru

ABSTRACT

I have determined the geometry of the subducting Nazca slab beneath central and southern Peru using data from the three recently deployed local seismic networks. This region offers a unique opportunity to study the link between Nazca Ridge buoyancy and occurrence of the flat slab in southern Peru, where the subducting Nazca plate flattens at ~100 km depth and then extends horizontally for several hundreds kilometers before resuming normal subduction. I determined new contours of the slab geometry between 9° and 18°S using 508 relocated hypocenters and constraints from teleseismic surface wave tomography. My slab contours have subtle but important differences from the other previous slab geometries for this region in several key aspects. My relocated hypocenters suggest that the shallowest portion of the southern Peruvian flat slab is either at or just south of the subducted Nazca Ridge, with a significant deepening of hypocenters to the north where previous models have reported flat or even shallower slab geometries. The fact that the shallowest portion of the Nazca plate is straddling the ridge and events deepen along strike and away from the ridge has important implications for the ridge buoyancy hypothesis. I also observe an absence of seismicity along the projected Nazca Ridge track in the horizontally subducting portion of the slab. I interpret this as possibly indicative of an absence of water in the mantle beneath the overthickened crust of the Nazca Ridge. This may provide important new constraints on the conditions required to produce intermediate depth seismicity.

1. INTRODUCTION AND TECTONIC SETTING

Flat slab subduction refers to subduction zones where the downgoing slab subducts normally (~30° dip) to a depth of ~100 km and then abruptly bends to travel horizontally for several hundred kilometers before resuming its descent (Hasegawa & Sacks, 1981; Cahill & Isacks, 1992). The depth of flattening and inboard extent of the horizontal segment varies between different regions of flat slab subduction for reasons that are not well understood (Gutscher et al., 2000). Flat slab subduction is of particular interest because it has often been causally linked to unusual tectonic processes such as the cessation of arc volcanism, inboard thick-skinned deformation of the overriding plate and the evolution of high plateaus (e.g. Isacks & Barazangi, 1977; Cross & Pilger, 1982; Jordan & Allmendinger, 1986; James & Sacks, 1999; Gutscher et al., 2000). In particular, the Laramide uplift of the Rocky Mountains and subsequent ignimbrite flare-up in the western United States has been attributed to a period of flat subduction of the Farallon plate (80-55 Ma) (e.g. Dickinson & Snyder, 1978; Humphreys et al., 2003).

There are a number of proposed contributing factors to the formation of flat slab subduction. These include: (1) the subduction of seafloor heterogeneities including buoyant aseismic ridges and volcanic seamount chains (Sacks 1983, Gutscher et al., 2000, van Hunen et al., 2002; Arrial & Billen, 2013); (2) rapid overriding plate motion and associated trench retreat (van Hunen et al., 2002; Lallemand et al., 2005; Heuret et al., 2007). (3) a critical yield strength of the slab below which bending becomes possible (van Hunen et al., 2002, 2004); (4) a young age (<50 Ma) of the subducting slab resulting in a low average density and less negative buoyancy (Vlaar & Wortel, 1976; Wortel & Vlaar, 1978; Barazangi & Isacks, 1979, Sacks, 1983); (5) the trenchward motion of a thick cratonic root in the overriding lithosphere (O' Driscoll et al., 2009; Manea et al., 2012); and (6) an increase in hydrodynamic suction forces between the overriding and the subducting plates (Jischke, 1975; van Hunen et al., 2004; Billen & Hirth, 2005; Manea et al., 2012). Of these proposed mechanisms, the first is perhaps the most commonly cited and the most controversial. The basic premise is that both the over thickened basaltic crust of the oceanic ridge and the underlying layer of harzburgite are less dense than undepleted mantle peridotite resulting in neutral buoyancy at some depth (~80-100 km). Espurt et al. (2008) used a 3D viscoelastic model and suggested a necessary contribution from ridge buoyancy in the formation of flat slabs. On the other hand, a recent plate tectonic reconstruction study by Skinner and Clayton (2013) appear to indicate no clear correlation between ridge subduction and flat or shallowly dipping slabs worldwide. Other studies have indicated that, while buoyant bathymetric features may play a role, they are not required for the formation of flat slab. For example, van Hunen et al. (2004) use 2D numerical model to simulate the conditions for present day flat slab subduction in Peru and attribute its formation solely due to rapidly overriding South American (SA) plate. Another numerical modeling study by Gerya et al. (2009) proposes a high overriding plate velocity as the main contributing factor for the formation of flat slabs and argues for an insignificant contribution of ridge buoyancy to slab flattening.

To address the question of how much ridges contribute to slab flattening, I have studied the southern portion of the Peruvian flat slab (Figure 1.1). The western margin of Peru between 2° and 15° S is characterized by the flat subduction of the oceanic Nazca plate beneath the continental South American plate (Barazangi & Isacks, 1976; Hasegawa & Sacks, 1981; Bevis & Isacks, 1984; Cahill & Isacks, 1992; Araujo & Suarez, 1994; Hayes et al., 2012; Dougherty & Clayton, 2014). Previous seismicity studies in Peru reveal normal subduction (dip angle ~30^{o}) for the first 100 km of descent. Below this depth, the slab bends to form a flat slab with a nearly horizontal dip angle and an observed inboard extent of ~700 km from the trench axis before it resumes normal subduction further to the east (e.g. Barazangi & Isacks, 1976, 1979; Hasegawa & Sacks, 1981; Sacks, 1983; McGeary et al., 1985; Cahill & Isacks, 1992). The Peruvian flat slab is associated with the marked absence of any known Quaternary arc volcanism and with generally low surface heat flow measurements (Noble et al., 1974; McGeary et al., 1985, Henry & Pollack, 1988; Hamza & Munoz, 1996). Previous studies on the geometry of the Peruvian flat slab suggest that it has a far greater along strike extent than other modern flat slabs (e.g. the Pampean flat slab in central Chile) (Barazangi & Isacks, 1976; Cahill & Isacks, 1992).

The southern Peruvian flat slab is an ideal location to evaluate the role of ridges on the evolution of the flat slabs in general because of the unique ridge geometry relative to the convergence direction of the plates. The trend of the Nazca Ridge and the convergence direction are not parallel (Figure 1.1) and consequently the ridge has been migrating southward relative to the overriding plate. Since it first began subducting ~11.2 Ma at ~11°S (Hampel, 2002), the ridge has migrated ~480 km south along the South American continental margin, and is currently subducting at 15° S (Hampel, 2002; Hampel et al., 2004). The timing of slab flattening is well constrained by radiometric ages of the cessation of arc volcanism, episodes of intense metallogenic activity (Rosenbaum et al., 2005) and basement involved thrust deformation (Shira uplift) on the overriding South American plate (Kley et al., 1999; Bissig et al., 2008; Ramos & Folguera, 2009).

My current study provides a detailed analysis of WBZ earthquake locations, hypocentral errors, and the state of stress (discussed in chapter 2) in the subducting Nazca plate in central and southern Peru and northern Bolivia. I include a local dataset of earthquake locations between 10°-18.5° S, which constitutes the flat slab region as well as the region of the slab that transitions from flat to regular subduction in southernmost Peru. I use my complete catalog of intermediate depth seismicity, in conjunction with constraints from Knezevic Antonijevic et al. (2015) and the updated teleseismic body wave tomography results of Scire et al. (2015) to calculate the most accurate contours to date of the slab geometry up to 200 km depth. My results indicate subtle but important differences between my slab geometry and that of Cahill and Isacks (1992), Kirby et al. (1995), and Hayes et al. (2012). I observe that the shallowest portion of the southern Peruvian flat slab coincides with either the projected location of the subducting Nazca Ridge or the area immediately south of it. I also notice a subtle deepening of events north of the Nazca Ridge, along the northern margin of the proposed flat slab. The fact that the shallowest portion of the Nazca plate is straddling the ridge and events deepen along strike and away from the ridge has important implications for the ridge buoyancy hypothesis. Along the projected ridge track, I observe a lack of seismicity, which is markedly different than the Juan Fernandez ridge associated with central Chile flat slab (Anderson et al., 2007, Hayes et al., 2012). I also notice a smooth continuation of seismicity across the slab dip transition at ~15 °S. This is consistent with a deformed slab rather than a tear between the ridge and a negatively buoyant normal slab further to the south.

2. DATA

I use data collected from the temporary broadband stations of three independent seismic arrays (Figure 1.1): The CAUGHT (**C**entral **A**ndean **U**plifts and **G**eodynamics of **H**igh **T**opography) experiment comprised 50 broadband seismometers deployed for 21 months between November, 2010 and July, 2012 between 13°S to 18°S across the northern Altiplano. Thirty stations were deployed in Bolivia and 20 stations in Peru with a higher density line across the cordillera that spanned both Peru and Bolivia. The "PULSE" (**P**er**U** **L**ithosphere and **S**lab **E**xperiment) network was deployed from May 2011 to June 2013 and consists of 40 broadband seismometers. The PULSE network is concentrated above the Peruvian flat slab roughly along three transects. The southern transect extends north and east from the city of Nazca to beyond Cusco. The middle and northern transects are located between Pisco and Ayacucho, and Lima and Satipo respectively. The northern transect is situated above the paleo-location of the subducted Nazca Ridge between 10-8 Ma (Rosenbaum et al., 2005). The southern and middle transects straddle the projected current location of the subducted Nazca Ridge. I also use data from the PERUSE project deployed by the California Institute of Technology and UCLA between July 2008 and June 2012. I use data for 8 stations from this deployment that lie along the coast in southern Peru and the southern transect of the PULSE network. The overall contributions (Figure 1.2) from individual CAUGHT stations are more than the PULSE and PERUSE stations in the location process due to more impulsive phase arrivals. The stations along the northernmost transect of the PULSE network had the least contribution to event locations. This is due to the relative sparsity of WBZ seismicity beneath the PULSE network, so arrivals had to travel further and were often diffracted, resulting in their emergent character.

3. METHODS

I auto-detect possible earthquakes recorded by three arrays using the dbdetect tool that is part of the ANTELOPE software package (http://www.brtt.com). This method is based on a short-term average (STA) versus long-term average (LTA) trigger mechanism. An event is detected if the ratio of energy between STA and LTA window exceeds a user-defined threshold. I use an energy threshold ratio of 5 and STA and LTA moving time windows of 1 second and 10 seconds respectively. Of the 3000 possible events identified, I selected 952 earthquakes after individual inspection of the seismic waveforms for each event.

I calculate absolute event hypocenter locations using the single event location algorithm HYP (Lienert & Havskov, 1995), incorporated into the SEISAN software package (Havskov & Ottemöeller, 1999; Ottemöeller et al., 2011). HYP determines earthquake locations using an iterative linearized least squares inversion of travel time data (Aki & Lee, 1976). I handpick P-arrivals on the vertical component and utilize the travel time information to find event location and back azimuth. The N-S and E-W components are rotated into radial and transverse components based on the event back azimuth. The S-arrivals are marked on the transverse component to avoid contamination from the phase converted SV arrivals and the events were relocated using P and SH travel time data. Phase readings utilized for the event locations are accomplished by MULPLT program available in the software package SEISAN [Havskov & Ottemöeller, 1999; Ottemöeller et al., 2011]. I use a modified version of the P-wave velocity model of Dorbath & Granet (1996) that takes into account the 65 km average crustal thickness in my study area as determined from recent analyses of teleseismic receiver functions (Phillips & Clayton, 2014; Bishop et al., 2014). S-wave velocities are determined using a Vp/Vs ratio of 1.75.

In order to determine the sensitivity of my event locations to starting depth, I calculate the hypocenters of all 952 events with a starting depth of 5 km, 100 km, 200 km, and the initial origin depth from dbdetect. Of the 952 events, 838 had event depths that varied by less than 10 km over all starting depths tested. From those 838 events, I then select events with depths greater than 50 km and azimuthal gaps < 270°. For events south of 15° S, I eliminate those events with depth errors of > 15 km. Given the sparsity of seismicity north of 15°S, I include some events with slightly larger depth errors whose latitudes, longitudes, and depths are stable over all tested starting depths. After these criteria are applied, I am left with 568 stable event locations.

I add to this list by investigating those 114 events where the range of event depths determined with different starting depths was > 10 km. I divide this list of 114 events into two sets depending on the number of similar depths recovered from my four starting depths. The first set of events includes 45 earthquakes for which three of the four original hypocentral locations differ in depth by less than 10 km. I calculate travel time residuals corresponding to each of the three starting depths and select the location with the minimum travel time residual as my preferred hypocenter. If travel time residuals are the same for more than one starting depth then I select the location whose starting depth is closest to the hypocentral depth. I recalculate event locations for each event in the first set using their best starting depth and obtain 16 robust event locations following the same cutoff criteria as used previously (e.g. depth > 50 km, azimuthal gap < 270°, with less than 15 km error in depth).

The second set of events includes 68 earthquakes for which the hypocenters corresponding to the four starting depths (5 km, 100 km, 200 km and the initial origin depth from dbdetect) have two or fewer final depths that are within 10 km of each other. I test several other starting depths at 25 km intervals for each of these events and calculate travel time residuals corresponding to each starting depth. I look for at least 3 similar depths (< 10 km difference) recovered from inversions with three adjacent starting depths, and travel time residuals of less than 3 seconds. Using these criteria, I obtain hypocentral locations for 36 events. I recalculate event locations for each event using their best starting depths and obtain 7 event locations that satisfy the additional aforementioned cutoff criteria (e.g. depth > 50 km, azimuthal gap < 270°, with less than 15 km error in depth). I finally add these 23 robust event locations (16 from the first group and 7 from the second) to the 568 events described earlier for a total of 591 robust event hypocenters (Table 1.1).

I relocate these 591 events using the double difference technique of Waldhauser & Ellsworth (2000). This method takes advantage of the nearly identical ray paths of two nearby events recorded at a common station. HypoDD uses both absolute and relative travel time data for each pair of events to determine relative event locations that are independent of regional structural variations. I calculate differential times between common phases recorded at a common station for all events pairs separated by ≤ 40km. Each event is grouped to a maximum of 10 neighboring events with inter-event distance ≤ 40km, each of which must have at least eight differential travel time observations. Of the 591 events located using HYP, I am able to relocate 508 events with HypoDD (Table 1.2). The remaining 83 events do not have sufficient neighboring earthquakes at small inter-event distances (≤ 40km) for stable relative relocation.

I determine new slab contours to describe the geometry of the subducting Nazca slab. The contours of the flat slab take into account the 508 HypoDD relocated earthquake locations where seismicity is present, and the tomography results of Knezevic Antonijevic et al. (2015) elsewhere. I define contours such that, with few exceptions, the observed seismicity is below the surface I am defining. This means that my slab surface is designed to indicate the top of the subducted slab, to the best of my ability to resolve it. At greater depths, my contours are consistent with available deep seismicity and with the latest teleseismic body wave tomography results indicating the location of the slab at depths > 300 km (Scire et al., 2015). The location of the slab inboard of the flat slab is also consistent with seismic reflections observed by James & Snoke (1990). I then use the triangulate and surface functions of Generic Mapping Tools (Wessel & Smith, 1991) to contour my slab geometry.

4. RESULTS

4.1. Earthquake location

The results of my single event locations and relative relocations are shown in Figures 1.3 and 1.4 respectively. Overall, my event depths are significantly shallower than those reported from global catalogs or previous slab geometry studies. I test the sensitivity of my event hypocenters to velocity models by subtracting and adding 5% to each layer in my velocity model. The results of these are shown in Figures 1.6 and 1.7. The average depth for the fast model is 0.86 km deeper than my preferred model, and the average depth for the slow model is 0.79 km shallower than my preferred model. The average spread in the depths of hypocenters for a given event between velocity models is 7 km with a standard deviation of 6 km. The most significant differences are seen for the deepest events with the longest travel paths, as expected. While individual events have slight differences in depth depending on the velocity model used, the overall patterns observed remain robust.

In general the relative event locations determined using HypoDD produce more tightly clustered hypocenters than the single event locations (Figure 1.8). My results allow me to resolve clearly a number of patterns that, while visible in previous studies (e.g. Cahill & Isacks, 1992; Gorbatov et al., 1996, Hayes et al., 2012) and in global catalogs (e.g. Advanced National Seismic System (ANSS) catalogs), have not been explicitly identified or discussed (Figs. 1.4 and 1.5).

My southernmost cluster (labeled "A") comprises a linear, northward trending band of seismicity between 69°W to 70°W. The distinct eastern margin of this cluster is well resolved, and is visible in previously existing catalogs of seismicity, albeit less clearly. The north-south trend of this cluster does not correspond to the local dip direction of the slab, the convergence direction of the plates, or any known structure within the subducted plate. The seismicity in this region generally defines a slab descending at a constant dip of ~30° (measured trench orthogonally) to at least 270 km depth (cross section P7-P10, Figure 1.12).

Seismicity is laterally continuous between clusters A and B at depths of < 120km. However, at greater depths I find evidence of a small seismic gap, triangular in shape (shaded triangle, Figure 1.4). This gap is concentrated in the middle of my seismic network, directly beneath one of the CAUGHT stations (CP07), and so is unlikely due to a lack of seismic observations. I also noticed a small gap in seismicity in the ANSS earthquake catalog of this area (Figure 1.5). The next cluster to the north (labeled B, Figure 1.4) comprises a large number of events between the northwest edge of the triangular seismic gap and the southern edge of the projected location of Nazca ridge. Events along the northern edge of this cluster, in the immediate vicinity of the projected location of subducted Nazca Ridge, are the shallowest I have found within the flat slab. There is a continuous increase in event depths within this cluster both from north to south as well as from west to east, showing a smooth contortion of the slab.

Between clusters B and C, along the projected location of the subducted Nazca ridge, seismicity is anomalously low at depths below 80 km (shaded rectangle, Figure 1.4; dotted ellipse, cross section BB′ in Figure 1.10). This observation is distinctly different than the reported seismicity along the Juan Fernandez ridge track in central Chile where seismicity is particularly abundant (Anderson et al., 2007, Hayes et al., 2012). The drop in the number of slab events along the Nazca ridge in this area is however consistent with the previous observations (Barazangi & Isacks 1976, Cahill & Isacks 1992, Hayes et al., 2012, Dougherty & Clayton, 2014). I also observe a marked decrease in seismicity along the Nazca Ridge for the events reported in the ANSS catalog in last 40 years (Figure 1.5, shaded area).

The trench parallel cluster C (Figure 1.4) beneath the Western Cordillera, north of the Nazca Ridge, is confined to the westernmost margin of the horizontal portion of the flat slab. This defines its own linear cluster of events, connecting the diffuse seismicity along the northern edge of PULSE network and seismic gap along the projected location of the subducted Nazca ridge. I find very few events inboard of this cluster except for a small number of relatively shallow events with depths between 50 and 70 km for which I am unable to determine relative relocations (Fig. 1.3).

Along the northernmost end of my study area, the observed slab seismicity (denoted as cluster D in Figure 1.4) has a maximum inboard extent of over 400km from the trench. The events in this cluster are generally diffuse and range in depth from ~100 to 120 km, significantly deeper than events found closer to the Nazca Ridge further south.

4.2. Slab geometry

My new slab contours refer to the top of the Wadati-Benioff zone (WBZ) (Figure 1.13). This is similar to Barazangi & Isacks (1976), but different from Cahill & Isacks (1992) and Kirby et al. (1995) who took the middle of the WBZ to define the slab geometry. South of 15°S, I can clearly see the normally dipping slab up to 250 km depth. My event locations define the change in dip from flat to normal, indicating a continuous but contorted plate between the flat and steep segments of the slab as previously reported by Bevis & Isacks

(1984), Schneider & Sacks (1987), Cahill & Isacks (1992), Phillips & Clayton (2014), and Dougherty & Clayton (2014). The inboard extent of my flat slab is dominantly defined by the Rayleigh wave results of Knezevic Antonijevic et al. (2015) due to the lack of flat slab seismicity more than 200 km from the trench. North of the ridge, my slab contours reflect the distinct deepening of the inboard seismicity relative to events located directly adjacent to the ridge. Following the results of Knezevic Antonijevic et al. (2015), I include the presence of a slab tear located in an area with very sparse seismicity (shaded pink area, Figure 1.13). The northernmost extent of this tear is not resolved by this study due to a lack of data north of the northernmost PULSE stations. East of this tear, the subhorizontal seismicity (transect P1, Fig. 1.11) occurs within the remnant flat slab (RFS) (east of shaded pink area, Fig. 1.13). I am not able to constrain the easternmost extent of RFS due to the lack of data east of my deployment.

DISCUSSION

5.1. New constraints on Slab Geometry and the causes of flat slab subduction

In the southernmost portion of my study area, my slab contours are in general agreement with Cahill & Isacks (1992) (Figure 1.13), Kirby et al. (1995), and Hayes et al. (2012) near the slab-dip transition zone at ~15°S. However, north of 15°S my models diverge significantly. Notably, I observe a significant difference between previous slab models and my model in the relative depth of the slab at the ridge compared to the depth of seismicity further to the north (Fig. 1.13). Previous models either show a perfectly flat slab (Cahill and Isacks, 1992; Kirby et al., 1995) or a shallowing of the slab well north of the Nazca Ridge (Hayes et al., 2012). My model shows that the slab is shallowest either at or along the subducted Nazca Ridge. While differences between my study and previous ones in velocity models or definitions of the slab surface relative to the WBZ could account for uniform variations in depth, relative differences in depth along the flat slab are unlikely to be artifacts of velocity model or slab boundary definitions.

The slab contours of Cahill & Isacks (1992) suggest a wide flat slab with an inboard extent of ~600 km along its entire length. Kirby et al. (1995) and Hayes et al. (2012) show flat slabs of smaller width with small along strike variations in the inboard extent of the flat slab. The maximum inboard extent of my flat slab is constrained by the Rayleigh wave tomography results (Knezevic Antonijevic et al., 2015). My slab width to the northeast is consistent with the receiver function results of Bishop et al. (2014), but is considerably broader than the receiver function study of Phillips and Clayton (2014). This could be due to the broader spatial extent of the seismic networks used in the present study.

My new slab geometry is consistent with that of a buoyant ridge that is migrating southward along the South American margin (Anderson et al., 2007, Knezevic Antonijevic et al., 2015). My event hypocenters are shallowest (~80 km) directly along the Nazca Ridge (Figure 1.4). To the north, beneath the portion of the South American continent beneath which the Nazca Ridge passed over the past 11 Ma, I observe a marked deepening of the WBZ. I have additional constraints from the state of stress in the Nazca plate from focal mechanisms and they are also in agreement with deepening of slab north of the Nazca Ridge (Refer: Chapter 2, for more detailed discussion). This is consistent with the interpretation that in the absence of ridge buoyancy, other contributing factors to the formation of flat slabs are not sufficient to maintain the flat slab. Instead, the existing flat slab begins to sag, and, as proposed by Knezevic Antonijevic et al. (2015) may also tear, allowing newly subducted slab north of the ridge to subduct at a normal dip angle.

5.2. Abrupt variations in seismicity within the subducted Nazca plate

The earthquake locations show abrupt spatial changes in seismic activity across my study area. Most of the patterns I observe are also visible in event locations from earlier studies (e.g. Cahill & Isacks, 1992; Gorbatov et al., 1996, Hayes et al., 2012) and global catalogs (e.g. International Seismological Center (ISC) and Advanced National Seismic System (ANSS)) but have not previously been discussed in any detail. While many of these are difficult to explain, I propose that one may in fact provide clues into processes involved in the genesis of intermediate depth earthquakes. Along the projected location of the Nazca Ridge, I observe a marked gap in seismicity within the flat slab (Figs 1.4 and 1.10). Given that other factors such as temperature, plate age, and pressure do not vary over these small distance ranges, one possible explanation for this change in seismicity could be related to differences in crustal thickness and the causes of intermediate depth seismicity.

While the causes of intermediate depth seismicity remain a subject of ongoing research, dehydration embrittlement likely plays a significant role in the genesis of these events in subduction zones worldwide. As the oceanic plate starts to subduct, it undergoes significant bending seaward of the trench axis and produces outer rise normal faults (Chapple & Forsyth, 1979; Kirby et al., 1996; Peacock, 2001). Previous studies have found evidence for seawater infiltration through these outer rise faults (Hussong et al., 1988). This seawater infiltration results in the formation of hydrous minerals along these fault planes to depths of 15-20 km or more (Peacock, 2001; Ranero et al., 2003; Grevemeyer et al., 2005; Marot et al., 2012). The breakdown of hydrous minerals at appropriate P-T condition can lead to increases in pore pressure that decrease hydrostatic pressure and hence promote brittle failure required for intermediate depth seismicity (Raleigh & Paterson, 1965; Green & Houston, 1995; Kirby et al., 1995; Hacker et al., 2003; van Keken et al., 2011).

The Nazca Ridge has abnormally thick crust (~17 km) compared to the normal ~ 7 km thick oceanic crust on either side of it (Woods & Okal, 1994; Tassara et al., 2006). I propose that the crust along the Nazca Ridge is thicker than the penetration depth of water into the outer rise faults in this area. This would mean that only the oceanic crust (not the oceanic mantle lithosphere) is hydrated along the Nazca Ridge, resulting in an absence of typical mantle hydrous phases (e.g. antigorite, talc, chlorite). In contrast, the outer rise faults in the normal oceanic plate on either side of the ridge would contain both crustal and upper mantle hydrous phases. Seismicity up to ~80 km depth, close to the trench, is relatively continuously distributed along strike. I hypothesize that this along strike continuity in seismicity, up-dip from the horizontal portion of the flat slab, is related to the dehydration of hydrous minerals in the oceanic crust both within the ridge and in the normal crust on either side. I further propose that by 80 km depth, the crust is either dehydrated or the remaining hydrous phases are stable at the existing P/T conditions along the flat slab and therefore do not produce sufficient pore pressure to induce seismicity. Earthquakes that do occur north and south of the ridge along the flat portion of the slab are then caused by the dehydration of hydrated mantle lithosphere, not crust. The metamorphic reactions, associated with the dehydration of subducting oceanic lithosphere, strongly depend on temperature (Peacock, 2009). In Peru, the southern portion of the flat slab has only recently assumed its current geometry, making steady state thermal models (e.g. English et al., 2003) inappropriate for this area. Further work to better constrain the likely temperatures across the Peruvian flat slab and the effect of these temperatures on dehydration reactions are needed to test these hypotheses and better understand the unusual patterns of observed seismicity across the subducted Nazca Ridge.

6. CONCLUSIONS

Previous studies on the geometry of the subducted Nazca plate in central and southern Peru have had to rely on primarily teleseismic data or local data collected from small seismic network. In this study, I use new data collected as part of three separate but temporally co-located deployments to study the WBZ of the subducted Nazca plate. This new data allows me to constrain subtle variations in the WBZ that provide important information about the geometry of the Nazca plate underneath central and southern Peru. The first of these observations is the shallowest portion on the southern Peruvian flat slab that coincides with either the projected location of the subducting Nazca Ridge or immediately south of it. This observation is significantly different than the previous slab models, which either show a perfectly flat slab (Cahill & Isacks, 1992; Kirby et al., 1995) or a shallowing of the slab well north of the Nazca Ridge (Hayes et al., 2012). The WBZ being shallowest along the Nazca ridge is consistent with the ridge buoyancy. I also notice a subtle deepening of events, north of the ridge, indicating that the older flat slab in the north is perhaps not stable. This suggests that irrespective of trench retreat and slab suction force, the long-term stability of the flat slab is perhaps not possible in the absence of ridge buoyancy.

Another intriguing observation is the lack of seismicity along the projected location of the subducting Nazca ridge track. This along strike variation in the slab seismicity across the ridge may suggest that by 80 km depth, the crust of the Nazca plate has dehydrated, and seismicity at these depths is due to mantle dehydration patterns alone.

7. ACKNOWLEDGMENTS

I am thankful to IRIS and personnel at the PASSCAL Instrument Center for their help and support throughout the CAUGHT and PULSE deployment. The seismic instruments were provided by UNC-Chapel Hill, Yale University, and the Incorporated Research Institutions for Seismology (IRIS) through the PASSCAL Instrument Center. I sincerely thank Dr. Hernando Tavera, Director, and C. Condori Quispe, of the Instituto Geofísico del Perú, Lima, Peru, and Dr. Estela Minaya of the San Calixto Observatory in Peru and for their help in deployment and demobilization efforts, as well as Mike Fort (PASSCAL) for his invaluable assistance in the field. The CAUGHT experiment was supported by NSF grants EAR-0908777 (Lara Wagner) and EAR-0907880 (Susan Beck). The PULSE experiment was funded by NSF grants EAR-0944184 (Lara Wagner), EAR-0943991 (Susan Beck), and EAR-0943962 (Maureen Long). Special thanks to C. Berk Biryol and S. Knezevic Antonijevic for helpful discussions. Maps were created using the Generic Mapping Tools (GMT) software (Wessel & Smith, 1991).

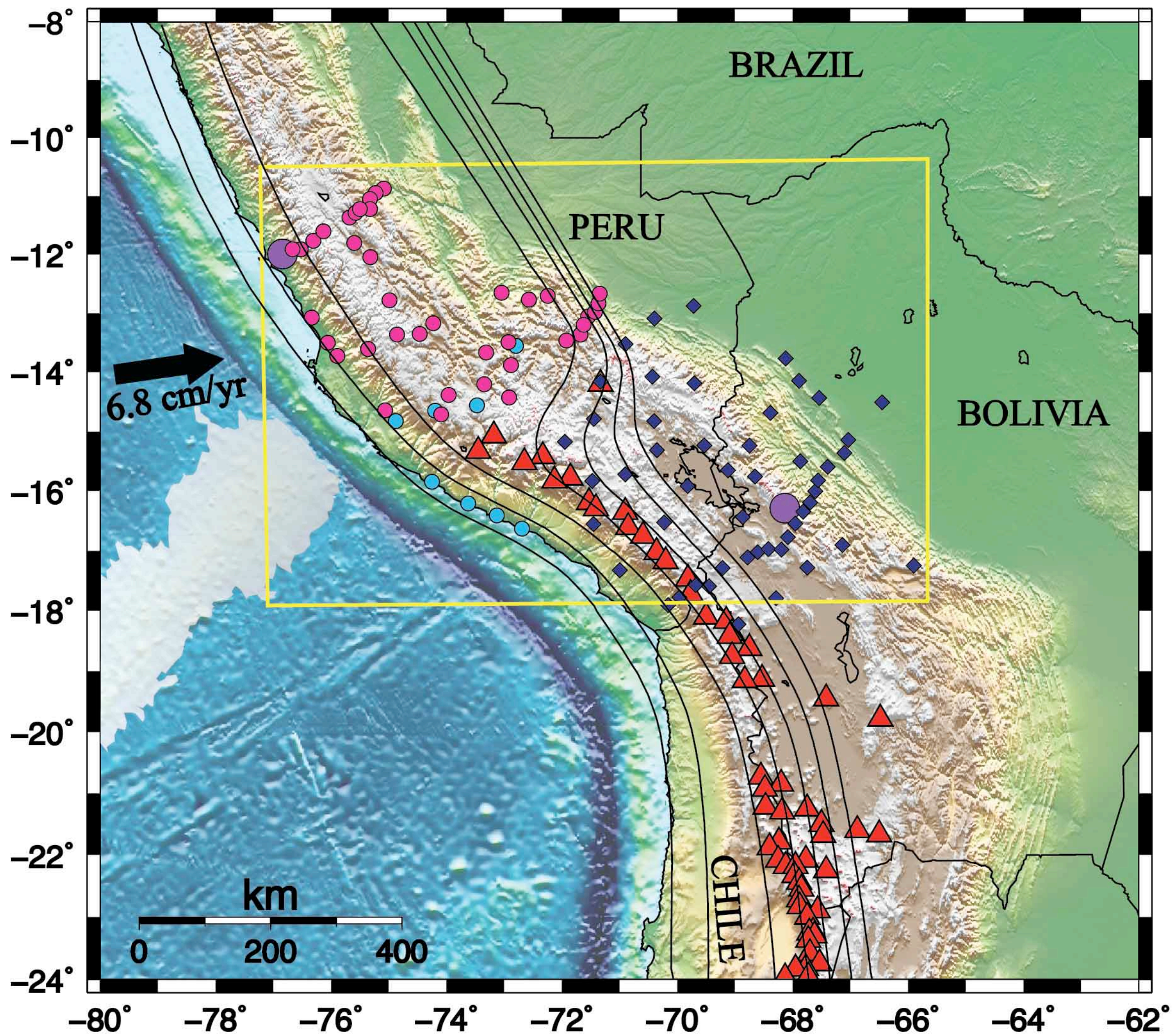

Figure 1.1- Map showing the Peruvian flat slab region, my current study area (yellow box), and location of seismic stations. Dark pink circles are PULSE stations. Dark blue diamonds are CAUGHT stations and light blue circles are PERUSE stations used in this study. Big purple circles represent GSN stations at Lima, Peru and LaPaz, Bolivia. Red triangles are Holocene volcanoes (INGEMMET, www.ingemmet.gob.pe). Solid lines are slab contours from Cahill & Isacks (1992). The light grey patch offshore represents the location of the Nazca Ridge. The black arrow offshore represents the plate motion of the Nazca plate from Hampel et al. (2004).

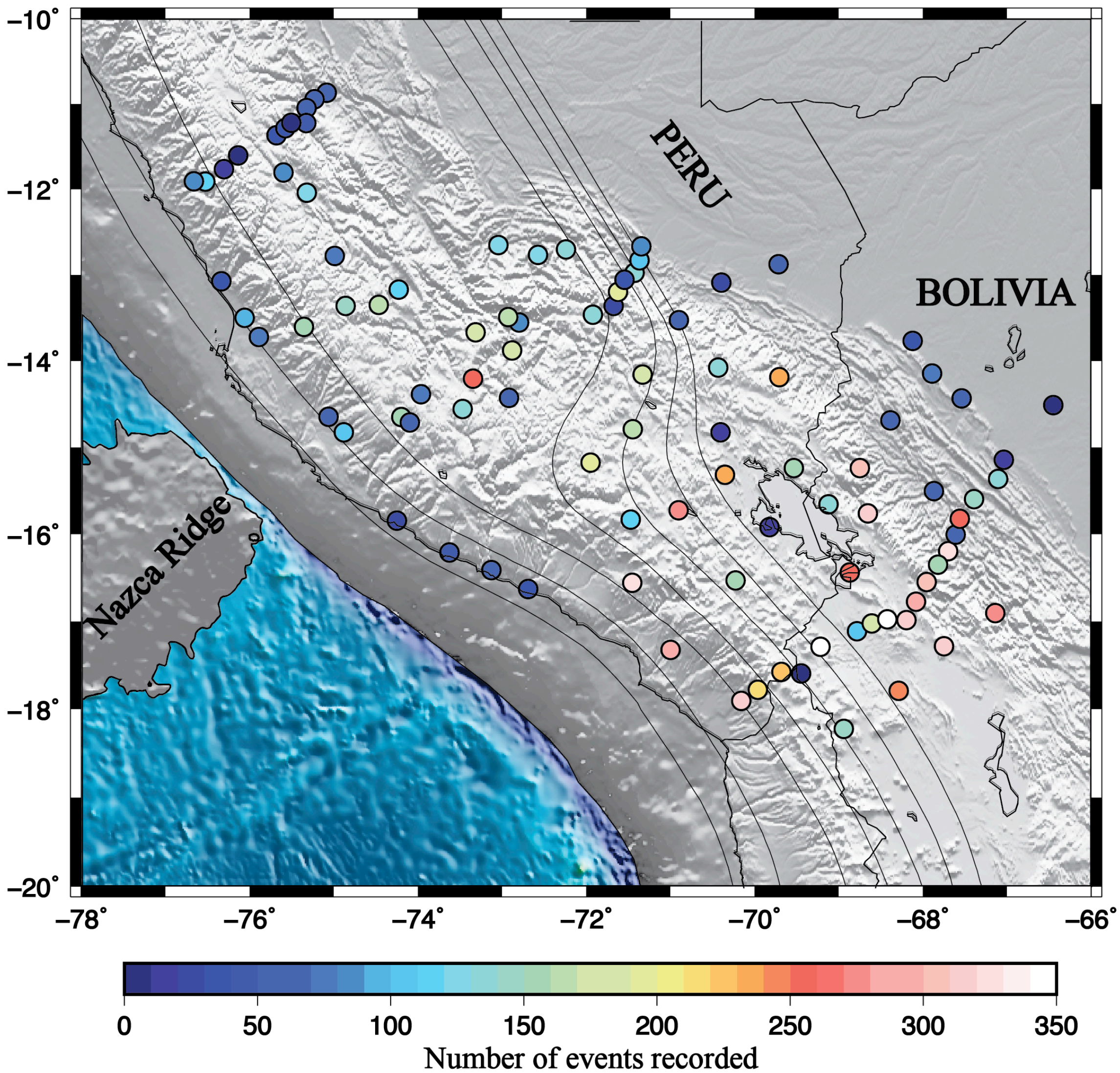

Figure 1.2- Map showing the contribution of individual station to the available dataset. Station symbols are color coded by the number of events recorded at each station.

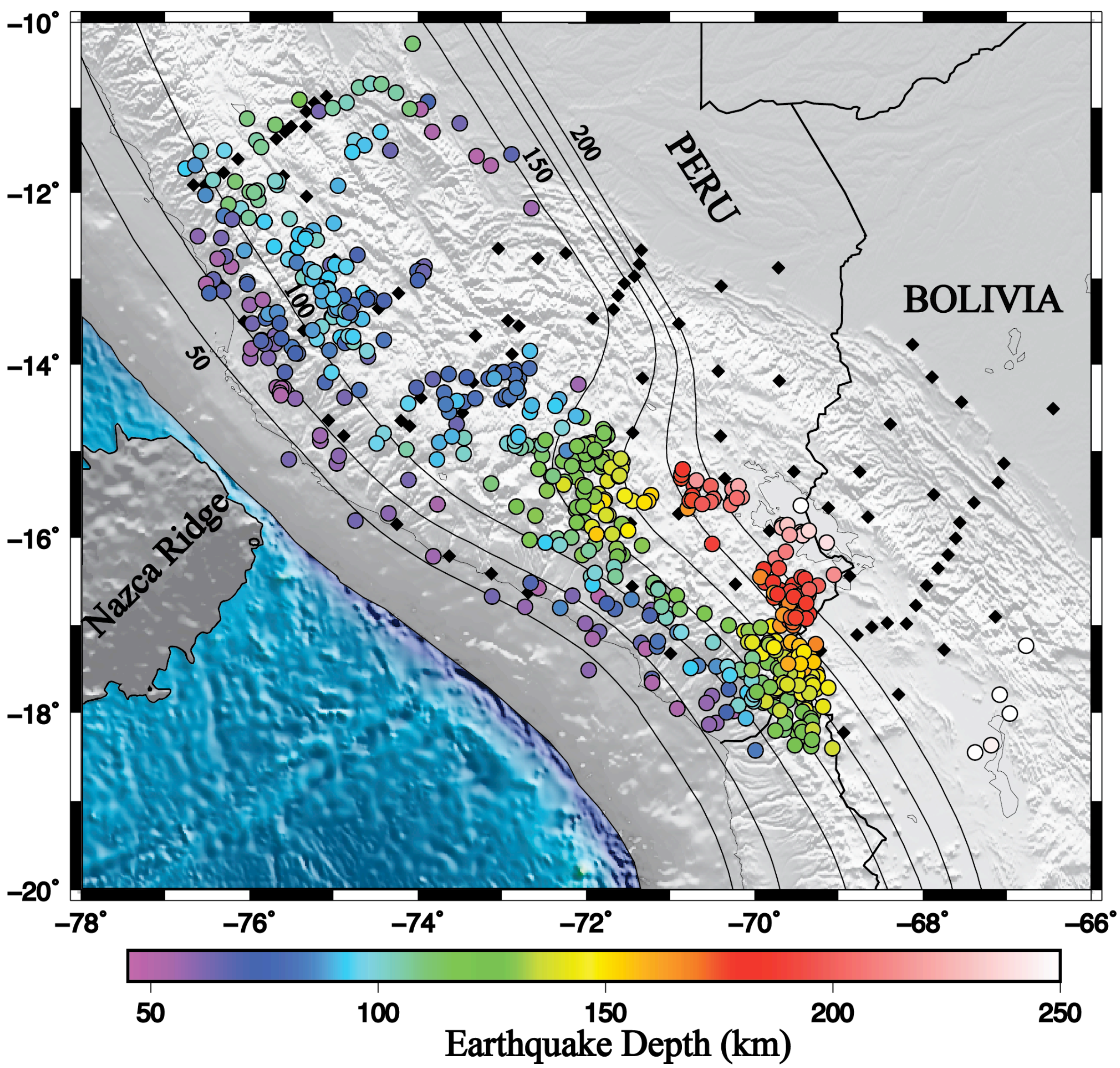

Figure 1.3- Earthquake hypocenters calculated using single event location method. The hypocenters are color coded by depth. Black diamonds are the stations used in the location process.

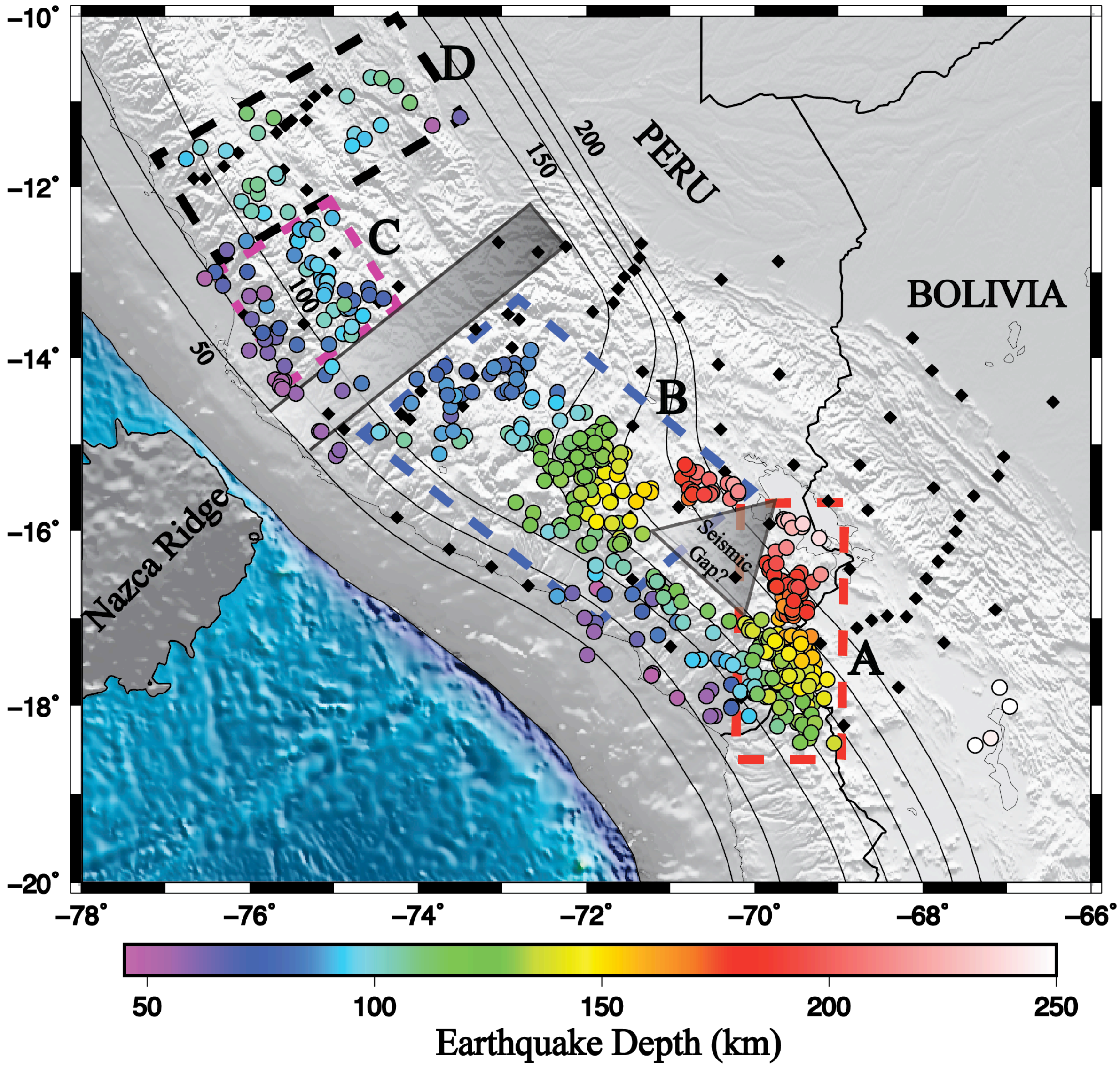

Figure 1.4- Earthquake hypocenters calculated using relative relocation method. The hypocenters are color coded by depth. Black diamonds are the stations used in the location process. Dashed boxes outline the regions of various clusters (A-D) of events identified in the study area. Shaded triangle represents the seismic gap between cluster A and B at depth ≥ 120 km. Note the absence of seismicity (shaded rectangle) along the projected location of the subducting Nazca Ridge.

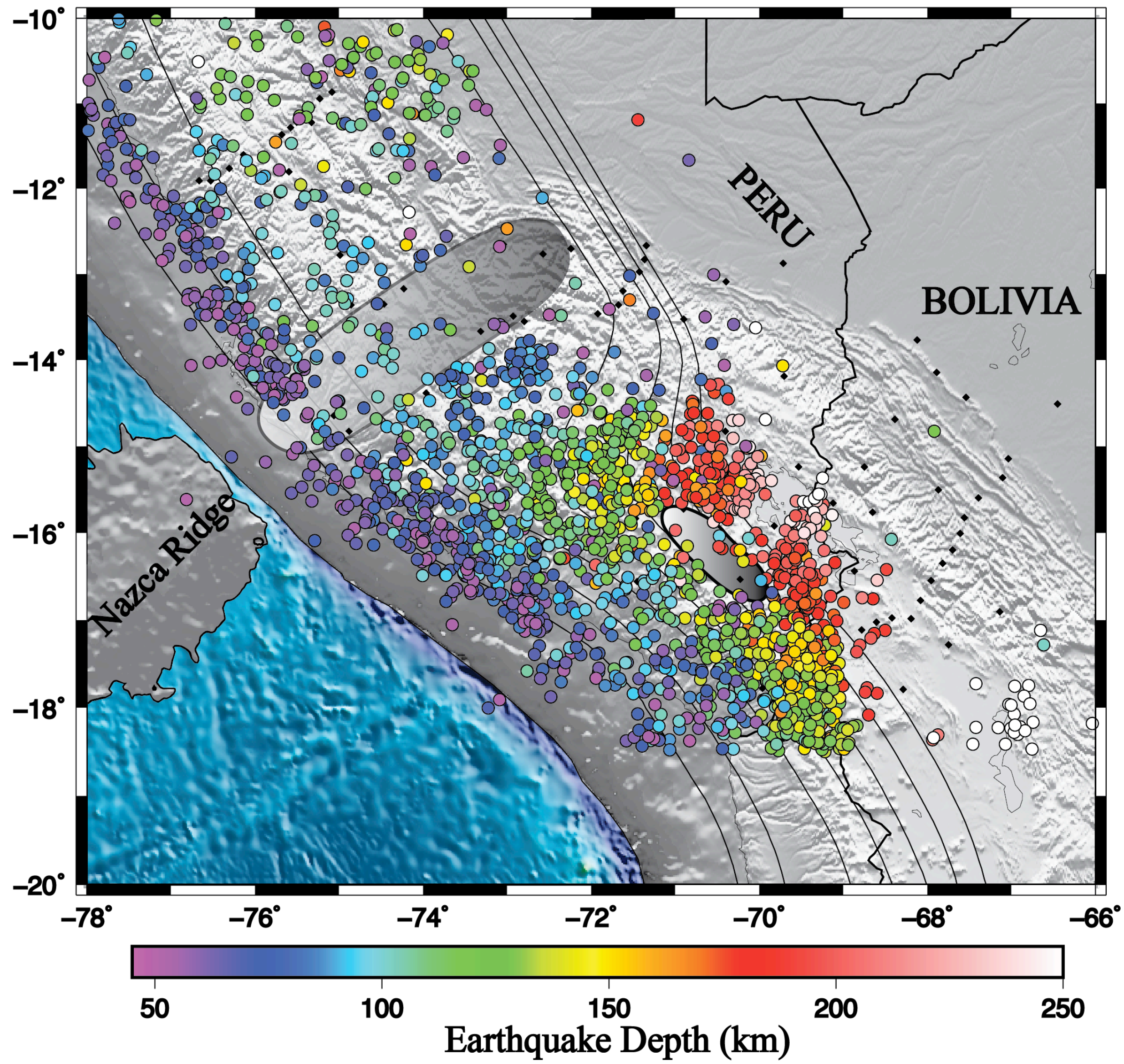

Figure 1.5- Earthquake hypocenters reported in the Advanced National Seismic System (ANSS) catalog during 1970-2013. The hypocenters are color coded by depth. Shaded area marks a notable decrease in seismicity along the projected location of subducted Nazca Ridge track

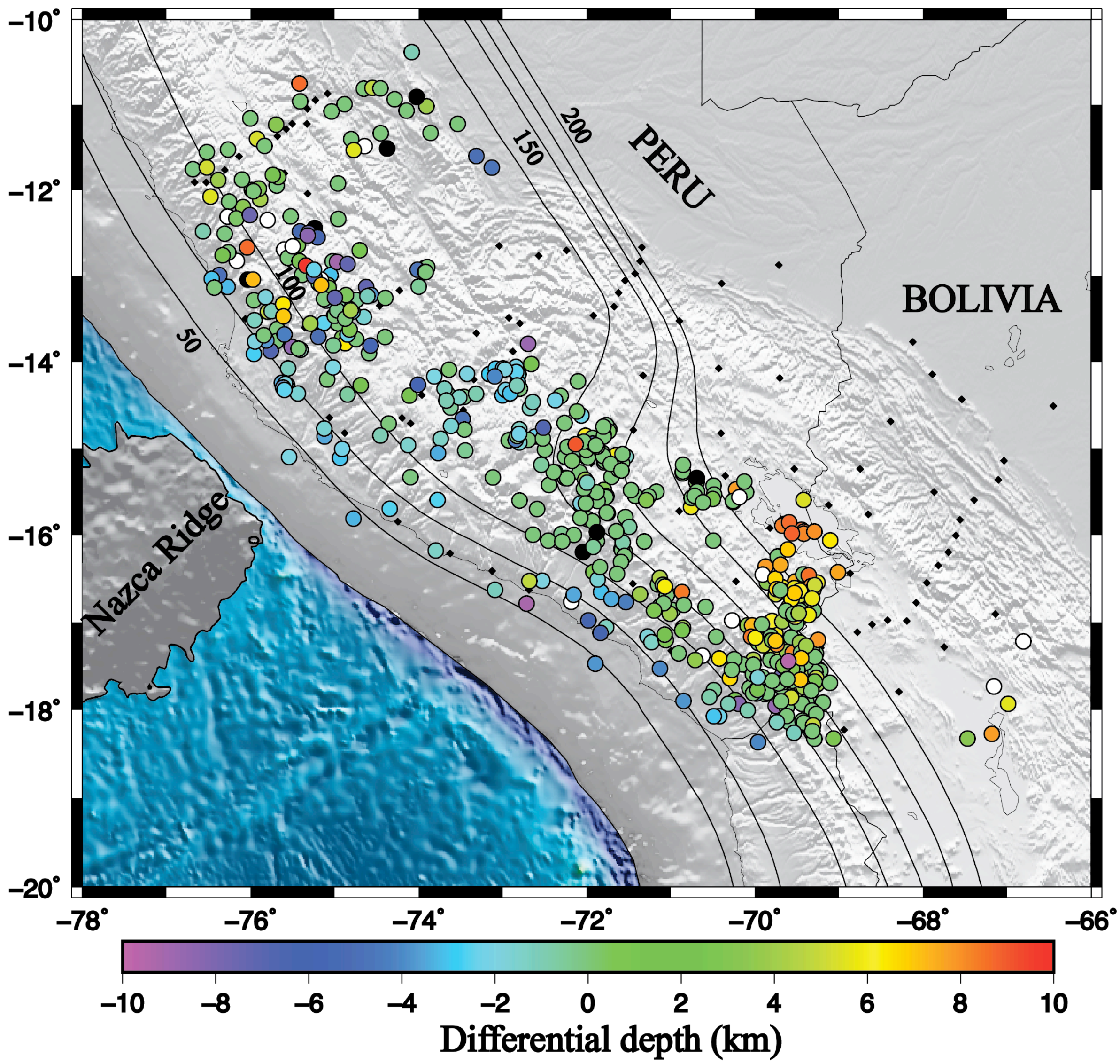

Figure 1.6- Map showing single event locations corresponding to 5% decrease in the reference model. The hypocenters are color coded by calculating the difference between hypocentral depth for my velocity model and the modified (slow) velocity model. Events with cool colors (left half of the color scale) represent downward shifted events and events shown in warm colors (right half of the color scale) are upward shifted events. Black diamonds are the stations used in the location process.

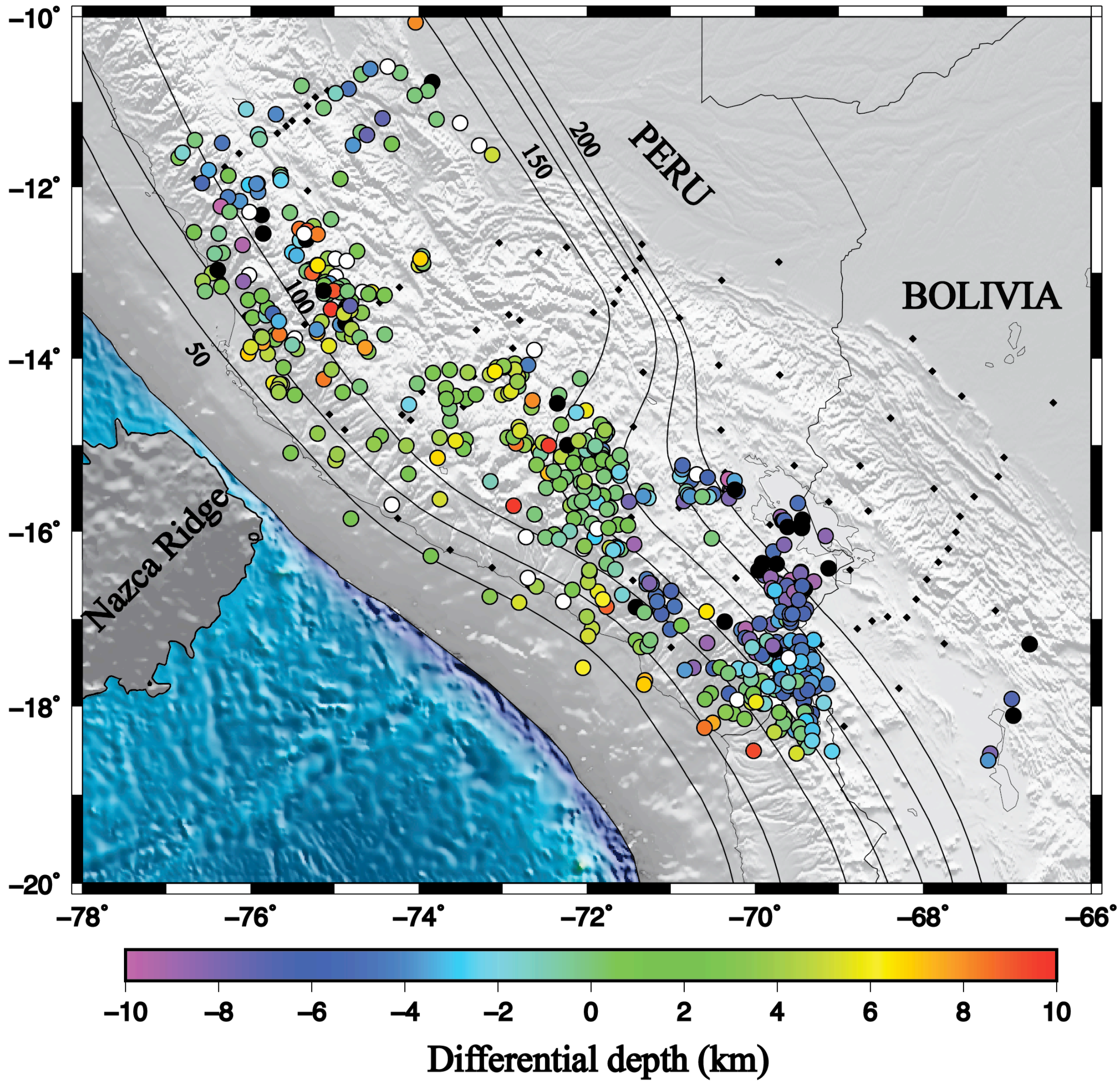

Figure 1.7- Map showing single event locations corresponding to 5% increase in the reference model. The hypocenters are color coded by calculating the difference between hypocentral depth for my velocity model and the modified (fast) velocity model. Events with cool colors (left half of the color scale) represent downward shifted events and events shown in warm colors (right half of the color scale) are upward shifted events. Black diamonds are the stations used in the location process.

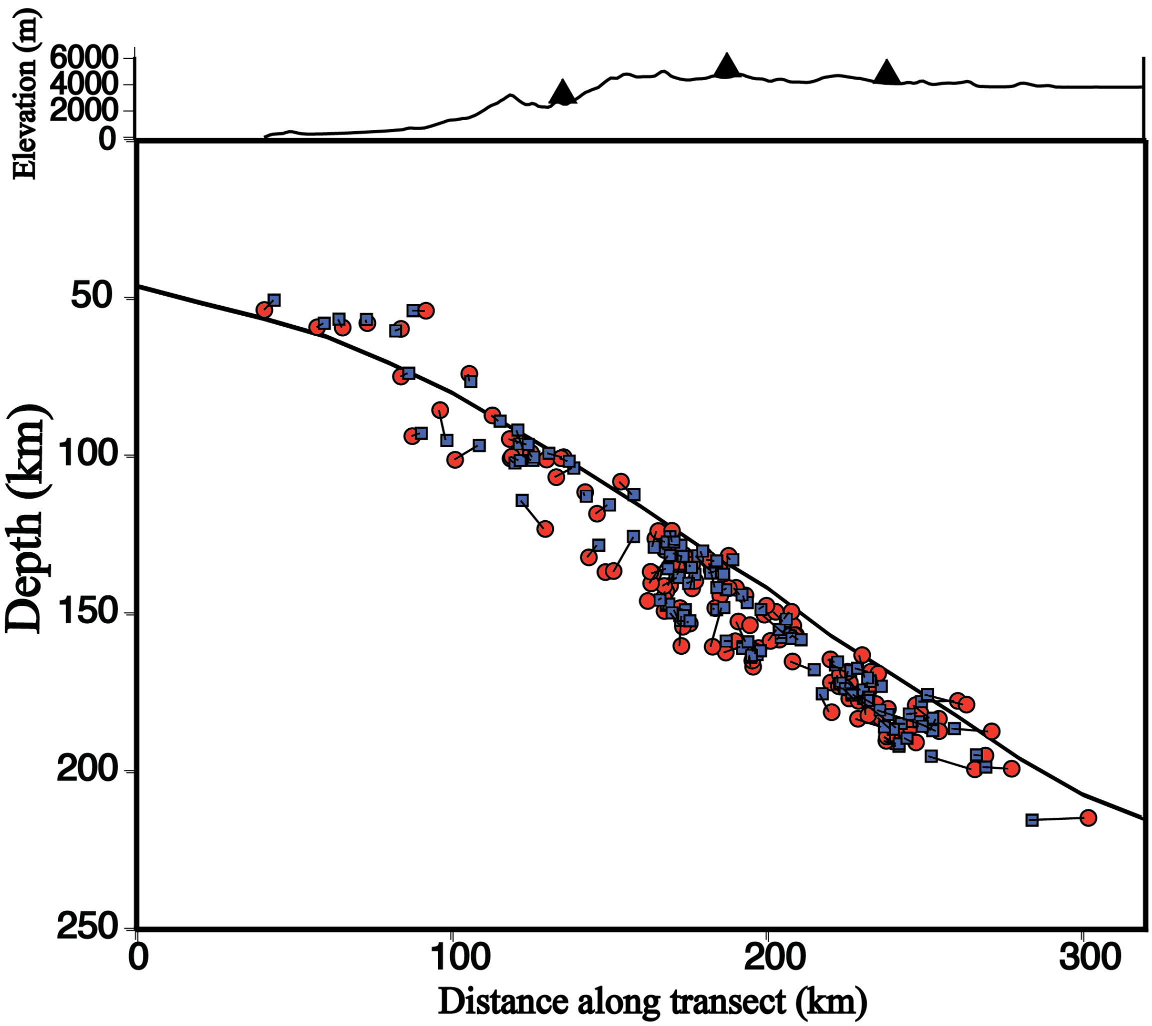

Figure 1.8- Seismicity cross section showing a comparison between single event locations determined from Seisan and relative relocations determined from HypoDD. Seisan locations are red circles and HypoDD locations are the blue squares. Black lines connect locations for the same event. Location of the cross section is P9 (Figure 1.9b), passing through cluster A (Figure 1.4) and events and stations (black triangles) are projected from ±35 km from this line.

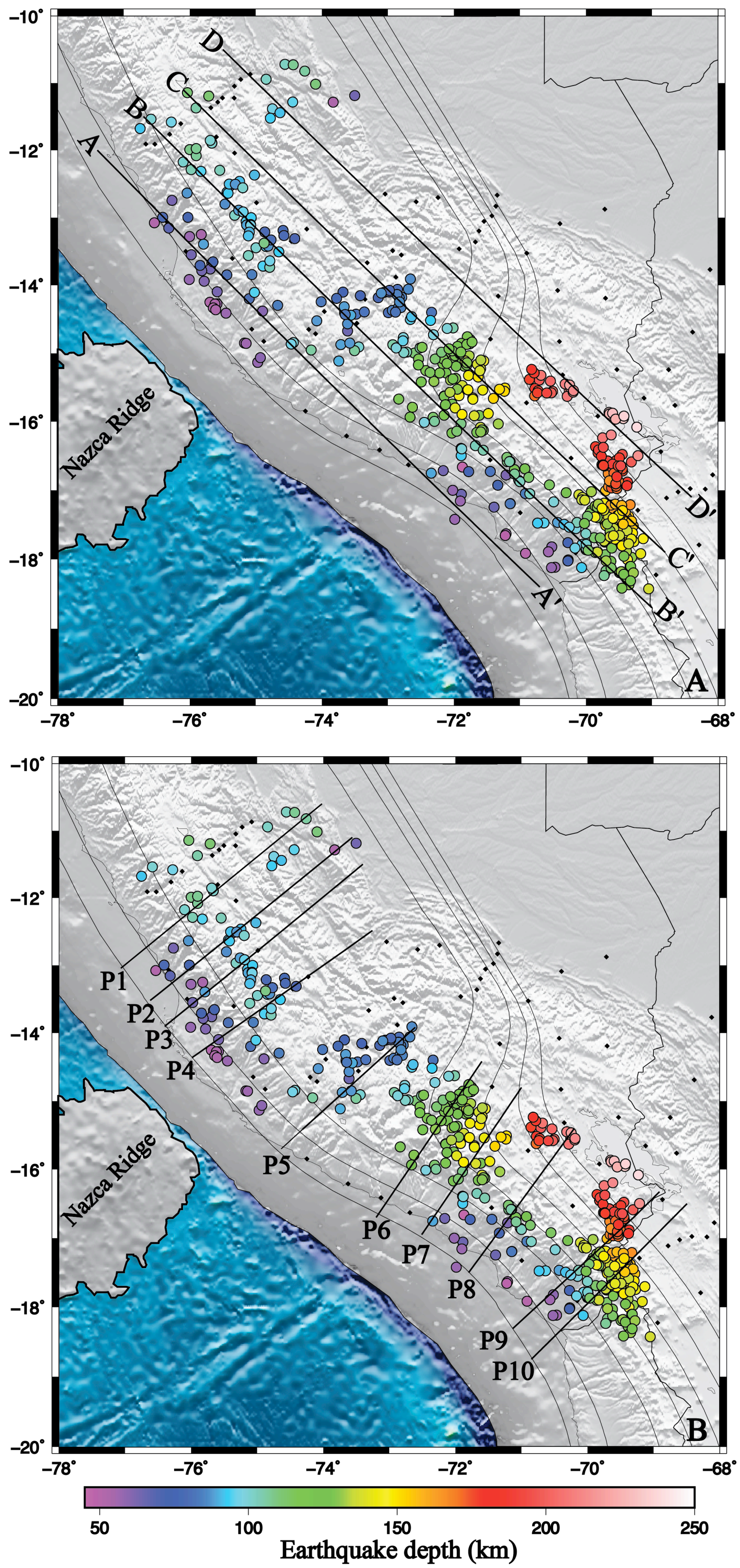

Figure 1.9- Map showing locations of **(a)** trench-parallel (A-D) transects used to plot seismicity cross-sections. Red tick marks on BB′ represents distance interval of 100 km **(b)** trench-perpendicular (P1-P10) transects.

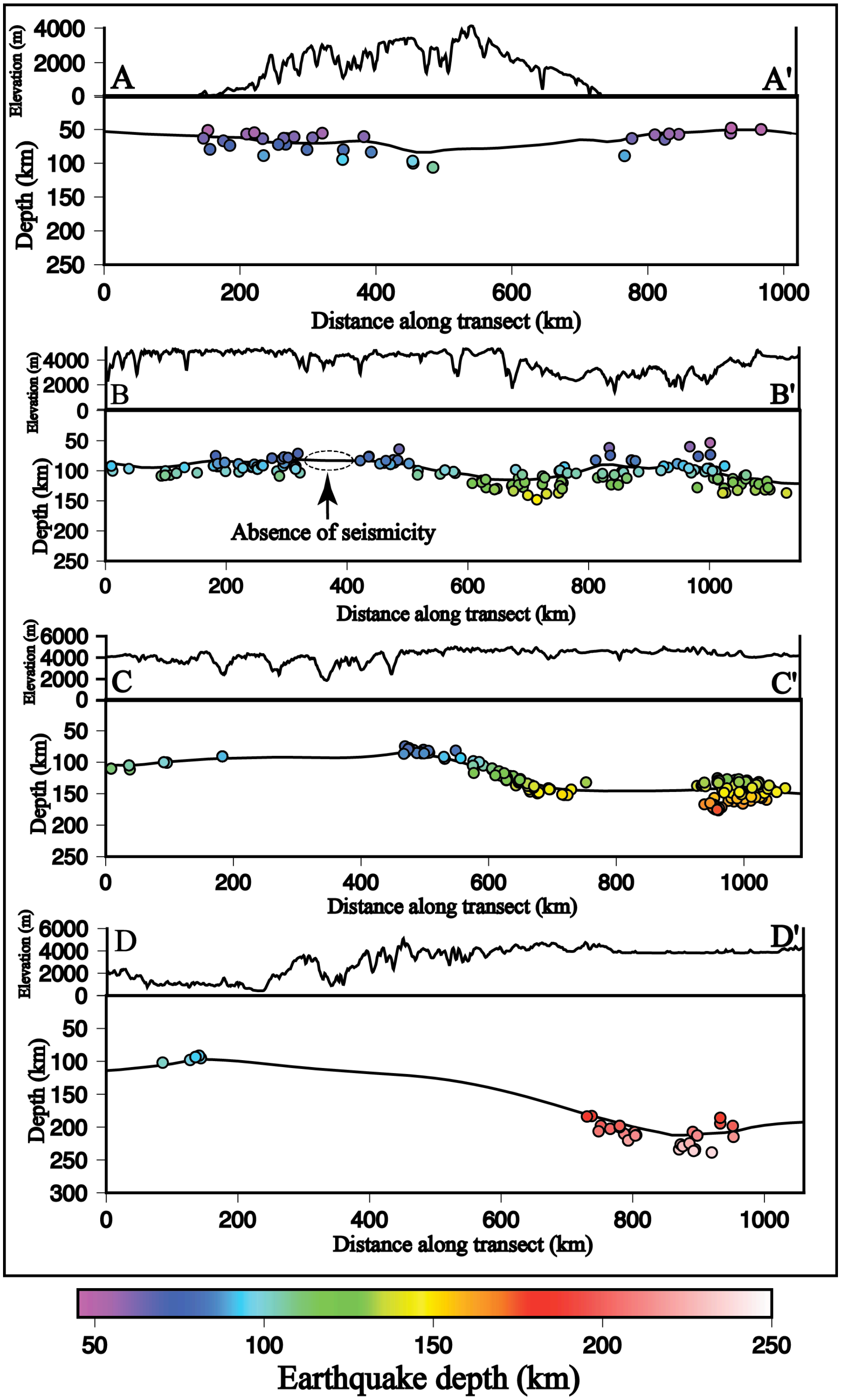

Figure 1.10- Seismicity cross-sections (A, B, C, and D) parallel to the trench. Locations of the cross-sections are shown in Figure 1.9a. Dotted ellipse (cross section BB') marks the absence of seismicity along the projected location of subducted Nazca ridge track.

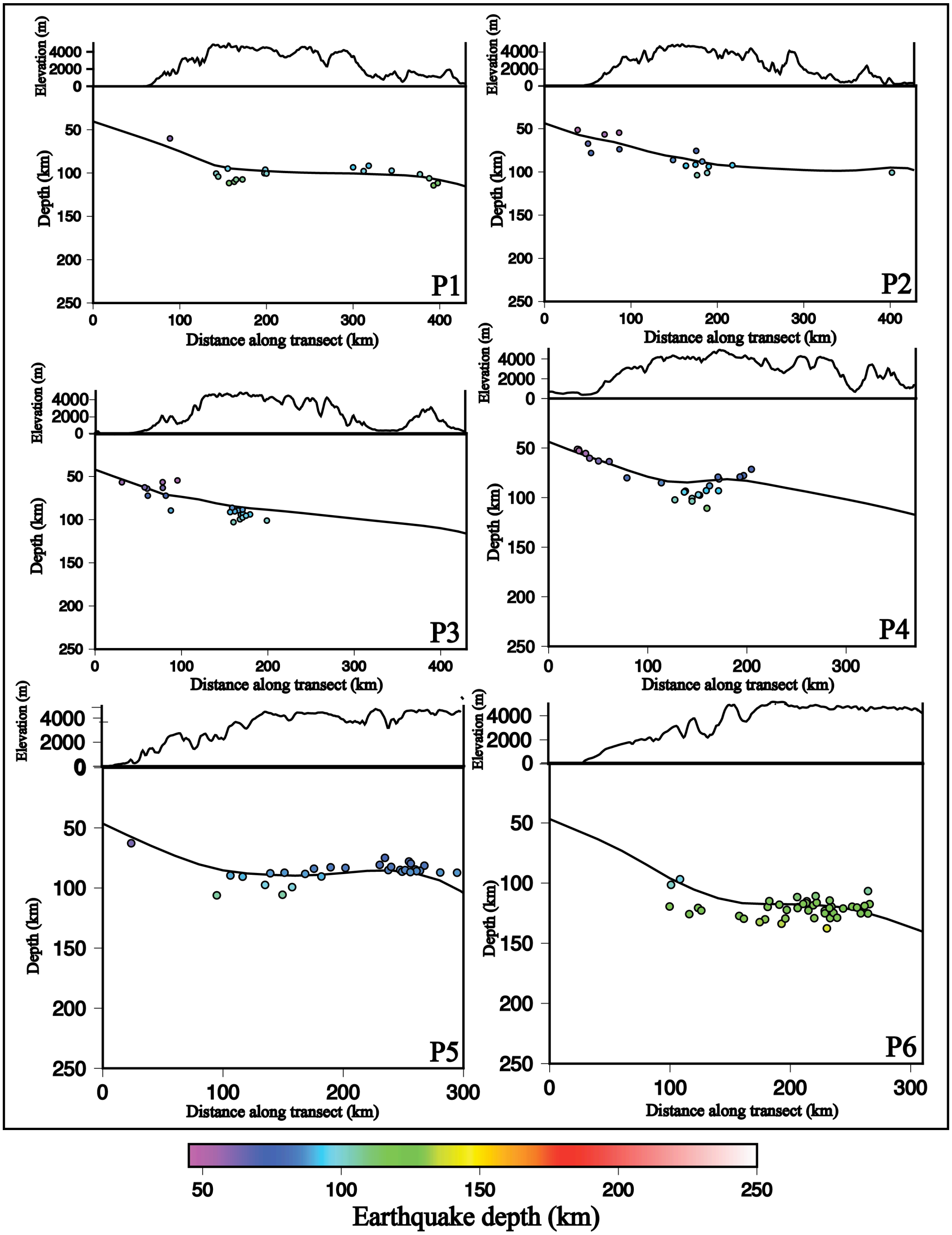

Figure 1.11- Seismicity cross-sections (P1 to P6) perpendicular to the trench. Locations of the cross-sections are shown in Figure 1.9b. Earthquakes within ±35 km are projected onto each cross-section. The solid line in each cross section is my new slab contour.

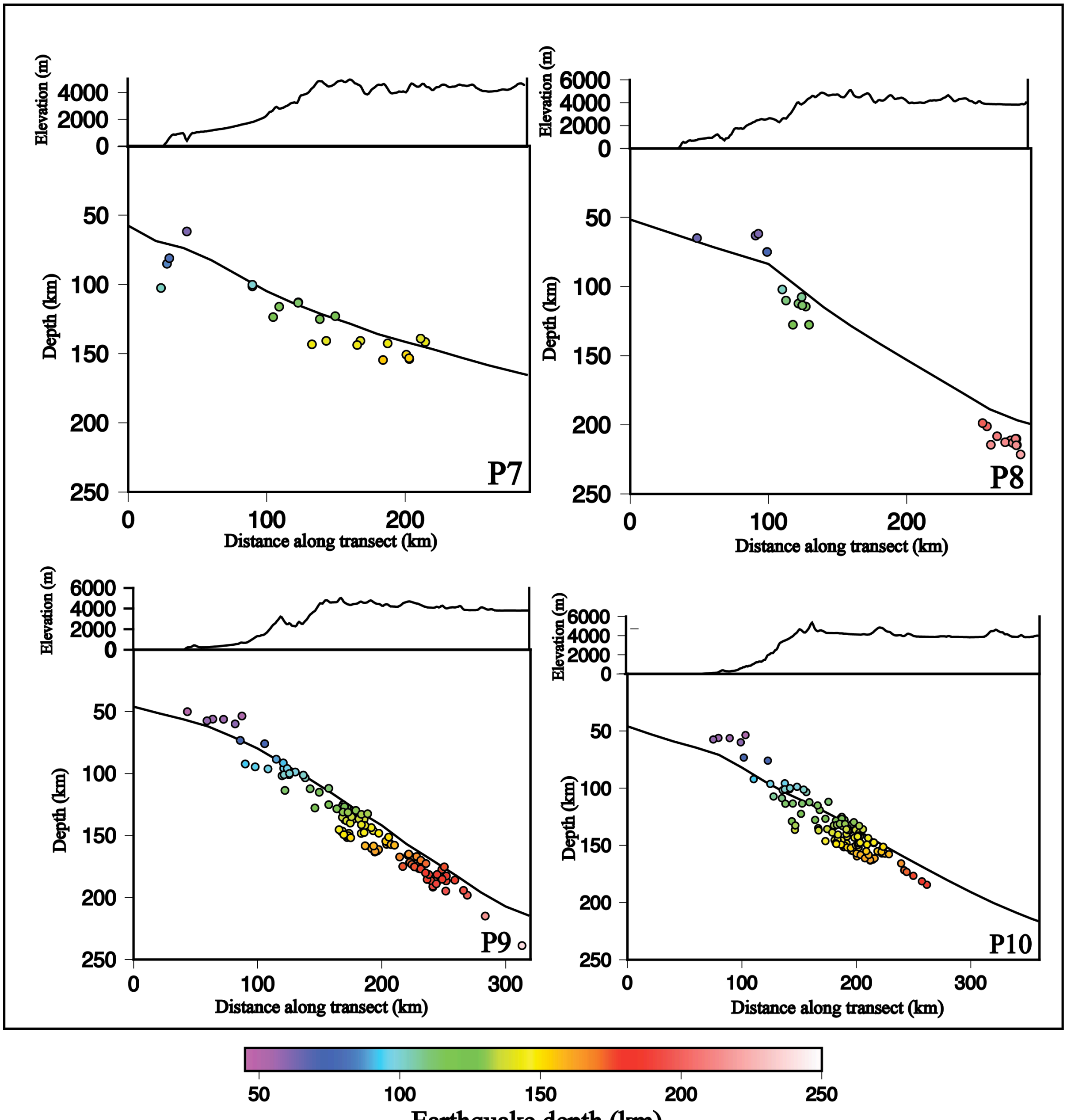

Figure 1.12- Seismicity cross-sections (P7 to P10) perpendicular to the trench. Locations of the cross-sections are shown in Figure 1.9b. Earthquakes within ±35 km are projected onto each cross-section. The solid line in each cross section is my new slab contour.

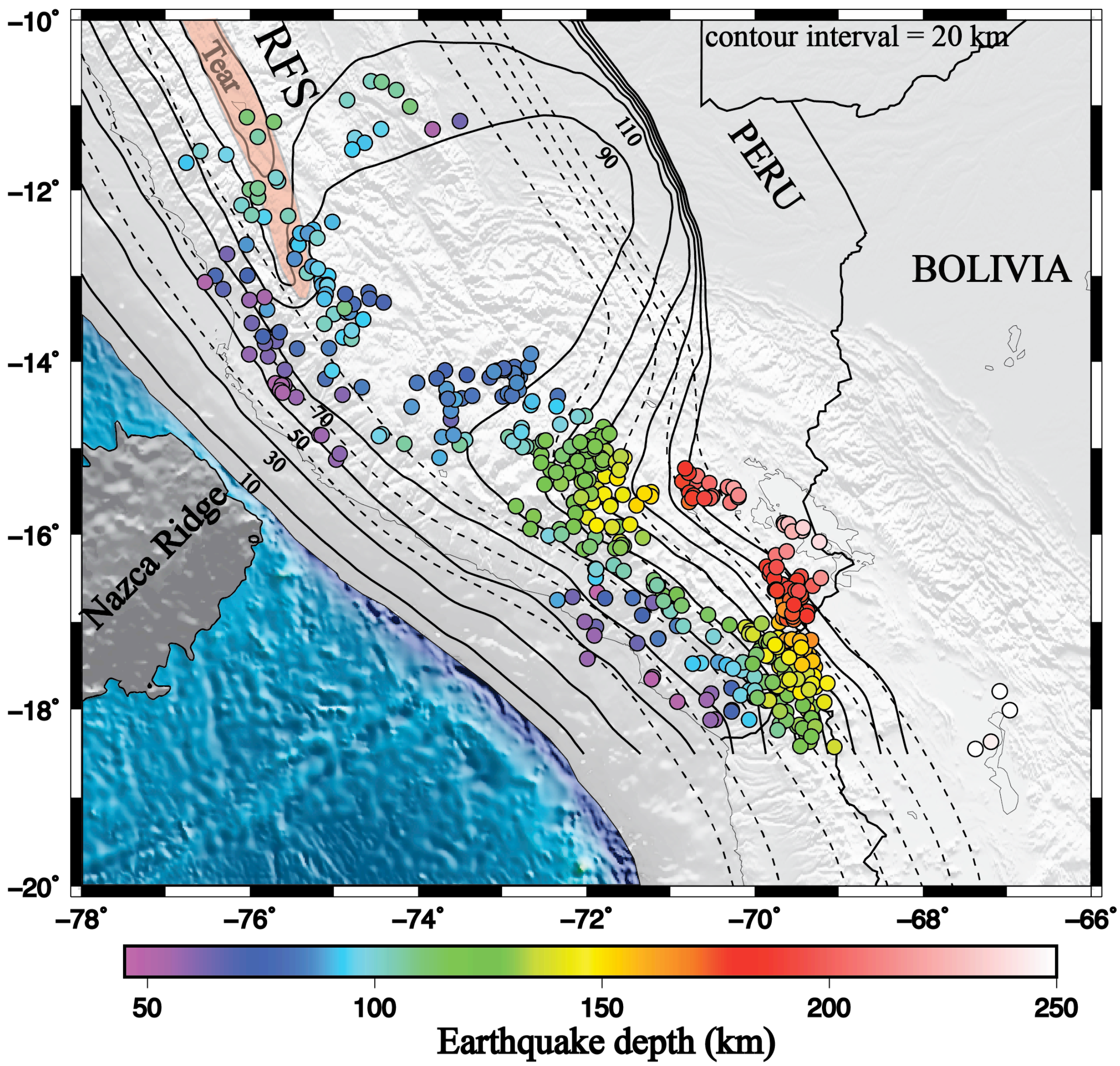

Figure 1.13- Map showing contours to depth of the top of the Wadati-Benioff zone (solid lines) based on my seismicity study and recent results of Rayleigh wave (Knezevic Antonijevic et al., 2014) and teleseismic body wave tomography (Scire et al., 2015). Epicenters of local events used to determine the contours are shown in small colored circles. Dashed black lines are contours from Cahill & Isacks (1992). Shaded pink area, north of the projected track, marks the approximate position of trench parallel tear.

Table 1.1. Absolute earthquake locations of 591 hypocenters as determined from Seisan

Lon	Lat	Dep	Lon err	Lat err	Dep err	Yr	Mo	Day	Hr	Min	Sec
-71.567	-15.119	142.7	4.8	3.3	6.5	2010	11	9	2	9	52.8
-71.612	-16.166	138.5	6.4	4.3	6.2	2010	11	16	5	57	26.4
-71.448	-15.575	145.5	7.5	6.3	7.9	2010	11	18	7	0	53.7
-69.593	-17.312	143.8	5.8	11.3	10	2010	11	18	20	32	10.9
-69.648	-17.597	129.4	3.7	5.4	6.6	2010	11	19	1	42	51.9
-69.946	-17.259	125.7	3.6	7.3	8.4	2010	11	20	16	33	19.1
-69.656	-17.59	148.7	6.4	8.4	6.4	2010	11	25	2	16	27.6
-69.313	-17.381	157.1	6.9	8.4	12.4	2010	11	25	17	25	45.1
-71.198	-16.578	110	4.2	2.3	5.3	2010	11	25	18	16	51.5
-71.461	-16.706	85	8	5.8	4	2010	11	26	3	36	55.2
-69.551	-17.3	160.5	7	10.5	10.6	2010	11	27	6	33	43.5
-72.115	-15.301	120	6.8	5.4	6.6	2010	11	27	12	59	56.8
-69.501	-17.61	152.4	6.6	14.8	14.9	2010	11	28	3	11	19.4
-71.755	-14.793	126.2	4.8	2.8	5.9	2010	11	28	14	49	21.6
-69.339	-18.231	130.4	4.3	6.7	6	2010	11	30	8	4	38.6
-70.12	-17.071	140.7	4.4	9.3	13.9	2010	11	30	14	27	55.7
-67.187	-18.369	244.3	5.5	10.4	8.2	2010	12	2	0	19	23
-70.263	-15.586	214.3	4.5	5.9	6.7	2010	12	2	2	56	11.5
-69.304	-18.019	132.1	3.5	5.5	5.9	2010	12	3	1	46	7.1
-71.657	-16.816	78.3	9	3.8	7.2	2010	12	6	14	13	42
-71.094	-16.706	119.6	4	2.6	5.8	2010	12	7	4	14	40.1
-72.056	-15.043	118.6	7.2	4.6	9.3	2010	12	8	8	3	53.2
-17.474	-70.452	86.7	4.4	7.7	9.9	2010	12	8	22	21	43.1
-69.502	-16.885	174.1	5.8	7.9	9.4	2010	12	11	2	4	19.2
-69.409	-17.861	130.9	4	9.5	14	2010	12	11	15	52	50.9
-70.109	-17.537	100	6.6	8.7	7	2010	12	13	3	51	42.9
-69.469	-17.57	151.7	6.5	7.5	7.9	2010	12	13	10	43	13.5
-69.589	-17.604	134.3	4.7	8.1	8	2010	12	14	14	32	22.2
-71.348	-17.204	66	19.4	11.9	11.7	2010	12	15	13	23	7.3
-69.297	-17.721	144	4.3	5.6	7	2010	12	15	18	22	23
-69.667	-17.57	142.5	3.4	5.6	6.7	2010	12	17	2	32	36.6
-71.744	-15.342	139.5	5.9	4.3	7.1	2010	12	18	13	7	52.5
-71.898	-15.061	122.5	5.4	3.6	5.8	2010	12	19	7	43	51.9
-70.719	-15.4	193.3	4.3	4.2	7.6	2010	12	21	20	4	46.7
-71.856	-15.497	135.4	7.3	7.7	7.1	2010	12	22	14	5	16.6
-69.393	-17.966	146.6	6	10.4	12.3	2010	12	22	19	58	0.1
-72.087	-15.051	117.3	6.7	6.9	7.3	2010	12	25	5	49	22

-16.575	-72.564	51.5	11.6	10.1	10.6	2010	12	26	19	25	24.9
-72.04	-14.612	115.9	3.7	5.5	15.8	2010	12	28	21	39	19.4
-69.789	-17.427	127.6	4.6	11.5	13.6	2010	12	29	4	44	16.5
-70.067	-17.068	131	4.4	5.1	8.9	2011	1	1	4	11	51.4
-69.448	-15.63	270	11.4	8.2	9	2011	1	1	18	39	55.4
-72.284	-14.734	99.7	5.6	3.1	6.8	2011	1	1	20	27	41.2
-69.668	-17.648	145.6	4.4	7.3	5.4	2011	1	2	6	56	26.1
-72.023	-15.102	127.6	9.5	6.1	6.7	2011	1	6	1	56	12.1
-69.75	-17.185	141.4	3.1	7.8	7.3	2011	1	6	14	40	20.2
-69.493	-17.502	161.9	5.9	7	9.9	2011	1	8	6	26	59.5
-71.734	-15.74	140	9.7	4.8	8.7	2011	1	9	1	43	37.6
-69.496	-18.214	119.3	6.6	7.7	9.6	2011	1	12	4	24	3.7
-69.795	-17.015	149.9	5.1	10.3	11.8	2011	1	12	23	28	4.7
-69.417	-16.845	185.8	9	7	13.6	2011	1	14	4	56	35.2
-69.541	-16.543	182.9	6.3	5.6	10.6	2011	1	15	1	0	34.2
-72.176	-15.138	121.6	6.1	6.3	6.8	2011	1	15	7	32	36.4
-71.796	-14.747	116.2	5.6	2.7	5.9	2011	1	16	8	9	19.9
-70.688	-15.339	217.2	6	4.6	12.4	2011	1	17	19	48	39
-70.671	-17.463	85.1	3	4.4	7.2	2011	1	19	10	23	37
-69.454	-17.577	150.6	8.2	13.9	9.9	2011	1	21	9	42	13.1
-70.251	-15.556	210	4.4	5.1	7.8	2011	1	22	21	31	19.9
-71.293	-17.273	50.3	9.9	4.4	5.6	2011	1	23	3	46	8.4
-70.246	-17.979	53.6	1.8	4.3	2.9	2011	1	24	15	17	54.2
-69.343	-17.735	170	4.8	8.1	14.7	2011	1	26	8	11	9.6
-69.661	-17.536	148.3	4.3	7.5	7.8	2011	2	2	9	5	27.3
-70.082	-17.771	93.8	4.8	8.2	4.3	2011	2	2	11	3	51.2
-69.909	-17.659	111.1	4.7	8.3	9.4	2011	2	3	7	42	49.6
-69.414	-17.373	149	5.8	9.8	8.7	2011	2	4	0	55	31.4
-69.406	-17.734	138.8	4.5	8.8	7.8	2011	2	4	14	47	38.4
-69.429	-17.639	153.5	5.8	9.4	9.2	2011	2	7	22	44	52.9
-66.964	-18.008	271.3	7	10	7.5	2011	2	8	4	54	41.4
-70.922	-16.663	118.5	3.5	3.4	6.5	2011	2	8	13	24	16.3
-70.238	-15.521	211.2	5.5	11	9.5	2011	2	11	6	39	42.3
-71.196	-16.515	109.9	4.6	3.1	6.8	2011	2	14	8	58	29.6
-73.537	-14.688	64.7	14	7.2	17.9	2011	2	17	10	31	6.8
-71.731	-15.076	131.9	7.6	3.8	7.7	2011	2	18	19	38	36.8
-71.54	-15.515	144.5	9.3	5.2	10.5	2011	2	21	15	54	1.3
-69.36	-16.656	177.2	7.9	5.6	8.8	2011	2	22	8	13	18.8
-70.072	-17.194	136.8	4.9	7	10.9	2011	2	22	16	53	12.6

-69.598	-16.678	190.1	6.6	8	10.8	2011	2	23	13	46	59.1
-70.307	-17.001	119.4	4	8.7	14.9	2011	2	25	7	42	25.8
-71.828	-15.182	130.4	12.2	6.7	9	2011	2	28	11	5	22.7
-17.005	-69.692	164.7	7.6	13.8	12.5	2011	3	2	18	8	54.7
-69.461	-17.603	154.6	6.2	11.5	10	2011	3	5	0	18	45.9
-69.669	-15.855	235.8	9	11.4	12.1	2011	3	5	18	9	22
-69.648	-18.192	110.8	4.7	6.4	7.9	2011	3	6	12	31	57.5
-70.519	-15.404	200	5.4	6.2	9.2	2011	3	11	2	34	18.2
-69.988	-18.427	83.5	4.7	6	7.8	2011	3	23	15	31	10.1
-70.262	-15.439	213.3	5.3	7.1	8.4	2011	3	25	1	50	46.7
-69.426	-17.99	125.6	7.8	10.2	9.3	2011	3	26	16	50	7.9
-73.129	-15.375	110	5.3	13.3	12.4	2011	3	27	3	7	30.1
-69.716	-17.75	131.4	4	5.4	5.6	2011	3	31	1	42	21
-71.566	-16.195	122.3	4.9	3.1	4.8	2011	4	2	4	41	44.5
-71.219	-17.614	68.6	11.6	11.5	7.6	2011	4	2	8	20	41.8
-69.615	-17.515	141.6	6.9	12.7	13.4	2011	4	3	16	14	30.6
-70.505	-17.809	59.3	5.4	9.3	2.6	2011	4	4	2	57	8.1
-69.616	-17.25	161.3	6	10.8	10.3	2011	4	6	11	13	10.7
-69.566	-17.196	157.8	7.6	12.5	9.9	2011	4	9	6	47	21.7
-69.436	-17.512	160.2	7.3	10.9	8.1	2011	4	9	10	12	50.8
-71.844	-17.077	63.4	11.9	7	4	2011	4	12	13	31	7.3
-69.331	-17.67	157.1	8.6	13.7	7.9	2011	4	13	0	37	25.5
-71.575	-15.842	130	4.7	8	5.8	2011	4	13	7	35	19.7
-69.768	-17.404	147.8	5.2	10.2	10.2	2011	4	16	2	27	29.7
-72.725	-16.792	58.2	11.9	11.1	6.5	2011	4	17	9	57	25.6
-71.615	-16.176	114.8	9.9	7.7	12.2	2011	4	24	7	55	38.8
-69.585	-16.953	180.8	7.8	9.7	12	2011	5	1	15	18	41
-69.872	-16.514	189.5	9.9	10.7	13.7	2011	5	3	14	8	5.8
-69.588	-17.66	152.2	9.7	17	8.2	2011	5	3	22	3	46.6
-69.426	-17.285	153.4	8.1	13.3	13.8	2011	5	6	2	55	11.2
-69.631	-17.544	159.8	5.5	7.1	13.7	2011	5	6	6	15	13.9
-70.279	-15.621	206.7	5	5.9	8.2	2011	5	7	19	33	32.8
-69.843	-17.429	125.8	5.1	10.2	8.6	2011	5	8	9	34	4
-69.562	-17.67	144.2	6.9	16.2	9.9	2011	5	10	4	43	5.9
-69.58	-16.89	173.1	9.5	21.4	14	2011	5	12	13	4	4.6
-69.185	-17.93	141.9	4.9	5.3	6	2011	5	13	3	40	10.5
-16.829	-71.226	61.4	22.8	7.8	14	2011	5	17	2	40	43.1
-69.14	-16.055	240	8.1	7.4	7.4	2011	5	17	22	5	28.9
-72.022	-15.824	127.9	10.4	6	9.9	2011	5	19	21	4	38.7

-69.617	-16.752	168	7.7	6.2	12.3	2011	5	21	18	7	6.8
-69.968	-17.284	123.4	3.7	9.4	13.8	2011	5	22	2	56	1.6
-69.525	-16.658	178.6	5.9	7.1	11.2	2011	5	22	16	24	50.7
-71.637	-16.123	130.4	4	7.2	5.5	2011	5	22	18	25	22.9
-69.754	-16.583	178.2	7.6	13.5	11.9	2011	5	22	23	10	51.5
-69.452	-17.648	135.7	6	10	8.5	2011	5	26	4	44	39.9
-70.15	-15.53	212.1	5.9	8.6	11	2011	5	26	9	30	34.8
-72.119	-15.677	130.1	10.5	5.5	10.7	2011	5	30	7	35	49.4
-72.107	-15.651	124.4	7.4	5.9	11.3	2011	5	30	7	35	50.5
-69.692	-16.605	189.9	6.1	8.2	11.9	2011	5	30	18	16	27.8
-69.697	-16.598	188.6	10	9.8	14	2011	5	30	18	16	28.3
-69.588	-17.554	152.7	5.2	9.6	7.2	2011	5	31	9	5	40
-71.027	-16.872	100.9	4.7	3.6	7.3	2011	6	1	0	34	23.1
-69.661	-17.735	136.3	5.1	8.3	6.1	2011	6	2	7	9	47.1
-69.269	-17.732	140	5.2	8.1	9.4	2011	6	3	9	5	58
-69.383	-17.428	158.2	6.6	10.8	8.7	2011	6	5	13	57	57.9
-69.563	-17.617	151.3	5.1	13.5	13.4	2011	6	5	17	31	52.1
-70.486	-15.551	199.7	6.3	6.1	8.3	2011	6	6	8	28	54.4
-17.939	-69.756	124.2	5.4	18.5	13	2011	6	7	13	18	7
-73.626	-14.549	84.6	5.2	7.2	8.6	2011	6	7	22	4	53.8
-69.83	-17.203	135.7	3.4	5.4	8.1	2011	6	8	3	6	20
-69.889	-16.361	182.9	4.3	4.5	9.2	2011	6	8	10	53	2.9
-69.351	-16.875	184.5	8.3	9.7	14.7	2011	6	8	18	38	46.4
-69.443	-16.647	186.8	7.2	7.4	11.2	2011	6	9	2	40	34
-72.149	-15.017	122.4	3.7	4.5	10.5	2011	6	15	14	16	49.8
-72.132	-15.04	114.4	4.7	5.1	7.2	2011	6	15	14	16	50.2
-71.612	-15.293	147	5	5	6.1	2011	6	17	7	59	58.2
-69.332	-18.062	127.8	4.4	8.2	8.4	2011	6	17	20	43	5.4
-69.997	-17.827	99.5	3.3	5.1	6.5	2011	6	18	5	38	22.2
-75.24	-12.439	90	5.2	5.8	10.5	2011	6	18	6	31	9.7
-70.304	-17.732	73.6	2.9	6.9	6.1	2011	6	18	10	28	35.9
-72.594	-14.947	112.1	4.6	5.8	8	2011	6	20	1	5	11.4
-74.698	-10.767	105.5	15.1	16.9	14.1	2011	6	21	0	11	41.6
-72.847	-14.059	76	2.5	2.6	4.7	2011	6	21	1	55	15.1
-71.777	-15.562	149.7	17.6	8.1	12.9	2011	6	23	12	32	60
-71.789	-15.58	150.6	17.6	6.9	11.3	2011	6	23	12	32	59.5
-69.502	-17.376	166.4	5.6	7.4	7.3	2011	6	23	20	7	23.5
-69.514	-17.366	164.5	5.2	7	7.4	2011	6	23	20	7	23.8
-69.719	-17.491	123.3	8.2	8.7	14.1	2011	6	25	5	19	49.6

-69.83	-17.235	131.2	4.1	5.4	8.2	2011	6	25	16	9	53.7
-73.155	-14.164	74.2	2.5	2.9	4.1	2011	6	26	17	11	5.5
-74.662	-13.472	90.9	2.6	5.2	6.1	2011	6	28	6	53	26.5
-69.749	-16.236	211.9	6.9	7.6	11.7	2011	6	28	9	35	6.5
-72.796	-14.165	82	3.4	3.3	4.8	2011	6	29	2	18	23.9
-71.851	-16.672	50.7	11.2	5.3	5.3	2011	6	29	6	20	22.8
-73.634	-14.109	78	4.6	5.7	11.2	2011	6	29	15	2	23.4
-75.995	-13.305	57.2	5.5	13.3	6.4	2011	6	30	13	59	7
-74.56	-10.721	102	11.8	11.4	15.1	2011	7	1	5	15	1.4
-71.977	-15.156	122.1	4.1	4.3	8.2	2011	7	4	9	9	31.3
-74.88	-13.701	92.9	3.4	4.5	7.3	2011	7	4	15	0	23.3
-72.707	-14.934	105.4	3.2	3.6	5.9	2011	7	6	1	47	58.5
-71.894	-16.073	112.6	6.2	4.9	9.5	2011	7	8	0	39	15.2
-76.578	-11.512	99.6	10.7	10.5	10.9	2011	7	8	3	54	42.8
-71.819	-15.074	133.4	4	4.8	6.3	2011	7	9	8	51	13.5
-72.827	-15.641	124.2	4.9	6.4	13.2	2011	7	10	11	49	5.5
-71.994	-14.917	119.1	3.6	6.1	7	2011	7	13	5	18	51.6
-71.872	-15.635	142.6	5.8	5.7	13.7	2011	7	13	8	23	25.8
-67.084	-17.793	284.2	10.1	8.6	7.8	2011	7	14	7	2	25.7
-69.448	-15.935	232.7	5.6	5.8	8.8	2011	7	14	18	34	40.1
-69.424	-15.95	235.8	5.4	5.8	8	2011	7	14	18	34	39.7
-69.426	-15.971	233.4	5.1	6.2	7.8	2011	7	14	22	53	54.2
-74.844	-10.943	102.1	13.7	9	12	2011	7	21	7	12	12.4
-73.449	-14.434	80.6	4.4	5.3	5.8	2011	7	22	22	28	52.8
-73.449	-14.85	103.2	4.4	5.9	6.2	2011	7	23	11	44	45
-73.664	-14.4	88.9	3.3	5.4	6.3	2011	7	24	2	3	12.8
-74.404	-14.795	99.2	7.1	7.3	8.3	2011	7	24	15	49	6.5
-74.489	-14.913	95.9	6.8	13.3	8	2011	7	24	15	49	5.1
-74.114	-14.451	95	4.2	8.5	10.7	2011	7	27	7	49	3
-73.005	-14.402	77.3	2.4	3	4.3	2011	7	27	8	36	0.4
-76.103	-12.183	99.2	4.1	3.4	8.1	2011	7	28	3	13	11.4
-69.597	-16.863	171.4	5.1	5.8	9.9	2011	7	28	5	7	14.2
-72.32	-14.404	89.3	2.3	2.7	9.4	2011	7	30	4	31	6.8
-72.603	-15.745	130	7.6	9.9	14.2	2011	7	30	5	28	58.2
-69.907	-17.325	144.6	5.4	9.8	7.8	2011	8	2	18	3	6.6
-71.903	-15.525	130	5.1	4.8	6.9	2011	8	5	4	54	19
-75.102	-14.207	79.4	5.3	7.7	27.1	2011	8	6	5	6	56.1
-72.674	-14.043	79.7	3.3	3.5	8.9	2011	8	7	8	41	6.3
-72.464	-15.457	130	5.6	7.2	10.4	2011	8	9	7	54	29.2

-69.665	-16.66	182.5	6.6	7.7	11.3	2011	8	11	7	52	34.4
-69.524	-17.429	158.3	6.7	9.8	9.4	2011	8	12	14	32	43.2
-75.158	-13.048	93.2	3.7	5.4	8.1	2011	8	12	23	25	31.4
-70.869	-15.317	175.5	4.2	5	6.6	2011	8	14	4	46	44.2
-75.968	-13.523	64.1	7.9	11.1	4.4	2011	8	18	3	23	49.1
-12.133	-76.251	110.7	11.5	13	19.2	2011	8	19	9	52	22.9
-70.191	-15.407	222.6	6.5	6.6	8.7	2011	8	19	18	28	4.8
-70.757	-17.49	93.3	11.6	13.1	11.1	2011	8	22	2	2	26.8
-73.456	-15.034	101.2	5.4	4.3	10.4	2011	8	24	2	10	48.1
-71.932	-15.875	140	4.8	4.3	13.5	2011	8	24	2	18	39.4
-69.386	-17.492	142.4	7.7	5.7	8.8	2011	8	25	5	4	6.6
-15.614	-73.764	55.1	8	3.4	8.1	2011	8	26	10	40	55.8
-69.245	-16.549	198.7	6.4	4.5	6	2011	8	28	1	21	3.9
-73.074	-14.091	84.3	2.6	3	4.3	2011	8	28	8	20	29.6
-73.419	-14.15	75.3	3.4	3.9	6.3	2011	8	29	10	35	29.9
-12.626	-75.707	92.9	18.4	8.9	16.4	2011	8	30	4	54	3.2
-70.867	-15.275	176.7	9	7.2	13	2011	8	30	13	37	11.8
-69.552	-17.737	133.8	4.6	6.4	7.3	2011	8	31	0	53	18.2
-69.548	-17.739	133.4	4.5	6.4	7.3	2011	8	31	0	53	18.3
-73.878	-10.933	74.5	5.5	11.5	4	2011	9	1	14	45	15.4
-75.367	-12.542	72	5.1	3.8	10	2011	9	2	8	27	48.3
-74.136	-14.983	105.3	6.6	6.9	10.2	2011	9	3	18	39	44.8
-74.916	-13.687	93.3	7.4	27.1	17.5	2011	9	4	6	35	53.7
-75.854	-13.716	53.1	3.8	11.4	4.7	2011	9	4	12	32	19.5
-75.525	-12.303	101.2	4.1	3	7.7	2011	9	4	17	56	39
-71.502	-15.916	148.1	7.3	6.7	9.9	2011	9	5	9	9	20.2
-71.794	-15.147	125.3	6.5	6.3	7.1	2011	9	7	1	7	44
-74.257	-10.825	105.6	4.7	7.9	19.4	2011	9	7	22	44	51.2
-72.776	-14.963	105.5	5.1	5.7	9.4	2011	9	8	5	26	13
-72.934	-14.912	100	3.9	3.9	9.2	2011	9	10	3	46	44.1
-71.748	-14.825	125.3	4.6	4.7	13.1	2011	9	13	0	14	23.8
-71.793	-14.863	125.7	4.4	5.9	16.2	2011	9	13	0	14	23.3
-72.668	-14.55	93.1	5.4	5.1	9.2	2011	9	13	3	37	58.8
-74.865	-13.748	76.5	3.6	32	37	2011	9	13	14	22	8.9
-71.969	-17.513	59.3	14.6	8.8	6.7	2011	9	14	3	0	2.2
-69.638	-17.371	135.9	4.6	6.3	8	2011	9	14	14	52	44.2
-72.038	-15.395	137.1	6.2	6.3	14.1	2011	9	16	0	42	28.6
-74.441	-11.285	94.9	6.2	9.4	23.3	2011	9	18	2	9	52.6
-71.806	-15.124	130	5.8	6.2	9.3	2011	9	18	7	43	39.3

-72.949	-14.36	83.5	4.5	4.8	6.1	2011	9	21	1	39	47.2
-75.036	-12.838	64.4	12.2	8.7	9.7	2011	9	22	22	7	44.5
-69.438	-16.455	194.6	5.8	4.3	7.6	2011	9	23	1	55	29
-70.492	-17.199	100.7	4	3.9	9.1	2011	9	23	5	21	38.7
-75.995	-11.99	109.2	4.1	4.4	6.7	2011	9	23	10	15	8.1
-75.082	-13.138	96.3	4.9	6.2	11.2	2011	9	24	3	19	9.7
-72.306	-16.803	85.7	5.4	8.3	13.3	2011	9	25	0	12	55.9
-73.316	-14.392	81.1	3.9	4.8	6.1	2011	9	30	9	14	6.6
-75.275	-12.968	96.7	10.1	5.6	25.8	2011	10	1	14	53	2.8
-71.155	-17.245	82.3	12.1	11	8.2	2011	10	5	12	4	30.9
-71.148	-17.186	82.2	12.9	8.7	9.9	2011	10	5	12	4	30.2
-70.739	-15.515	183.5	4	3.5	5.2	2011	10	8	12	29	24.5
-75.024	-14.092	94.6	4.5	10.1	17.8	2011	10	12	6	12	20.2
-73.744	-14.902	90	6.4	7.1	10.5	2011	10	15	19	31	31.1
-72.82	-14.227	83.8	3.8	3.9	7.7	2011	10	16	7	25	26.7
-69.672	-15.884	227.4	6.3	5.8	8.6	2011	10	19	22	59	36.9
-75.694	-13.665	61.4	2.5	8.9	2.3	2011	10	20	14	56	42.2
-74.645	-13.168	92.7	8	14.6	16.1	2011	10	21	17	24	17
-69.632	-18.039	122.6	3.6	5.5	5.2	2011	10	22	10	7	41.4
-75.058	-12.998	93.3	3.4	3.2	5.9	2011	10	23	12	22	54.2
-75.021	-13.446	102.5	3.8	3.5	9	2011	10	26	3	1	20
-71.58	-15.203	137.9	5.7	7	6.6	2011	11	1	3	27	14.2
-75.007	-13.447	100.5	15.3	50.5	12.8	2011	11	3	14	13	2.3
-74.766	-13.739	102.6	3.9	3.6	6.9	2011	11	3	16	26	33.8
-69.628	-17.541	153.7	10.9	10	13.5	2011	11	4	2	46	56.6
-69.539	-17.005	171.4	5.5	12	11.4	2011	11	5	16	55	28.5
-71.876	-15.96	154.7	9	5.9	12.5	2011	11	6	15	21	21
-71.143	-16.583	109.4	3.8	2.3	5.2	2011	11	7	4	14	5.4
-71.143	-16.583	109.4	3.8	2.3	5.2	2011	11	7	4	14	5.4
-69.258	-17.548	156.9	6.3	9.4	8.7	2011	11	11	22	21	0.1
-72.411	-15.297	125.7	4.9	6.3	14.7	2011	11	14	2	38	22.3
-69.055	-16.425	214.3	6.7	5.1	6.5	2011	11	14	15	40	12.5
-69.61	-15.854	231.2	7	6.4	8.9	2011	11	15	7	24	14.6
-69.892	-17.886	127.1	5	9.5	6.7	2011	11	15	20	42	12.9
-69.525	-17.491	143.9	3.9	8.1	10.7	2011	11	16	1	57	45.5
-70.452	-18.116	58.9	11.6	17.8	6	2011	11	16	15	38	57.2
-75.141	-13.559	100	4.7	5	6.5	2011	11	16	19	8	58.7
-69.493	-16.889	172.9	6	7.5	10.3	2011	11	16	21	48	31.7
-69.333	-17.373	156.3	4.9	7.7	7.8	2011	11	18	1	25	40.4

-69.613	-16.888	169	5.8	9.6	12.1	2011	11	18	5	42	7
-71.226	-15.511	153.3	4.4	4.5	5.6	2011	11	20	5	27	14.4
-71.336	-16.088	130	7.9	5.7	10.7	2011	11	21	10	46	39.9
-11.043	-75.174	62.5	63.4	83.7	11	2011	11	22	5	47	41.1
-69.75	-17.742	136.4	5	12.7	8.7	2011	11	22	22	3	51.9
-72.849	-14.123	81.7	2.1	2.4	3.9	2011	11	22	23	2	11.1
-72.849	-14.123	81.7	2.1	2.3	3.9	2011	11	22	23	2	11.1
-66.773	-17.236	309.2	4.5	12.6	5.7	2011	11	24	2	30	53.6
-69.25	-17.591	149.3	5.7	6.9	7.4	2011	11	27	8	35	14.7
-71.923	-17.156	55	13.8	7.1	5.8	2011	11	28	0	14	23.4
-69.611	-16.813	182.9	7	14.5	13.7	2011	11	28	16	9	42.5
-69.483	-17.499	141.5	4.8	9.1	8.6	2011	11	29	8	49	30.1
-73.535	-14.423	91.6	2.6	3.1	3.7	2011	11	30	3	23	1.8
-73.814	-16.214	56	22.5	29.6	14.5	2011	11	30	19	34	21.9
-70.794	-15.663	164.8	4.7	5.6	9.5	2011	12	1	3	40	57.8
-70.023	-17.199	140.8	5	8.4	10.7	2011	12	5	1	44	1.8
-74.432	-10.726	107.6	10	13.8	27.5	2011	12	7	14	25	34.4
-69.49	-17.722	125.1	3.7	8.2	9.2	2011	12	8	20	5	47
-69.606	-17.856	113.7	9.2	13.4	10.4	2011	12	10	7	21	51.7
-11.679	-73.133	51.8	11.9	12	9.2	2011	12	10	14	44	41.9
-69.32	-18.098	126.8	5.8	5.2	7.1	2011	12	11	8	48	28.1
-69.317	-17.587	139.5	9.7	6.6	7.6	2011	12	11	11	14	15.2
-69.578	-17.541	139.2	5.7	12.7	11.4	2011	12	11	21	0	38.5
-69.928	-16.45	167.8	5.9	6.3	14	2011	12	12	21	50	33.5
-75.67	-11.906	100.7	3.3	4.7	9.4	2011	12	13	5	42	16.3
-70.025	-17.382	107.7	2.3	9.3	6.7	2011	12	13	10	56	58.7
-74.848	-13.387	91.5	3.3	5.7	6	2011	12	13	23	16	27.5
-69.751	-17.29	133.6	5.1	8.7	12.7	2011	12	14	12	0	56.2
-69.398	-16.471	186.9	6.9	6.2	9.4	2011	12	14	15	54	0
-71.048	-16.917	102.1	8.7	6.7	11.3	2011	12	14	17	36	37.8
-69.544	-16.966	172.6	5.4	9.1	10.5	2011	12	14	18	59	30.2
-13.758	-75.696	60.8	12.1	16.6	7.3	2011	12	15	6	6	10.8
-69.865	-17.871	136.7	3.6	6.4	4.6	2011	12	16	4	53	50.3
-71.942	-16.446	101.8	13.7	5.8	7.2	2011	12	17	14	4	21.4
-69.411	-17.5	159.4	8.4	11.5	11.2	2011	12	18	18	40	27.6
-72.275	-15.115	116.3	4.6	4	6.6	2011	12	19	7	6	28.7
-69.489	-17.552	148.4	8.6	15.3	8.3	2011	12	19	19	58	38.9
-71.921	-16.541	92.6	8.9	5.2	8.2	2011	12	20	3	40	39.9
-69.485	-16.692	183.7	7	6.8	9.6	2011	12	20	22	42	48.6

-72.03	-15.478	119.5	5.6	7.1	7.4	2011	12	21	8	44	32.1
-69.271	-17.219	168	7.3	8.9	10.3	2011	12	23	9	13	21.8
-69.324	-17.656	135.5	4.2	7.4	8.5	2011	12	23	20	41	13.2
-69.369	-18.278	126.7	4.6	6.3	10.1	2011	12	24	8	37	8.4
-69.541	-17.397	152.1	5	8.1	12.6	2011	12	25	4	41	19.9
-17.954	-70.916	53.3	6.7	4.9	4.4	2011	12	25	9	11	24
-74.799	-13.426	89	3.8	4.4	5.8	2011	12	25	19	24	10.9
-70.914	-17.082	86.5	6.9	6	7.8	2011	12	25	19	36	31.7
-69.363	-16.615	178.4	8.1	7.4	8.7	2011	12	26	0	44	37.5
-70.52	-15.589	200	3.9	4.2	6.4	2011	12	29	3	32	43.2
-76.613	-12.507	59.5	9.2	7.6	6.1	2011	12	29	13	45	42
-69.481	-17.707	131.8	4.4	10.5	11.3	2012	1	1	14	7	9.4
-72.993	-14.088	81.6	4.5	4.3	6.9	2012	1	1	17	54	51.1
-70.592	-16.869	120	5.6	8	10.6	2012	1	2	9	22	1.1
-74.062	-10.25	110.3	6.7	8.6	15.7	2012	1	4	5	37	35.7
-69.305	-17.689	141.2	4.2	6	7	2012	1	4	8	57	31.3
-75.496	-13.801	84.1	8.5	13.1	8.5	2012	1	4	11	33	2.6
-72.009	-16.981	58.6	22.5	10.9	5.6	2012	1	5	5	27	4.3
-72.162	-16.664	62.1	4.3	7.6	4.5	2012	1	10	12	10	22.7
-72.842	-14.939	101.7	5	3.5	10.9	2012	1	11	18	58	32.8
-72.846	-14.882	100.9	4	4.1	8.1	2012	1	11	18	58	33.6
-69.558	-17.71	130.8	4.4	6.6	8.1	2012	1	11	20	24	22.5
-72.254	-15.354	116.1	6.5	5.4	14.7	2012	1	12	0	43	19.9
-74.769	-13.306	80.2	3.9	6.5	4.4	2012	1	13	17	41	43.1
-72.229	-14.997	86.6	8	6.3	52.3	2012	1	18	0	15	48.9
-76.028	-13.038	85.9	17.4	10.5	38.7	2012	1	18	4	57	54.2
-69.45	-18.172	129.4	6.5	7.5	10.4	2012	1	20	12	45	7.1
-70.167	-17.507	106.3	3.5	8.3	7.6	2012	1	21	20	11	48.3
-72.267	-15.388	139	5.9	5.8	12.9	2012	1	22	8	7	31.9
-75.013	-11.006	106.1	6.4	9.1	15.4	2012	1	22	18	5	16.5
-69.073	-18.402	137	8.1	10.1	12.5	2012	1	23	17	22	29.1
-69.823	-17.225	132.4	3.6	7.6	12.7	2012	1	26	10	31	35.5
-69.297	-17.423	154.6	6.7	12.1	9.8	2012	1	27	7	9	8.9
-76.311	-13.148	66.7	9.6	8.3	9.9	2012	1	28	0	59	32.6
-72.836	-14.321	87.5	4.4	4.2	9.3	2012	1	28	7	32	21.7
-72.807	-14.786	92.3	4	3.5	11.3	2012	1	28	9	31	54.2
-74.564	-13.225	77.9	3.7	4	4.7	2012	1	28	11	50	33.4
-69.779	-16.51	180.1	4.9	4.5	8.3	2012	1	29	6	8	23.1
-75.59	-14.274	54.5	7.9	5.3	4.5	2012	1	30	2	26	23.5

-75.675	-14.265	53.2	11.5	6.2	7.9	2012	1	30	14	20	41.2
-75.047	-13.836	83.9	5	3.6	9.5	2012	2	2	1	48	17.7
-70.852	-15.212	180	5.9	5	8.1	2012	2	2	10	1	48.5
-74.961	-15.143	58.6	8.6	8.2	3.7	2012	2	4	4	40	53.2
-70.77	-15.572	180	4.8	4.6	5.8	2012	2	5	20	58	45.5
-72.004	-15.037	127.3	4.5	3.7	7.2	2012	2	6	16	45	15.2
-69.581	-15.967	220.9	5.8	5.3	9.7	2012	2	6	19	17	57.4
-71.704	-15.191	138.8	5	4.3	8	2012	2	6	20	47	15.8
-74.939	-15.055	59.3	7.4	9.1	3.2	2012	2	11	0	40	3.1
-71.588	-15.09	135.8	4.9	3.8	6.7	2012	2	11	21	30	41.4
-71.754	-16.755	75.9	6.3	4.5	4.8	2012	2	12	4	19	47.1
-70.033	-17.63	100.3	2.7	6.6	6.5	2012	2	12	5	23	25
-74.346	-15.719	59.1	11.2	8.5	5.5	2012	2	12	9	28	13.2
-72.521	-15.054	112.8	7.8	6.4	9.5	2012	2	12	15	52	12.2
-69.465	-17.24	156.4	6.8	13.9	12	2012	2	13	13	50	39.8
-69.598	-17.68	149.5	5.7	11.4	8.6	2012	2	13	14	32	18.9
-69.637	-18.117	113	3.9	8.2	6.7	2012	2	14	2	15	38.1
-69.43	-18.219	124.8	3.6	5.6	6	2012	2	14	14	8	39.7
-69.751	-18.202	116.5	4.3	9	8.8	2012	2	14	19	58	19.2
-69.579	-17.554	134	4.8	8.8	7.2	2012	2	15	3	58	3.3
-69.766	-16.684	176.5	6.4	9.6	13.5	2012	2	16	2	34	42.8
-71.689	-15.958	136.3	5.5	4.7	5.5	2012	2	16	4	23	26.5
-70.869	-17.083	98.1	5.2	4.3	7.5	2012	2	16	8	6	50.2
-13.404	-74.848	110.8	7.6	8.2	36.7	2012	2	17	7	11	47.3
-72.34	-16.007	107.5	9.4	5.2	14.2	2012	2	19	7	32	2.3
-70.539	-18.132	58.8	8.2	13.6	4.1	2012	2	20	1	35	58.9
-69.326	-18.38	127	5.9	7.1	6.6	2012	2	20	10	44	39.9
-72.804	-14.316	87	6	5.7	14.7	2012	2	22	19	6	40.8
-70.031	-17.513	131.7	4.6	9.2	7.5	2012	2	25	5	15	11.5
-69.353	-15.918	236.4	9.4	8.5	7.4	2012	2	27	2	37	27.9
-71.762	-15.741	137.6	7.6	6.7	8.6	2012	2	27	10	12	11.2
-72.982	-14.088	80.2	4.5	4.4	6.8	2012	2	27	18	30	7.9
-69.682	-17.619	140	3.4	5.7	9.7	2012	3	5	20	20	11.3
-72.046	-16.197	130	4	4	10.5	2012	3	6	9	40	22.1
-73.684	-14.326	81.2	4.6	5.8	11.1	2012	3	8	19	39	55.8
-75.152	-13.097	90.1	4.9	3.6	8.8	2012	3	8	20	3	23.8
-17.908	-70.188	100	5.9	13.1	10.2	2012	3	9	1	43	16.2
-74.877	-13.471	95.2	5.1	5	10	2012	3	9	8	54	28.5
-72.907	-14.372	83.3	3.2	3.4	6.6	2012	3	10	5	20	31.4

-75.622	-14.277	51.2	12.2	8	7.3	2012	3	12	7	17	11.7
-71.896	-16.402	99.5	7.1	5.3	8.1	2012	3	15	13	26	37.6
-69.47	-17.353	147.1	4.5	6	7.3	2012	3	16	1	53	51.1
-11.571	-73.302	50.1	3.7	4.7	3.9	2012	3	16	6	52	39.5
-74.11	-15.334	62.6	6.6	4.5	4.8	2012	3	16	18	37	53.7
-75.693	-11.202	111.6	8	8.4	9.6	2012	3	17	18	31	3.4
-76.428	-13.011	66.7	9.2	6.1	10.7	2012	3	20	2	36	23.6
-69.567	-16.613	190.4	7.7	11.8	12.4	2012	3	20	15	59	58.5
-71.143	-16.592	104.1	6.6	3.7	9	2012	3	21	8	43	14.6
-72.392	-15.289	108.7	4.9	5.3	10.5	2012	3	22	3	13	14.8
-74.014	-14.269	70	3.8	5.6	12.3	2012	3	23	10	31	12.7
-69.436	-17.782	146.6	4.6	7.8	7.8	2012	3	24	11	46	23
-70.737	-15.568	176.1	4.1	4.4	6.3	2012	3	24	14	39	25.4
-69.769	-17.253	147.8	6.1	13.5	12.9	2012	3	24	16	1	56
-69.765	-16.631	162.7	5.5	4.9	11.1	2012	3	26	8	23	0.9
-69.384	-16.928	179.7	5.5	6.2	6.7	2012	3	26	15	22	55.6
-73.944	-12.876	66.2	5.6	7.7	12.3	2012	3	27	16	7	29.3
-69.496	-16.67	181.1	8	8.6	12.2	2012	3	28	22	38	9.7
-69.588	-16.751	168.6	4.7	8.2	10.7	2012	3	29	23	31	7.2
-70.207	-15.544	204.2	5.6	4.5	10	2012	3	30	3	2	27
-71.261	-15.579	154.3	7.9	5.4	8.4	2012	3	30	4	9	57.7
-69.413	-17.307	149	5.1	8.9	8.2	2012	3	30	10	48	44.3
-71.889	-15.003	123.4	6	4.8	8.2	2012	4	1	2	30	42.8
-69.122	-17.714	144.5	5.5	7.2	7.3	2012	4	1	22	4	35.8
-69.627	-16.159	208.4	6.7	5.8	8.5	2012	4	4	3	15	14.2
-72.091	-14.23	56.7	6.7	7.2	18.5	2012	4	4	19	34	14.3
-69.684	-17.516	130.4	4.6	7.1	5.9	2012	4	5	22	16	19.6
-69.348	-17.78	136.2	4.8	9.3	11.6	2012	4	8	23	4	57.2
-70.318	-17.477	98.2	3.3	5.2	5	2012	4	9	0	40	39.1
-75.989	-13.927	56.9	9.7	7.2	5.1	2012	4	12	1	1	11.3
-72.118	-14.595	90.8	5.2	6	17.1	2012	4	14	20	30	59.3
-71.968	-16.149	105.9	6.4	5.5	10.9	2012	4	16	13	24	55.7
-73.772	-15.098	91.6	3.9	7	9.3	2012	4	17	3	44	58.7
-71.928	-14.901	111.2	6.9	7.6	12.9	2012	4	17	9	43	12.9
-75.623	-13.697	73.3	6.2	5.5	8.1	2012	4	18	18	37	52.2
-71.934	-14.923	132.9	4.1	3.7	10	2012	4	19	23	2	43.2
-72.11	-15.822	118	7	4.7	8.3	2012	4	20	2	43	25.2
-71.805	-14.872	120.6	3.6	3	5.5	2012	4	21	11	36	3.8
-72.031	-14.934	115.8	3.8	3.9	7.4	2012	4	23	17	2	44.8

-75.774	-13.923	61.2	11.2	8.7	6.6	2012	4	24	0	43	49.3
-71.628	-16.216	125.5	11	7.8	6.3	2012	4	24	2	14	16.6
-75.819	-13.761	65.5	11.3	8.2	18	2012	4	24	6	20	35.1
-71.668	-16.334	102.5	5.8	4.8	6.9	2012	4	25	16	19	38.4
-74.871	-14.383	62.3	4.4	4.9	4.1	2012	4	25	22	37	15.5
-75.807	-13.463	77.3	11.6	14.3	13.1	2012	4	29	2	30	14.4
-70.567	-17.887	57.5	8.2	16.3	4.4	2012	4	30	8	4	21.2
-69.308	-18.196	134.9	5.8	24.4	11.7	2012	4	30	12	32	18.8
-72.365	-14.479	92.7	4.9	5.2	16.5	2012	5	2	10	52	59.8
-75.157	-14.883	56.1	8.4	7.1	3.2	2012	5	2	11	34	43.9
-73.821	-14.171	65.4	5.3	7.4	18	2012	5	2	16	54	26.4
-71.215	-17.66	52.8	23.3	22.9	13.3	2012	5	2	21	57	11.3
-69.925	-17.029	131.2	4.7	6.9	13.9	2012	5	3	11	31	52
-73.919	-12.859	63.6	9.9	11.8	6.8	2012	5	3	20	57	45.9
-72.522	-14.926	103.6	5.2	7.8	20	2012	5	4	11	26	12.9
-70.501	-16.07	190	5.8	6.2	9.8	2012	5	4	18	50	48.2
-74.715	-12.725	71.2	6.8	5.7	15.7	2012	5	5	2	7	15.7
-75.539	-12.776	95.7	11.2	5.7	24.5	2012	5	9	10	36	36.6
-69.739	-17.719	136.1	4.3	7.3	7.3	2012	5	12	11	28	53.3
-73.667	-14.461	83.6	6	8.3	9.1	2012	5	12	16	57	38.9
-69.477	-17.687	137.1	5.6	10.3	9.6	2012	5	13	7	47	34.4
-70.008	-17.872	100.4	3.8	6.3	8.6	2012	5	14	10	0	39.1
-72.482	-16.055	93	4.1	4.7	10.1	2012	5	15	2	38	27.4
-71.65	-16.445	106.8	2.9	4.4	7.4	2012	5	15	7	14	31.8
-70.028	-17.845	99.8	2.9	5.2	4.3	2012	5	15	21	20	33.6
-72.658	-16.515	70	6	6.4	3.8	2012	5	16	1	54	8.5
-76.17	-11.869	111	10.2	7.2	12	2012	5	17	3	45	27.9
-69.451	-17.444	153.2	7.2	11.9	12.1	2012	5	17	8	5	37.5
-76.512	-13.062	51.7	9.3	6.8	5.4	2012	5	18	9	22	31.6
-69.53	-16.677	185.5	5.8	5.3	8.6	2012	5	21	3	37	1.6
-72.802	-14.837	91.8	4	4.2	16.2	2012	5	22	6	50	1.5
-70.885	-16.82	113.1	3.8	3.1	7.4	2012	5	23	1	4	33.8
-74.741	-15.802	63.2	25.3	17.3	6.1	2012	5	23	14	36	39.1
-71.895	-14.986	126.7	6.6	6.2	7	2012	5	25	13	27	7.9
-76.336	-12.528	62.5	12.3	7.1	6.2	2012	5	28	16	46	41.4
-70.102	-18.062	91.1	4.2	6.7	4.2	2012	5	31	11	29	54.7
-69.519	-18.369	123.4	6.9	19.8	10.6	2012	6	1	3	45	54.8
-69.6	-17.444	160.1	4.4	7.4	14.9	2012	6	2	0	22	17.3
-71.787	-14.792	115.2	7.3	11.7	12.8	2012	6	2	9	20	47.3

-72.176	-15.996	109.3	4.1	3.9	8.4	2012	6	3	0	40	14.4
-75.16	-14.82	56.1	10.5	11.7	5.2	2012	6	4	17	11	19.9
-75.533	-15.099	62.8	34.2	18.6	10.1	2012	6	4	21	37	29.6
-71.306	-15.595	150.3	7.3	4.5	8.2	2012	6	5	15	20	18.9
-72.67	-16.027	120	4.1	4.7	14.2	2012	6	7	16	3	14.7
-70.332	-17.994	74.4	5.6	10.4	5.4	2012	6	9	16	11	13.1
-74.59	-13.907	64.7	4.6	5	4.1	2012	6	11	0	17	38.2
-67.379	-18.449	254.7	18.2	14.8	11.4	2012	6	11	4	41	35.4
-75.426	-13.872	80	4.5	4.1	8	2012	6	11	9	55	23.7
-72.828	-14.271	85.9	2.9	3.9	9.5	2012	6	12	7	23	37.2
-72.033	-15.64	128.8	6.2	4.9	8.2	2012	6	13	3	21	22.1
-74.694	-14.297	81.2	4.2	6	15.1	2012	6	14	5	41	41.2
-69.35	-16.594	198.9	7.2	5.6	7.9	2012	6	14	5	43	1.9
-70.622	-15.612	197.9	4.4	4.6	11	2012	6	14	7	48	8.2
-69.711	-16.349	192.7	4.7	4.9	9.3	2012	6	15	3	33	3.4
-72.169	-15.172	115.1	7	5.7	8.5	2012	6	15	10	47	56.3
-75.578	-14.089	69.7	8.2	7	10.3	2012	6	15	22	13	47.2
-72.106	-14.945	120	5.3	5.6	14	2012	6	18	6	9	34.1
-72.009	-15.409	125.6	10.9	5.9	14.4	2012	6	20	13	30	19.4
-76.759	-11.715	93	12.3	9.3	10.6	2012	6	21	22	17	9.6
-76.645	-11.677	87.4	10	8.9	5.3	2012	6	21	23	20	24.5
-71.105	-16.789	105.6	8.5	4.7	10.3	2012	6	23	9	35	11.6
-69.647	-17.659	136.3	3.7	5.2	6.4	2012	6	25	2	7	23.9
-74.979	-13.27	89.6	13.4	131.9	69.2	2012	6	25	9	17	23.8
-76.297	-11.503	95.8	11.5	12.5	13.4	2012	6	27	8	4	20.8
-76.024	-13.064	78.3	7.5	8	17	2012	6	27	12	41	7.9
-72.645	-14.474	90.6	5.1	6.1	14.7	2012	6	28	2	12	5.3
-16.846	-71.161	65.3	30.6	12.2	13.5	2012	6	30	2	0	16.8
-72.31	-16.082	100.1	4.5	4.7	11.1	2012	7	1	4	38	6.6
-69.657	-16.882	164.1	5.9	7.8	12.1	2012	7	1	14	25	59.6
-75.638	-14.325	51.7	8.4	7.3	5.6	2012	7	3	5	31	16.9
-11.271	-73.819	53.7	5.8	9.7	6.4	2012	7	4	16	25	10.9
-69.609	-17.679	139.1	5.3	10.2	8.6	2012	7	4	18	19	12.1
-70.291	-17.573	94.2	2.6	5.6	6.2	2012	7	9	10	15	33.6
-75.454	-14.396	59.2	9.5	8.1	5.7	2012	7	9	19	21	57
-69.566	-16.915	173.1	7.5	10.3	12.9	2012	7	9	20	53	52.6
-69.511	-16.917	177.2	9.3	9.6	12.4	2012	7	9	20	53	52.4
-75.822	-12.337	93.9	9.4	2.8	20.1	2012	7	9	21	50	47.9
-72.564	-15.208	117.3	6.1	5.2	11.2	2012	7	10	18	42	20.6

-73.093	-14.162	89.3	3.7	5	7.6	2012	7	12	5	5	29.7
-69.814	-17.709	117.9	2.7	3.7	5.3	2012	7	13	0	57	55.7
-69.315	-18.305	126	4.4	5.9	8	2012	7	14	5	28	6.6
-70.003	-17.791	98.6	6.1	6.4	4.8	2012	7	19	3	26	57
-69.726	-16.646	181.8	7	10.9	13.7	2012	7	19	17	16	17.7
-14.357	-75.628	51.2	8.9	7.3	6.9	2012	7	22	17	9	47.8
-71.601	-15.284	136.7	5	3.9	6.7	2012	7	22	20	33	34.2
-69.972	-17.762	122.7	4.7	10.7	8.8	2012	7	25	22	28	49.2
-69.696	-17.973	135.4	7.3	11	6.3	2012	7	26	7	36	56.2
-75.774	-13.412	88.8	7	7.3	9.9	2012	7	27	18	41	0.3
-74.749	-11.386	97.8	9.1	6	11.6	2012	7	28	12	43	60
-69.385	-16.75	185.2	12.7	7.5	11.9	2012	7	31	19	58	31.2
-76.22	-12.861	51.2	10.8	6.5	18.1	2012	8	1	2	31	52.6
-75.07	-13.117	93.4	6.3	13.3	23.8	2012	8	3	23	25	8.1
-74.824	-13.671	98.8	3.8	9.9	8.7	2012	8	8	1	59	15.9
-10.816	74.023	96.4	15.3	13.3	29.7	2012	8	9	14	43	54
-75.427	-12.636	92.8	3.5	3.1	12.7	2012	8	16	13	44	31.5
-75.082	-13.171	100	7.2	16.4	22.9	2012	8	28	0	57	18.4
-75.658	-11.865	100	6.1	6.8	17	2012	8	31	11	19	46.8
-75.067	-13.131	97.3	6.9	12.1	21	2012	9	1	4	0	7.9
-74.995	-12.355	90.8	10.1	5.7	10.8	2012	9	1	5	32	19.9
-76.305	-12.269	84.4	12.3	4.8	7.3	2012	9	5	2	18	43.7
-13.802	-75.976	53.2	9.6	20	7.8	2012	9	5	4	10	24.9
-74.769	-13.678	93.9	8.9	33.8	25.6	2012	9	5	16	52	14.9
-74.632	-11.443	91.3	7.2	6.1	15.2	2012	9	8	1	47	38.3
-75.425	-12.637	92.9	3.5	2.3	11.1	2012	9	8	12	2	57.9
-75.919	-11.385	105.7	10.4	15.7	13.6	2012	9	24	13	29	15.6
-74.001	-12.915	71.9	5.6	7.8	11.4	2012	9	24	17	53	16.3
-73.115	-16.673	64	11.1	19.8	5.2	2012	9	24	23	25	8.6
-75.362	-12.986	102.1	5.4	5.3	16.3	2012	9	26	6	10	51.5
-74.948	-11.915	90	16.9	5.1	11.5	2012	9	27	2	51	9
-76.432	-11.849	101.4	12	9.8	11	2012	9	28	4	38	59.9
-75.251	-13.004	91.7	6.5	3.4	9.9	2012	10	8	6	46	3.1
-11.186	-73.501	64	7.6	8.4	15.4	2012	10	9	8	24	10.3
-75.67	-13.395	86.6	9.8	8	7.3	2012	10	12	3	53	17.3
-73.592	-14.833	90.3	4.9	7.2	8.1	2012	10	15	7	45	8.1
-75.413	-12.485	92.3	6.7	4.1	14.3	2012	10	16	5	46	57.5
-74.98	-12.839	92.2	8.3	6.1	20.4	2012	10	20	5	44	16.6
-76.523	-12.024	86.2	6.3	5.7	5.6	2012	10	30	13	5	53.9

-73.933	-12.929	69.8	3.9	9.4	7.8	2012	11	2	18	57	53.6
-75.896	-12.084	106.8	6.8	5.3	12	2012	11	4	1	52	11.5
-75.845	-13.25	54.7	10	10.2	4.9	2012	11	4	20	29	38.8
-75.317	-12.505	88.4	6.4	5.1	12.8	2012	11	7	17	56	17.6
-74.602	-13.243	77.3	6.2	15.1	8.8	2012	11	13	9	1	39.5
-73.933	-12.924	65	6.7	15.9	4.3	2012	11	13	14	54	47.3
-76.286	-12.743	65.4	13.1	8.8	7.9	2012	11	14	6	20	11.8
-76.027	-11.131	109.2	11.2	15.2	11.7	2012	11	17	11	13	32.4
-73.995	-13.019	75.1	3.9	24.3	5.1	2012	11	23	1	31	56.6
-75.108	-13.226	91.8	5.5	15.5	9.4	2012	11	26	0	35	31.1
-74.878	-13.194	78.5	3.9	6.3	9.5	2012	11	29	10	50	36.2
-75.86	-11.465	107.3	18	16.6	13.5	2012	12	1	17	54	10.9
-14.874	-72.483	124.7	7.4	10.5	14.7	2012	12	10	16	9	41
-75.2	-12.553	101.6	8.7	3.5	12.4	2012	12	20	5	18	29.5
-75.907	-11.973	106.4	4.7	5.4	9.8	2012	12	21	5	38	30.7
-75.64	-13.52	74.1	11.5	15.7	19.2	2012	12	25	20	11	15.3
-75.944	-11.995	107.5	5.2	7	11.8	2012	12	30	1	34	14.3
-75.435	-12.816	83.6	4.3	4.6	26.9	2012	12	31	4	40	23.1
-75.199	-13.705	95.5	4.1	6.4	10.5	2013	1	22	10	4	33.9
-74.403	-13.717	81.4	11.8	18.6	21.8	2013	1	23	8	40	12.8
-75.124	-13.261	89.4	8.4	27.9	22.2	2013	2	17	17	55	10.1
-76.205	-12.311	64.5	36.1	7.3	17.2	2013	2	19	15	44	22.6
-74.981	-13.368	88.2	4.7	43.3	23.2	2013	2	27	1	19	51.4
-74.4	-13.259	70.8	5.1	6.2	4.6	2013	3	8	20	0	47.9
-74.094	-11.016	109.8	19.7	10.4	42.4	2013	3	27	20	59	27.5
-74.779	-11.522	93.6	8.2	3.4	9.4	2013	4	7	10	53	47
-75.455	-13.868	72.8	8.9	19	8.9	2013	4	7	13	18	14.3
-75.253	-13.602	87.8	2.6	9.2	3.7	2013	4	9	9	30	3.1
-76.011	-12.292	106.5	4.3	4.6	15.7	2013	4	10	7	11	14.7
-75.406	-10.908	122.3	11	9.8	10	2013	4	10	16	20	23.2
-75.861	-13.725	70.1	13.3	15.3	12.4	2013	4	21	9	39	59
-75.694	-11.861	100.8	7	14.3	16	2013	4	28	15	28	13.9
-11.503	-74.325	64.5	9.1	4.6	14	2013	5	3	9	0	30.6
-76.062	-12.672	88.5	7.7	2.8	14.3	2013	5	3	15	59	48.8
-74.954	-13.342	89.6	4.8	40.9	23.1	2013	5	5	12	44	32
-75.001	-13.24	94.6	4	14.4	11.2	2013	5	5	16	28	30
-74.859	-13.383	101.5	5.3	22.9	23.4	2013	5	5	18	5	31.9
-75.336	-12.536	92.9	6.5	4.8	13.6	2013	5	8	6	28	47.7
-74.602	-13.841	99.2	7.6	11.8	24	2013	5	12	20	22	9.8

-75.148	-13.148	90	7.3	13.9	23	2013	5	15	13	30	13.9
-72.666	-13.841	91.3	3.2	7.4	10.6	2013	5	21	23	2	42.4
-75.281	-12.892	90.2	3.5	2.6	7.9	2013	5	25	16	4	42.3
-74.85	-12.862	94.8	6	5.9	19.4	2013	5	27	2	35	44.2
-76.38	-12.769	54.9	22.2	6.2	11.5	2013	6	2	20	58	54.8
-74.81	-13.398	79.6	19.4	49.2	17.3	2013	6	3	1	7	13.8
-75.223	-12.922	97.4	4	3.9	10.9	2013	6	7	3	22	23.3
-76.478	-13.171	77.9	10	10.9	32.4	2013	6	7	7	51	38.7

Table 1.2. Coordinates of 508 relocated hypocenters as determined from HypoDD

Lon	Lat	Dep	Lon err	Lat err	Dep err	Yr	Mo	Day	Hr	Min	Sec
-71.547	-15.112	146.9	0.34	0.32	0.47	2010	11	9	2	9	52.8
-71.598	-16.082	136.9	0.33	0.43	0.43	2010	11	16	5	57	26.4
-71.403	-15.661	152.4	0.37	0.47	0.35	2010	11	18	7	0	53.7
-69.572	-17.327	146.0	0.19	0.24	0.28	2010	11	18	20	32	10.9
-69.636	-17.607	128.9	0.20	0.15	0.17	2010	11	19	1	42	51.9
-69.917	-17.289	125.2	0.21	0.27	0.24	2010	11	20	16	33	19.1
-69.634	-17.606	147.0	0.19	0.18	0.22	2010	11	25	2	16	27.6
-69.353	-17.375	156.7	0.19	0.22	0.15	2010	11	25	17	25	45.1
-71.192	-16.582	109.2	0.21	0.19	0.37	2010	11	25	18	16	51.5
-71.449	-16.728	82.6	0.28	0.31	0.23	2010	11	26	3	36	55.2
-69.576	-17.281	162.5	0.24	0.26	0.26	2010	11	27	6	33	43.5
-72.121	-15.288	121.8	0.34	0.27	0.50	2010	11	27	12	59	56.8
-69.456	-17.608	151.3	0.19	0.16	0.18	2010	11	28	3	11	19.4
-71.754	-14.801	125.2	0.43	0.38	0.56	2010	11	28	14	49	21.6
-69.365	-18.191	128.2	0.25	0.34	0.34	2010	11	30	8	4	38.6
-70.106	-17.065	137.5	0.20	0.33	0.27	2010	11	30	14	27	55.7
-67.190	-18.369	244.3	4.25	2.65	2.41	2010	12	2	0	19	23
-70.246	-15.559	211.3	0.19	0.17	0.29	2010	12	2	2	56	11.5
-69.306	-17.973	131.1	0.25	0.27	0.28	2010	12	3	1	46	7.1
-71.085	-16.698	123.3	0.26	0.25	0.35	2010	12	7	4	14	40.1
-72.111	-15.055	118.2	0.25	0.24	0.34	2010	12	8	8	3	53.2
-70.431	-17.465	88.5	0.58	0.51	0.73	2010	12	8	22	21	43.1
-69.515	-16.893	176.6	0.21	0.19	0.30	2010	12	11	2	4	19.2
-69.387	-17.885	132.9	0.25	0.28	0.27	2010	12	11	15	52	50.9
-70.152	-17.556	98.7	0.49	0.63	0.61	2010	12	13	3	51	42.9
-69.447	-17.583	152.6	0.18	0.16	0.15	2010	12	13	10	43	13.5
-69.571	-17.602	133.7	0.19	0.14	0.17	2010	12	14	14	32	22.2
-71.392	-17.245	64.4	0.41	0.54	0.52	2010	12	15	13	23	7.3
-69.329	-17.728	143.2	0.22	0.22	0.27	2010	12	15	18	22	23
-69.630	-17.600	146.5	0.20	0.22	0.30	2010	12	17	2	32	36.6
-71.779	-15.325	143.5	0.35	0.45	0.44	2010	12	18	13	7	52.5
-71.927	-15.073	122.8	0.27	0.25	0.32	2010	12	19	7	43	51.9
-70.706	-15.392	197.8	0.27	0.32	0.35	2010	12	21	20	4	46.7
-71.874	-15.473	136.6	0.44	0.42	0.56	2010	12	22	14	5	16.6
-69.372	-18.004	146.3	0.25	0.26	0.20	2010	12	22	19	58	0.1
-72.081	-15.044	116.1	0.30	0.29	0.34	2010	12	25	5	49	22
-72.013	-14.628	105.3	0.72	0.58	0.65	2010	12	28	21	39	19.4

-69.717	-17.455	127.8	0.25	0.34	0.28	2010	12	29	4	44	16.5
-70.053	-17.103	137.4	0.20	0.29	0.39	2011	1	1	4	11	51.4
-72.310	-14.728	98.3	1.11	0.47	0.99	2011	1	1	20	27	41.2
-69.630	-17.651	145.4	0.19	0.18	0.18	2011	1	2	6	56	26.1
-72.017	-15.104	128.6	0.29	0.28	0.32	2011	1	6	1	56	12.1
-69.724	-17.187	143.6	0.24	0.31	0.27	2011	1	6	14	40	20.2
-69.463	-17.461	160.0	0.18	0.20	0.27	2011	1	8	6	26	59.5
-71.714	-15.654	141.2	0.40	0.50	0.40	2011	1	9	1	43	37.6
-69.493	-18.192	120.8	0.30	0.27	0.27	2011	1	12	4	24	3.7
-69.705	-17.007	156.6	0.42	0.52	0.42	2011	1	12	23	28	4.7
-69.558	-16.880	175.1	0.42	0.23	0.41	2011	1	14	4	56	35.2
-69.542	-16.568	186.7	0.28	0.31	0.29	2011	1	15	1	0	34.2
-72.166	-15.154	119.7	0.28	0.29	0.34	2011	1	15	7	32	36.4
-71.797	-14.758	117.0	0.48	0.66	0.66	2011	1	16	8	9	19.9
-70.683	-15.322	206.4	0.47	0.43	0.64	2011	1	17	19	48	39
-70.635	-17.474	94.7	0.38	0.43	0.56	2011	1	19	10	23	37
-69.454	-17.557	151.8	0.17	0.17	0.15	2011	1	21	9	42	13.1
-70.252	-15.544	210.6	0.23	0.17	0.18	2011	1	22	21	31	19.9
-70.269	-18.010	53.5	0.85	1.00	0.70	2011	1	24	15	17	54.2
-69.330	-17.698	159.7	0.59	0.63	0.88	2011	1	26	8	11	9.6
-69.615	-17.565	151.7	0.20	0.22	0.30	2011	2	2	9	5	27.3
-70.058	-17.783	95.8	0.24	0.26	0.25	2011	2	2	11	3	51.2
-69.877	-17.689	112.3	0.41	0.57	0.30	2011	2	3	7	42	49.6
-69.423	-17.323	152.1	0.18	0.20	0.23	2011	2	4	0	55	31.4
-69.399	-17.740	142.3	0.20	0.24	0.28	2011	2	4	14	47	38.4
-69.431	-17.661	154.6	0.23	0.21	0.20	2011	2	7	22	44	52.9
-66.964	-18.008	271.3	1.66	1.32	1.69	2011	2	8	4	54	41.4
-70.924	-16.687	123.6	0.36	0.46	0.55	2011	2	8	13	24	16.3
-70.234	-15.511	212.3	0.27	0.24	0.30	2011	2	11	6	39	42.3
-71.198	-16.521	111.6	0.16	0.18	0.34	2011	2	14	8	58	29.6
-73.609	-14.672	64.3	0.36	0.28	0.30	2011	2	17	10	31	6.8
-71.767	-15.035	133.2	0.33	0.36	0.42	2011	2	18	19	38	36.8
-71.565	-15.539	143.0	0.39	0.57	0.40	2011	2	21	15	54	1.3
-69.446	-16.719	177.5	0.41	0.41	0.44	2011	2	22	8	13	18.8
-70.063	-17.140	135.3	0.20	0.26	0.23	2011	2	22	16	53	12.6
-69.612	-16.664	186.0	0.28	0.36	0.37	2011	2	23	13	46	59.1
-70.298	-17.036	125.1	0.33	0.42	0.71	2011	2	25	7	42	25.8
-71.842	-15.189	129.7	0.27	0.32	0.32	2011	2	28	11	5	22.7
-69.659	-16.948	167.4	0.32	0.35	0.32	2011	3	2	18	8	54.7

-69.453	-17.616	155.3	0.25	0.28	0.22	2011	3	5	0	18	45.9
-69.652	-15.865	234.0	0.17	0.20	0.36	2011	3	5	18	9	22
-69.697	-18.167	108.8	0.33	0.35	0.40	2011	3	6	12	31	57.5
-70.537	-15.407	202.6	0.24	0.28	0.39	2011	3	11	2	34	18.2
-70.315	-15.451	210.0	0.21	0.18	0.25	2011	3	25	1	50	46.7
-69.425	-17.954	126.8	0.23	0.24	0.26	2011	3	26	16	50	7.9
-69.715	-17.750	135.0	0.29	0.29	0.32	2011	3	31	1	42	21
-71.554	-16.128	120.0	0.38	0.41	0.46	2011	4	2	4	41	44.5
-71.209	-17.631	55.6	0.62	0.64	0.62	2011	4	2	8	20	41.8
-69.641	-17.476	137.1	0.21	0.23	0.31	2011	4	3	16	14	30.6
-70.516	-17.820	59.9	0.53	0.68	0.48	2011	4	4	2	57	8.1
-69.623	-17.215	161.3	0.23	0.27	0.21	2011	4	6	11	13	10.7
-69.555	-17.201	157.1	0.22	0.24	0.22	2011	4	9	6	47	21.7
-69.478	-17.447	160.5	0.19	0.20	0.13	2011	4	9	10	12	50.8
-71.887	-17.057	64.8	0.93	1.15	1.20	2011	4	12	13	31	7.3
-69.381	-17.653	157.2	0.26	0.24	0.19	2011	4	13	0	37	25.5
-71.616	-15.909	122.3	0.37	0.49	0.51	2011	4	13	7	35	19.7
-69.746	-17.405	148.3	0.21	0.24	0.28	2011	4	16	2	27	29.7
-71.577	-16.119	118.0	0.33	0.45	0.46	2011	4	24	7	55	38.8
-69.611	-16.965	175.0	0.24	0.24	0.40	2011	5	1	15	18	41
-69.786	-16.471	190.1	0.34	0.38	0.35	2011	5	3	14	8	5.8
-69.609	-17.575	150.1	0.20	0.25	0.29	2011	5	3	22	3	46.6
-69.412	-17.340	155.6	0.19	0.26	0.27	2011	5	6	2	55	11.2
-69.603	-17.565	150.2	0.32	0.46	0.48	2011	5	6	6	15	13.9
-70.285	-15.631	207.6	0.21	0.16	0.25	2011	5	7	19	33	32.8
-69.828	-17.396	126.8	0.22	0.31	0.24	2011	5	8	9	34	4
-69.524	-17.678	145.8	0.19	0.18	0.18	2011	5	10	4	43	5.9
-69.587	-16.870	167.7	0.23	0.40	0.44	2011	5	12	13	4	4.6
-69.171	-17.919	141.2	0.32	0.34	0.33	2011	5	13	3	40	10.5
-71.209	-16.779	61.8	0.23	0.55	0.24	2011	5	17	2	40	43.2
-69.230	-16.082	238.8	0.18	0.24	0.20	2011	5	17	22	5	28.9
-72.024	-15.743	127.2	0.39	0.45	0.56	2011	5	19	21	4	38.7
-69.663	-16.760	166.9	0.24	0.25	0.26	2011	5	21	18	7	6.8
-69.940	-17.332	128.4	0.26	0.39	0.41	2011	5	22	2	56	1.6
-69.467	-16.649	182.7	0.35	0.38	0.29	2011	5	22	16	24	50.7
-71.654	-16.158	124.8	0.33	0.46	0.49	2011	5	22	18	25	22.9
-69.757	-16.628	176.2	0.26	0.28	0.35	2011	5	22	23	10	51.5
-69.480	-17.619	134.9	0.17	0.14	0.19	2011	5	26	4	44	39.9
-70.194	-15.569	212.3	0.23	0.14	0.19	2011	5	26	9	30	34.8

-72.148	-15.627	125.2	0.41	0.42	0.62	2011	5	30	7	35	49.4
-72.144	-15.631	123.4	0.45	0.37	0.51	2011	5	30	7	35	50.5
-69.672	-16.573	191.6	0.22	0.33	0.20	2011	5	30	18	16	27.8
-69.671	-16.575	190.9	0.21	0.39	0.25	2011	5	30	18	16	28.3
-69.602	-17.540	151.8	0.21	0.18	0.20	2011	5	31	9	5	40
-71.017	-16.855	101.2	0.37	0.39	0.49	2011	6	1	0	34	23.1
-69.646	-17.719	135.8	0.19	0.16	0.18	2011	6	2	7	9	47.1
-69.275	-17.745	142.8	0.26	0.31	0.25	2011	6	3	9	5	58
-69.393	-17.382	154.6	0.23	0.33	0.39	2011	6	5	13	57	57.9
-69.491	-17.608	152.3	0.19	0.21	0.18	2011	6	5	17	31	52.1
-70.504	-15.558	200.3	0.29	0.31	0.38	2011	6	6	8	28	54.4
-69.710	-17.932	113.4	0.33	0.59	0.45	2011	6	7	13	18	7
-73.610	-14.568	87.1	0.26	0.23	0.33	2011	6	7	22	4	53.8
-69.861	-17.230	131.3	0.24	0.29	0.37	2011	6	8	3	6	20
-69.855	-16.367	186.1	0.38	0.26	0.22	2011	6	8	10	53	2.9
-69.372	-16.883	184.4	0.23	0.24	0.20	2011	6	8	18	38	46.4
-69.488	-16.686	183.8	0.31	0.36	0.29	2011	6	9	2	40	34
-72.159	-15.081	114.9	0.29	0.28	0.30	2011	6	15	14	16	49.8
-72.163	-15.082	116.5	0.28	0.26	0.31	2011	6	15	14	16	50.2
-71.633	-15.349	149.5	0.42	0.45	0.42	2011	6	17	7	59	58.2
-69.330	-18.102	128.0	0.27	0.28	0.30	2011	6	17	20	43	5.4
-69.992	-17.794	100.9	0.26	0.26	0.26	2011	6	18	5	38	22.2
-75.246	-12.462	91.2	2.06	2.81	2.01	2011	6	18	6	31	9.7
-70.274	-17.758	76.0	0.70	1.34	0.87	2011	6	18	10	28	35.9
-72.599	-14.998	110.2	0.54	0.40	0.40	2011	6	20	1	5	11.4
-72.852	-14.060	80.7	0.21	0.25	0.33	2011	6	21	1	55	15.1
-71.789	-15.534	148.3	0.39	0.38	0.38	2011	6	23	12	32	60
-71.787	-15.535	148.0	0.35	0.39	0.38	2011	6	23	12	32	59.5
-69.520	-17.365	163.3	0.18	0.26	0.31	2011	6	23	20	7	23.5
-69.520	-17.364	162.8	0.19	0.21	0.20	2011	6	23	20	7	23.8
-69.698	-17.505	126.9	0.27	0.29	0.32	2011	6	25	5	19	49.6
-69.829	-17.242	129.8	0.22	0.25	0.25	2011	6	25	16	9	53.7
-73.146	-14.182	74.5	0.26	0.39	0.48	2011	6	26	17	11	5.5
-74.652	-13.507	92.5	1.58	2.56	2.26	2011	6	28	6	53	26.5
-69.747	-16.237	207.5	0.51	0.38	0.47	2011	6	28	9	35	6.5
-72.789	-14.175	84.7	0.21	0.22	0.31	2011	6	29	2	18	23.9
-71.870	-16.663	45.9	0.74	0.74	0.61	2011	6	29	6	20	22.8
-73.679	-14.101	76.0	0.25	0.42	0.38	2011	6	29	15	2	23.4
-76.002	-13.281	56.9	3.41	5.04	3.38	2011	6	30	13	59	7

-74.559	-10.720	102.1	1.93	1.65	2.47	2011	7	1	5	15	1.4
-71.966	-15.192	122.2	0.33	0.31	0.29	2011	7	4	9	9	31.3
-74.878	-13.718	93.0	1.51	1.45	0.88	2011	7	4	15	0	23.3
-72.714	-14.981	104.0	0.42	0.43	0.40	2011	7	6	1	47	58.5
-71.893	-16.031	108.8	0.24	0.38	0.51	2011	7	8	0	39	15.2
-76.586	-11.539	100.2	3.96	3.62	4.84	2011	7	8	3	54	42.8
-71.831	-15.112	136.8	0.27	0.28	0.32	2011	7	9	8	51	13.5
-72.836	-15.671	116.0	0.55	0.48	0.97	2011	7	10	11	49	5.5
-72.000	-14.965	119.7	0.35	0.32	0.37	2011	7	13	5	18	51.6
-71.922	-15.623	145.2	0.46	0.37	0.36	2011	7	13	8	23	25.8
-67.084	-17.793	284.2	1.86	1.61	1.61	2011	7	14	7	2	25.7
-69.433	-15.951	235.4	0.25	0.31	0.17	2011	7	14	18	34	40.1
-69.432	-15.951	235.3	0.19	0.22	0.25	2011	7	14	18	34	39.7
-69.435	-15.955	234.0	0.29	0.36	0.16	2011	7	14	22	53	54.2
-74.843	-10.943	102.1	2.50	2.15	2.66	2011	7	21	7	12	12.4
-73.480	-14.424	81.9	0.36	0.26	0.36	2011	7	22	22	28	52.8
-73.439	-14.906	99.9	0.77	0.59	0.73	2011	7	23	11	44	45
-73.656	-14.406	87.4	0.24	0.19	0.29	2011	7	24	2	3	12.8
-74.431	-14.842	99.9	0.46	0.49	0.67	2011	7	24	15	49	6.5
-74.464	-14.863	96.8	0.46	0.49	0.69	2011	7	24	15	49	5.1
-74.076	-14.523	87.9	0.81	0.96	1.48	2011	7	27	7	49	3
-72.992	-14.403	80.2	0.30	0.30	0.36	2011	7	27	8	36	0.4
-76.099	-12.174	100.5	1.50	1.07	1.06	2011	7	28	3	13	11.4
-69.556	-16.848	173.8	0.20	0.21	0.19	2011	7	28	5	7	14.2
-72.338	-14.397	81.4	0.35	0.44	0.71	2011	7	30	4	31	6.8
-72.627	-15.790	129.7	0.56	0.32	0.88	2011	7	30	5	28	58.2
-69.863	-17.388	145.3	0.25	0.30	0.23	2011	8	2	18	3	6.6
-71.948	-15.526	130.1	0.44	0.29	0.37	2011	8	5	4	54	19
-75.100	-14.198	80.1	1.44	2.06	2.91	2011	8	6	5	6	56.1
-72.689	-14.058	86.0	0.28	0.29	0.42	2011	8	7	8	41	6.3
-72.495	-15.421	127.9	0.39	0.46	0.58	2011	8	9	7	54	29.2
-69.604	-16.670	186.2	0.30	0.27	0.20	2011	8	11	7	52	34.4
-69.522	-17.470	158.3	0.18	0.15	0.16	2011	8	12	14	32	43.2
-75.146	-13.060	94.1	1.05	1.74	1.14	2011	8	12	23	25	31.4
-70.857	-15.384	176.3	0.23	0.32	0.27	2011	8	14	4	46	44.2
-75.976	-13.550	63.9	3.52	3.34	2.93	2011	8	18	3	23	49.1
-70.249	-15.465	220.4	0.26	0.31	0.30	2011	8	19	9	52	22.9
-70.734	-17.477	92.4	0.45	0.45	0.59	2011	8	22	2	2	26.8
-73.504	-14.963	106.8	0.74	0.61	0.77	2011	8	24	2	10	48.1

-71.981	-15.801	140.8	0.47	0.39	0.62	2011	8	24	2	18	39.4
-69.491	-17.513	137.0	0.35	0.25	0.33	2011	8	25	5	4	6.6
-69.311	-16.588	198.2	0.39	0.35	0.30	2011	8	28	1	21	3.9
-73.061	-14.105	84.7	0.20	0.28	0.29	2011	8	28	8	20	29.6
-73.417	-14.152	74.7	0.44	0.47	0.51	2011	8	29	10	35	29.9
-70.784	-15.288	183.1	0.26	0.35	0.32	2011	8	30	13	37	11.8
-69.537	-17.752	132.7	0.21	0.22	0.25	2011	8	31	0	53	18.2
-69.538	-17.751	132.7	0.21	0.21	0.22	2011	8	31	0	53	18.3
-75.378	-12.523	74.9	1.27	1.99	3.12	2011	9	2	8	27	48.3
-74.162	-14.952	106.0	0.67	0.69	0.84	2011	9	3	18	39	44.8
-74.891	-13.717	94.2	1.54	2.03	1.60	2011	9	4	6	35	53.7
-75.545	-12.300	103.3	1.65	1.89	1.40	2011	9	4	17	56	39
-71.479	-15.882	143.3	0.51	0.58	0.56	2011	9	5	9	9	20.2
-71.804	-15.174	126.8	0.30	0.30	0.35	2011	9	7	1	7	44
-74.258	-10.823	105.9	1.85	1.77	2.13	2011	9	7	22	44	51.2
-72.758	-14.990	101.3	0.26	0.29	0.41	2011	9	8	5	26	13
-72.926	-14.874	105.3	0.17	0.29	0.27	2011	9	10	3	46	44.1
-71.761	-14.858	124.3	0.50	0.49	0.45	2011	9	13	0	14	23.8
-71.762	-14.862	125.2	0.54	0.49	0.52	2011	9	13	0	14	23.3
-72.659	-14.502	94.5	0.51	0.68	0.83	2011	9	13	3	37	58.8
-71.987	-17.422	57.2	1.16	2.24	1.57	2011	9	14	3	0	2.2
-69.659	-17.391	136.7	0.24	0.25	0.33	2011	9	14	14	52	44.2
-72.050	-15.391	132.4	0.36	0.41	0.43	2011	9	16	0	42	28.6
-74.441	-11.284	95.0	1.30	1.70	1.71	2011	9	18	2	9	52.6
-71.802	-15.139	129.8	0.28	0.27	0.30	2011	9	18	7	43	39.3
-72.933	-14.370	84.3	0.28	0.26	0.28	2011	9	21	1	39	47.2
-69.450	-16.480	194.3	0.35	0.34	0.38	2011	9	23	1	55	29
-70.489	-17.169	99.6	1.10	1.19	1.42	2011	9	23	5	21	38.7
-76.001	-11.992	108.7	0.83	0.94	0.80	2011	9	23	10	15	8.1
-75.098	-13.131	97.2	1.40	1.41	2.00	2011	9	24	3	19	9.7
-72.343	-16.750	89.1	0.42	0.64	0.62	2011	9	25	0	12	55.9
-73.357	-14.394	82.5	0.46	0.33	0.34	2011	9	30	9	14	6.6
-71.145	-17.192	82.3	0.16	0.26	0.32	2011	10	5	12	4	30.9
-71.147	-17.195	82.7	0.18	0.24	0.33	2011	10	5	12	4	30.2
-70.774	-15.517	181.1	0.23	0.44	0.28	2011	10	8	12	29	24.5
-75.020	-14.105	94.5	1.39	2.25	2.46	2011	10	12	6	12	20.2
-73.713	-14.873	88.5	0.33	0.37	0.50	2011	10	15	19	31	31.1
-72.829	-14.183	83.9	0.18	0.21	0.30	2011	10	16	7	25	26.7
-69.642	-15.887	226.4	0.15	0.17	0.24	2011	10	19	22	59	36.9

-75.667	-13.677	63.3	1.91	2.76	1.59	2011	10	20	14	56	42.2
-69.623	-18.029	122.4	0.29	0.30	0.31	2011	10	22	10	7	41.4
-75.068	-13.002	93.4	1.07	1.35	1.04	2011	10	23	12	22	54.2
-74.998	-13.446	100.7	2.02	1.88	2.66	2011	10	26	3	1	20
-71.595	-15.225	140.5	0.30	0.31	0.26	2011	11	1	3	27	14.2
-74.790	-13.735	103.3	1.58	1.88	1.69	2011	11	3	16	26	33.8
-69.700	-17.511	149.3	0.21	0.22	0.23	2011	11	4	2	46	56.6
-69.532	-16.977	171.8	0.25	0.23	0.24	2011	11	5	16	55	28.5
-71.877	-15.894	148.1	0.49	0.46	0.71	2011	11	6	15	21	21
-71.149	-16.582	110.3	0.15	0.18	0.33	2011	11	7	4	14	5.4
-71.149	-16.582	110.2	0.16	0.18	0.33	2011	11	7	4	14	5.4
-69.284	-17.516	155.2	0.25	0.27	0.27	2011	11	11	22	21	0.1
-72.424	-15.253	119.1	0.30	0.36	0.53	2011	11	14	2	38	22.3
-69.212	-16.497	215.0	0.53	0.51	0.40	2011	11	14	15	40	12.5
-69.596	-15.877	229.3	0.13	0.16	0.27	2011	11	15	7	24	14.6
-69.859	-17.901	129.0	0.30	0.35	0.30	2011	11	15	20	42	12.9
-69.484	-17.558	150.1	0.26	0.40	0.43	2011	11	16	1	57	45.5
-70.469	-18.114	56.2	0.26	0.32	0.23	2011	11	16	15	38	57.2
-75.113	-13.561	102.2	2.65	2.85	3.54	2011	11	16	19	8	58.7
-69.508	-16.871	171.0	0.21	0.22	0.27	2011	11	16	21	48	31.7
-69.405	-17.314	157.3	0.23	0.23	0.27	2011	11	18	1	25	40.4
-69.617	-16.882	171.6	0.24	0.20	0.29	2011	11	18	5	42	7
-71.228	-15.511	150.1	0.33	0.39	0.36	2011	11	20	5	27	14.4
-71.329	-16.033	132.2	0.38	0.45	0.49	2011	11	21	10	46	39.9
-69.715	-17.746	136.5	0.20	0.20	0.20	2011	11	22	22	3	51.9
-72.860	-14.135	85.3	0.16	0.18	0.26	2011	11	22	23	2	11.1
-72.860	-14.135	85.3	0.16	0.18	0.27	2011	11	22	23	2	11.1
-69.295	-17.621	149.2	0.20	0.25	0.25	2011	11	27	8	35	14.7
-71.903	-17.157	56.7	0.79	0.88	1.20	2011	11	28	0	14	23.4
-69.545	-16.771	185.4	0.26	0.25	0.21	2011	11	28	16	9	42.5
-69.486	-17.509	142.0	0.18	0.16	0.19	2011	11	29	8	49	30.1
-73.560	-14.440	89.4	0.24	0.22	0.32	2011	11	30	3	23	1.8
-70.777	-15.624	171.7	0.24	0.25	0.38	2011	12	1	3	40	57.8
-70.016	-17.144	138.1	0.20	0.29	0.22	2011	12	5	1	44	1.8
-74.432	-10.728	107.4	1.76	1.53	2.06	2011	12	7	14	25	34.4
-69.492	-17.705	131.3	0.26	0.32	0.38	2011	12	8	20	5	47
-69.610	-17.837	119.2	0.32	0.33	0.35	2011	12	10	7	21	51.7
-69.322	-18.101	127.9	0.31	0.23	0.27	2011	12	11	8	48	28.1
-69.385	-17.619	138.9	0.30	0.30	0.38	2011	12	11	11	14	15.2

-69.570	-17.579	140.0	0.19	0.17	0.21	2011	12	11	21	0	38.5
-69.817	-16.455	182.2	0.40	0.42	0.59	2011	12	12	21	50	33.5
-75.664	-11.893	100.4	1.01	1.71	1.09	2011	12	13	5	42	16.3
-69.977	-17.378	111.9	0.36	0.56	0.50	2011	12	13	10	56	58.7
-74.846	-13.428	92.1	1.72	2.01	1.90	2011	12	13	23	16	27.5
-69.728	-17.290	141.3	0.25	0.35	0.44	2011	12	14	12	0	56.2
-69.494	-16.528	186.0	0.54	0.36	0.48	2011	12	14	15	54	0
-70.999	-16.875	102.3	0.34	0.38	0.49	2011	12	14	17	36	37.8
-69.543	-16.940	173.4	0.23	0.19	0.22	2011	12	14	18	59	30.2
-75.689	-13.760	63.7	1.94	2.75	1.56	2011	12	15	6	6	10.8
-69.828	-17.897	136.5	0.27	0.26	0.26	2011	12	16	4	53	50.3
-71.892	-16.391	100.5	0.51	0.47	0.53	2011	12	17	14	4	21.4
-69.449	-17.495	161.2	0.19	0.22	0.23	2011	12	18	18	40	27.6
-72.285	-15.085	111.6	0.30	0.30	0.48	2011	12	19	7	6	28.7
-69.452	-17.566	149.7	0.17	0.18	0.18	2011	12	19	19	58	38.9
-71.889	-16.496	93.8	0.50	0.47	0.63	2011	12	20	3	40	39.9
-69.810	-16.411	190.8	0.38	0.35	0.39	2011	12	20	22	42	48.6
-71.974	-15.367	129.2	0.47	0.43	0.43	2011	12	21	8	44	32.1
-69.330	-17.209	165.8	0.27	0.33	0.31	2011	12	23	9	13	21.8
-69.376	-17.586	135.9	0.25	0.28	0.38	2011	12	23	20	41	13.2
-69.387	-18.276	124.2	0.23	0.25	0.26	2011	12	24	8	37	8.4
-69.495	-17.407	158.5	0.21	0.31	0.40	2011	12	25	4	41	19.9
-70.915	-17.913	50.2	0.68	1.19	0.47	2011	12	25	9	11	26.5
-74.812	-13.422	87.2	1.32	1.34	2.05	2011	12	25	19	24	10.9
-70.919	-17.048	83.7	0.37	0.45	0.53	2011	12	25	19	36	31.7
-69.450	-16.689	175.2	0.67	0.64	0.59	2011	12	26	0	44	37.5
-70.526	-15.580	198.3	0.23	0.27	0.33	2011	12	29	3	32	43.2
-69.493	-17.699	133.2	0.20	0.21	0.20	2012	1	1	14	7	9.4
-72.979	-14.097	77.6	0.25	0.30	0.39	2012	1	1	17	54	51.1
-70.554	-16.921	114.3	0.53	0.94	0.90	2012	1	2	9	22	1.1
-69.313	-17.708	142.3	0.21	0.22	0.23	2012	1	4	8	57	31.3
-72.017	-17.000	57.9	0.71	1.40	1.28	2012	1	5	5	27	4.3
-72.162	-16.715	63.5	0.41	0.61	0.40	2012	1	10	12	10	22.7
-72.870	-14.919	99.1	0.20	0.29	0.33	2012	1	11	18	58	32.8
-72.873	-14.922	99.0	0.23	0.33	0.40	2012	1	11	18	58	33.6
-69.541	-17.715	132.2	0.19	0.20	0.19	2012	1	11	20	24	22.5
-72.216	-15.289	117.5	0.43	0.36	0.54	2012	1	12	0	43	19.9
-74.770	-13.332	80.5	2.61	2.22	2.37	2012	1	13	17	41	43.1
-72.187	-14.984	109.7	0.37	0.32	0.63	2012	1	18	0	15	48.9

-69.466	-18.178	131.9	0.26	0.28	0.32	2012	1	20	12	45	7.1
-70.136	-17.465	103.4	0.48	0.57	0.61	2012	1	21	20	11	48.3
-72.301	-15.412	131.0	0.35	0.41	0.42	2012	1	22	8	7	31.9
-69.051	-18.427	137.0	1.44	0.93	0.95	2012	1	23	17	22	29.1
-69.813	-17.200	132.9	0.20	0.21	0.18	2012	1	26	10	31	35.5
-69.309	-17.448	155.7	0.22	0.23	0.19	2012	1	27	7	9	8.9
-76.318	-13.156	67.0	1.87	1.70	18.21	2012	1	28	0	59	32.6
-72.836	-14.319	85.3	0.20	0.22	0.29	2012	1	28	7	32	21.7
-72.767	-14.770	98.8	0.21	0.30	0.38	2012	1	28	9	31	54.2
-74.586	-13.191	77.1	1.45	1.82	1.95	2012	1	28	11	50	33.4
-69.765	-16.507	181.2	0.26	0.20	0.20	2012	1	29	6	8	23.1
-75.587	-14.272	55.6	1.72	1.67	1.77	2012	1	30	2	26	23.5
-75.693	-14.249	51.9	1.92	1.96	1.92	2012	1	30	14	20	41.2
-75.059	-13.843	83.7	1.16	1.81	2.03	2012	2	2	1	48	17.7
-70.824	-15.236	183.8	0.39	0.45	0.36	2012	2	2	10	1	48.5
-74.971	-15.135	57.9	2.44	2.32	2.01	2012	2	4	4	40	53.2
-70.725	-15.550	179.6	0.29	0.48	0.36	2012	2	5	20	58	45.5
-71.983	-15.035	124.8	0.31	0.31	0.45	2012	2	6	16	45	15.2
-69.549	-15.964	224.6	0.19	0.19	0.26	2012	2	6	19	17	57.4
-71.646	-15.160	138.0	0.28	0.28	0.32	2012	2	6	20	47	15.8
-74.930	-15.065	59.8	2.45	2.37	1.98	2012	2	11	0	40	3.1
-71.591	-15.099	133.8	0.28	0.30	0.35	2012	2	11	21	30	41.4
-71.777	-16.729	76.0	0.66	0.71	1.06	2012	2	12	4	19	47.1
-70.001	-17.629	101.3	0.31	0.34	0.33	2012	2	12	5	23	25
-72.535	-15.085	118.6	0.48	0.41	0.60	2012	2	12	15	52	12.2
-69.458	-17.219	157.9	0.19	0.23	0.19	2012	2	13	13	50	39.8
-69.560	-17.708	147.9	0.19	0.20	0.25	2012	2	13	14	32	18.9
-69.619	-18.125	113.5	0.25	0.29	0.25	2012	2	14	2	15	38.1
-69.428	-18.214	122.3	0.24	0.31	0.31	2012	2	14	14	8	39.7
-69.725	-18.236	107.2	0.35	0.39	0.48	2012	2	14	19	58	19.2
-69.580	-17.556	134.9	0.19	0.19	0.23	2012	2	15	3	58	3.3
-69.723	-16.648	176.0	0.23	0.24	0.25	2012	2	16	2	34	42.8
-71.691	-15.914	138.4	0.36	0.49	0.54	2012	2	16	4	23	26.5
-70.850	-17.049	101.7	0.38	0.46	0.47	2012	2	16	8	6	50.2
-74.874	-13.378	108.8	1.81	2.12	3.48	2012	2	17	7	11	45.9
-72.316	-15.938	112.2	0.50	0.75	0.66	2012	2	19	7	32	2.3
-70.522	-18.121	57.5	0.23	0.26	0.22	2012	2	20	1	35	58.9
-69.348	-18.368	131.4	0.30	0.30	0.30	2012	2	20	10	44	39.9
-72.801	-14.329	85.0	0.31	0.29	0.47	2012	2	22	19	6	40.8

-70.022	-17.481	127.8	0.35	0.44	0.40	2012	2	25	5	15	11.5
-69.425	-15.920	236.2	0.15	0.20	0.22	2012	2	27	2	37	27.9
-71.713	-15.673	143.0	0.34	0.49	0.33	2012	2	27	10	12	11.2
-72.977	-14.075	79.0	0.25	0.29	0.30	2012	2	27	18	30	7.9
-69.635	-17.588	131.2	0.19	0.29	0.46	2012	3	5	20	20	11.3
-72.031	-16.168	122.6	0.25	0.38	0.52	2012	3	6	9	40	22.1
-73.660	-14.316	88.2	0.24	0.27	0.31	2012	3	8	19	39	55.8
-75.137	-13.109	89.3	1.40	1.21	2.09	2012	3	8	20	3	23.8
-70.165	-17.838	96.2	0.43	0.55	0.32	2012	3	9	1	43	16.1
-75.137	-13.109	89.3	1.40	1.21	2.09	2012	3	9	8	54	28.5
-72.883	-14.395	81.8	0.21	0.19	0.25	2012	3	10	5	20	31.4
-75.618	-14.274	52.3	1.80	1.49	1.89	2012	3	12	7	17	11.7
-71.883	-16.397	99.4	0.46	0.49	0.58	2012	3	15	13	26	37.6
-69.494	-17.351	148.2	0.24	0.29	0.26	2012	3	16	1	53	51.1
-75.713	-11.196	111.7	2.29	3.22	2.62	2012	3	17	18	31	3.4
-76.410	-12.997	79.5	2.07	1.65	5.00	2012	3	20	2	36	23.6
-69.596	-16.620	189.0	0.28	0.32	0.21	2012	3	20	15	59	58.5
-71.158	-16.583	104.9	0.22	0.21	0.34	2012	3	21	8	43	14.6
-72.360	-15.281	114.5	0.39	0.44	0.55	2012	3	22	3	13	14.8
-74.010	-14.244	83.2	0.26	0.48	0.56	2012	3	23	10	31	12.7
-69.453	-17.806	148.7	0.24	0.25	0.24	2012	3	24	11	46	23
-70.736	-15.578	177.2	0.20	0.25	0.30	2012	3	24	14	39	25.4
-69.755	-17.262	148.3	0.25	0.29	0.27	2012	3	24	16	1	56
-69.744	-16.630	169.9	0.25	0.25	0.45	2012	3	26	8	23	0.9
-69.378	-16.933	181.5	0.31	0.22	0.27	2012	3	26	15	22	55.6
-69.516	-16.696	181.4	0.30	0.37	0.24	2012	3	28	22	38	9.7
-69.576	-16.752	172.6	0.21	0.28	0.35	2012	3	29	23	31	7.2
-70.188	-15.546	212.7	0.25	0.20	0.38	2012	3	30	3	2	27
-71.234	-15.557	152.2	0.33	0.39	0.37	2012	3	30	4	9	57.7
-69.445	-17.295	151.3	0.19	0.23	0.28	2012	3	30	10	48	44.3
-71.906	-15.008	124.4	0.31	0.31	0.33	2012	4	1	2	30	42.8
-69.134	-17.702	147.5	0.27	0.34	0.32	2012	4	1	22	4	35.8
-69.618	-16.194	212.8	0.54	0.44	0.46	2012	4	4	3	15	14.2
-69.677	-17.489	131.4	0.22	0.27	0.31	2012	4	5	22	16	19.6
-69.353	-17.776	136.8	0.24	0.28	0.27	2012	4	8	23	4	57.2
-70.333	-17.493	91.4	0.47	0.70	0.65	2012	4	9	0	40	39.1
-76.006	-13.915	58.1	2.18	3.00	1.88	2012	4	12	1	1	11.3
-72.102	-14.636	99.5	0.65	0.49	0.60	2012	4	14	20	30	59.3
-71.957	-16.139	111.7	0.24	0.36	0.52	2012	4	16	13	24	55.7

-73.743	-15.113	90.0	0.44	0.44	0.58	2012	4	17	3	44	58.7
-71.887	-14.855	119.4	0.35	0.37	0.44	2012	4	17	9	43	12.9
-75.647	-13.656	72.0	1.94	3.36	2.88	2012	4	18	18	37	52.2
-71.942	-14.901	121.1	0.33	0.32	0.48	2012	4	19	23	2	43.2
-72.128	-15.753	123.1	0.52	0.42	0.44	2012	4	20	2	43	25.2
-71.803	-14.869	120.3	0.38	0.37	0.55	2012	4	21	11	36	3.8
-72.026	-14.963	114.3	0.28	0.34	0.37	2012	4	23	17	2	44.8
-75.781	-13.939	61.1	2.70	2.49	2.05	2012	4	24	0	43	49.3
-71.593	-16.151	129.9	0.31	0.45	0.45	2012	4	24	2	14	16.6
-75.819	-13.785	63.2	2.67	1.68	2.43	2012	4	24	6	20	35.1
-71.674	-16.350	103.6	0.50	0.52	0.67	2012	4	25	16	19	38.4
-74.897	-14.381	60.7	2.15	1.68	1.85	2012	4	25	22	37	15.5
-70.568	-17.890	56.3	0.53	0.74	0.47	2012	4	30	8	4	21.2
-69.281	-18.196	131.8	0.34	0.36	0.32	2012	4	30	12	32	18.8
-72.354	-14.517	93.3	0.32	0.42	0.61	2012	5	2	10	52	59.8
-75.171	-14.851	55.9	1.95	2.15	1.10	2012	5	2	11	34	43.9
-73.776	-14.193	76.8	0.21	0.41	0.37	2012	5	2	16	54	26.4
-71.223	-17.656	48.2	0.59	0.65	0.82	2012	5	2	21	57	11.3
-69.917	-17.020	132.5	0.23	0.26	0.22	2012	5	3	11	31	52
-72.512	-14.923	105.5	0.39	0.46	0.47	2012	5	4	11	26	12.9
-69.726	-17.734	136.9	0.20	0.19	0.17	2012	5	12	11	28	53.3
-73.646	-14.429	83.1	0.24	0.23	0.32	2012	5	12	16	57	38.9
-69.491	-17.656	135.9	0.20	0.24	0.25	2012	5	13	7	47	34.4
-69.999	-17.863	101.7	0.26	0.21	0.26	2012	5	14	10	0	39.1
-72.448	-16.010	98.3	0.59	0.83	0.76	2012	5	15	2	38	27.4
-71.557	-16.417	104.3	0.55	0.57	0.73	2012	5	15	7	14	31.8
-69.994	-17.846	101.0	0.25	0.24	0.27	2012	5	15	21	20	33.6
-69.436	-17.490	155.1	0.18	0.21	0.20	2012	5	17	8	5	37.5
-76.534	-13.076	51.5	2.46	1.62	1.99	2012	5	18	9	22	31.6
-69.512	-16.645	185.3	0.28	0.31	0.28	2012	5	21	3	37	1.6
-72.771	-14.816	95.3	0.21	0.29	0.37	2012	5	22	6	50	1.5
-70.866	-16.812	112.2	0.38	0.37	0.49	2012	5	23	1	4	33.8
-71.895	-14.982	128.5	0.28	0.30	0.29	2012	5	25	13	27	7.9
-70.065	-18.119	92.2	0.49	0.52	0.58	2012	5	31	11	29	54.7
-69.456	-18.417	117.9	0.40	0.34	0.35	2012	6	1	3	45	54.8
-69.590	-17.408	147.6	0.34	0.46	0.60	2012	6	2	0	22	17.3
-71.725	-14.836	117.6	0.83	1.18	1.09	2012	6	2	9	20	47.3
-72.149	-15.907	119.0	0.57	0.74	0.71	2012	6	3	0	40	14.4
-75.146	-14.854	56.4	1.98	2.14	1.10	2012	6	4	17	11	19.9

-71.310	-15.526	151.4	0.32	0.40	0.35	2012	6	5	15	20	18.9
-72.663	-15.935	126.7	0.57	0.34	0.92	2012	6	7	16	3	14.7
-70.274	-18.023	73.3	0.87	1.03	0.82	2012	6	9	16	11	13.1
-67.375	-18.449	254.7	5.06	2.60	2.37	2012	6	11	4	41	35.4
-75.437	-13.847	79.8	3.60	4.79	3.45	2012	6	11	9	55	23.7
-72.823	-14.245	86.1	0.21	0.29	0.33	2012	6	12	7	23	37.2
-72.059	-15.571	133.3	0.44	0.33	0.37	2012	6	13	3	21	22.1
-74.668	-14.296	83.6	1.88	2.24	3.12	2012	6	14	5	41	41.2
-69.475	-16.646	194.7	0.39	0.35	0.26	2012	6	14	5	43	1.9
-70.595	-15.582	190.9	0.24	0.34	0.39	2012	6	14	7	48	8.2
-69.739	-16.374	194.9	0.38	0.27	0.28	2012	6	15	3	33	3.4
-72.105	-15.149	117.3	0.31	0.33	0.41	2012	6	15	10	47	56.3
-75.584	-14.094	62.4	2.84	3.44	3.96	2012	6	15	22	13	47.2
-72.072	-14.935	120.7	0.33	0.37	0.33	2012	6	18	6	9	34.1
-72.014	-15.376	128.0	0.42	0.26	0.33	2012	6	20	13	30	19.4
-76.753	-11.677	92.1	3.95	3.46	4.97	2012	6	21	22	17	9.6
-71.083	-16.764	106.9	0.36	0.38	0.45	2012	6	23	9	35	11.6
-69.634	-17.673	138.8	0.21	0.24	0.28	2012	6	25	2	7	23.9
-76.280	-11.582	96.7	4.95	4.12	5.04	2012	6	27	8	4	20.8
-76.027	-12.997	73.8	5.31	4.42	6.78	2012	6	27	12	41	7.9
-72.641	-14.462	91.3	0.47	0.59	0.72	2012	6	28	2	12	5.3
-71.335	-16.926	74.4	0.23	0.28	0.24	2012	6	30	2	0	13.2
-72.293	-15.997	106.5	0.47	0.74	0.67	2012	7	1	4	38	6.6
-69.647	-16.862	164.9	0.26	0.27	0.24	2012	7	1	14	25	59.6
-75.642	-14.332	51.5	1.39	1.40	1.59	2012	7	3	5	31	16.9
-73.828	-11.285	53.1	0.51	1.15	1.74	2012	7	4	16	25	10.4
-69.583	-17.659	140.7	0.21	0.17	0.17	2012	7	4	18	19	12.1
-70.254	-17.535	96.0	0.51	0.50	0.54	2012	7	9	10	15	33.6
-75.451	-14.411	57.1	1.79	2.31	2.32	2012	7	9	19	21	57
-69.549	-16.906	175.1	0.22	0.25	0.23	2012	7	9	20	53	52.6
-69.549	-16.905	175.3	0.23	0.30	0.25	2012	7	9	20	53	52.4
-75.831	-12.314	94.4	1.56	1.48	1.62	2012	7	9	21	50	47.9
-72.537	-15.170	120.7	0.44	0.51	0.52	2012	7	10	18	42	20.6
-73.098	-14.114	86.8	0.25	0.41	0.33	2012	7	12	5	5	29.7
-69.783	-17.690	115.1	0.36	0.37	0.35	2012	7	13	0	57	55.7
-69.325	-18.310	128.1	0.29	0.47	0.42	2012	7	14	5	28	6.6
-69.997	-17.784	100.0	0.29	0.28	0.28	2012	7	19	3	26	57
-69.735	-16.640	177.0	0.23	0.26	0.39	2012	7	19	17	16	17.7
-75.608	-14.359	52.9	1.56	0.96	1.94	2012	7	22	17	9	46.5

-71.607	-15.255	138.2	0.34	0.36	0.29	2012	7	22	20	33	34.2
-69.965	-17.869	113.7	0.33	0.42	0.35	2012	7	25	22	28	49.2
-69.697	-18.022	132.5	0.35	0.37	0.35	2012	7	26	7	36	56.2
-75.794	-13.394	88.5	4.98	3.57	3.78	2012	7	27	18	41	0.3
-74.749	-11.386	97.8	0.88	0.63	1.29	2012	7	28	12	43	60
-69.532	-16.804	180.1	0.32	0.21	0.31	2012	7	31	19	58	31.2
-75.080	-13.103	93.6	1.53	1.45	1.12	2012	8	3	23	25	8.1
-74.787	-13.638	97.2	2.17	2.93	2.68	2012	8	8	1	59	15.9
-75.435	-12.624	93.2	1.42	1.01	1.05	2012	8	16	13	44	31.5
-75.666	-11.896	101.0	1.18	1.39	1.22	2012	8	31	11	19	46.8
-75.076	-13.116	97.2	1.77	1.62	1.14	2012	9	1	4	0	7.9
-75.019	-12.369	90.7	3.14	2.39	2.32	2012	9	1	5	32	19.9
-74.632	-11.442	91.4	1.21	1.06	1.06	2012	9	8	1	47	38.3
-75.421	-12.640	92.2	1.51	0.99	0.72	2012	9	8	12	2	57.9
-75.905	-11.373	105.1	1.81	2.75	2.45	2012	9	24	13	29	15.6
-75.320	-12.965	101.8	3.31	2.17	1.44	2012	9	26	6	10	51.5
-73.501	-11.187	64.0	0.69	1.29	0.57	2012	10	9	8	24	10.3
-73.577	-14.850	88.0	0.29	0.42	0.44	2012	10	15	7	45	8.1
-75.401	-12.503	91.6	1.03	1.24	1.58	2012	10	16	5	46	57.5
-75.902	-12.082	107.1	1.19	1.18	1.77	2012	11	4	1	52	11.5
-75.826	-13.250	54.8	3.56	5.15	3.17	2012	11	4	20	29	38.8
-75.310	-12.505	87.9	1.13	0.78	1.00	2012	11	7	17	56	17.6
-74.574	-13.266	78.3	1.40	2.26	1.02	2012	11	13	9	1	39.5
-76.270	-12.745	63.0	1.64	2.75	1.66	2012	11	14	6	20	11.8
-76.036	-11.144	110.3	2.36	2.94	2.63	2012	11	17	11	13	32.4
-75.097	-13.216	90.5	1.81	2.12	1.39	2012	11	26	0	35	31.1
-74.862	-13.213	79.3	2.21	3.84	2.48	2012	11	29	10	50	36.2
-72.482	-14.913	117.0	0.54	0.52	0.63	2012	12	10	16	9	41
-75.197	-12.559	101.0	1.27	1.54	1.31	2012	12	20	5	18	29.5
-75.902	-11.977	107.5	1.14	1.05	1.16	2012	12	21	5	38	30.7
-75.466	-12.801	86.5	2.64	1.21	1.71	2012	12	31	4	40	23.1
-75.113	-13.270	91.3	1.30	3.30	1.94	2013	2	17	17	55	10.1
-74.409	-13.310	71.4	2.11	2.83	2.23	2013	3	8	20	0	47.9
-74.094	-11.018	109.8	1.79	1.83	2.37	2013	3	27	20	59	27.5
-74.780	-11.523	93.5	1.44	1.47	1.58	2013	4	7	10	53	47
-75.980	-12.288	104.2	2.09	1.82	2.48	2013	4	10	7	11	14.7
-75.843	-13.708	72.3	2.12	1.97	3.52	2013	4	21	9	39	59
-75.688	-11.854	100.1	1.16	1.81	0.97	2013	4	28	15	28	13.9
-76.041	-12.636	87.5	3.70	3.75	4.93	2013	5	3	15	59	48.8

-72.657	-13.908	86.6	0.32	0.42	0.41	2013	5	21	23	2	42.4
-75.257	-12.891	88.5	3.05	1.77	2.56	2013	5	25	16	4	42.3
-75.191	-12.917	95.6	2.54	1.69	1.17	2013	6	7	3	22	23.3

REFERENCES

Aki, K. & Lee, W. H. K., 1976. Determination of three-dimensional velocity anomalies under a seismic array using first P arrival times from local earthquakes: 1. A homogeneous initial model, *J. Geophys. Res.,* **81**, 4381-4399.

Anderson, M., Alvarado, P., Zandt, G. & Beck, S., 2007. Geometry and brittle deformation of the subducting Nazca Plate, Central Chile and Argentina, *Geophys. J. Int.,* **171**, 419–434.

Araujo, M. & Suarez*,* G., 1994. Geometry and state of stress of the subducted Nazca Plate beneath central Chile and Argentina; evidence from teleseismic data*, Geophys. J. Int.*, **116***,* 283–303.

Arrial, P-A & Billen, M.I., 2013. Influence of geometry and eclogitization on oceanic plateau subduction, *Earth Planet. Sci. Lett.,* **363**, 34-43.

Barazangi, M., & Isacks B.L.*,* 1976. Spatial distribution of earthquakes and subduction of the Nazca plate beneath South America*, Geology,* **4***,* 686–692.

Barazangi, M ., & Isacks, B. L., 1979. Subduction of the Nazca plate beneath Peru: Evidence from spatial distribution of earthquakes Geophys. J. R. Astron. Soc., 57, 537-555, 1979.

Bevis, M. & Isacks, B.L., 1984. Hypocentral trend surface analysis: Probing the geometry of Benioff Zones, *J. Geophys. Res.,* **89**, 6153- 6170.

Billen, M. I.*,* & G. Hirth, 2005. Newtonian versus non-Newtonian upper mantle viscosity: Implications for subduction initiation*, Geophys. Res. Lett*.*,* **32***, L19304,* doi: 10.1029/2005GL023457.

Bishop, B., Beck, S. L., Zandt, G., Scire, A., Wagner, L. S., Long, M.D. & Tavera, H., 2014. Peruvian Trench to Andean Thrust Front: Evidence for Coupling of the Peruvian Flat Slab to the Over-riding South American Plate, *AGU Fall Meeting*, San Francisco, California.

Bissig, T., Ullrich, T. D., Tosdal, R. M., Friedman, R. & Ebert, S., 2008. The time-space distribution of Eocene to Miocene magmatism in the central Peruvian polymetallic province and its metallogenetic implications, *J. South Am. Earth Sci.*, **26**, 16-35.

Cahill T. & Isacks B.L.*,* 1992. Seismicity and shape of the subducted Nazca plate*, J. Geophys. Res.,* **97***,* 17,503–17,529.

Chapple, W.M., & Forsyth, D.W., 1979. Earthquakes and bending of plates at trenches, *J. Geophys Res*, **84**, 6729–6749.

Cross, T. A., & Pilger, Jr. R. H., 1982. Control of subduction geometry, location of magmatic arcs, and tectonics of arc and back-arc regions, *Geol. Soc. Am. Bull*., **93**, 545-562.

Dickinson, W. & Snyder, W.S., 1978. Plate tectonics of the Laramide orogeny, *Geol. Soc. Am. Mem*., **151**, 335–366.

Dorbath, C. & Granet, M., 1996. Local earthquake tomography of the Altiplano and Eastern Cordillera of northern Bolivia, *Tectonophysics,* **259**, 117–136.

Dougherty, S. L. & Clayton, R. W., 2014. Seismic structure in southern Peru: evidence for a smooth contortion between flat and normal subduction of the Nazca Plate, *Geophys. J. Int*. **200**, 534-555.

English, J., Johnston, S.T. & Wang, K., 2003. Thermal modelling of the Laramide orogeny: Testing the flat slab subduction hypothesis: *Earth Planet. Sci Lett*, **214**, 619–632, doi: 10.1016/S0012-821X(03)00399-6.

Espurt, N., Funiciello, F., Martinod, J., Guillaume, B., Regard, V., Faccenna, C., & Brusset, S., 2008. Flat subduction dynamics and deformation of the South American plate: Insights from analog modeling, *Tectonics*, **27**, TC3011, doi:10.1029/2007TC002175.

Gerya, T.V., Fossati, D., Cantieni, C. & Seward, D., 2009. Dynamic effects of aseismic ridge subduction: numerical modelling, *Eur. J. Mineral*, **21(3)**, 649–661.

Gorbatov, A., Kostoglodov, V. & Burov, E., 1996. Maximum seismic depth versus thermal parameter of subducted slab: application to deep earthquakes in Chile and Bolivia, *Geofís. Int.*, **35***,* 41–50.

Green, H. W. & Houston, H., 1995. The mechanics of deep earthquakes, Annu. Rev. *Earth Planet. Sci*., **23***,* 169–213.

Gutscher M.A., Spakman W., Bijwaard H. & Engdahl E.R., 2000. Geodynamics of flat subduction: seismicity and tomographic constraints from the Andean margin, *Tectonics,* **19***,* 814–833.

Grevemeyer, I., Kaul, N., Diaz-Naveas, J.L., Villinger, H.W., Ranero, C.R. & Reichert, C., 2005. Heat flow and bending-related faulting at subduction trenches: case studies of Nicaragua and CentralChile. *Earth Planet. Sci. Lett*., **236**, 238–248.

Hacker, B.R., Peacock, S., Abers, G.A. & Holloway, S.D., 2003. Subduction factory 2:Are intermediate-depth earthquakes in subducting slabs linked to metamorphic dehydration reactions?, *J. Geophys. Res.,* **108** (B1), 2030, doi: 10.1029/2001JB001129.

Hamza, V.M. & Muñoz, M., 1996. Heat flow map of South America, *Geothermics,* **25**, 599-646.

Hampel, A., 2002. The migration history of the Nazca Ridge along the Peruvian active margin: A re-evaluation, *Earth Planet. Sci. Lett.*, **203**, 665–679.

Hampel, A., Kukowski, N., Bialas, J., Huebscher, C. & Heinbockel, R., 2004. Ridge subduction at an erosive margin: The collision zone of the Nazca Ridge in southern Peru, *J. Geophys. Res.*, **109**(2), doi:10.1029/2003JB002593.

Hasegawa,A. & Sacks, I. S., 1981. Subduction of the Nazca Plate beneath Peru as determined from seismic observations, *J. Geophys. Res.,* **86**, 4971-4980.

Hayes, G. P., Wald, D. J. & Johnson, R. L., 2012. Slab1.0: A new three-dimensional model of global subduction interface geometry, *J. Geophys. Res.*, **117**, B01302, doi:10.1029/2011JB008524.

Havskov, J. & Ottemoller, L., 1999. SeisAn Earthquake Analysis Software, *Seis. Res. Lett*.,**70**, 532-534, doi:10.1785/gssrl.70.5.532.

Henry, S.G. & Pollack, H.N., 1988. Terrestrial heat flow above the Andean subduction zone in Bolivia and Peru: *J. Geophys Res*, **93**, 15,153–15,162.

Heuret, A., Funiciello, F., Faccenna, C. & Lallemand, S., 2007. Plate kinematics, slab shape and back-arc stress: a comparison between laboratory models and current subduction zones, *Earth Planet Sci Lett.,* **256**, 473–483.

Humphreys, E., Hessler, E., Dueker, K., Farmer, G.L., Erslev, E. & Atwater, T., 2003. How laramide-age hydration of North American Lithosphere by the Farallon Slab controlled subsequent activity in the Western United States, Int. Geol. Rev., **45**(7), 575–595.

Hussong, D.M., Reed, T.B. & Bartlett, W.A., 1988. SEA-MARC II sonar imagery and bathymetry of the Nazca plate and forearc, ODP Leg 112, in Suess, E., and von Huene, R., et al., Proceedings of the Ocean Drilling Program, Scientific results, 112: College Station, Texas, Ocean Drilling Program, 125–130.

Instituto Geológico Minero y Metalúrgico – INGEMMET, On-line Catalog, accessed at http://www.ingemmet.gob.pe, Peru (2014).

Isacks, B. L. & Barazangi, M., 1977. Geometry of Benioff zones: lateral segmentation and downwards bending of' the subducted lithosphere, *in Island Arcs, Deep Sea Trenches and Backarc Basins,* pp. 99-114, eds Talwani, M. & Pitman, W. C., American Geophysical Union, Washington.

James, D.E. & Sacks, S., 1999. Cenozoic formation of the Central Andes: a geophysical perspective. In: Skinner. Geology and Mineral Deposits of Central Andes. Society of Economic Geology, Special Publication 7, pp. 1-25.

James, D.E., & Snoke, J.A. 1990. Seismic evidence for continuity of the deep slab beneath central and eastern Peru, *J. Geophys. Res.*, **95**, 4989-5001.

Jischke, M., 1975. On the dynamics of descending lithospheric plates and slip zones, *J. geophys. Res*., **80**,4809-4813.

Jordan, T.E. & Allmendinger, R.W., 1986. The Sierras Pampeanas of Argentina: a modern analogue of Rocky Mountain foreland deformation, Am. J. Sci., **286**, 737–764.

Kirby, S.H., Okal, E.A. & Engdahl, E.R., 1995. The 9 June 94 Bolivian deep earthquake: an exceptional event in an extraordinary subduction zone. *Geophys. Res. Lett*. **22**, 2233–2236.

Kirby, S.H., Engdahl, E.R. & Denlinger, R., 1996. Intraslab earthquakes and arc volcanism: Dual physical expressions of crustal and uppermost mantle metamorphism in subducting slabs, in Bebout, G.E., et al., eds., Subduction: Top to bottom: American Geophysical Union Geophysical Monograph 96, p. 195–214.

Kley, J., Monaldi, C. & Salfity, J., 1999. Along-strike segmentation of the Andean foreland; causes and consequences. *Tectonophysics*, **301**, 75 -94.

Knezevic Antonijevic, S., Wagner, L. S., Kumar, A., Beck, S. l., Long, M. D., Zandt, G., Tavera, H. & Condori, C., 2015. The Role of Slab Buoyancy in the Formation of Flat Slabs, *Nature,* in review.

Lallemand, S., Heuret, A. & Boutelier, D., 2005. On the relationships between slab dip, back-arc stress, upper plate absolute motion, and crustal nature in subduction zones, *Geochem. Geophys. Geosyst*., 6, doi: 10.1029/2005GC000917.

Lienert, B. & Havskov J., 1995. A computer program for locating earthquakes both locally and globally, *Seismol. Res. Lett.*, **55**(5), 26–36.

Manea, V., Pérez-Gussinyé M. & Manea, M., 2012, Chilean flat slab subduction controlled by overriding plate thickness and trench rollback*,* *Geology,* **40***,* 35–38.

McGeary, S., Nur, A. & Ben-Avraham, Z., 1985. Spatial gaps in arc volcanism: The effect of collision or subduction of oceanic plateaus, *Tectonophysics*, **119**, 195–221.

Marot, M., Monfret, T., Pardo, M., Ranalli, G. & Nolet, G., 2012. An intermediate depth tensional earthquake (MW 5.7) and its aftershocks within the Nazca slab, central Chile: a reactivated outer rise fault? *Earth Planet. Sci. Lett*., **327,** 9–16.

Noble, D., McKee, E., Farrar, E. & Petersen, U., 1974. Episodic Cenozoic volcanism and tectonism in the Andes of Peru, *Earth Planet. Sci. Lett*., **21**, 213-220.

O'Driscoll, L. J., Humphreys, E. D., Saucier, F., 2009. Subduction adjacent to deep continental roots: Enhanced negative pressure in the mantle wedge, mountain building and continental motion, *Earth Planet. Sci. Lett*., **280**, 61–70, doi:10.1016/j.epsl.2009.01.020.

Ottemöller, L., Voss, P. & Havskov, J., 2011.SEISAN: the Earthquake Analysis Software for Windows, Solaris, LINUX, and MACOSX, version 9.0.1, University of Bergen, pp. 361.

Peacock, S.M., 2001. Are the lower planes of double seismic zones caused by serpentine dehydration in subducting oceanic mantle? *Geology,* **29**, 299–302.

Peacock, S. M. 2009. Thermal and metamorphic environment of subduction zone episodic tremor and slip*, J. Geophys. Res*.*,* **114***, B00A07,* doi: 10.1029/2008JB005978.

Phillips, K. & Clayton, R. W., 2014. Structure of the subduction transition region from seismic array data in southern Peru, *Geophys. J. Int*., **196**, 1889 – 1905, doi:10.1093/gji/ggt504.

Raleigh, C.B. & Paterson, M.S., 1965. Experimental deformation of serpentinite and its tectonic implications. *J. Geophys. Res.,* **70**, 3965–3985.

Ranero, C.R., Phipps Morgan, J., McIntosh, K. & Reichert, C., 2003. Bending-related faulting and mantle serpentinization at the Middle America trench. *Nature,* **425**, 367–373.

Ramos, V. A.*,* and Folguera, A., 2009. Andean flat-slab subduction through time*, in* Ancient Orogens and Modern Analogues*, edited by* J. B. Murphy*,* J. D. Keppie*, and* A. J. Hynes*, Geol. Soc. Spec. Publ.,* **327***,* 31–54*,* doi: 10.1144/SP327.3.

Rosenbaum, G., Giles, D., Saxon, M., Betts, P. G., Weinberg, R.F. & Duboz, C. 2005. Subduction of the Nazca Ridge and the Inca Plateau: insights into the formation of ore deposits in Peru, *Earth planet. Sci. Lett.,* **239**, 18–32.

Sacks, I., 1983. The subduction of young lithosphere, *J. Geophys. Res*., **88**, 3355–3366.

Schneider, J. F. & Sacks, I. S., 1987. Stress in the contorted Nazca plate beneath southern Peru from local earthquakes, *J. Geophys. Res.,* **92**, 13,887-13,902.

Scire, A., Zandt, G., Beck, S., Long, M., Wagner, L., Minaya, E. & Tavera, H., 2015. Imaging the transition from flat to normal subduction: Variations in the structure of the Nazca slab and upper mantle under southern Peru and northwestern Bolivia, *submitted to Geophys J. Int.*

Skinner, S. & Clayton, R. W., 2013. The lack of correlation between flat slabs and bathymetric impactors in South America, *Earth Planet. Sci.Lett*., **371**, 1–5.

Tassara, A., Götze, H. J., Schmidt, S. & Hackney, R., 2006. Three-dimensional density model of the Nazca plate and the Andean continental margin. *J. Geophys. Res.,***111** (B09404). doi:10.1029/2005JB003976.

van Keken, P.E., Hacker, B.R., Syracuse, E.M. & Abers, G.A., 2011. Subduction Factory 4: Depth-dependent flux of H2O from subducting slabs worldwide,. *J. Geophys. Res.,* **116**, BO41401. doi:10.1029/2010/JB007922.

van Hunen, J., van der Berg, A.P. & Vlaar, N.J., 2002. On the role of subducting oceanic plateaus in the development of shallow flat subduction, *Tectonophysics*, **352**, 317–333.

van Hunen, J., vandenBerg, A. P. & Vlaar, N. J., 2004. Various mechanisms to induce present-day shallow flat subduction and implications for the younger Earth: a numerical parameter study. *Phys. Earth Planet. Inter.,* **146**, 179–194.

Vlaar, N. J. & Wortel, M. J. R., 1976. Lithospheric aging, instability and subduction, *Tectonophys*., **32**, 331-351.

Waldhauser, F. & Ellsworth, W. L., 2000. A double-difference earthquake location algorithm: Method and application to the Northern Hayward Fault, California. *Bull. Seismol. Soc. Am.,* **90**, 1353–1368.

Wessel, P. & Smith, W. H. F., 1991. Free software helps map and display data, *Trans. Am. Geophys. Union*, , **72**, 441-445.

Woods, M. T. & Okal, E. A., 1994. The structure of the Nazca Ridge and Sala y Gomez seamount chain from the dispersion of Rayleigh waves*, Geophys. J. Int.,* **117***,* 205–222.

Wortel, M. & Vlaar, N., 1978. Age-dependent subduction of oceanic lithosphere beneath western South America, *Phys. Earth planet. Int*., **17**, 201-208.

Chapter 2: Stress distribution in the southern Peru subduction zone

ABSTRACT

The downgoing Nazca Plate beneath central and southern Peru and northern Bolivia exhibits strong along-strike variability in slab geometry, from flat slab subduction north of 15 °S, to uniform normal subduction south of 15 °S. This flat slab geometry has often been linked to the subduction of the Nazca Ridge. I use data collected from three recently deployed local broadband seismic networks to determine the state of stress of the subducting Nazca slab between 9° and 18°S. I obtained high quality focal mechanisms for ~173 slab events to better understand how the slab is deforming along strike. My T-axes immediately south of the Nazca Ridge are oriented parallel to the contorted slab geometry, down dip from the ridge. This observation is independent of convergence direction, slab morphology, or trench orientation. Down dip tension is consistent with a highly deformed, but not torn, subducting slab between the normally dipping plate and the flat slab along the Nazca Ridge. North of the Nazca Ridge, the T-axes are largely ridge-parallel in map view, but with a distinct downward dip that is not parallel to the slab. These steeply dipping T-axes differ from the expected stress pattern for a fully supported flat slab and indicate that the flat slab north of the ridge may not stable.

1. INTRODUCTION

The subducting oceanic Nazca Plate beneath South America exhibits strong along-strike variability in its geometry (Isacks & Molnar, 1971; Stauder, 1975; Barazangi & Isacks, 1976; Bevis & Isacks, 1984; Schneider & Sacks, 1987; Cahill and Isacks, 1992; Dougherty &

Clayton, 2014). One example of a pronounced change in subduction geometry can be found at ~15 °S. (Barazangi & Isacks, 1976; Isacks & Barazangi, 1977; Hasegawa & Sacks, 1981; Cahill & Isacks, 1992; James and Sacks, 1999; Hayes et al., 2012, Phillips & Clayton, 2014). North of 15 °S, the Nazca Plate descends at an approximately 30° dip angle near the trench, but then assumes a nearly horizontal orientation at ~100 km depth. This “flat slab” geometry extends for almost 700 km inboard beneath the South American lithosphere before resuming its normal descent. In contrast, just south of 15 °S, the Wadati-Benioff zone (WBZ) has a constant dip of ~30° to at least 270 km depth (Sacks, 1983; McGeary et al., 1985; Schneider & Sacks, 1987; Cahill & Isacks, 1992). This flat slab geometry has commonly been linked to the subduction of buoyant aseismic ridges, but the exact cause of flattening is still a matter of debate (See Chapter 1 for more detailed list of contributing factors that might be playing a role in the formation of the flat slab). In southern Peru, the subducting Nazca Ridge is located at the southern edge of the Peruvian flat slab, and has been proposed to be a likely contributor to the formation of the flat slab in this region (Sacks, 1983; Gutscher et al., 2000; van Hunen et al., 2002; Arrial & Billen, 2013). Recent tomography and seismicity studies show the flat slab extending further inboard than previously reported, and show the associated WBZ to be shallowest along the projected location of the subducted Nazca Ridge (Refer: Figure 1.13, Chapter 1) (Knezevic Antonijevic et al., 2015; Kumar et al., 2015).

Although historically there have been debates over whether the change in dip angle in southern Peru is accommodated by deformation in the slab or by a slab tear, recent studies have consistently favored a continuous contortion of the Nazca plate (Stauder, 1975; Barazangi & Isacks, 1976; Hasegawa & Sacks, 1981; Bevis & Isacks, 1984). Schneider & Sacks (1987) use composite focal mechanisms and observe a fan-shaped trend in T-axes pointing down dip in all directions between the flat slab and normally dipping slab in southern Peru, consistent with extensional deformation of a continuous plate. A recent analysis of teleseismic receiver function also indicates gentle bending as opposed to slab tearing in southern Peru (Phillips & Clayton, 2014). A detailed stress analysis based on high quality focal mechanisms, north and south of the Nazca Ridge, will help us better understand the nature of along-strike variation in the slab deformation.

Global studies of the WBZ worldwide suggest that intermediate depth earthquakes are associated with the crust and shallow upper mantle of the downgoing slab (Kirby 1995; Kirby et al. 1996; Abers, 1996; Hacker et al., 2003). Although the exact cause of intermediate depth seismicity is still being debated, temperature dependent metamorphic dehydration reactions likely play a significant role in the occurrence of these events (Green & Houston, 1995; Kirby et al., 1996; Peacock, 2001; Hacker et al., 2003; Omori et al., 2004; Kirby et al., 2006; Faccenda, 2014). With continued descent, the slab undergoes changes in pressure and temperature, which facilitates the basalt to eclogite transformation in the slab (Peacock, 1993; Kirby et al., 1996; Hacker et al., 2003). Kirby et al. (1996) use finite element models to demonstrate a significant change in the slab stress state (extensional stresses) due to this densification (basalt→eclogite) reaction. This, along with other tectonic forces (e.g. ridge push and slab pull), dominantly affects the slab stress state. The focal mechanisms and P and T-axes orientations of the WBZ earthquakes should allow us to infer the stress state of the subducting slab and may provide some information about the forces prevalent in the subduction zones (Isacks & Molnar, 1971; Stauder, 1975; Schneider & Sacks, 1987; Dougherty & Clayton, 2014).

Previous focal mechanism studies and stress analyses of the WBZ in southern Peru were mainly focused on the transition between normal and flat subduction (Isacks & Molnar, 1971; Stauder, 1975; Schneider & Sacks, 1987). However, north of 15° S in the Peruvian flat slab region, no stress analyses of the WBZ have been carried out using local data and the best available results are mainly obtained using teleseismic arrivals (Isacks & Molnar, 1971; Stauder 1975). I present 173 high quality focal mechanism solutions and stress analyses for four different sub-regions, spanning the flat slab in the north, to uniform normal subduction in the south. My observed stress patterns are consistent with a sagging older flat slab north of the ridge and dominant slab extension associated with change in the geometry of subduction immediately south of the ridge.

2. DATA AND METHOD

Focal mechanism

I use P-wave first motion polarity data of relocated earthquakes recorded at temporary broadband stations from three seismic arrays, CAUGHT, PULSE and PERUSE (Refer: Figure 1.1 and data section of Chapter 1 for complete description of the seismic networks). I determine the best fitting double-couple fault plane solution (Table 2.1) using FPFIT (Reasenberg & Oppenheimer, 1985), included in the software package SEISAN (Ottemöeller et al., 2011). The program determines the double-couple fault plane solution that best fits a given set of P wave first motion polarities for each individual earthquake. It estimates source model parameters (strike, dip and rake) through a two-step grid search by iteratively minimizing the weighted sum of first motion polarity errors. FPFIT does not consider non-double-couple solutions so my obtained focal mechanisms are always pure double-couples. I perform an initial grid search at coarse increments of 20° in strike, dip and rake and then use a finer grid of 1° increments to determine the best fitting solution. I determine 308 focal mechanism solutions after the second step grid search. Solutions with sparse polarity readings and those for which all readings are close to nodal planes are not included in further analyses. Of the 308 focal mechanism solutions, 173 solutions were selected with the following characteristics: at least 10 polarity readings, a maximum of 2 incorrect polarities and a maximum 10° error in strike and dip and 20° error in rake. Figure 2.1 shows an example of a well-determined focal mechanism solution, where I observed an excellent agreement between the first motion polarities and the nodal plane position. After determining the strike, dip and rake of the fault planes from FPFIT, I used RFOC to calculate the P and T-axes orientations (Figs 2.4 and 2.8; Table 2.2) of 173 intermediate depth earthquakes.

3. RESULTS

I determine 173 well-constrained focal mechanisms with average polarity readings of 12 per event. The results of my focal mechanism analyses indicate a predominance of normal faulting across my study area (Figure 2.2). Figure 2.3 shows the classification of focal mechanisms in normal, oblique normal, thrust and oblique thrust, based on the rake angle. The majority of my events (62%) have normal mechanisms with some strike-slip component. This suggests that slab bending and/or slab pull is the dominant mechanism of deformation across my study area. However, individual areas show variations depending on the local slab geometry.

In order to systematically investigate the stress state of the slab, I divide my study area into four regions from south to north depending upon the slab geometry (Figure 2.4). Box 1 includes all the events of cluster A, where the “normal” slab has a consistent dip angle. Box 2 covers the contorted region between flat subduction in the north and steep subduction in the south. Box 3 comprises those events located in the flat slab just south of the Nazca Ridge and Box 4 includes all of the events north of the projected ridge track.

For Box 1, first motion focal mechanism solutions are dominantly normal and indicating E-W and NE-SW extension (Figs 2.2 and 2.3). The rose diagram shows a dominant E-W to NE-SW trend in the T-axes orientations, nearly perpendicular to the strike of the trench (Figure 2.5a). There is a noticeable rotation of the T-axis orientations from contour perpendicular to contour parallel at depths of greater than 170km (Figure 2.4). A recent study of Dougherty & Clayton (2014) also suggests similar rotation in T-axis orientations, with increasing depth, for this region. The T-axes are dominantly oriented E-W at shallow depth (<170 km) (Figure 2.5b). At greater depth (>170km), the T-axes are directed along NNW-SSE and nearly parallel to the local slab contour (Figure 2.5c).

For events in Box 2 (Figure 2.4), the focal mechanisms are much more variable (Figs. 2.2 and 2.3). In map view, I see a well-distributed range of T-axis orientations (Figs 2.4 and 2.6a). The even distribution of directions corresponds to the abrupt local change in the downdip direction of the slab across the transition region (15°S-17°S) that extends from WNW to SSE. In addition, I see a rotation in T-axis orientations at depth, similar to what is seen in Box 1.

The flat slab region just south of the Nazca Ridge (area inside Box 3, Figure 2.4) is characterized by normal faulting, with focal planes mainly oriented in NE-SW direction, indicating NW-SE extension (Figs. 2.2 and 2.3). The T-axes are nearly horizontal and therefore parallel to the flat slab (cross-section SS′, Figure 2.7). I see a dominant trend of T-axis orientations to the ESE (Figs. 2.4 and 2.6b), which is downdip from the Nazca ridge and directed towards the contortion in the slab. This is similar to the observations of Anderson et al. (2007) for T-axis orientations in the central Chile flat slab adjacent to the subducted Juan Fernandez Ridge.

There is a significant difference in the T-axis orientations between those observed just south of the ridge (Box 3, Figure 2.4) and those observed just north of the ridge (Box 4, Figure 2.4). While the T-axes south of the ridge are dominantly oriented obliquely to the ridge, events north of the ridge have T-axes orientations oriented towards the northeast, perpendicular to the trench and nearly parallel to the ridge track (Figs 2.4 and 2.6c). The T-axes are also not horizontal but rather dip down to the northeast (cross-section NN′, Figure 2.7).

4. DISCUSSION

In normal subduction zones, T-axes associated with intermediate depth seismicity usually follow the downdip direction of the subducting slab (Stauder, 1975; Schneider & Sacks, 1987; Vassiliou & Hager, 1988; Cahill & Isacks, 1992). This has also been shown to be the case near the central Chilean flat slab, where all T-axis orientations point down-dip from the horizontally subducting Juan Fernandez ridge track (Anderson et al., 2007, Linkimer, 2011). The geometry of the central Chilean flat slab also closely follows the projected location of the subducted ridge (Linkimer, 2011). In Chile, unlike in Peru, the ridge has been parallel to the convergence direction for last 10 Ma, resulting in no significant southward migration along the trench during that time (Yanez et al., 2001). In Peru, the flat slab extends significantly north of the ridge due to the difference in convergence direction and the trend of the Nazca Ridge. I would therefore expect a difference in the slab stress state between Peru and Chile north of the ridge track, but not south of the ridge track. Indeed, I note that south of the ridge, the T-axis orientations are downdip, consistent with extension caused by the deformation of the Nazca plate between the normally dipping portion beneath Bolivia and the flat slab at the ridge (cross-section SS′, Figs 2.7 and 2.4). My observations agree with the regional stress pattern observed by Schneider & Sacks (1987) and Cahill & Isacks (1992) for the same area.

Recent results looking at seismicity distribution, source mechanisms, and teleseismic receiver functions indicate that the change in dip angle from flat to normal along the southern margin of the Peruvian flat slab is accommodated by deformation, not tearing, of the subducted plate (Phillips & Clayton, 2014; Dougherty & Clayton, 2014). As discussed in Chapter 1, the Peruvian flat slab evolved over the last 11.2 Ma as the Nazca Ridge migrated southward from 11°S to 15°S (Hampel, 2002). Knezevic Antonijevic et al. (2015) suggest that the combination of hydrodynamic slab suction and trench retreat can only support the flat slab for a limited amount of time once the ridge has migrated further south. If the older flat slab north of the ridge is stable then I should expect to see horizontal, trench perpendicular T-axes. If the flat slab to the north is entirely unstable, I would expect to see similar T-axis orientations as I see south of the ridge: parallel to the dip direction, oriented orthogonally to the ridge track. What I observe is a combination of the two. North of the ridge, the T-axes are largely ridge-parallel (Figure 2.4), consistent remnant support provided the flat slab by suction between the slab and the overriding continent. However, these T-axes differ from what would be expected from a fully supported flat slab in that their dip is not slab parallel (horizontal), as is the case everywhere else, but rather has a distinct downward dip component (cross-section NN′, Figure 2.7).

As discussed in Chapter 1, I observed subtle deepening of events north of the ridge. This combined with steeply dipping T-axes suggest that the older flat slab north of the ridge is perhaps not stable due to reduced support from the ridge buoyancy and may suffer a trench parallel tear (shaded pink area, Figure 2.4). Recently, Knezevic Antonijevic et al. (2015) also observe a dipping high velocity anomaly under a dipping low velocity anomaly, north of the ridge and interpreted it as a tear in the slab and reinitiation of normal subduction west of this tear. Some of the down-dipping T-axes, north of the ridge, are associated with events that are west of this tear and may be occurring in the newly steepened slab (Figure 2.4). My observation indicates that the T-axes west of the tear are pointing in the downdip direction of this newly steepened slab. East of the tear, the down-dipping T-axes are associated with the remnant flat slab (RFS). These steeply dipping T-axes in the RFS region indicate that the slab to the east of the tear is only being partially supported by suction and trench rollback and may be starting to sink. The downdip component of force due to the negative buoyancy of the ridge-free slab results in dipping the T-axes east of the tear. This implies that as the ridge buoyancy drops below a critical threshold due to southward migration of the ridge trench retreat and slab suction alone are not sufficient to maintain stability of the flat slab in the north.

Within the normally dipping slab south of the flat slab (Box 1, Figure 2.4), the state of stress varies with depth. The T-axes from events with hypocentral depths < 170 km are roughly trench normal and are aligned roughly parallel to the slab dip. This is consistent with slab pull as has previously been suggested in other studies (Stauder, 1975; Cahill & Isacks, 1992; Araujo & Suarez, 1994). At greater depths (>170 km), the T-axes for my events are roughly contour parallel. I observed corresponding change in the P-axes orientation from contour parallel at shallow depth (< 170 km) to contour perpendicular at greater depth (>170 km). Anderson et al. (2007) also found contour parallel T-axis orientations in central Chile at intermediate depths (120-140 km) and interpreted it as strain partitioning on pre-existing faults related to the outer-rise bending. Previous studies suggest that the slab dehydration reactions lead to an increase in pore pressure and facilitate slip along preexisting weak zones under the action of ambient stress field (Raleigh & Paterson, 1965; Jiao et al., 2000, Ranero et al., 2005). If the descending slab contains uniformly oriented faults and fractures, their reactivation at all depth should give similar fault plane orientation and possibly similar P and T axes, provided the ambient stress field is same (Warren et al., 2007). The global bathymetry model of Becker et al. (2009) clearly indicates a complex distribution of variably oriented fractures and faults on the sea floor, off the coast of southern Peru. It is possible that the variation in individual T and P axes orientation with depth is either related to the slip along subducted faults and fractures, that are equally variable in orientation or it may be the result of change in ambient stress field with depth.

5. CONCLUSIONS

My current study indicates that slab pull is the dominant contributor in the observed stress pattern across my study area in southern Peru and northern Bolivia. However, given the changes in slab geometry in this region, the orientation of my T-axes varies greatly. My conclusions from these orientations are as follows:

1) The steeply dipping T-axes north of the Nazca Ridge indicate that the older flat slab north of the ridge is not stable and is likely beginning to founder. The fact that the T-axis orientations are not orthogonal to the ridge as they are further south suggest that the slab is partially (though not sufficiently) supported by other forces such as trench rollback and suction.

2) The downdip orientation of T-axes in the transitional region between the flat and normally dipping segments is consistent with extension along a continuous but highly deformed slab. I find no evidence for slab tearing in this study.

3) The change in T-axis orientations in the normally dipping slab as a function of depth indicates a change from down dip extension to slab contour parallel extension. This change in T-axes orientation is either related to slip along variably oriented faults and fractures inherited by the slab or changes in the ambient stress field with depth.

6. ACKNOWLEDGMENTS

We are thankful to IRIS and personnel at the PASSCAL Instrument Center for their help and support throughout the CAUGHT and PULSE deployment. The seismic instruments were provided by the UNC-Chapel Hill, Yale University and Incorporated Research Institutions for Seismology (IRIS) through the PASSCAL Instrument Center. I sincerely thank Dr. Hernando Tavera, Director, Instituto Geofísico del Perú, Lima, Peru, and C. Condori Quispe for their help in deployment and demobilization efforts, as well as Mike (PASSCAL) for his invaluable assistance in the field. The CAUGHT experiment was supported by NSF grants EAR-0908777 (Lara Wagner) and EAR-0907880 (Susan Beck). The PULSE experiment was funded by NSF grants EAR-0944184 (Lara Wagner), EAR-0943991 (Susan Beck), and EAR-0943962 (Maureen Long). Special thanks to Kevin Stewart, C. Berk Biryol, S. Knezevic Antonijevic, and Linda M. Warren for helpful discussions. Maps were created using the Generic Mapping Tools (GMT) software [Wessel and Smith, 1998].

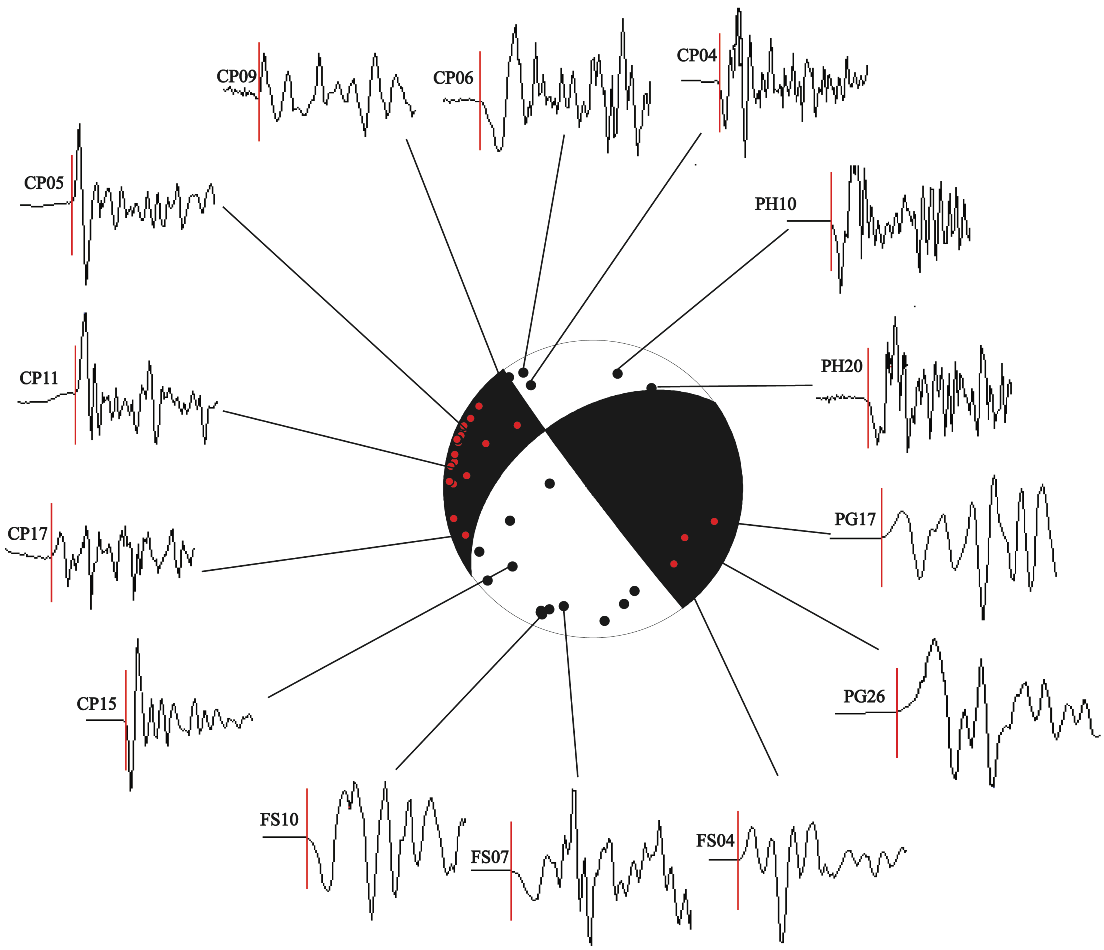

Figure 2.1- An example of a high-quality focal mechanism solution (lower hemisphere projection) determined from first motion polarity at 36 stations. Red dots indicate compression (up) arrival and black dots tensional (down) arrival. P-waveform used to determine this solution is shown with marked position of first arrival (red vertical line).

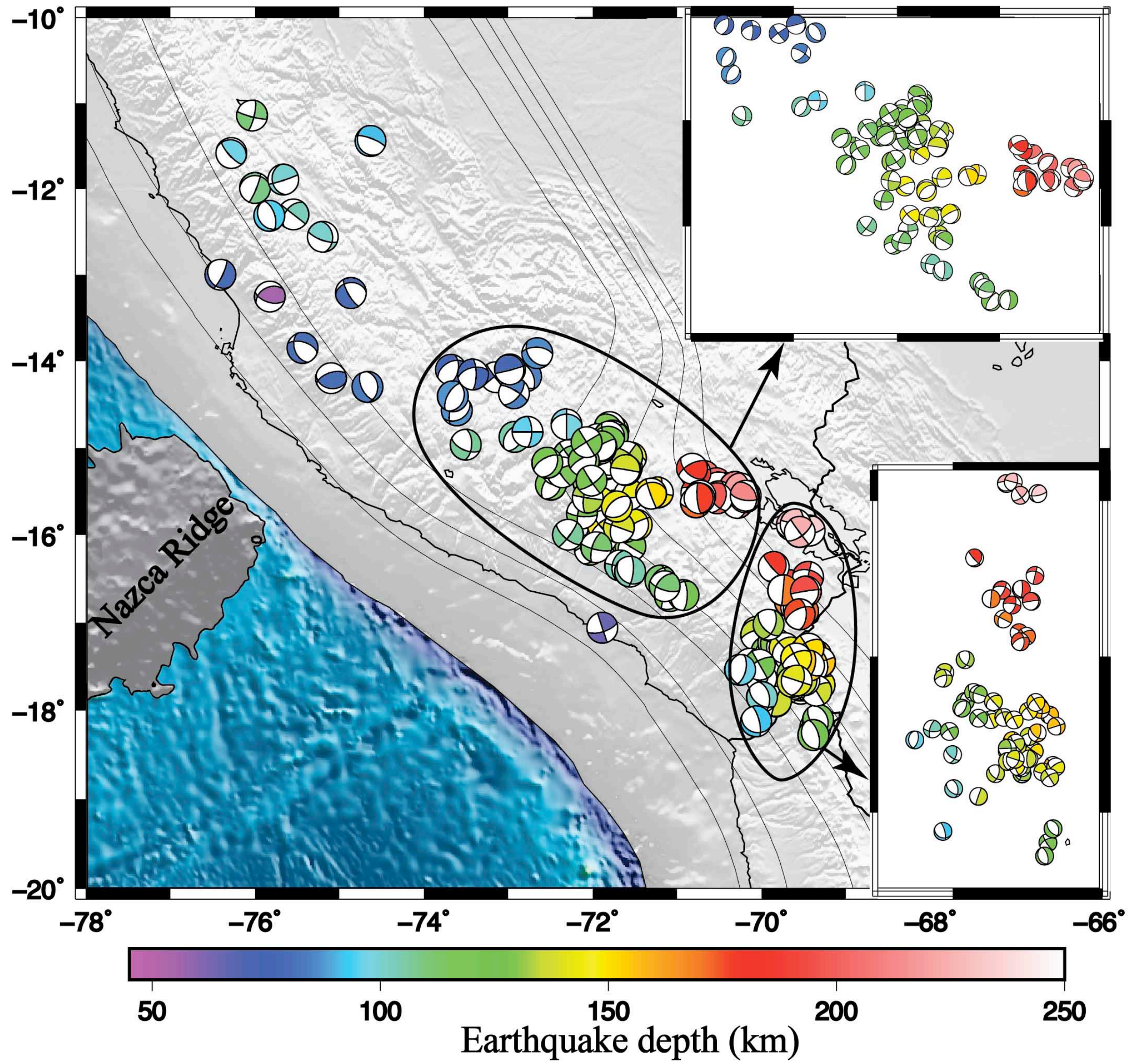

Figure 2.2- Map of first motion focal mechanisms plotted in a lower hemisphere projection. Mechanisms are color coded by earthquake depth and mainly show normal faulting across the study area.

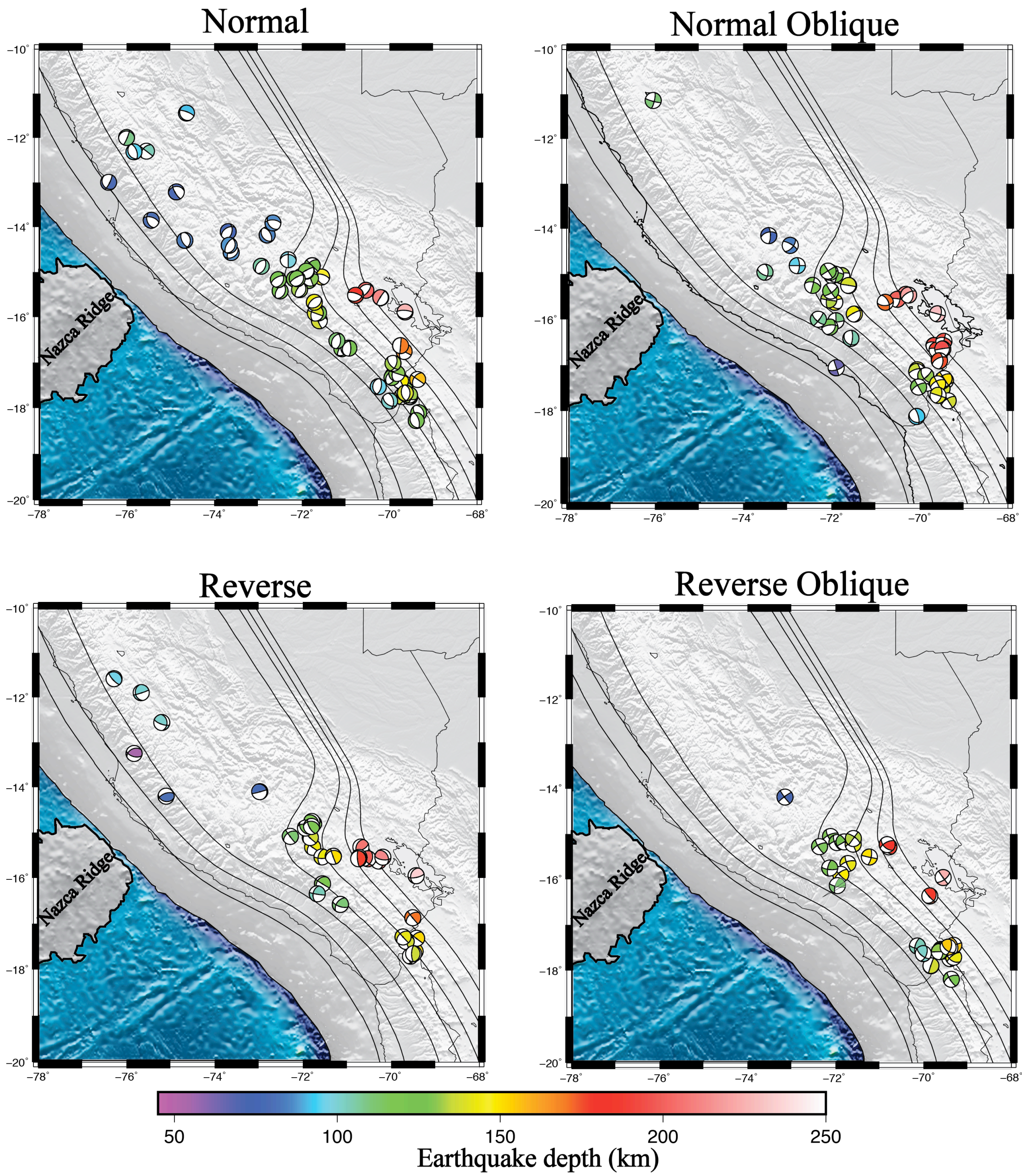

Figure 2.3- Focal mechanism solutions plotted as a function of rake angle. Mechanisms are color coded by earthquake depth. Solid lines are slab contours from Cahill & Isacks (1992).

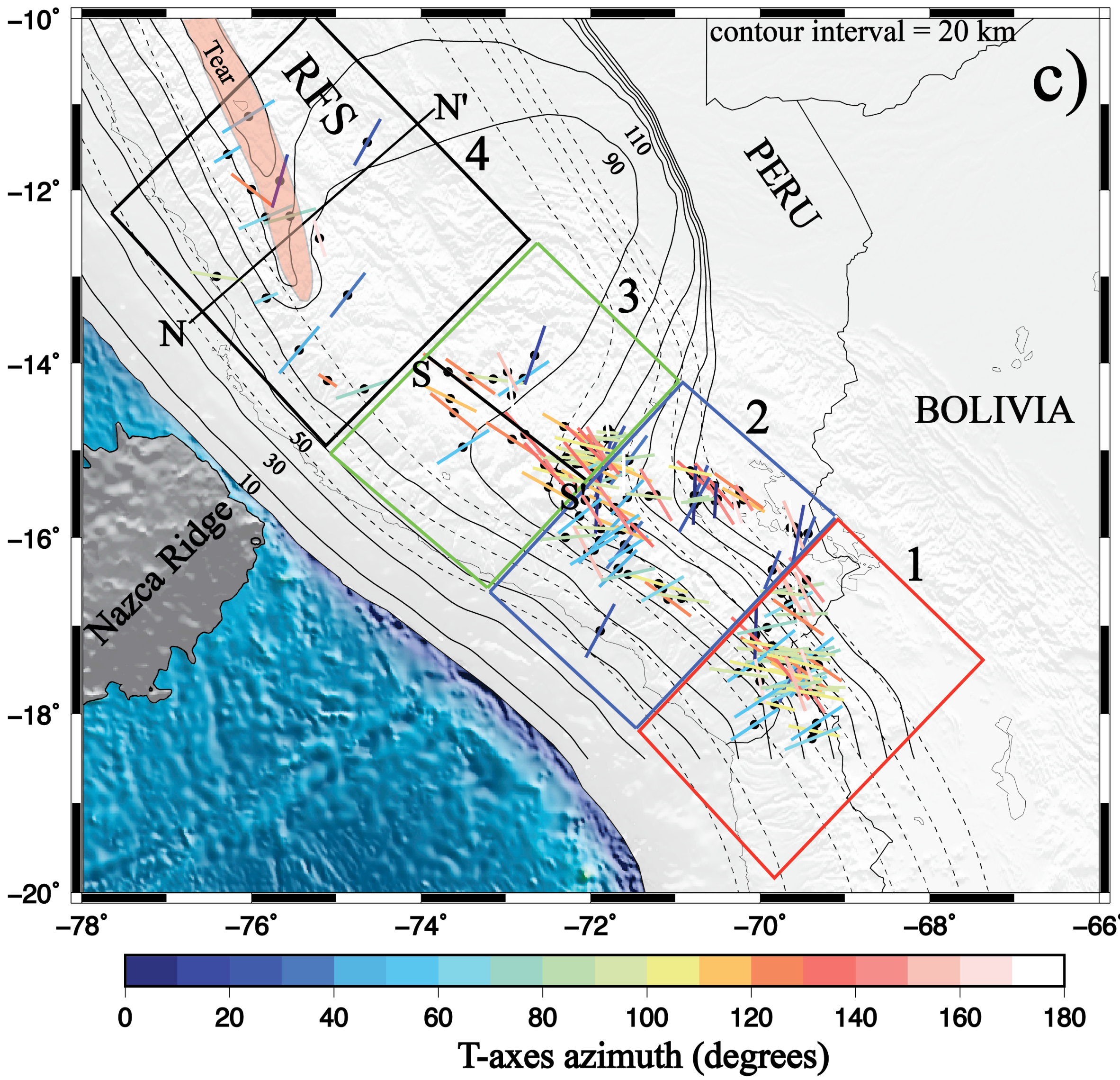

Figure 2.4- Map showing T-axes orientations determined from focal mechanism solutions. Length of the T-axes segment is proportional to the dip of T-axes, with smaller segments representing steeper T-axes. Black dots indicate the location of associated slab events. Colored boxes divide the study area into four different regions based on the geometry of subduction. Solid black lines are the slab contour based on my seismicity study and recent tomography results of Knezevic Antonijevic et al. (2015) and Scire et al. (2015), as outlined in Chapter 1. Dashed black lines are contours from Cahill & Isacks (1992). Shaded pink area, north of the projected track, marks the approximate position of trench parallel tear based on seismicity and Raleigh wave results of Knezevic Antonijevic et al. (2015).

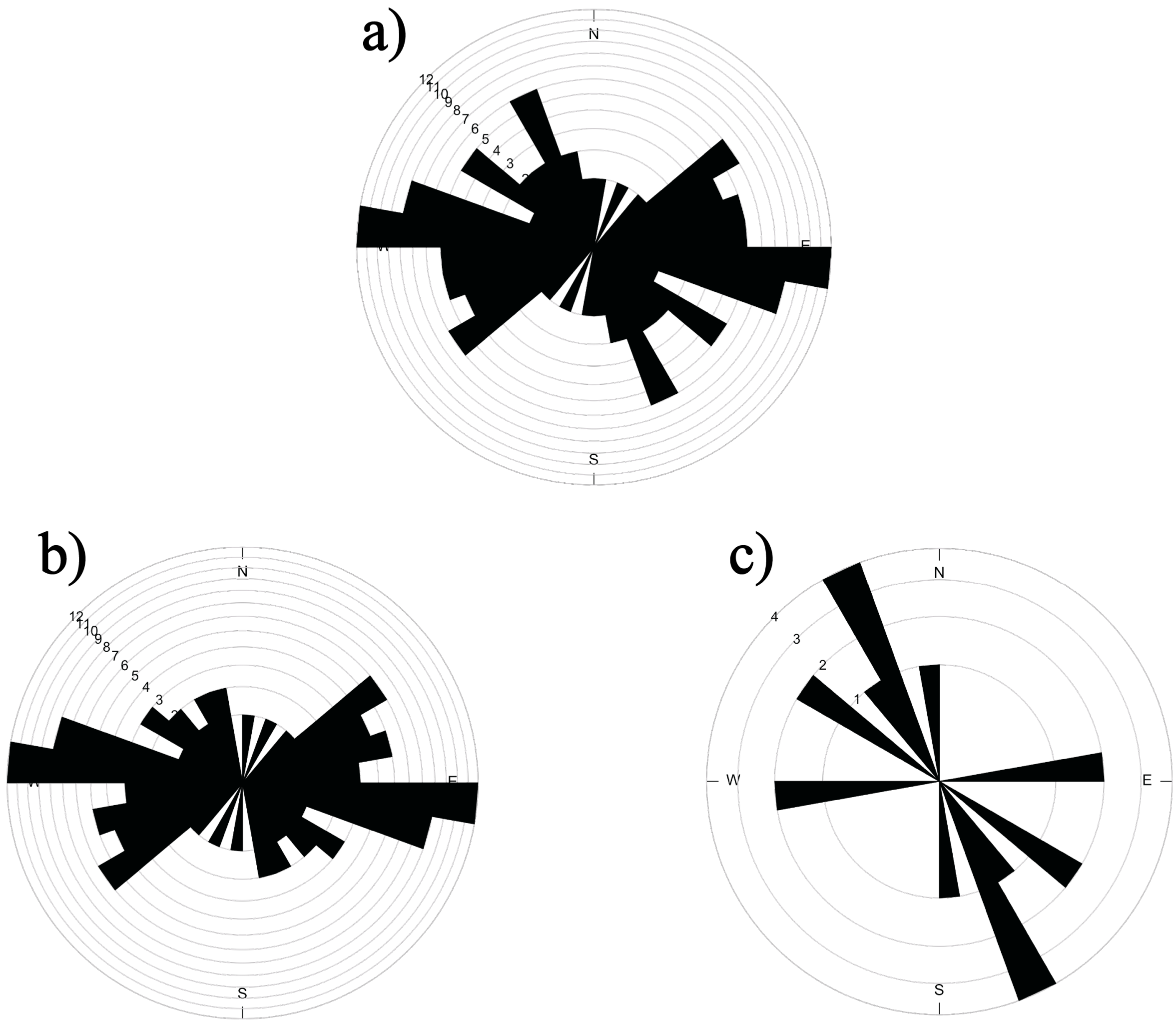

Figure 2.5- (a) Rose diagram for all events in box 1. (b) rose diagram for shallow events (<170 km depth) in box 1. (c) rose diagram for deep events (>170 km depth) in box 1.

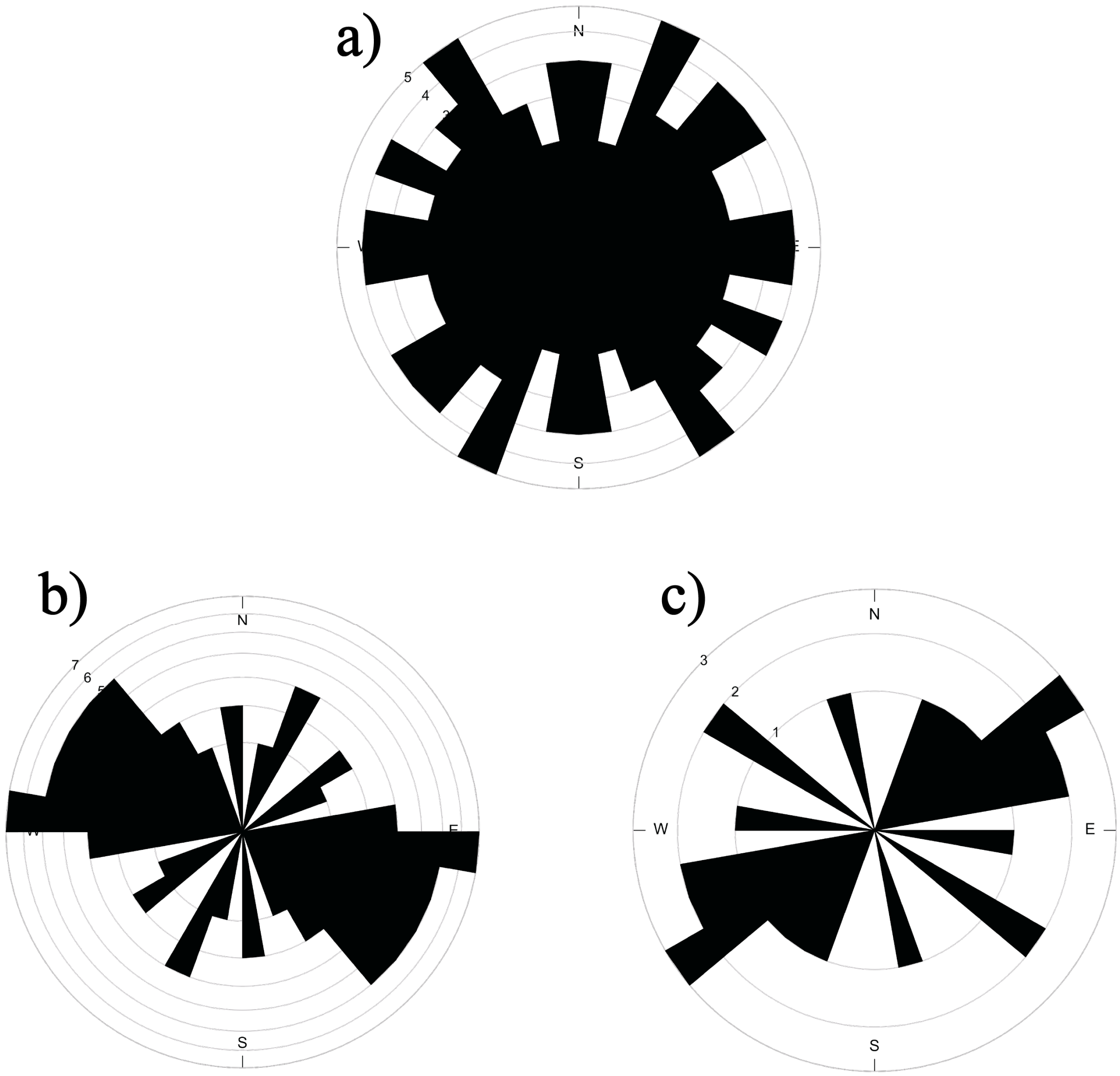

Figure 2.6- (a-c) Rose diagram for events in box 2-4.

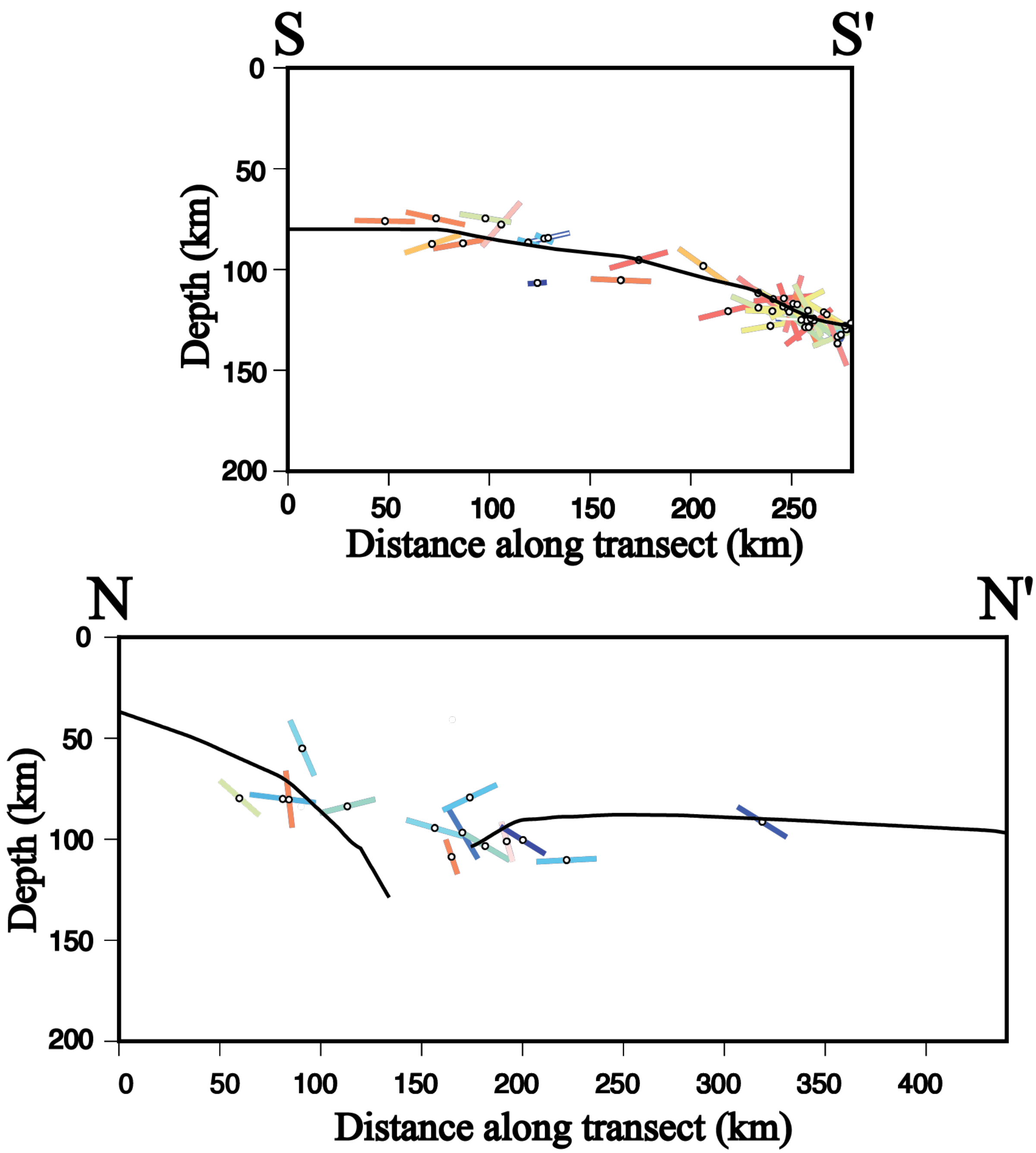

Figure 2.7- T-axis cross sections. Location of cross sections SS′ (south of the Nazca Ridge) and NN′ (north of the Nazca Ridge) are shown in Figure 2.4. Open circles are earthquakes and the projected T-axes are shown as colored sticks. Color of the T-axes varies as a function of azimuth and same as in Figure 2.4. The solid black line in each cross section is my new slab contour.

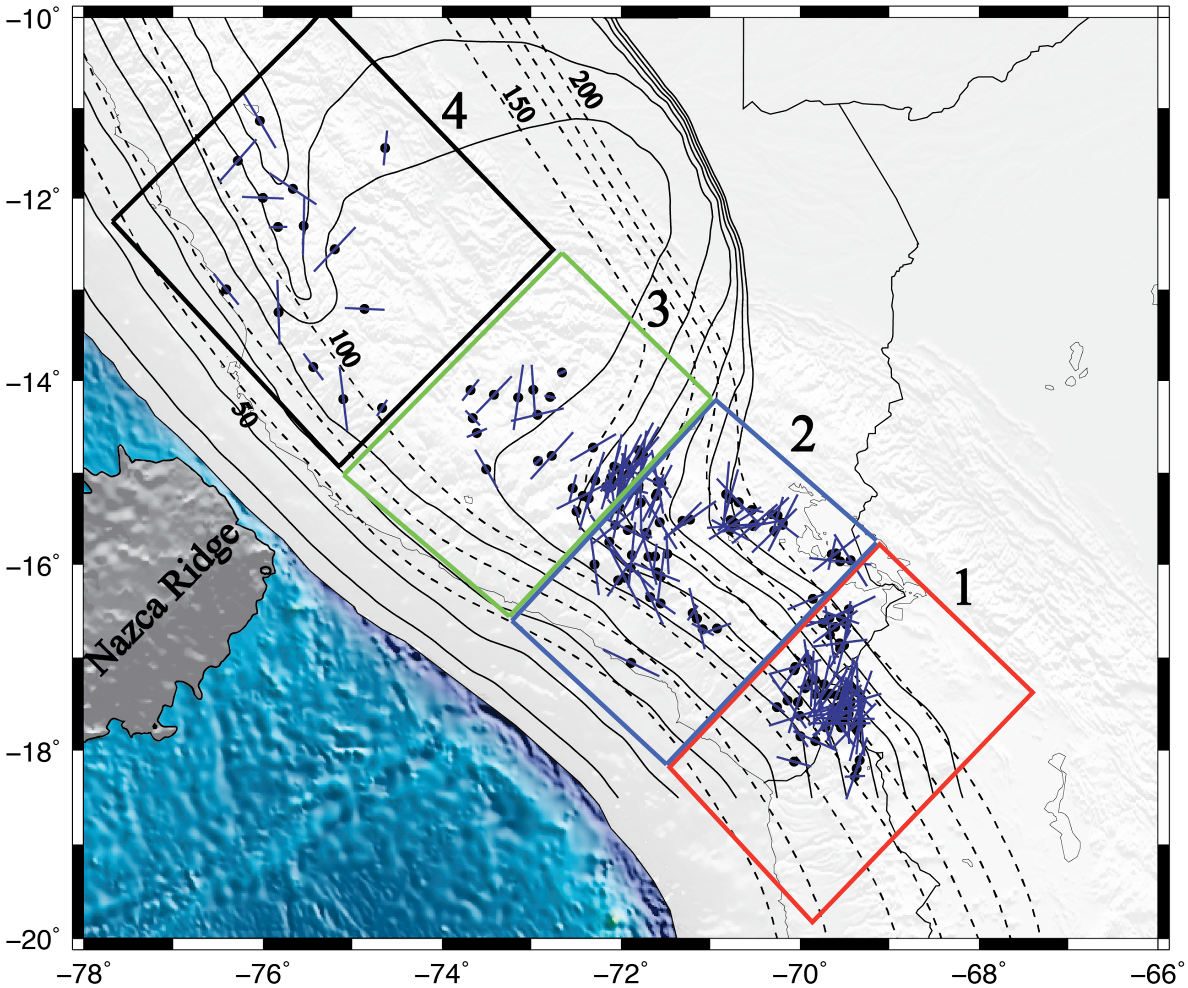

Figure 2.8- Map showing P-axes (blue segments) orientations determined from focal mechanism solutions. Length of the P-axes segment is proportional to the dip of P-axes, with smaller segments representing steeper P-axes. Black dots indicate the location of associated slab events. Solid lines are slab contours based on my seismicity study and recent results of Rayleigh wave (Knezevic Antonijevic et al., 2015) and teleseismic body wave tomography (Scire et al., 2014). Dashed black lines are slab contours from Cahill & Isacks (1992).

Table 2.1. Best fitting double couple fault plane solutions for 173 intermediate depth events

Longitude	Latitude	Depth	Strike	Err Strike	Dip	Err Dip	Rake	Err Rake
-69.636	-17.607	128.9	143	9	20	0	-111	10
-69.917	-17.289	125.2	11	5	49	3	-82	3
-69.353	-17.375	156.7	-55	8	90	1	-138	1
-69.456	-17.608	151.3	125	6	88	1	138	1
-69.365	-18.191	128.2	147	3	78	5	147	7
-69.630	-17.600	146.5	63	9	31	1	-169	10
-70.053	-17.103	137.4	42	3	48	4	-172	18
-69.542	-16.568	186.7	129	1	17	4	-142	2
-69.330	-17.698	159.7	138	8	88	6	154	3
-69.423	-17.323	152.1	128	9	88	1	137	2
-69.399	-17.740	142.3	100	5	77	6	38	15
-70.063	-17.140	135.3	2	5	58	5	-151	8
-69.715	-17.750	135.0	17	2	60	7	-42	3
-69.746	-17.405	148.3	-25	5	90	0	-127	7
-69.412	-17.340	155.6	99	7	52	5	-163	10
-69.828	-17.396	126.8	-45	10	90	2	-155	9
-69.663	-16.760	166.9	-63	4	90	5	-138	2
-69.940	-17.332	128.4	30	5	58	4	-97	9
-69.672	-16.573	191.6	27	9	72	5	-142	3
-69.671	-16.575	190.9	27	9	72	5	-142	3
-69.602	-17.540	151.8	104	5	88	4	18	1
-69.861	-17.230	131.3	147	3	58	10	-163	7
-69.855	-16.367	186.1	28	7	25	8	158	3
-69.330	-18.102	128.0	139	6	53	4	-102	4
-69.829	-17.242	129.8	-72	10	90	0	-132	5
-69.433	-15.951	235.4	78	7	72	3	118	2
-69.432	-15.951	235.3	78	7	72	3	118	2
-69.556	-16.848	173.8	44	3	64	4	-163	4
-69.604	-16.670	186.2	18	8	60	2	-162	10
-69.491	-17.513	137.0	0	0	66	4	-148	5
-69.537	-17.752	132.7	26	2	84	5	-62	3
-69.538	-17.751	132.7	26	2	84	5	-62	3
-69.537	-17.752	132.7	26	2	84	5	-62	3
-69.538	-17.751	132.7	26	2	84	5	-62	3
-69.659	-17.391	136.7	160	1	89	1	131	15
-69.450	-16.480	194.3	13	6	90	0	-142	3
-69.642	-15.887	226.4	73	4	18	4	-110	8

-69.596	-15.877	229.3	-75	4	90	2	-38	12
-69.508	-16.871	171.0	141	6	87	4	138	1
-69.570	-17.579	140.0	70	4	90	2	28	7
-69.728	-17.290	141.3	138	10	88	5	135	3
-69.828	-17.897	136.5	80	5	5	7	151	5
-69.387	-18.276	124.2	150	5	28	3	-102	6
-69.313	-17.708	142.3	124	3	49	1	151	5
-69.541	-17.715	132.2	9	10	65	8	-42	10
-70.136	-17.465	103.4	95	3	66	5	155	7
-69.309	-17.448	155.7	72	5	90	1	38	3
-69.549	-15.964	224.6	53	5	66	4	178	10
-70.001	-17.629	101.3	129	6	64	4	38	10
-69.560	-17.708	147.9	20	9	34	5	118	8
-69.580	-17.556	134.9	146	8	78	10	153	4
-70.022	-17.481	127.8	-30	1	90	1	-158	2
-69.635	-17.588	131.2	88	6	90	2	36	8
-69.494	-17.351	148.2	-33	2	90	0	-147	7
-69.744	-16.630	169.9	5	5	90	3	-90	5
-69.445	-17.295	151.3	-33	10	90	0	-146	7
-69.353	-17.776	136.8	-32	2	90	0	-158	1
-69.917	-17.020	132.5	20	5	54	8	-42	14
-69.491	-17.656	135.9	0	5	20	6	89	9
-69.994	-17.846	101.0	126	7	48	8	-122	10
-69.436	-17.490	155.1	130	5	55	3	38	18
-70.065	-18.119	92.2	110	9	28	7	-142	20
-69.590	-17.408	147.6	-27	4	90	0	-150	5
-69.475	-16.646	194.7	0	5	18	9	-171	6
-69.634	-17.673	138.8	0	5	42	4	-82	6
-69.583	-17.659	140.7	18	7	54	5	-180	0
-70.254	-17.535	96.0	14	3	60	6	-82	1
-69.549	-16.906	175.1	0	2	54	4	-142	17
-69.549	-16.905	175.3	0	2	54	4	-142	17
-71.547	-15.112	146.9	160	1	43	3	-42	2
-71.598	-16.082	136.9	160	1	77	4	-45	5
-71.754	-14.801	125.2	141	1	64	5	118	1
-71.085	-16.698	123.3	42	10	23	3	-82	15
-72.111	-15.055	118.2	148	5	68	9	158	7
-71.779	-15.325	143.5	125	7	88	5	138	2
-72.310	-14.728	98.3	0	0	90	0	-125	3

-72.017	-15.104	128.6	-45	10	90	2	-138	15
-71.714	-15.654	141.2	158	5	78	9	158	9
-72.166	-15.154	119.7	20	5	48	6	-71	7
-71.797	-14.758	117.0	108	4	64	7	77	3
-70.683	-15.322	206.4	66	7	60	1	118	5
-70.924	-16.687	123.6	0	3	70	1	-102	4
-71.198	-16.521	111.6	3	8	52	6	-109	7
-71.767	-15.035	133.2	160	1	78	9	-22	9
-71.767	-15.035	133.2	160	1	78	9	-22	9
-71.565	-15.539	143.0	90	5	74	6	138	5
-71.842	-15.189	129.7	83	2	49	2	-123	2
-70.537	-15.407	202.6	38	7	63	2	-104	2
-70.315	-15.451	210.0	28	4	31	10	-168	8
-71.554	-16.128	120.0	122	10	88	5	118	15
-71.887	-17.057	64.8	72	7	68	5	-180	20
-71.616	-15.909	122.3	0	15	43	15	-122	17
-70.285	-15.631	207.6	112	5	69	3	56	8
-70.194	-15.569	212.3	0	8	8	7	-122	20
-70.504	-15.558	200.3	10	1	63	4	-173	4
-73.610	-14.568	87.1	58	4	38	7	-62	2
-73.146	-14.182	74.5	143	3	85	6	174	4
-72.789	-14.175	84.7	138	10	38	9	-102	6
-73.679	-14.101	76.0	14	10	51	5	-122	16
-71.966	-15.192	122.2	156	4	68	7	158	19
-71.893	-16.031	108.8	88	3	78	10	-180	0
-71.893	-16.031	108.8	88	3	78	10	-180	0
-71.831	-15.112	136.8	133	2	85	5	111	5
-71.922	-15.623	145.2	138	1	41	1	-22	1
-73.656	-14.406	87.4	17	3	28	10	-102	3
-72.495	-15.421	127.9	20	5	36	4	-102	15
-70.249	-15.465	220.4	0	5	43	4	-142	18
-73.504	-14.963	106.8	114	5	60	6	-142	2
-73.417	-14.152	74.7	0	1	73	3	-142	3
-70.784	-15.288	183.1	151	8	40	6	158	2
-71.479	-15.882	143.3	0	5	24	4	-150	8
-71.804	-15.174	126.8	59	3	88	5	18	4
-72.926	-14.874	105.3	24	3	48	10	-102	2
-71.761	-14.858	124.3	-45	10	90	2	-138	15
-71.762	-14.862	125.2	-45	10	90	2	-138	15

-72.050	-15.391	132.4	20	5	24	3	-103	4
-71.802	-15.139	129.8	-21	3	90	5	-138	8
-72.933	-14.370	84.3	40	3	60	4	-162	5
-70.774	-15.517	181.1	60	5	30	4	-135	9
-71.595	-15.225	140.5	160	1	88	6	156	10
-71.877	-15.894	148.1	137	4	78	7	157	10
-71.149	-16.582	110.3	108	4	68	10	138	14
-71.149	-16.582	110.2	108	4	68	10	138	14
-72.424	-15.253	119.1	14	3	88	4	-145	3
-71.228	-15.511	150.1	102	2	88	4	18	2
-70.777	-15.624	171.7	86	7	56	7	-142	3
-72.285	-15.085	111.6	143	7	87	8	138	15
-70.526	-15.580	198.3	22	3	46	5	138	2
-72.979	-14.097	77.6	75	5	87	5	78	17
-70.824	-15.236	183.8	133	4	55	3	150	9
-70.725	-15.550	179.6	155	10	65	5	98	15
-71.983	-15.035	124.8	51	5	78	10	-15	8
-71.591	-15.099	133.8	36	6	90	2	18	4
-71.691	-15.914	138.4	-70	1	90	1	-138	2
-71.713	-15.673	143.0	60	9	35	3	-82	8
-72.031	-16.168	122.6	24	3	38	4	-144	4
-72.360	-15.281	114.5	148	2	78	8	158	10
-70.736	-15.578	177.2	0	5	12	9	95	6
-70.188	-15.546	212.7	98	6	64	3	62	19
-71.906	-15.008	124.4	5	5	76	5	-162	12
-71.957	-16.139	111.7	103	3	77	10	158	9
-71.942	-14.901	121.1	138	3	45	5	118	2
-72.128	-15.753	123.1	95	4	74	8	158	4
-71.803	-14.869	120.3	151	3	67	4	117	3
-72.026	-14.963	114.3	0	1	66	10	-162	13
-71.674	-16.350	103.6	99	1	86	5	137	8
-71.557	-16.417	104.3	130	8	28	5	-142	10
-72.771	-14.816	95.3	0	3	68	10	-180	0
-71.895	-14.982	128.5	49	4	9	5	-102	3
-71.310	-15.526	151.4	160	3	87	8	118	14
-71.310	-15.526	151.4	160	3	87	8	118	14
-72.059	-15.571	133.3	99	1	88	5	-22	2
-72.105	-15.149	117.3	20	5	22	5	-129	5
-72.072	-14.935	120.7	-32	4	90	2	-178	5

-72.014	-15.376	128.0	146	5	86	6	-162	4
-72.293	-15.997	106.5	37	3	81	9	-22	10
-72.537	-15.170	120.7	20	5	36	5	-127	4
-71.607	-15.255	138.2	20	5	10	7	-169	9
-72.657	-13.908	86.6	141	1	43	4	-51	6
-75.100	-14.198	80.1	103	5	34	5	118	2
-75.545	-12.300	103.3	-52	3	90	3	-138	2
-76.001	-11.992	108.7	22	5	82	1	-108	4
-75.664	-11.893	100.4	67	6	88	7	138	3
-76.410	-12.997	79.5	26	9	78	6	-69	7
-75.437	-13.847	79.8	160	0	46	3	-47	8
-74.668	-14.296	83.6	153	5	59	2	-102	3
-75.831	-12.314	94.4	148	2	30	1	-102	2
-75.826	-13.250	54.8	107	9	58	4	117	2
-74.862	-13.213	79.3	150	5	75	5	-62	13
-75.197	-12.559	101.0	110	1	72	2	58	5
-74.632	-11.442	91.4	150	5	18	10	-52	10
-76.280	-11.582	96.7	138	6	75	5	98	1
-76.036	-11.144	110.3	13	8	78	8	-8	7

Table 2.2. Stress axes orientations for 173 intermediate depth events

Longitude	Latitude	Depth	P-strike	P-dip	T-strike	T-dip
-69.636	-17.607	128.9	266.803	62.904	69.379	26.020
-69.917	-17.289	125.2	333.958	82.918	95.341	3.702
-69.353	-17.375	156.7	178.382	28.239	71.618	28.239
-69.456	-17.608	151.3	178.997	26.627	72.285	29.837
-69.365	-18.191	128.2	199.460	13.279	101.118	31.582
-69.630	-17.600	146.5	262.700	42.501	28.344	32.454
-70.053	-17.103	137.4	255.281	33.112	1.819	23.579
-69.542	-16.568	186.7	288.388	53.465	80.807	33.294
-69.330	-17.698	159.7	186.466	16.565	90.406	19.540
-69.423	-17.323	152.1	182.444	27.211	74.857	30.440
-69.399	-17.740	142.3	225.302	15.374	326.688	35.679
-70.063	-17.140	135.3	216.054	41.715	310.363	4.818
-69.715	-17.750	135.0	341.430	49.757	75.243	3.222
-69.746	-17.405	148.3	213.960	34.383	96.040	34.383
-69.412	-17.340	155.6	311.448	36.745	53.651	15.809
-69.828	-17.396	126.8	182.814	17.388	87.186	17.388
-69.663	-16.760	166.9	170.382	28.239	63.618	28.239
-69.940	-17.332	128.4	279.274	75.907	125.069	12.737
-69.672	-16.573	191.6	250.994	39.238	151.623	11.275
-69.671	-16.575	190.9	250.994	39.238	151.623	11.275
-69.602	-17.540	151.8	237.273	11.169	330.109	14.067
-69.861	-17.230	131.3	2.934	33.369	100.635	11.501
-69.855	-16.367	186.1	247.420	31.932	22.878	48.834
-69.330	-18.102	128.0	4.282	77.940	237.523	7.287
-69.829	-17.242	129.8	164.212	31.701	51.788	31.701
-69.433	-15.951	235.4	147.014	22.041	22.692	54.320
-69.432	-15.951	235.3	147.014	22.041	22.692	54.320
-69.556	-16.848	173.8	262.863	29.722	356.960	7.132
-69.604	-16.670	186.2	234.801	32.874	330.982	9.458
-69.491	-17.513	137.0	219.457	39.044	126.910	3.136
-69.537	-17.752	132.7	323.490	44.014	92.637	33.162
-69.538	-17.751	132.7	323.490	44.014	92.637	33.162
-69.537	-17.752	132.7	323.490	44.014	92.637	33.162
-69.538	-17.751	132.7	323.490	44.014	92.637	33.162
-69.659	-17.391	136.7	217.072	31.415	103.621	33.088
-69.450	-16.480	194.3	244.762	25.807	141.238	25.807
-69.642	-15.887	226.4	193.326	61.382	358.874	27.851

-69.596	-15.877	229.3	233.238	25.807	336.762	25.807
-69.508	-16.871	171.0	195.286	25.817	88.640	30.631
-69.570	-17.579	140.0	201.443	19.388	298.557	19.388
-69.728	-17.290	141.3	193.375	28.361	83.959	31.626
-69.828	-17.897	136.5	293.098	42.418	104.349	47.248
-69.387	-18.276	124.2	267.809	71.632	68.864	17.435
-69.313	-17.708	142.3	354.810	11.840	97.470	46.272
-69.541	-17.715	132.2	329.002	46.690	66.996	7.468
-70.136	-17.465	103.4	325.139	0.837	55.706	34.098
-69.309	-17.448	155.7	200.238	25.807	303.762	25.807
-69.549	-15.964	224.6	275.871	15.371	11.016	18.068
-70.001	-17.629	101.3	252.991	4.664	347.593	44.528
-69.560	-17.708	147.9	270.019	13.715	40.208	69.284
-69.580	-17.556	134.9	196.282	9.613	101.234	27.453
-70.022	-17.481	127.8	197.164	15.360	102.836	15.360
-69.635	-17.588	131.2	216.973	24.559	319.027	24.559
-69.494	-17.351	148.2	197.014	22.651	96.986	22.651
-69.744	-16.630	169.9	275.000	45.000	95.000	45.000
-69.445	-17.295	151.3	197.340	23.291	96.660	23.291
-69.353	-17.776	136.8	195.164	15.360	100.836	15.360
-69.917	-17.020	132.5	350.778	52.979	258.280	1.882
-69.491	-17.656	135.9	270.780	25.002	91.673	64.995
-69.994	-17.846	101.0	324.342	66.749	58.015	1.577
-69.436	-17.490	155.1	73.909	2.807	340.600	49.657
-70.065	-18.119	92.2	284.626	55.967	57.877	24.832
-69.590	-17.408	147.6	202.107	20.705	103.893	20.705
-69.475	-16.646	194.7	189.215	44.965	335.132	39.666
-69.634	-17.673	138.8	25.634	83.733	264.343	3.264
-69.583	-17.659	140.7	236.973	24.559	339.027	24.559
-70.254	-17.535	96.0	304.568	73.733	98.162	14.647
-69.549	-16.906	175.1	209.572	50.159	303.941	3.637
-69.549	-16.905	175.3	209.572	50.159	303.941	3.637
-71.547	-15.112	146.9	145.468	57.122	37.608	11.213
-71.598	-16.082	136.9	110.935	40.259	218.042	19.155
-71.754	-14.801	125.2	210.943	14.547	93.534	60.590
-71.085	-16.698	123.3	117.039	67.592	305.900	22.166
-72.111	-15.055	118.2	17.024	1.105	107.680	30.696
-71.779	-15.325	143.5	178.997	26.627	72.285	29.837
-72.310	-14.728	98.3	240.162	35.396	119.838	35.396

-72.017	-15.104	128.6	188.382	28.239	81.618	28.239
-71.714	-15.654	141.2	206.717	6.435	113.844	23.961
-72.166	-15.154	119.7	1.257	75.930	96.687	1.358
-71.797	-14.758	117.0	207.629	18.016	352.502	68.315
-70.683	-15.322	206.4	136.249	10.786	23.876	63.412
-70.924	-16.687	123.6	251.039	63.099	99.267	24.085
-71.198	-16.521	111.6	215.310	74.194	106.367	5.251
-71.767	-15.035	133.2	115.844	23.961	208.717	6.435
-71.767	-15.035	133.2	115.844	23.961	208.717	6.435
-71.565	-15.539	143.0	147.031	15.065	43.731	40.521
-71.842	-15.189	129.7	283.579	65.709	15.654	0.936
-70.537	-15.407	202.6	279.764	68.803	138.298	16.876
-70.315	-15.451	210.0	227.001	42.987	352.673	32.032
-71.554	-16.128	120.0	187.501	36.818	57.860	40.439
-71.887	-17.057	64.8	294.836	15.360	29.164	15.360
-71.616	-15.909	122.3	186.649	67.837	292.143	6.210
-70.285	-15.631	207.6	226.436	17.090	340.698	53.196
-70.194	-15.569	212.3	127.102	51.599	298.427	38.081
-70.504	-15.558	200.3	230.096	23.441	326.365	14.137
-73.610	-14.568	87.1	67.684	70.320	308.303	9.952
-73.146	-14.182	74.5	188.309	0.688	98.215	7.774
-72.789	-14.175	84.7	281.272	79.430	56.528	7.549
-73.679	-14.101	76.0	218.675	65.647	126.011	1.205
-71.966	-15.192	122.2	25.024	1.105	115.680	30.696
-71.893	-16.031	108.8	312.367	8.454	43.633	8.454
-71.893	-16.031	108.8	312.367	8.454	43.633	8.454
-71.831	-15.112	136.8	204.604	36.584	64.392	45.993
-71.922	-15.623	145.2	116.067	45.027	3.356	21.093
-73.656	-14.406	87.4	134.809	71.632	295.864	17.435
-72.495	-15.421	127.9	155.607	78.127	298.573	9.527
-70.249	-15.465	220.4	196.387	54.493	304.836	12.723
-73.504	-14.963	106.8	329.312	46.934	237.873	1.344
-73.417	-14.152	74.7	224.571	38.540	124.741	12.098
-70.784	-15.288	183.1	16.079	21.803	130.005	45.393
-71.479	-15.882	143.3	176.693	52.165	315.083	30.144
-71.804	-15.174	126.8	192.273	11.169	285.109	14.067
-72.926	-14.874	105.3	227.089	80.804	122.461	2.341
-71.761	-14.858	124.3	188.382	28.239	81.618	28.239
-71.762	-14.862	125.2	188.382	28.239	81.618	28.239

-72.050	-15.391	132.4	134.955	67.851	299.840	21.453
-71.802	-15.139	129.8	212.382	28.239	105.618	28.239
-72.933	-14.370	84.3	256.801	32.874	352.982	9.458
-70.774	-15.517	181.1	230.970	59.584	2.443	21.246
-71.595	-15.225	140.5	207.972	15.234	112.839	18.186
-71.877	-15.894	148.1	186.012	7.079	92.744	24.662
-71.149	-16.582	110.3	165.370	18.409	60.532	37.577
-71.149	-16.582	110.2	165.370	18.409	60.532	37.577
-72.424	-15.253	119.1	244.091	25.468	142.784	22.374
-71.228	-15.511	150.1	235.273	11.169	328.109	14.067
-70.777	-15.624	171.7	297.599	49.141	29.886	1.977
-72.285	-15.085	111.6	197.286	25.817	90.640	30.631
-70.526	-15.580	198.3	259.889	8.676	3.094	56.258
-72.979	-14.097	77.6	176.202	40.821	332.623	46.695
-70.824	-15.236	183.8	4.937	6.659	101.420	44.043
-70.725	-15.550	179.6	239.003	19.620	80.924	68.980
-71.983	-15.035	124.8	7.260	19.028	97.893	1.834
-71.591	-15.099	133.8	169.563	12.621	262.437	12.621
-71.691	-15.914	138.4	163.382	28.239	56.618	28.239
-71.713	-15.673	143.0	119.641	78.772	324.261	10.230
-72.031	-16.168	122.6	214.674	54.399	330.866	17.537
-72.360	-15.281	114.5	196.717	6.435	103.844	23.961
-70.736	-15.578	177.2	265.784	33.038	83.513	56.941
-70.188	-15.546	212.7	208.057	14.547	325.466	60.590
-71.906	-15.008	124.4	228.278	22.525	137.304	2.347
-71.957	-16.139	111.7	151.787	5.684	59.169	24.656
-71.942	-14.901	121.1	28.577	3.355	128.001	70.301
-72.128	-15.753	123.1	143.944	3.424	52.219	26.714
-71.803	-14.869	120.3	221.310	17.678	99.421	58.897
-72.026	-14.963	114.3	219.638	29.158	312.463	5.048
-71.674	-16.350	103.6	154.017	25.578	46.591	32.032
-71.557	-16.417	104.3	304.626	55.967	77.877	24.832
-72.771	-14.816	95.3	222.836	15.360	317.164	15.360
-71.895	-14.982	128.5	153.402	53.765	329.493	36.171
-71.310	-15.526	151.4	225.804	35.907	96.240	41.337
-71.310	-15.526	151.4	225.804	35.907	96.240	41.337
-72.059	-15.571	133.3	52.230	16.822	146.518	13.889
-72.105	-15.149	117.3	171.201	59.482	319.883	26.728
-72.072	-14.935	120.7	193.017	1.414	102.983	1.414

-72.014	-15.376	128.0	11.742	15.504	279.021	9.709
-72.293	-15.997	106.5	351.941	21.854	85.454	8.685
-72.537	-15.170	120.7	194.465	64.688	316.000	13.894
-71.607	-15.255	138.2	199.168	46.037	359.780	42.294
-72.657	-13.908	86.6	67.114	81.562	199.324	5.692
-75.100	-14.198	80.1	353.019	13.715	123.208	69.284
-75.545	-12.300	103.3	181.382	28.239	74.618	28.239
-76.001	-11.992	108.7	272.191	49.850	127.390	34.579
-75.664	-11.893	100.4	123.237	29.438	16.487	27.053
-76.410	-12.997	79.5	320.564	52.441	99.001	29.914
-75.437	-13.847	79.8	142.786	59.678	40.941	6.846
-74.668	-14.296	83.6	32.530	73.147	251.686	13.219
-75.831	-12.314	94.4	268.921	73.375	66.774	15.459
-75.826	-13.250	54.8	178.023	9.183	67.377	65.369
-74.862	-13.213	79.3	92.483	51.820	218.543	24.838
-75.197	-12.559	101.0	223.597	20.598	342.435	52.075
-74.632	-11.442	91.4	185.579	57.638	29.815	30.021
-76.280	-11.582	96.7	221.504	29.561	59.096	59.247
-76.036	-11.144	110.3	329.213	14.080	238.482	2.909

REFERENCES

Abers, G. A. & Sarker, G., 1996. Dispersion of regional body waves at 100–150 km depth beneath Alaska: In situ constraints on metamorphism of subducted crust, *Geophys. Res. Lett*., **23**, 1171– 1174.

Anderson, M., Alvarado, P., Zandt, G. & Beck, S., 2007. Geometry and brittle deformation of the subducting Nazca Plate, Central Chile and Argentina, *Geophys. J. Int.,* **171**, 419–434.

Angelier, J., Tarantola, A., Manoussis, S. & Valette, B., 1982. Inversion of field data in fault tectonics to obtain the regional stress tensor, *Geophys. J. R. Astron. Soc*., **69**, 607-621.

Araujo, M. & Suarez*,* G., 1994. Geometry and state of stress of the subducted Nazca Plate beneath central Chile and Argentina; evidence from teleseismic data*, Geophys. J. Int.*, **116***,* 283–303.

Arrial, P-A & Billen, M.I., 2013. Influence of geometry and eclogitization on oceanic plateau subduction, *Earth Planet. Sci. Lett.,* **363**, 34-43.

Barazangi M. & Isacks B.L.*,* 1976*.* Spatial distribution of earthquakes and subduction of the Nazca plate beneath South America*, Geology,* **4***,* 686–692.

Becker, J.J., Sandwell, D. T., Smith, W.H.F., Braud, J., Binder, B., Depner, J., Fabre, D., Factor, J., Ingalls, S., Kim, S.-H. & others. 2009. Global bathymetry and elevation data at 30 arc seconds resolution: SRTM30_PLUS. *Marine Geodesy* 32(4):355–371

Bevis, M. & Isacks, B.L., 1984. Hypocentral trend surface analysis: Probing the geometry of Benioff Zones, *J. Geophys. Res.,* **89**, 6153- 6170.

Bott, M. H. p., 1959. The mechanisms of oblique slip faulting, *Geol. Mag*., **96**,109-1 17.

Cahill T. & Isacks B.L.*,* 1992*.* Seismicity and shape of the subducted Nazca plate*, J. Geophys. Res.,* **97**, 17,503–17,529.

Dougherty, S. L. & Clayton, R. W., 2014. Seismic structure in southern Peru: evidence for a smooth contortion between flat and normal subduction of the Nazca Plate, *Geophys. J. Int*. **200**, 534-555.

Faccenda, M., 2014. Water in the slab: A trilogy, Tectonophysics, **614**,1–30, doi:10.1016/j.tecto.2013.12.020.

Green, H. W. & Houston, H., 1995. The mechanics of deep earthquakes, *Annu. Rev. Earth Planet*, 169– 213.

Gutscher M.A., Spakman W., Bijwaard H. & Engdahl E.R., 2000. Geodynamics of flat subduction: seismicity and tomographic constraints from the Andean margin, *Tectonics,* **19**, 814–833.

Hacker, B. R., Peacock, S. M. & Abers,G. A., 2003. Subduction factory, 2, Intermediate-depth earthquakes in subducting slabs are linked to metamorphic dehydration reactions, *J. Geophys. Res.,* 108, doi:10.1029/2001JB001129.

Hampel, A., 2002. The migration history of the Nazca Ridge along the Peruvian active margin: A re-evaluation, *Earth Planet. Sci. Lett.*, **203**, 665–679.

Hasegawa,A. & Sacks, I. S., 1981. Subduction of the Nazca Plate beneath Peru as determined from seismic observations, *J. Geophys. Res.,* **86**, 4971-4980.

Hayes, G. P., Wald, D. J. & Johnson, R. L., 2012. Slab1.0: A new three-dimensional model of global subduction interface geometry, *J. Geophys. Res.*, **117**, B01302, doi:10.1029/2011JB008524.

Igarashi, T., Matsuzawa, T., Umino, N. & Hasegawa, A., 2001. Spatial distribution of focal mechanisms for interplate and intraplate earthquakes associated with the subducting Pacific plate beneath the northeastern Japan arc: A tripled-planed deep seismic zone, *J. Geophys. Res.*, **106**, 2177–2191.

Isacks, B. L. & Molnar, P., 1971. Distribution of stresses in the descending lithosphere from a global survey of focal-mechanism solutions of mantle earthquakes, *Rev. Geophys.,* **9**, 103-174.

Isacks, B. L. & Barazangi, M., 1977. Geometry of Benioff zones: lateral segmentation and downwards bending of' the subducted lithosphere, in *Island Arcs, Deep Sea Trenches and Backarc Basins,* pp. 99-114, eds Talwani, M. & Pitman, W. C., American Geophysical Union, Washington.

James, D.E. & Sacks, S.,1999. Cenozoic formation of the Central Andes: a geophysical perspective, in *Geology and Ore Deposits of the Central Andes* ,Vol. **7**, pp. 1–26. ed. Skinner, B.J., Society of Economic Geology, Special Publication.

Kirby, S. H., 1995. Interslab earthquakes and phase changes in subducting lithosphere, U.S. Natl. Rep. Int. Union Geod. Geophys. 1991 – 1994, *Rev. Geophys*., **33**, 287–297.

Kirby, S. H., Engdahl, E. R. & Denlinger, R.,1996. Intermediate-depth intraslab earthquakes and arc volcanism as physical expressions of crustal and uppermost mantle metamorphism in subducting slabs, in Subduction: Top to Bottom, Geophys. Monogr. Ser., vol. 96, edited by G. E. Bebout et al., 195– 214, AGU, Washington, D. C.

Kirby, S.H, Engdahl, E.R. & Denlinger, R., 2006. Intermediate-depth intraslab earthquakes and arc volcanism as physical expressions of crustal and uppermost mantle metamorphism in subducting slabs. Subduction Top to Bottom, **96**, pp. 195–214.

Knezevic, S. K., Wagner, L. S., Kumar, A., Beck, S. l., Long, M. D., Zandt, G., Tavera, H., Condori, C., 2015. The Role of Slab Buoyancy in the Formation of Flat Slabs, *Nature,* in review.

Kumar, A., Wagner, L. S., Beck, S. L., Long, M. D., Young, B., Tavera, H. & Minaya, E., 2015. Geometry and state of stress in the central and southern Peruvian flat slab, *in prep*.

Linkimer, L., 2011. Lithospheric structure of Pampean flat slab (latitude 30-33°S) and northern Costa Rica (latitude 9-11°N) subduction zones, *Ph.D. thesis*, Univ. of Arizona, Tucson.

McGeary, S., Nur, A. & Ben-Avraham, Z., 1985. Spatial gaps in arc volcanism: The effect of collision or subduction of oceanic plateaus, *Tectonophysics*, **119**, 195–221.

McKenzie, D. P., 1969. The relation between fault plane solutions for earthquakes and the directions of the principal stresses, *Bull. Seism. Soc. Am*., **59**, 591.

Olsen, K., Anderson, M. L., Linkimer, L., Gilbert, H. J., Beck, S. L., Zandt, G., Alvarado, P. M., 2010. Dynamics of flat subduction: Focal mechanisms, ridge buoyancy, and slab tear in central Argentina, *AGU Fall Meeting*, San Francisco, California.

Omori, S., Komabayashi, T., Maruyama, S., 2004. Dehydration and earthquakes in the subducting slab: empirical link in intermediate and deep seismic zones. Phys. Earth Planet. Inter. **146**, 297–311.

Ottemöller, L., Voss, P. & Havskov, J., 2011.SEISAN: the Earthquake Analysis Software for Windows, Solaris, LINUX, and MACOSX, version 9.0.1, University of Bergen, pp. 361.

Peacock, S. M., 1993. Large-scale hydration of the lithosphere above subducting slabs, Chem. Geol., **108**, 49–59.

Peacock, S. M., 2001. Are the lower planes of double seismic zones caused by serpentine dehydration in subducting oceanic mantle?, Geology, **29**, 299–302.

Phillips, K. & Clayton, R. W., 2014. Structure of the subduction transition region from seismic array data in southern Peru, *Geophys. J. Int*., **196**, 1889 – 1905, doi:10.1093/gji/ggt504.

Reasenberg, P. & Oppenheimer, D., 1985. FPFIT, FPPLOT and FPPAGE: FORTRAN computer programs for calculating and displaying earthquake fault-plane solutions, *USGS. Open file Rept*., 85-739.

Sacks, I., 1983. The subduction of young lithosphere, *J. Geophys. Res*., **88**, 3355–3366.

Schneider, J. F. & Sacks, I. S., 1987. Stress in the contorted Nazca plate beneath southern Peru from local earthquakes, *J. Geophys. Res.,* **92**, 13,887-13,902.

Scire, A., Zandt, G., Beck, S., Long, M., Wagner, L., Minaya, E. & Tavera, H., 2015. Imaging the transition from flat to normal subduction: Variations in the structure of the Nazca slab and upper mantle under southern Peru and northwestern Bolivia, *submitted to Geophys J. Int.*

Stauder, W., 1975. Subduction of the Nazca plate under Peru as evidenced by focal mechanism and seismicity, *J. Geophys. Res.,* **80**, 1053-1064.

van Hunen, J., van der Berg, A.P. & Vlaar, N.J., 2002. On the role of subducting oceanic plateaus in the development of shallow flat subduction, *Tectonophysics*, **352**, 317–333.

Vassiliou, M. S. & Hager, B. H., 1988. Subduction zone earthquakes and stress in slabs, *Pure Appl. Geophys*., **128**, 547-624.

Yáñez, G.A., Ranero, C.R., von Huene, R. & Díaz, J., 2001. Magnetic anomaly interpretation across the southern central Andes (32°-34°S): The role of the Juan Fernandez Ridge in the late Tertiary evolution of the margin, *J. Geophys. Res*., **106**, 6325-6345, doi:10.1029/2000jb900337.

Chapter 3: Crust and upper mantle structure beneath the north Central Andes

ABSTRACT

The Central Andean Plateau of southern Peru, Bolivia and northwestern Argentina is the second largest tectonically active orogen along the western margin of South America. This plateau has influenced both local and far field lithospheric deformation, global sediment flux, atmospheric circulation and climate since the early Miocene. Significant geologic and geophysical efforts have been made to constrain the tectonomorphic evolution of the central Andean plateau, yet the role of surface and deep lithospheric processes in the evolution of the plateau is unclear. Isotopic paleoaltimeters suggest rapid and recent surface uplift during the late Miocene, whereas, structural reconstructions support an earlier and steady uplift between ~30 and 10 Ma. Previous studies have emphasized the variable importance of both the crust and upper mantle in the evolution of central Andean plateau. In order to investigate the current state of lithospheric structure below the northern Altiplano between 14-18°S, I calculate three-dimensional seismic tomography models for V_P and V_S using P and S-wave travel time data. In this effort, I also determined crustal and upper mantle velocity structure in the Peruvian flat slab region between 12-14°S. My tomographic models show some typical structures found in subduction zones including a high velocity slab and widespread low velocities under the active volcanic arc. In the northern Altiplano, I observed the absence of a high velocity lower crust, suggesting a weak lower crust of felsic composition or the loss of a high velocity mafic lower crust due to delamination. The upper mantle under the northern Altiplano is heterogeneous, consistent with piecemeal delamination. My tomography results

for the lower crust and upper mantle beneath the northern Altiplano are in better agreement with the slow and steady uplift model.

1. INTRODUCTION

The central Andean plateau of southern Peru, Bolivia, and northwestern Argentina is the second largest plateau in the world. It extends between 14°-28° S in western South America (Isacks, 1988; Allmendinger et al., 1997) and overrides a normally dipping (~30°) portion of the subducting Nazca plate between zones of flat slab subduction to the north and south. The average elevation of the plateau is ~4 km and spans ~2000 km along strike and ~200-450 km west to east (Oncken et al., 2006; Barnes & Ehlers, 2009). It has strongly influenced both local and far field lithospheric deformation, atmospheric circulation, precipitation and climate since the early Miocene (Masek et al., 1994, Lenters & Cook, 1995).

Numerous geologic (structure, paleoclimate, thermochronology) and geophysical (receiver function, seismic refraction, teleseismic and local tomography) studies have been carried out in last three decades to constrain the Cenozoic evolution of the central Andean plateau (Isacks, 1988; Dorbath et al., 1993; Wigger et al., 1994; Dorbath & Granet, 1996; Allmendinger et al., 1997; Horton & DeCelles, 1997; Jordan et al., 1997; Myers et al., 1998; Kley et al., 1999; Beck & Zandt, 2002; McQuarrie et al., 2005; Oncken et al., 2006; McQuarrie et al., 2008), yet the surface and subsurface processes responsible for plateau formation and evolution are disputed. Two end member models have been suggested. The first is the rapid and recent uplift model, which argues for surface uplift on the order of ~2.5 km during the late Miocene (~10.3 to 6.8 Ma) triggered by the wholesale removal of the eclogitized lower crust and upper mantle lithosphere (Garzione et al., 2006; Ghosh et al., 2006, Hoke & Garzione, 2008). Evidence supporting the model of rapid uplift comes from the plaeoaltimetry record based on the study of $\delta^{18}O$ of meteoric water in paleosol carbonates (Garzione et al., 2006, Ghosh et al, 2006), paleotemperature estimates from Jakokkota flora of northern Altiplano (Gregory-Wodzicki et al., 1998), and a contemporaneous shift of the deformation front towards the lowlands of the Sub Andes. The second model is the slow and steady uplift model, which emphasizes the role of crustal shortening and thickening in the total elevation gain of the Altiplano since the late Eocene (~40 Ma), with some local contribution from small scale lithospheric delamination (Jordan et al., 1997; McQuarrie et al., 2005, Hoke & Lamb, 2007; Ehlers & Poulsen, 2009). This model assumes that surface uplift and deformation are coupled. The supporting evidence for gradual uplift comes from the exhumation history based on low temperature thermochronology (cooling history) in bedrock, extensive shortening (200-250 km) estimates in the fold-thrust belt, the onset of mafic volcanism, and climatic records. As previously suggested, increases in mountain building activity usually generates topography and relief necessary to enhance the exhumation rate (Coughlin et al., 1998; Carrapa et al., 2005). The increased rate of exhumation for the Altiplano and the western part of the Eastern Cordillera dates to ~40 and ~40-20 Ma respectively. This indicates that the modern plateau width was established by ~20 to 15 Ma (Barnes & Ehlers, 2009), much before the period of rapid uplift (~10 Ma). Kay and Mahlburg Kay (1993) and Lamb and Hoke (2007) suggest that the onset of mafic volcanism and helium in natural gas (geothermal and mineral water springs, fumaroles) emissions provides the most direct evidence of mantle melting and can be used as a proxy for the delamination. In the Altiplano, a surge in volcanic activity and high $^{3}He/^{4}He$ ratio (~10^{-5}) in natural helium emissions started at nearly ~25 Ma (Davidson & de Silva, 1992; Lamb &

Hoke, 1997), which indicates a thin Altiplano lithosphere or partial delamination since the late Oligocene. If the central Andean plateau evolved mainly during the late Miocene (Garzione et al., 2006; Ghosh et al., 2006, Hoke & Garzione, 2008) then it should have coincided with a marked decrease in precipitation, east of the Western Cordillera, due to the development of a rain shadow (Rech et al., 2006). Measures of aridity in the Atacama basin of the central Andes (~23° S) indicates hyper arid conditions have existed for the past ~19 Ma due to higher elevations, which also favors the slow and steady evolution of Altiplano-Puna plateau since the early Miocene.

One possible discriminating factor between these two theories is seismic evidence for the presence or absence of mantle lithosphere. If the lithosphere is present I should see high velocities in the upper mantle beneath the northern Altiplano. In contrast, if lithospheric removal has occurred on the regional scale (wholesale removal) I should see upper mantle of asthenospheric character, with low seismic velocity, under the northern Altiplano. The majority of the available geophysical observations of shallow and deep lithospheric structures in the central Andean plateau, are related to the central and southern Altiplano (between 18°S and 28°S), with very little focus on the northern Altiplano (Wigger et al., 1994; Myers et al., 1998; Graeber & Asch, 1999; Beck & Zandt, 2002; Yuan et al., 2002; Ward et al., 2013). Much of the work in the central and southern Altiplano indicates strong along strike variations in the crust and upper mantle properties. The tomographic studies of Dorbath et al. (1993) and Dorbath & Granet (1996) are two of the very limited number of geophysical studies conducted to gain insight into the modern lithospheric structures under the northern Altiplano. These studies use a linear array of seismic stations in the northern Altiplano to determine the subsurface velocity structure between 16°S and 18°S. They find strong across-strike variations in the upper mantle but have very limited along strike resolution due to the geometry of the seismic network.

My current study seeks to characterize the velocity structure of the crust and upper mantle under the northern Altiplano of southern Peru and northern Bolivia (between 14°S and 18.5°S) (Figure 3.1). It has an average elevation of ~3.7km and relatively low relief compared to the Puna further to the south and is flanked by the Western and Eastern Cordilleras. My study area also extends north of the Altiplano Plateau, well into the Peruvian flat slab region. I use an extensive 2-D grid of seismic stations for better tomographic coverage than has previously been possible for this region. My results indicate the absence of a high velocity lower crust under the northern Altiplano that may indicate a weak lower crust of felsic composition. The upper mantle under the northern Altiplano is heterogeneous and shows along strike variations in velocity structure. I observe the presence of high velocity mantle lithosphere beneath the northern Altiplano, with some possibility of piecemeal delamination at local scales. North of the Nazca Ridge, in the Peruvian flat slab region, I observe low-V_S in the upper mantle that may be related to a tear previously identified by surface wave tomography and earthquake hypocenters and focal mechanisms. The results of my study can be used along with previous studies that are mainly focused on the central and southern Altiplano to provide important constraints on the along strike variation in the lithospheric structures in central Andes and thereby improve our understanding of the formation of the Altiplano plateau.

2. DATA

This study incorporates data collected at 96 broadband seismic stations from three independent seismic networks in south-central Peru and northwestern Bolivia: PULSE (PerU

Lithosphere and Slab Experiment), CAUGHT (Central Andean Uplift and Geodynamics of High Topography) and PERUSE (PERU Slab Experiment) (Refer: Figure 1.1, Chapter 1). These networks roughly cover an area of 1000 km by 750 km. The PULSE network includes 40 broadband seismometers, comprising a combination of Nanometrics Trillium 120 and Guralp CMG-3T sensors. Data were collected using Taurus and Quanterra Q330 dataloggers recording at 40 sps and stored on flashcards and external Balers, respectively, that were exchanged every ~6 months. The CAUGHT seismic deployment includes a 2D deployment of 48 STS-2 sensors with Quanterra Q330 dataloggers. For both networks, the exact location and timing at each station were determined using GPS receivers. Instrumentation for the CAUGHT deployment was provided by Portable Array Seismic Studies of the Continental Lithopshere (PASSCAL) of the Incorporated Research Institutions for Seismology (IRIS) and for the PULSE deployment, 10 stations were from UNC-Chapel Hill, 20 stations from Yale and 10 stations from IRIS-PASSCAL (Refer: Data section of Chapter 1 for more detailed description of the PULSE and CAUGHT networks). The PERUSE project was jointly operated by the Caltech Tectonics Observatory (TO) and the Center for Embedded Network Sensors (CENS) at UCLA. The data were recorded at 100 sps, using Guralp CMG-3T sensors. I collaborated for 8 stations of the TO project, to obtain better regional coverage for my 3D tomographic study.

My current tomography study uses a total of 712 well-located events, including 593 events below 50 km depth associated with the subducting Nazca plate and 119 crustal events (depth<50 km), associated with the overriding South American (SA) plate (Figure 3.2). For these events, the epicentral distance to the nearest station varies between 2 - 210 km, with a mean value close to ~55 km. These events have an azimuthal gap of ≤ 270° and mean error of ~12 and 10 km for the epicentral locations and depth respectively. Figure 3.3 shows the map of events plotted according to back azimuthal gap. A histogram of back azimuthal gaps for all events is shown in Figure 3.4. I picked P- and S-wave arrivals using the programs MULPLT and HYP included in the software package SEISAN (Havskov & Ottemöeller, 1999; Ottemöeller et al., 2011). P-waves were picked solely on the vertical component and S-wave arrivals were picked on the transverse component and hypocenters were recalculated using P- and SH-wave picks. More details about my database can be found in Chapter 1. The complete dataset includes about 18,631 arrival times of which 13,118 are P-wave picks and 5,513 are S-wave picks. In the northern half of my study area (north of 15°S), P- and S-wave coverage is best at 85 and 105 km depth. At greater depth (>105 km), coverage in south-central Peru, north of 15°S, decreases due to the sparsity of local seismicity below 100 km depth. South of 15°S, in southernmost Peru and northern Bolivia, ray path coverage is much better than to the north due to a large number of locally recorded deeper earthquakes (Figs. 3.5 and 3.6).

3. METHOD

I used the local-scale tomographic inversion method of Zhao et al. (1992), to simultaneously determine three-dimensional variation in V_P and V_S structure and hypocentral parameters using P and S wave arrival time data. This algorithm allows for the incorporation of a 3D starting velocity structure defined by user-inputted 2D seismic discontinuities. Using a priori information about velocity discontinuities in the crust and the upper mantle (including the geometry of the subducting slab) helps improve ray tracing and reduces the final travel time residuals. For the calculation of ray paths within the model volume, this method uses the pseudo-bending technique of Um & Thurber (1987) between adjacent velocity discontinuities and Snell's law across the discontinuities. The inversion uses the LSQR algorithm (Paige and Saunders, 1982) to solve for sparse system of linearized travel time equations. Velocity deviations are defined at uniformly spaced grid nodes within the model volume. The earth structure (seismic velocity) and the velocity partial derivatives at any arbitrary point along the ray path are determined by the linear interpolation (weighted sum) of the velocity deviations from the 8 surrounding grid nodes. My inversion grid nodes are uniformly spaced at 40 km in the horizontal direction and 20 km vertically (Figure 3.7).

Model parameterization strongly affects the quality of tomographic images. In the original tomography code, Zhao et al. (1992) use a priori information about the Conrad, Moho and slab geometry from local Pn studies and phase converted waves (Hasegawa et al., 1983; Zhao et al., 1990) to parameterize the model volume. This is accomplished by defining four layers corresponding to the upper crust, lower crust, upper mantle and subducting Pacific plate. As the top surface of the descending slab is usually associated with large abrupt velocity deviations, Zhao et al. (1992) inverts for two complete and independent sets of grid nodes, grid A and grid B, to account for deviations above and below the top surface of the slab, respectively. In the current study, I am uncertain of the exact geometry of the Nazca slab and therefore do not to define the grid nodes (grid A or grid B) with respect to the top surface of the slab or to include any initial velocity deviation for the slab. As I have no constraints on the slab geometry, I use the Moho as my third velocity discontinuity and divide my volume of interest into two grids (A and B) depending on the lateral depth variations in the Moho. At any particular location, if the depth of a grid node is less than the depth to the Moho, then it is assumed to be in the A grid and vice versa. I use two additional velocity discontinuities above the Moho in my starting velocity model. However, I find that these discontinuities are artificially affecting my results. I therefore choose to minimize their impact by moving the first two discontinuities in the uppermost grid layers at 1 and 2 km depth, where I do not have any effective resolution.

Before the inversion, the starting velocity is assigned to each grid node depending on what layer it is in with respect to the inputted discontinuities. The inversion attributes velocity deviations for points below the third discontinuity (in my case, the Moho) to the B-grid of model parameters, and to the A grid for points above. Velocity deviation at any arbitrary point in the model volume is calculated by interpolating the deviations from 8 surrounding grid nodes, whose deviations are distance weighted. The grid nodes are either from B grid or from the A grid. This allows for more abrupt variations in the velocity deviations across the Moho and helps us to differentiate between crustal versus mantle anomalies.

I started the inversion with a one dimensional input velocity model and use starting P- and S-wave velocities of 6 and 3.42 km/s above the Moho. Below the Moho, my starting P- and S-wave velocity model is that of IASPEI-91 (Kennett & Engdahl, 1991). I calculate new earthquake coordinates at the beginning of each iteration, using the revised velocity model and predict the travel time through the revised earth structure. The travel time residuals are recalculated before each iteration using the revised locations and updated velocity model. To reduce the control of large residuals (data outliers) on the inversion process, I put a threshold of 3 s and 4 s for the P- and S-wave travel time residuals respectively. This threshold was chosen based on the distribution of P- and S-wave residuals corresponding to the initial velocity model (Figure 3.8). As all the travel time residuals are revised at the beginning of each iteration, if any residual was discarded in a previous iteration for being too large could be included in a later iteration if it drops below the threshold for the revised and improved velocity model.

In seismic tomography, regularization is necessary to stabilize the inversion and reduce the effect of noise (Thurber, 1981, Menke, 1984). Damping penalizes variations in the model with respect to the starting model of a given iteration. Higher values of damping penalize larger model vectors, resulting in an increase in data variance (Thurber & Ritsema, 2007). As the value of damping decreases, the model vector increases and data variance decreases. I use the empirical approach of Eberhart-Phillips (1986) to determine an optimum value of damping using trade-off curves. These are constructed by running single iteration tomographic inversions for a large suite of damping values and plotting data variance versus model variance for each damping value tested. The damping value is selected that significantly reduces the data variance without causing a large increase in the model variance (Eberhart-Phillips, 1986; Zhang & Thurber, 2007). I choose a damping of 60 for my travel time inversion (Figure 3.9).

In order to determine the number of iterations, I follow a similar analytical approach, using a trade-off curve between data variance and model variance. I perform my inversion using my preferred damping value of 60 for 10 iterations and, for each iteration, calculated the achieved model and data variance at that stage. From this "L" curve, I select an optimum number of iterations to be 2, because subsequent increases in the number of iterations dominantly serve to increase model variance without producing significant decreases in data variance (Figure 3.9). Initially, data variance was 0.7807 sec^2, corresponding to the input model, with model variance of 0. After 2 iterations, my data variance is reduced to 0.2606 sec^2 (a 66.6% reduction), corresponding to a model variance of 3.47.

4. RESULTS

I present tomography results (V_P and V_S) on vertical cross-sections (Figure 3.21) and depth maps, for the South American crust as well as the upper mantle beneath the South American moho, in central and southern Peru and northern Bolivia. As the overall seismicity of the upper mantle is significantly higher than the crust, my resolution for the upper mantle is better than the South American crust. Specifically, in the southern half of my study area (between 14-18°S), the upper mantle velocity structure is well resolved up to ~165 km depth due to higher concentration of intermediate depth seismicity in southern Peru, as described in the Resolution section.

4.1 Crustal anomaly

4.1.1 South-central Peru

My tomographic inversion shows a prevalence of high-V_P and high-V_S (labeled “A”, Figs. 3.10-3.13 and 3.24-3.27) in the crust above the southern margin of the Peruvian flat slab. This feature is clearly visible at depths between 5 and 65-km-depth. For the P-wave velocity anomaly, these high velocities extend between 13-14.5°S and 72.5-74.5°W. In V_S, this anomaly appears to be laterally more elongated in the E-W direction and extends between 72-74.5°W and 13-14.5°S. The absolute velocity of this crustal anomaly ranges from 6.2 to 6.4 km/s for P waves and 3.4 to 3.6 km/s for S waves. This corresponds to a 3.3-6.6% increase over the P-wave starting model and ~5% increase over the S-wave starting model. This anomaly is very well resolved in both V_P and V_S and described in more detail in the next section.

4.1.2 Southern Peru and northern Bolivia

The crust beneath the active volcanic arc of Western Cordillera is characterized by low-V_P and low-V_S (V_P≈5.8 km/s; V_S≈3.4 km/s) along its entire length in southern Peru (Figs. 3.10-3.13). This low velocity region almost exactly terminates along the northern margin of the Central Volcanic Zone (CVZ) and transitions into high velocity crustal anomaly (anomaly A), observed above the southern margin of the Peruvian flat slab. This low velocity region, beneath the Western Cordillera, is consistently visible in the depth range of 5-65 km in the South American crust.

East of the active volcanic arc, the crust beneath the northern Altiplano (dashed line, Figs. 3.10-3.13) has low average velocity (labeled "AP", Figs. 3.29-3.32; V_P≈5.8 km/s; V_S≈3.4 km/s). This is considerably slower than the crust above the southern Peruvian flat-slab segment. This velocity contrast, between the Altiplano crust and crust above the southern margin of the Peruvian flat slab, is apparent in a comparison of the cross-sections EE′ vs HH′ (Figs. 3.26 and 3.29 respectively).

Southeast of lake Titicaca and east of the Altiplano/Eastern Cordillera boundary, I observe a very distinctive crustal velocity structure. The low average velocity of the Altiplano crust (V_S < 3.4km/s) stands in sharp contrast to the high velocity Eastern Cordillera crust. This velocity contrast across the eastern margin of the Altiplano is persistent to depths of 5-65 km in the SA crust and extends between 15-18°S and 67-68.5°W, as can be seen in the depth slice of the S-wave velocity anomaly (labeled "B", Figs. 3.10-3.13 and 3.31-3.32). The absolute velocity of this anomaly is 3.6 km/s for V_S, indicating ~5% increase over the starting velocity model. This feature is much less clear in my P-wave velocity anomaly map.

4.2 Upper mantle anomaly

4.2.1 Peruvian flat slab region

North of 14°S, I have limited resolution between 75-105 km depth, with almost no resolution at greater depths due to the shallow (75-110 km) hypocentral depths of most of my local events. In the flat slab region, between 13-15°S and 73.5-75°W, I observed a high-V_P anomaly (labeled "C", Figs. 3.14 and 3.15). This anomaly can be seen clearly at 75 and 85 km depth and in the cross-sections of P-wave velocity anomalies in Figures 3.24-3.27. This anomaly is almost continuous between the projected location of the subducting Nazca Ridge track and southern edge of the Peruvian flat slab. The absolute velocities of this anomaly range from 8 to 8.4 km/s for P-waves. This range is 0.6-5% higher than the input model at 75-85 km depth. I observe complex variations in S-wave velocities across the Nazca Ridge between 12-15°S and 73-76°W at shallow depth (75-85 km). North of the Nazca Ridge, S-wave velocities vary from slow to neutral, with absolute velocities of 4.4 km/s (labeled "L", Figure 3.14). South of the Nazca Ridge, the S-wave velocities are higher and vary between 4.6-4.8 km/s (labeled "C", Figs. 3.14-3.15 and 3.25-3.27). This corresponds to a 2% decrease and 2.42-6.8% increase over the starting model, north and south of the Nazca Ridge, respectively.

4.2.2 Southern Peru and northern Bolivia

In the region between the Peruvian flat slab to the north and the normally dipping portion beneath southernmost Peru to the south lies the transition region where the slab undergoes an abrupt change in geometry from flat to normal subduction. I find a high-V_P and high-V_S anomaly in the transition region and further south (labeled "E"), roughly following the slab contours of Cahill and Isacks (1992). It appears as a continuous N-S feature between

14-18°S and 70-73°W in the 85-105-km-depth maps of P- and S-wave velocity anomalies (Figs. 3.15 and 3.16). At greater depths (between 125-185 km), this anomaly continues farther inboard between 15-18°S and 69-72°W (Figs. 3.17-3.20). Most of the WBZ seismicity is located within this high velocity feature (Figs. 3.28-3.32). The range of absolute velocities varies from 8 to 8.4 km/s for P-waves and this is 0.5-5% higher than the input model. Absolute S wave velocities range between 4.6 to 4.8 km/s and correspond to a 2-6% increase over the starting model.

I observed a low-V_P and low-V_S anomaly (labeled "AS", Figs. 3.14-3.17) in the upper mantle below the active volcanic arc, in a small region under the northern Altiplano and northeast of northern Altiplano. This feature is clearly seen in small patches in the 75-85-km-depth maps of P- and S-wave velocity anomalies. At greater depths (105-125 km), it has a more continuous N-S extent in V_P than in V_S, west of the lake Titicaca. In the cross-sections of Figures 3.29-3.31, it appears to overlie the normally dipping WBZ. The absolute velocity of anomaly "AS" ranges from 7.6 to 7.8 km/s for P waves and 4.2 to 4.4 km/s for S waves.

I observed a small patch (labeled "M", Figs. 3.14 and 3.15) of neutral to modestly high P-wave velocities and high S-wave velocities in the shallow mantle (75-85 km depth) of the northernmost Altiplano. This feature extends between 71-71.5°W and 14.5-15.2°S. It is clearly visible as a high velocity anomaly in the S wave cross section in Figure 3.29 immediately below the continental Moho and well above the WBZ.

Southeast of lake Titicaca, I observe a high velocity anomaly (labeled "D", Figs. 3.14-3.19) in the upper mantle. It appears as a normal to moderately high P-wave velocity anomaly under the northern Altiplano, as can be seen in the 75 to 85-km-depth map in Figures 3.14 and 3.15. This anomaly has much stronger positive deviations for the S-wave anomalies and is consistently visible in the 75 to 165-km-depth maps (Figs. 3.14-3.19) for V_S, with smaller deviations at greater depths. This high velocity feature appears to extend east of the northern Altiplano/Eastern Cordillera boundary and appear as a westward dipping feature in the S-wave cross sections of Figures 3.30-3.32. It extends between 16-17°S and 68-69.5°W under the northern Altiplano. East of the Altiplano/Eastern Cordillera boundary, this high velocity feature strikes in the NW-SE direction and extends between 15-18°S and 67-69°W immediately below the high velocity crustal anomaly B (Figs. 3.31 and 3.32). I do not have enough resolution, east of 67°W, to constrain the eastward limit of this high velocity anomaly. The S-wave velocity is characterized by ~3.5% positive deviation corresponding to an absolute velocity of ~4.6 km/s.

5. RESOLUTION ANALYSIS

The concept of resolution in seismic tomography is the capacity of reconstruction of true Earth structure in the calculated image (Inoue et al., 1990). I carry out recovery tests to examine the ability of my tomographic inversion to recover specific structures. I create synthetic anomalies and deviations comparable to my observations and calculate predicted travel times through the model that incorporates these synthetic anomalies. I then invert these travel times using my original velocity model to check if the synthetic anomalies can be recovered.

5.1 Resolution of crustal anomalies

The high P- and S-wave velocity anomaly (anomaly A) in the crust above the flat slab region is relatively well resolved in the center (Test 1 and Test 2), though the eastern and western edges are blurred (Figs 3.35 and 3.36). Amplitudes for V_S are somewhat underestimated whereas amplitudes for V_P are well recovered. This is likely due to better P-wave coverage than S-wave coverage.

The recovery test (Test 3) for the high shear wave velocity anomaly in the crust (anomaly B), southeast of lake Titicaca, is relatively well resolved, though the easternmost edge is blurred, and the northward extent is somewhat underestimated (Figure 3.37). Notably, the high-V_S anomaly is imaged to show some bleed-over effect into the mantle below it, but the bleed-over effect is not significant. This high velocity feature is comparatively less prominent in the P-wave velocity anomaly map. To test whether the observed amplitude in the P-wave anomaly map is real or an artifact of poor resolution, I perform a recovery test (Test 4) for P-wave using the same synthetic anomaly as tested for S-wave. The amplitude of recovered anomaly for P-waves is comparable to the S-wave recovery test (Figure 3.38), indicating that the small amplitude observed in the P-wave anomaly map is not due to limited resolution. The recovery of high-V_P anomaly does not show any noticeable bleed-over effect into the mantle below it.

My recovery tests (Test 5 and Test 6) for the low-V_P and low-V_S anomalies (anomaly AP) under the northern Altiplano crust (Figs. 3.39 and 3.40) show a decent recovery of the negative deviations between 16-18°S and 68-70°W. Although the amplitudes of the recovered anomalies decreases with increasing depth, the overall recovery along cross section KK′ in figures 3.39 and 3.40 suggests that the low average velocity, observed in the northern Altiplano crust, is a well-resolved feature.

5.2 Resolution of mantle anomalies

Figures 3.43 and 3.44 show recovery tests (Test 9 and Test 10) for high-V_P and high-V_S anomalies that roughly coincide with the location of my anomaly C, in the flat slab region. I observe that the general trend of the synthetic anomaly is well recovered at 75 and 85 km depth, with a slight reduction in the amplitude.

The recovery test (Test 11) for the low shear wave velocity anomaly north of the Nazca Ridge, modeled after anomaly L (Figure 3.45) indicates that the negative deviations are recoverable to a very small extent. I test the recoverability of the same synthetic anomaly as used in Test 11 for V_P (Test 12) and observe a significant decrease in the amplitude of the recovered anomaly (Figure 3.46). This significant reduction in the amplitude of the recovered anomaly, for both V_P and V_S is likely related to the limited ray path coverage north of the Nazca Ridge.

The recovery tests (Test 13 and Test 14) for the high-V_P and high-V_S anomaly in the transition region, modeled after anomaly E, is well resolved between 14.5-16°S and 71-72°W (3.47 and 3.48). I observe a good recovery of synthetic anomalies at 105 and 125 km depth, with a significant reduction in amplitude at greater depth (~145 km). Notably, this high velocity anomaly, aligned with the WBZ seismicity, does not show any bleed over effect immediately below the Moho (cross section HH′, Figs 3.48) and suggests that the high velocity feature in the S-wave cross section of Figure 3.29 (labeled "M", immediately sub-Moho) is not an artifact of vertical smearing from anomaly E.

Our recovery tests (Test 15 and Test 16) for the low-V_P and low-V_S anomaly in the upper mantle (labeled "AS"), beneath the northern Altiplano, is relatively well resolved, though the southward extent is somewhat blurred. Amplitudes for both V_P and V_S are approximately recovered at 75 and 85 km depth (Figs 3.49 and 3.50).

For the high-V_S structure (labeled as anomaly "D", Figs. 3.14-3.19) in the upper mantle southeast of the lake Titicaca I perform recovery tests (Test 17) by putting synthetic anomalies, both in the overriding plate and the downgoing slab (Figure 3.51), to check whether this is a true structure or an artifact of vertical smearing. Recovery tests indicate that if high velocities are present in both slab and crust, some streaking into the uppermost mantle will occur (Figs 3.51 and 3.52). However, the amplitude of the high velocity anomaly that is streaked into the mantle is much smaller than what I observe, as is the spatial extent. This suggests that some amount of the high velocities from Anomaly D must be due to structure directly beneath the crust.

I perform recovery tests for anomaly D alone (Figs. 3.53 and 3.54), by inverting for synthetic travel times, with and without random noise (Test 19 and Test 20). These tests show that I am able to recover a high velocity anomaly. However, its westward dip is likely an artifact of streaking. This high velocity feature is less prominent in the P-wave velocity anomaly map. I perform a recovery test (Test 21) by inserting synthetic anomalies of high-V_P that roughly coincides with the location of my anomaly D to check if the observed deviation in the P-wave velocity anomaly map is real. I am able to recover synthetic anomalies at 85, 105 and 125 km depth (Figure 3.55), indicating that the neutral to moderately high-V_P observed, southwest of lake Titicaca, is a real feature.

DISCUSSION

Of the various features that I observed in my tomography results, I focused my discussion on the tectonic implications of crustal and upper mantle anomalies in the Peruvian flat slab region of south-central Peru and northern Altiplano region of southern Peru and northern Bolivia. In this section, I compare my results with previous seismic observations where there is an overlap, and used other geophysical or geological evidence for better interpretation of these observed anomalies. I observed some expected features of the subduction zone environment including high velocity slab and dominant low velocity in the crust and mantle wedge beneath the active volcanic arc in Western Cordillera.

6.1 Peruvian flat slab region

6.1.1 Crust

The high-V_P and high-V_S anomaly (labeled "A", Figs. 3.10-3.13) in the South American crust, above the southernmost portion of the Peruvian flat slab, is likely related to the subduction geometry of the downgoing slab and its effect on the thermal structure of the overlying plate. This region of Peru is characterized by flat slab subduction of the cold oceanic Nazca plate which is believed to be altering the thermal structure of the overriding South American plate due to pinching out of hot asthenospheric wedge (Gutscher et al., 2000; Gutscher & Peacock, 2003). This is supported by low heat flow measurements in central Peru, above the flat slab, with a mean heat flow of ~41mWm^{-2} (Henry & Pollack, 1988). Thermal modelling of the subduction zone by English et al. (2003) also predicts a colder thermal regime, with temperature as low as ~300°C above the flat slab. As suggested earlier, seismic velocities increase with decreasing temperature (Kern, 1978; Abers, 2005; Xu et al., 2008). It is likely that my observed high velocity anomaly is a consequence of low temperature due to local thermal shielding of the South American crust provided by the Peruvian flat slab.

6.1.2 Upper mantle

I observe a high-V_P and high-V_S anomaly (anomaly C) in the upper mantle between the projected ridge track and southern edge of the Peruvian flat slab (Figure 1.13, Chapter 1). This high velocity anomaly is associated with a subhorizontal band of seismicity (Figs. 3.25-3.27). The seismicity in the flat slab is so shallow (immediately sub-Moho) that it is hard to differentiate whether the anomaly C only represents the Peruvian flat slab or some combination of the flat slab and a thin layer of continental mantle lithosphere that may be above the slab and below the mantle. If there is any mantle lithosphere above the flat slab, it is likely cold and seismically indistinguishable from the underlying slab. In the south, anomaly C laterally merges with a dipping high velocity anomaly (anomaly E), which follows the slab contour of Cahill & Isacks (1992) in the transition region. Anomaly E is closely aligned with local WBZ seismicity (Figs 3.28-3.32) is most likely the subducting Nazca slab.

North of the Nazca Ridge, I observed a low-V_S anomaly in the upper mantle (labeled "L", Figure 3.14), in the region of the previously proposed flat slab (Cahill and Isacks, 1992, Kirby et al., 1995; Hayes et al., 2012). Recent results of Knezevic Antonijevic et al. (2015) also indicate evidence of low surface wave velocity approximately in the same area. Knezevic Antonijevic et al. (2015) interpret this low velocity feature as an indication of hot asthenospheric inflow and a possible tear in the slab, north of the Nazca Ridge. This feature is much less clear in my P-wave velocity anomaly map (Figs 3.14 and 3.15). My recovery tests (Test 11 and Test 12, Figs. 3.45 and 3.46) indicate a significant reduction in the amplitude of the recovered anomaly for both V_P and V_S. To the limited extent that I am able to recover synthetic anomalies, my shear wave velocity is consistent with the surface wave tomography results (Knezevic Antonijevic et al., 2015) and the V_P is neutral to slightly fast but given the lack of resolution, it is hard to interpret whether that is related to the subsurface structure or an artifact of poor resolution.

6.2 Western Cordillera

I observe low-V_P and low-V_S in the crust and upper mantle beneath the active volcanic arc in southern Peru (Figs. 3.10-3.15 and 3.29-3.31). This is consistent with both the tomographic studies of Cunningham et al. (1986), who observe low P wave velocities in the upper mantle below the Western Cordillera in southern Peru, and Myers et al. (1998), who found low-V_P and low-V_S in the upper mantle of the Western Cordillera in Bolivia. Seismic velocities, in general, decreases with increasing temperature and percentage of melt or water fraction within the rock matrix (O'Connell & Budiansky, 1974; Kern, 1978; Sato et al., 1998). My observed low velocity in the mantle wedge of the Western Cordillera could be related to the increased water content due to slab dehydration and formation of hydrous minerals (e.g. Serpentine, Chlorite) in the mantle peridotites or flux melting (Kirby et al., 1996; Giese, 1996; Hacker et al., 2003). Low velocity in the Western Cordillera crust could be either related to the elevated thermal regime or presence of small volume percents of melt. Nakajima et al. (2001) and Matsubara et al. (2009) also obtained similar results for the crust below the volcanic arc, in the northeastern Japan, and attributed it to the presence of small volume percent of melt.

6.3 Eastern Cordillera crust

East of the northern Altiplano/Eastern Cordillera boundary, I observe a high-V_S anomaly (labeled "B", Figs, 3.10-3.13 and 3.31-3.32) in the crust. This is consistent with the previous tomographic observations for the Eastern Cordillera crust (Dorbath & Granet, 1996; Myers et al., 1998, Ward et al., 2013). As suggested by Dorbath & Granet (1996) and Ward et al. (2013), this high velocity feature could be related to the shallow basement rocks (granodioritic batholiths) of the Eastern Cordillera.

6.4 Northern Altiplano

Previous studies, which mainly focus on the central Altiplano plateau in Bolivia and northern Argentina, have pointed out the variable role of lower crustal shortening or delamination of mantle lithosphere or both, on the temporal evolution of the central Andes (Isacks, 1988; Whitman et al., 1992; Wigger et al., 1994; Allmendinger et al., 1997; Myers et al., 1998; Kley et al., 1999; Beck & Zandt, 2002; McQuarrie et al., 2005; Garzione et al., 2006; Hoke & Garzione, 2008; McQuarrie et al., 2008). Despite the many studies carried out in the last two decades, there still exist two opposing models for surface uplift of the Central Andean Plateau (CAP), as briefly outlined in the introduction. The main aim of my study is to understand the current state of the lower crust and upper mantle beneath the northern Altiplano. This will help us understand the possible role of deeper lithospheric processes (i.e. lower crustal thickening, wholesale removal or piecemeal delamination of the mantle lithosphere) in the evolution of the northern Altiplano.

6.4.1 Crust

From 14°S to 18°S, I observe low average velocities (anomaly AP, Figs. 3.29-3.32; $V_P \approx 5.8$ km/s; $V_S \approx 3.4$ km/s) in the northern Altiplano crust, down to the Moho depth of ~65 km (Dorbath et al., 1993; Bishop et al., 2014). The seismic tomography between 16°S and 18°S by Dorbath & Granet (1996) also finds low crustal velocities ($V_P < 6$ km/s) down to about 40km under the northern Altiplano. They attribute it to the more than 10-km-thick sedimentary infill present in this region, with extremely low seismic velocities. My tomographic inversion does not take into account of any correction for the thick sedimentary cover. It is possible that the observed low velocity, in the upper crust (5-25 km depth) of the northern Altiplano basin, is partially related to the low velocity sedimentary rocks.

Low average velocities ($V_P \approx 5.8$ km/s) between 25 and 65 km depth in the lower crust beneath the northern Altiplano are significantly lower than the expected velocity ($V_P > 6.9$ km/s) for the granulite facies, a dominant rock type in the lower continental crust (Rudnick & Fountain, 1995). I do not have enough constraints from previous tomographic studies for the northern Altiplano crust but my results agrees well with other geophysical studies mainly focused on the central Altiplano and immediately south (~20°S) of my study area. Myers et al. (1998), Swenson et al. (2000) and Beck & Zandt (2002) also find low velocity crust in the central Altiplano at ~20°S. Myers et al. (1998) and Beck & Zandt (2002) interpret this low velocity as an indicator of predominantly felsic composition of the central Altiplano crust, even in the lower crust. Swenson et al. (2000) use existing laboratory measurements of P wave velocity for rocks at crustal conditions (Christensen, 1996) and estimate the probable rock composition for the northern and central Altiplano crust to be Granite gneiss or Metagraywacke. They suggest that the lower crust in the Altiplano is felsic quartz rich and either the high-velocity mafic lower crust got removed due to lithospheric delamination or metamorphically transformed to denser phases (eclogite facies) with mantle like seismic velocities. Larger percentages of partial melt in the lower crust could be another possible explanation for the low velocities in the northern Altiplano crust (Schmitz et al., 1996). However, the absence of recent volcanism in the northern and central Altiplano (Trumbull et al., 2006) indicates the absence of widespread melt in the lower crust. Recently, Ward et al. (2013) used ambient noise tomography (ANT) to determine a high-resolution shear wave velocity structure of the Central Andean crust. The crust underneath the Central Andean Plateau (CAP), including the northern Altiplano, appears as a low-V_S region along its entire N-S extent. Ward et al. (2013) interpret this low velocity crust in the northern and southern

Altiplano as being due to felsic compositions and the presence of melt, respectively. I test the reliability of my tomographic results for the low velocity Altiplano crust by introducing a low-V_S and a low-V_P anomaly of similar shape and size as Ward et al. (2013) observed along their northernmost transect (transect AA′, Figure 9, Ward et al. (2013)) and perform recovery test (Test 7 and Test 8, Figs 3.41 and 3.42). Although the shape and size of the recovered anomaly is different from the input model, it compares well with my observed anomaly along one of the similar transects (cross section JJ′, Figure 3.31).

These observations suggest that my observed low velocity in the northern Altiplano crust may be related to the felsic composition of the lower crust. If the crust underneath the northern Altiplano is felsic, then it may be weak at lower crustal P-T conditions (1-1.5 GPa, > 650° C) (Rudnick & Fountain, 1995; Christensen, 1996). The tectonic shortening of weak crust has been proposed as a dominant mechanism of crustal thickening and uplift of the central Altiplano in Bolivia (Swenson et al., 2000, Beck & Zandt, 2002). My results suggest a similar mechanism for the uplift of the northern Altiplano in southern Peru and northern Bolivia.

6.4.2 Upper mantle

The upper mantle beneath the northern Altiplano is very heterogeneous, with significant along strike variations in P- and S-wave velocities. I observed a small anomaly characterized by high-V_P and high-V_S ($V_P \approx 8.2$ km/s; $V_S \approx 4.6$ km/s) beneath the northernmost edge of the northern Altiplano (anomaly M), consistent with mantle lithospheric composition. This high velocity feature is significantly above the WBZ seismicity and immediately sub-Moho (Figure 3.29). My recovery tests (Test 13 and Test 14) for anomaly E (cross section HH', Figs 3.47 and 3.48) clearly indicate that this high velocity feature is not an artifact of vertical smearing and may represent the relict continental mantle lithosphere of the overriding South American plate.

Northwest of lake Titicaca, the upper mantle beneath the northern Altiplano is characterized by low-V_P and low-V_S, (Figs. 3.14-3.15 and 3.30) in marked contrast with the high velocity upper mantle (anomaly M) observed beneath the northernmost edge of the northern Altiplano. Previous tomography studies in the central Altiplano also notice complex along strike variations in upper mantle seismic properties (Myers et al., 1998; Whitman et al., 1992) with some parts of the central Altiplano having high velocity mantle lithosphere or eclogitic lower crustal roots present, but low velocity upper mantle consistent with asthenosphere beneath other portions of the central Altiplano. Dorbath et al. (1993) also find low velocity upper mantle beneath the northern Altiplano at ~17.5°S and interpret it as hot mantle or a thinning of the lithosphere. My observed low velocity, northwest of lake Titicaca, is more consistent with the mantle of asthenospheric seismic character and suggests that much of the mantle lithosphere in this small region has been removed (piecemeal delamination).

Southeast of lake Titicaca, I observe a high-V_S anomaly (anomaly D, $V_S \approx 4.6$ km/s) in the upper mantle beneath the northern Altiplano that also extends beyond the Altiplano/Eastern Cordillera boundary in the east. East of the Altiplano, my results compare well with those of Dorbath et al. (1993). Dorbath et al. (1993) find high P-wave velocities in the upper mantle east of the Altiplano/Eastern Cordillera boundary and interpret them as underthrust Brazilian craton from the east. The western half of anomaly D, below the northern Altiplano, is consistent with either the mantle of continental lithosphere or cratonic lithosphere. Previous studies (Myer et al., 1998; Polet et al., 2000; Watts et al., 1995;

Aitcheson et al., 1995) did not see evidence of a high velocity anomaly in the upper mantle east of the Altiplano/Eastern Cordillera. From my current observation, I can conclude that some form of mantle lithosphere exists beneath the northern Altiplano but it is not possible for me to discriminate between underthrust cratonic and in situ continental lithosphere.

Given that some mantle lithosphere is still present beneath the Northern Altiplano, it is unlikely that the current mantle lithosphere under the northern Altiplano has experienced pervasive and large-scale delamination or wholesale removal. This finding is particularly important in the context of the ongoing debate on the evolution of the Altiplano plateau, as mentioned in the introduction. It indicates that the idea of rapid surface uplift (Garzione et al., 2006; Ghosh et al., 2006; Molnar & Garzione, 2007; Garzione et al., 2008; Hoke & Garzione, 2008), which requires the wholesale removal of the mantle lithosphere is unlikely for the evolution of the northern Altiplano. My tomography results for the lower crust and upper mantle beneath the northern Altiplano are in better agreement with the slow and steady uplift model (Isacks, 1988; Allmendinger et al., 1997; Jordan et al., 1997; McQuarrie et al., 2005; Hoke & Lamb, 2007; Ehlers & Poulsen, 2009), which suggests that shortening of weak crust and localized removal of excess mantle through the small-scale lithospheric delamination, is the main cause of the Altiplano uplift.

7. CONCLUSION

I have used P- and S-wave travel time delays from locally recorded earthquakes to estimate the crustal and upper mantle velocity structure in the Peruvian flat slab region in south central Peru and in the northern Altiplano region of southern Peru and northern Bolivia. My conclusions from the current tomography results are as follows:

1) The high velocity crust above the southern margin of the Peruvian flat slab is related to the thermal shielding of the South American crust from slab flattening and the pinching out of the asthenospheric wedge (Gutscher et al., 2000; English et al., 2003).
2) The low average velocity in the northern Altiplano crust, even in the lower crust, is similar to the central Altiplano, further south in central Bolivia. This is consistent with felsic quartz rich lower crust as opposed to high velocity granulite facies. This felsic crust is likely weak at lower crustal P-T conditions and may contribute in the slow and steady uplift of the northern Altiplano via lower crustal shortening and thickening.
3) The upper mantle under the northern Altiplano is heterogeneous and suggests piecemeal delamination of the mantle lithosphere as opposed to wholesale removal. This observation favors the slow and steady uplift model (Isacks, 1988; Allmendinger et al., 1997; McQuarrie et al., 2005;), which suggests localized removal of excess mantle due to prolonged shortening and thickening.

8. ACKNOWLEDGMENTS

I am thankful to IRIS and personnel at the PASSCAL Instrument Center for their help and support throughout the CAUGHT and PULSE deployment. The seismic instruments were provided by UNC-Chapel Hill, Yale University, and the Incorporated Research Institutions for Seismology (IRIS) through the PASSCAL Instrument Center. I sincerely thank Dr. Hernando Tavera, Director, and C. Condori Quispe, of the Instituto Geofísico del Perú, Lima, Peru, and Dr. Estela Minaya of the San Calixto Observatory in Bolivia and for their help in deployment and demobilization efforts, as well as Mike Fort (PASSCAL) for his invaluable assistance in the field. The CAUGHT experiment was supported by NSF grants

EAR-0908777 (Lara Wagner) and EAR-0907880 (Susan Beck). The PULSE experiment was funded by NSF grants EAR-0944184 (Lara Wagner), EAR-0943991 (Susan Beck), and EAR-0943962 (Maureen Long). Special thanks to C. Berk Biryol and S. Knezevic Antonijevic for helpful discussions. Maps were created using the Generic Mapping Tools (GMT) software (Wessel & Smith, 1991).

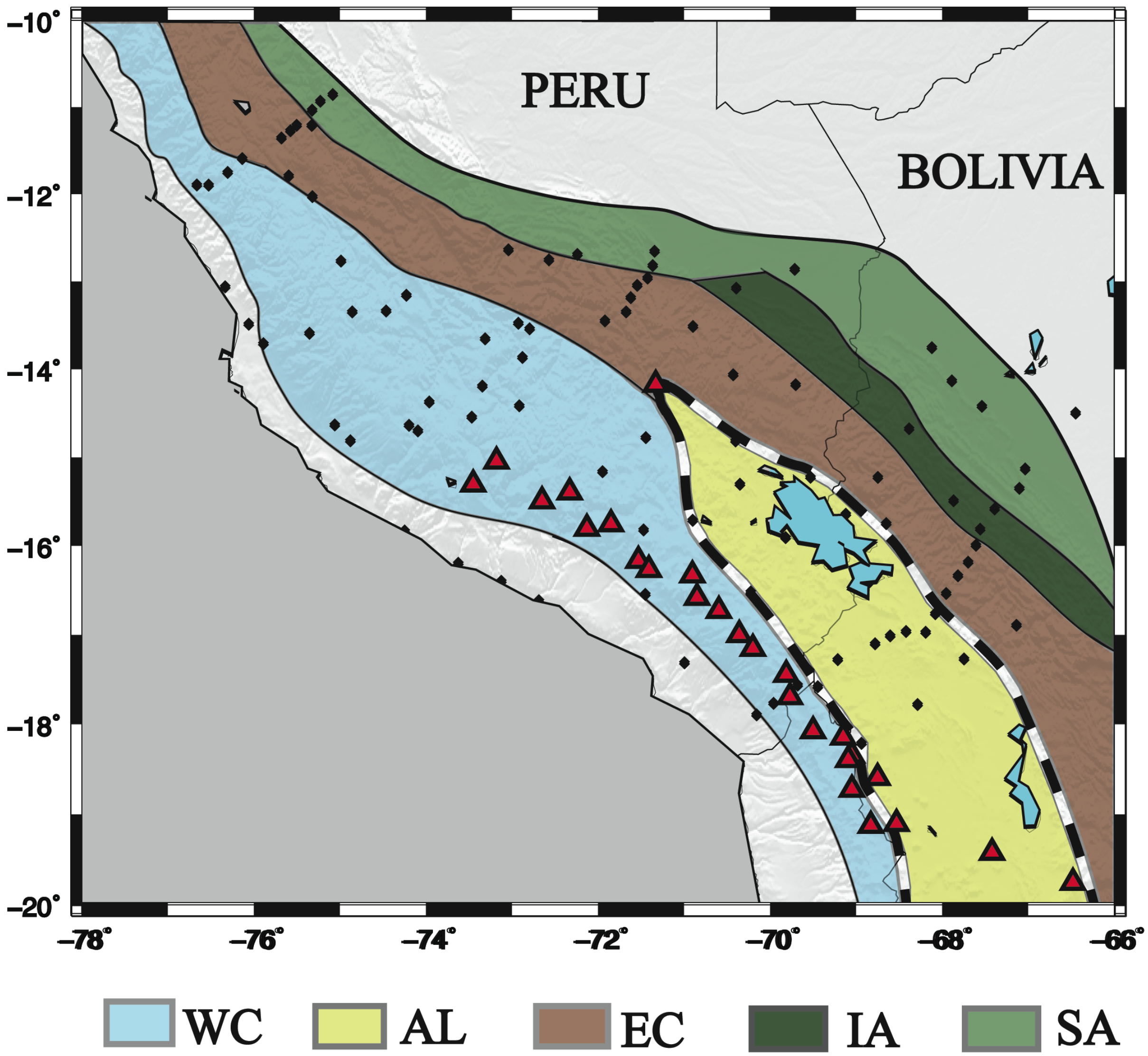

Figure 3.1- Geologic map showing major physiographic divisons in my study area (after Kley & Monaldi, 1999; Oncken et al., 2006; McQuarrie et al., 2008; Barnes & Ehlers, 2009): the Western Cordillera (WC), the Altiplano (AL), the Eastern Cordillera (EC), the Interandean zone, and the Subandes (SA). Black diamonds are locations of the broadband stations used in this study. Holocene volcanic activity (red triangles) from Siebert & Simkin (2002).

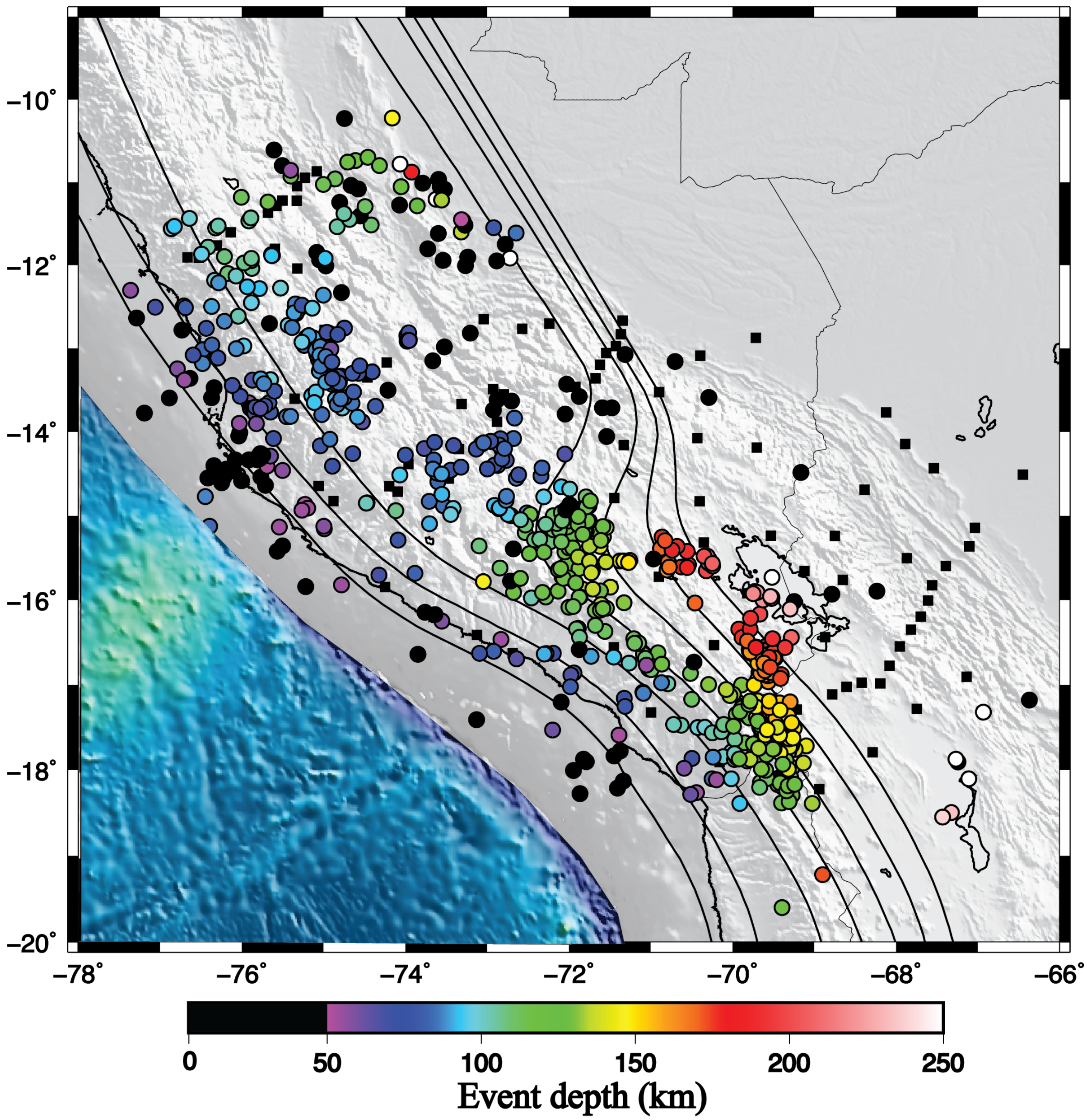

Figure 3.2- Map showing the final locations of 712 events relocated with the inversion, after second iteration. The hypocenters are color coded by depth.

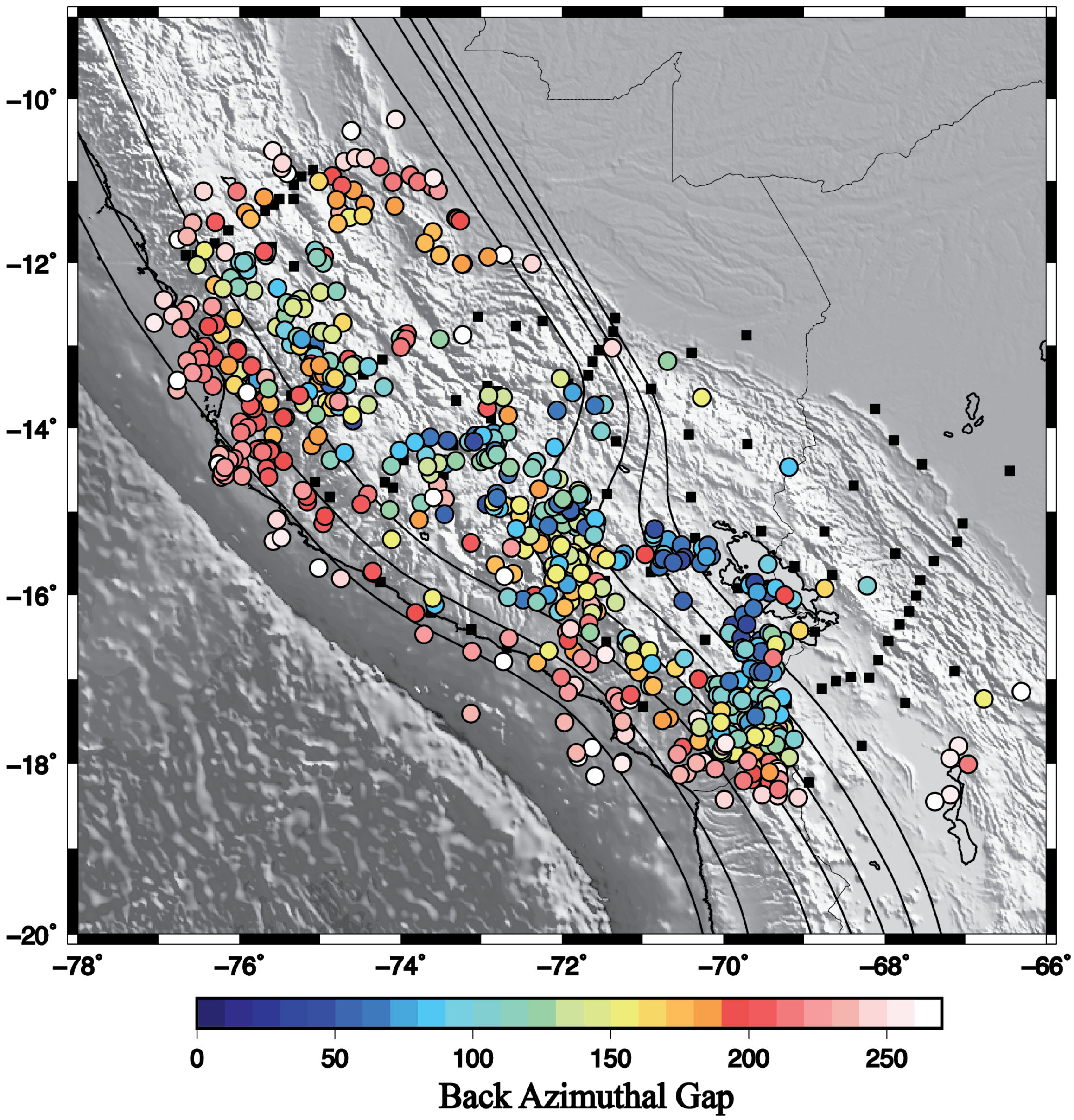

Figure 3.3- Map showing the final locations of 712 events used in this study. The hypocenters are color coded by azimuthal gap.

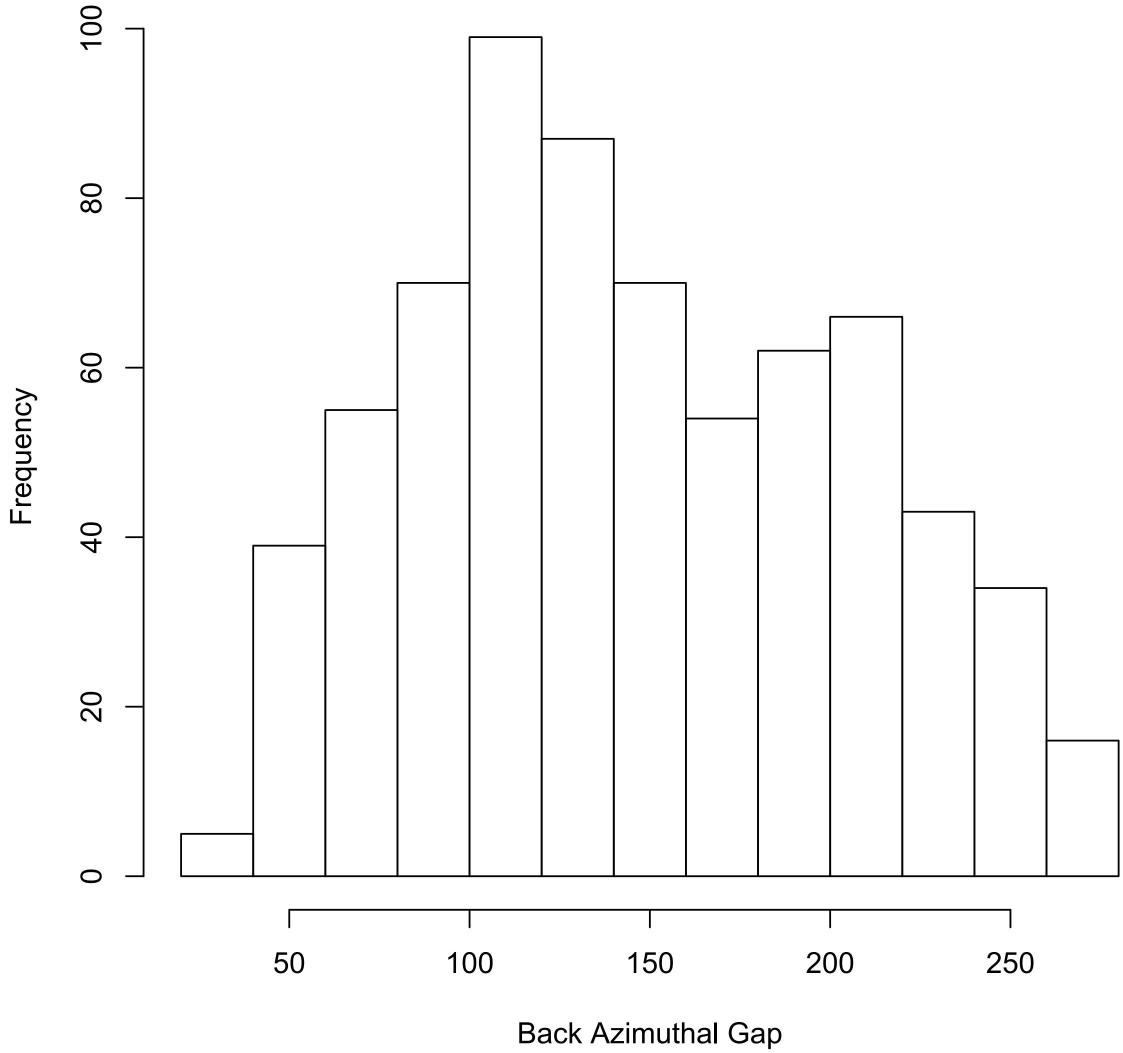

Figure 3.4- Histogram of azimuthal gaps for events used in this study. I used all events with azimuthal gap less than qual to 270°.

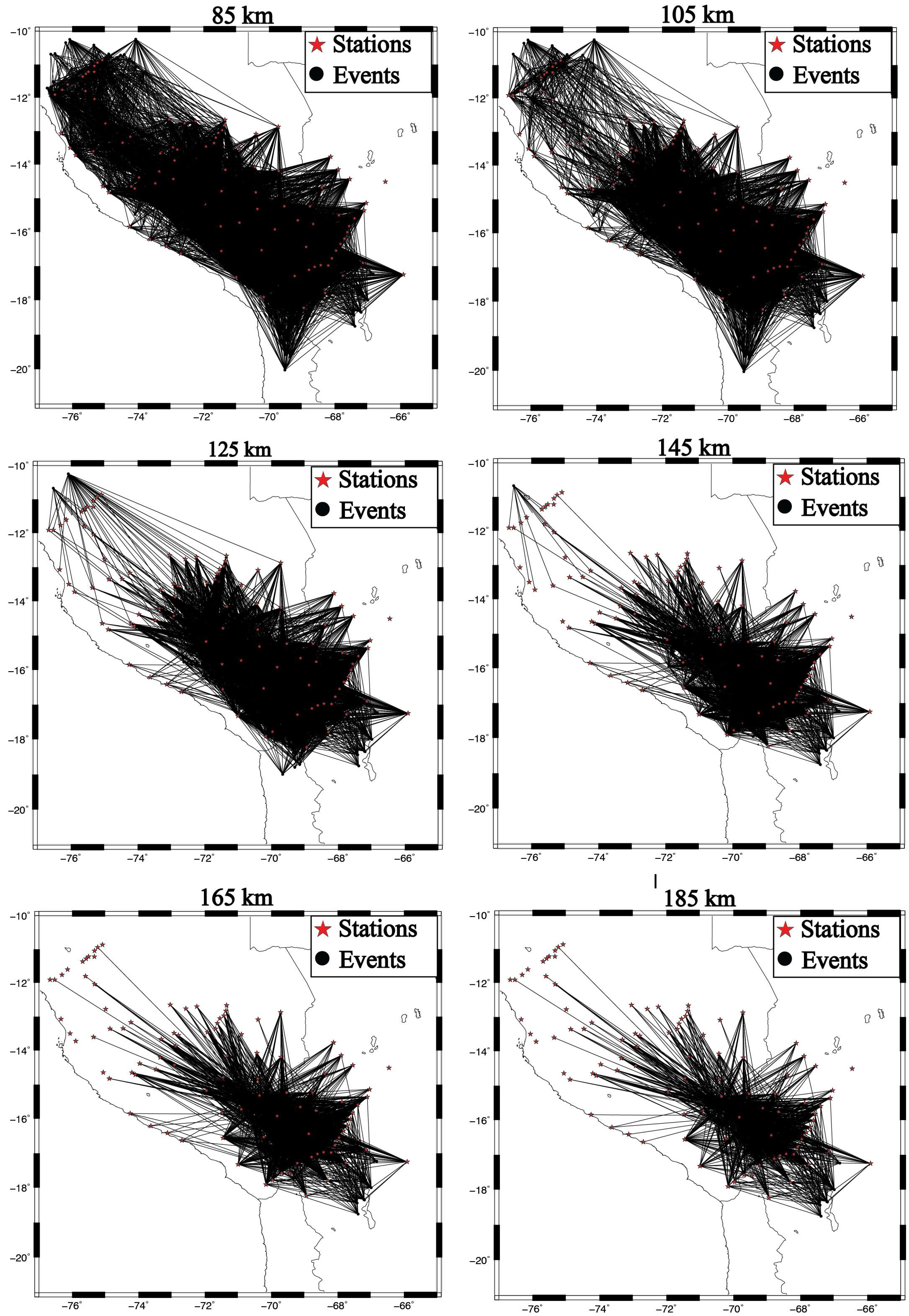

Figure 3.5- Ray path coverage of P wave for events at different depth slices in my study area. Ray paths are estimated as straight line distance between the seismic stations (red stars) and events (black dots).

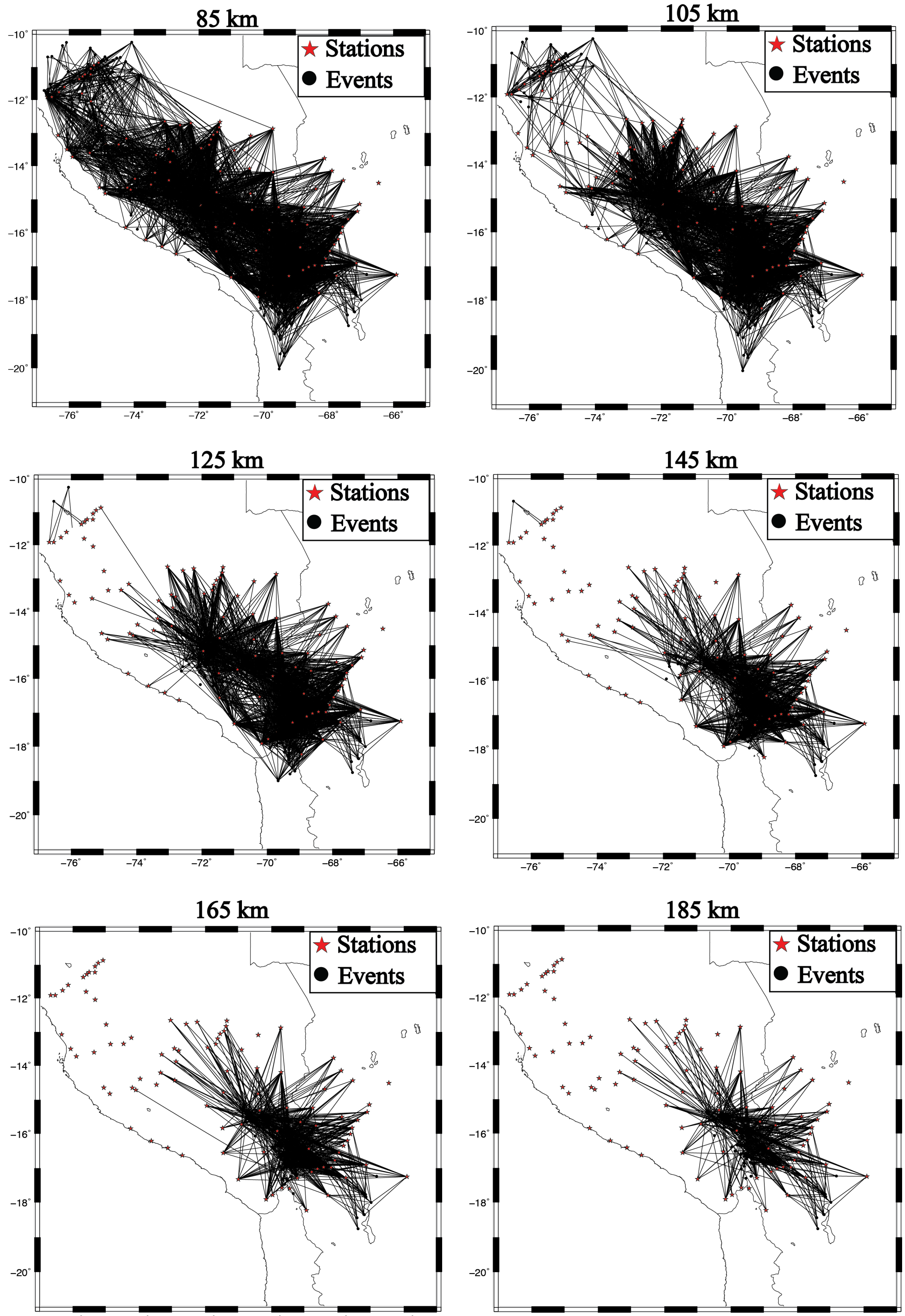

Figure 3.6- Ray path coverage of S wave for events at different depth slices in my study area. Ray paths are estimated as straight line distance between the seismic stations (red stars) and events (black dots).

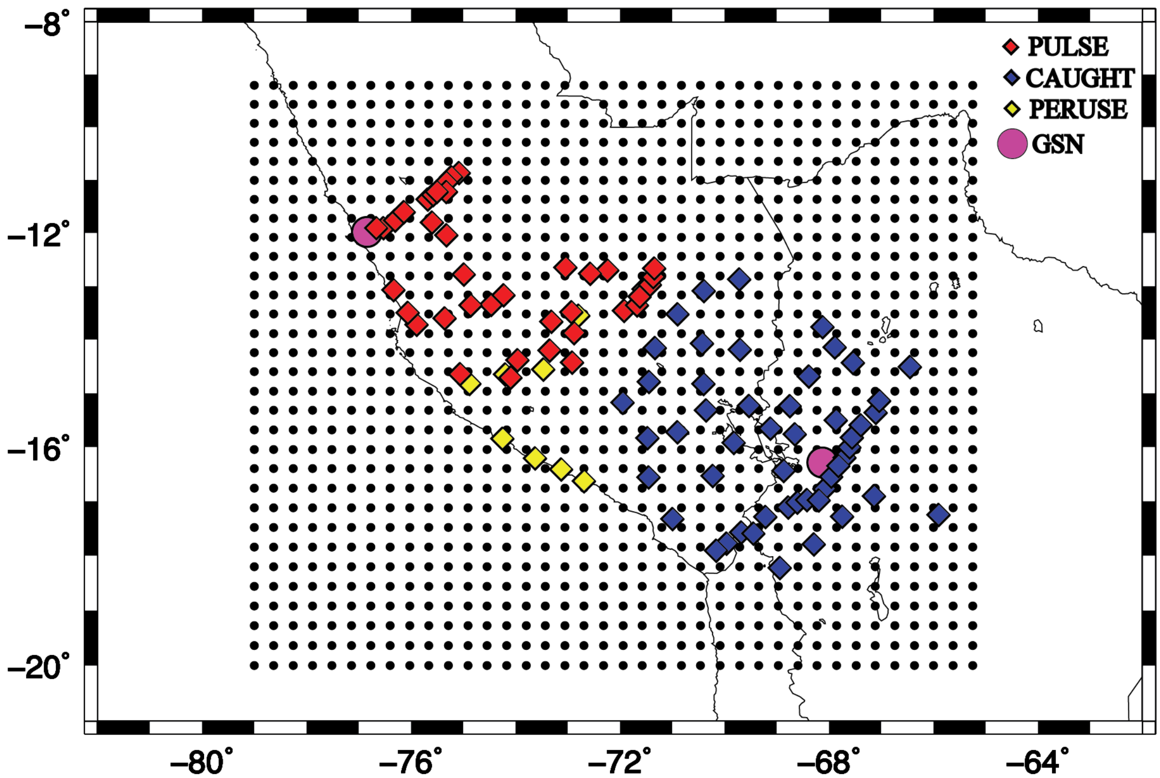

Figure 3.7- Map of velocity grid nodes and seismic stations used in the inversion

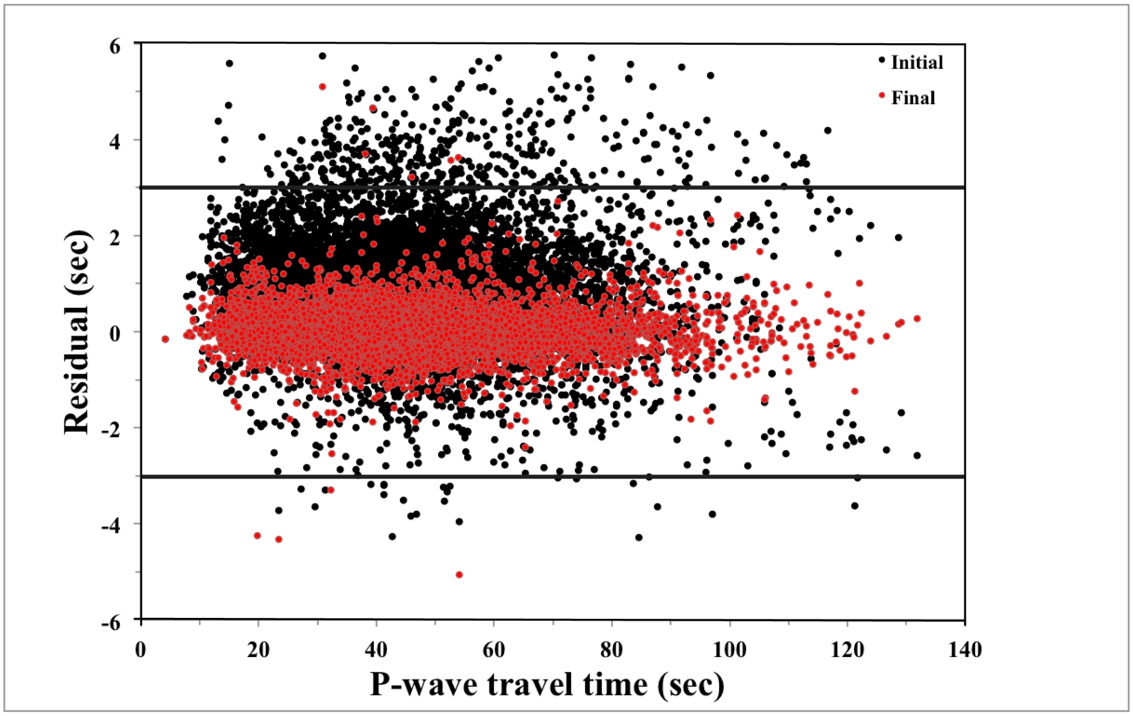

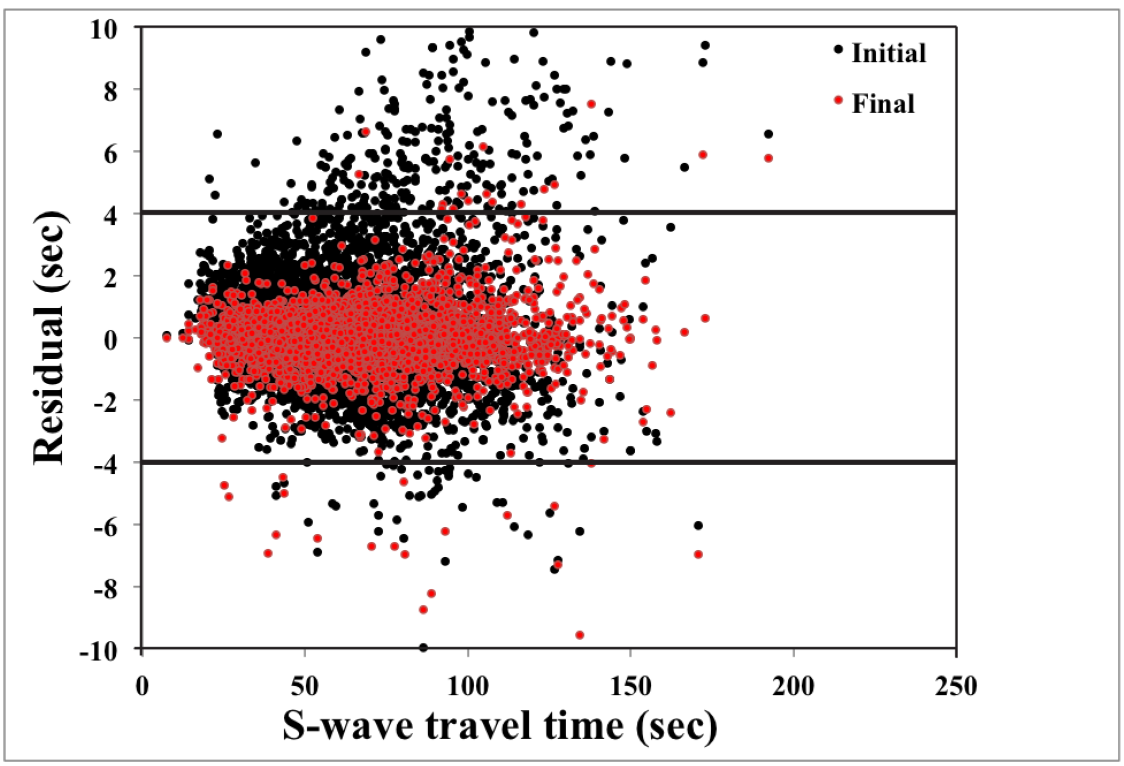

Figure 3.8- Scatter plot of residuals versus travel time for all events. Residuals before the inversion are shown in black for P (top) and S (bottom). Final residuals after second inversion are overlain in red. Solid black lines indicate residual cutoff of 3 and 4 seconds for P and S times respectively.

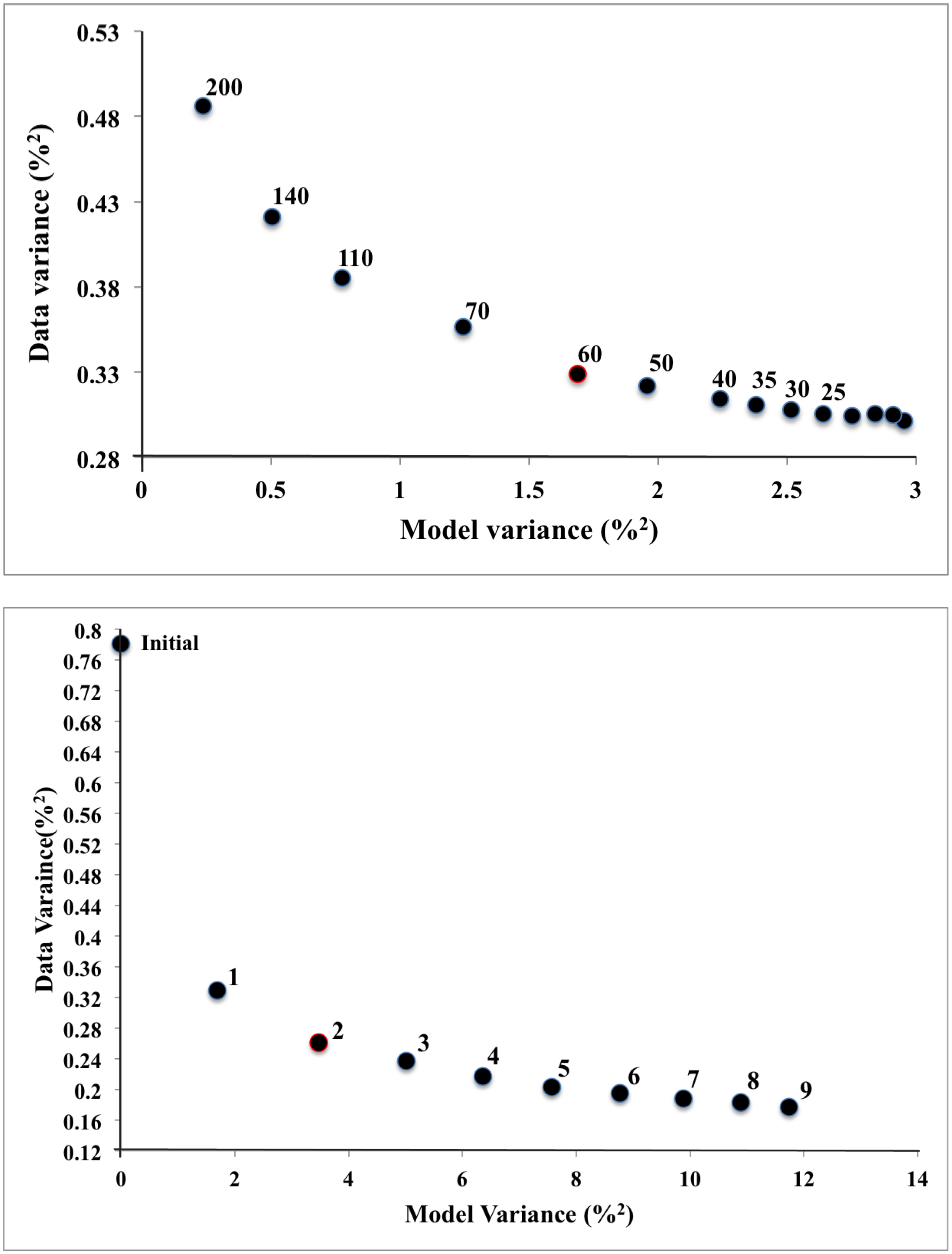

Figure 3.9- Model versus data variance plot for different damping parameters (top) and different numbers of iterations (bottom). Circles with red edges indicate optimal damping value and the ideal number of iterations respectively. I choose to use two iterations with damping equal to 60 to effectively minimize variance in both data and model.

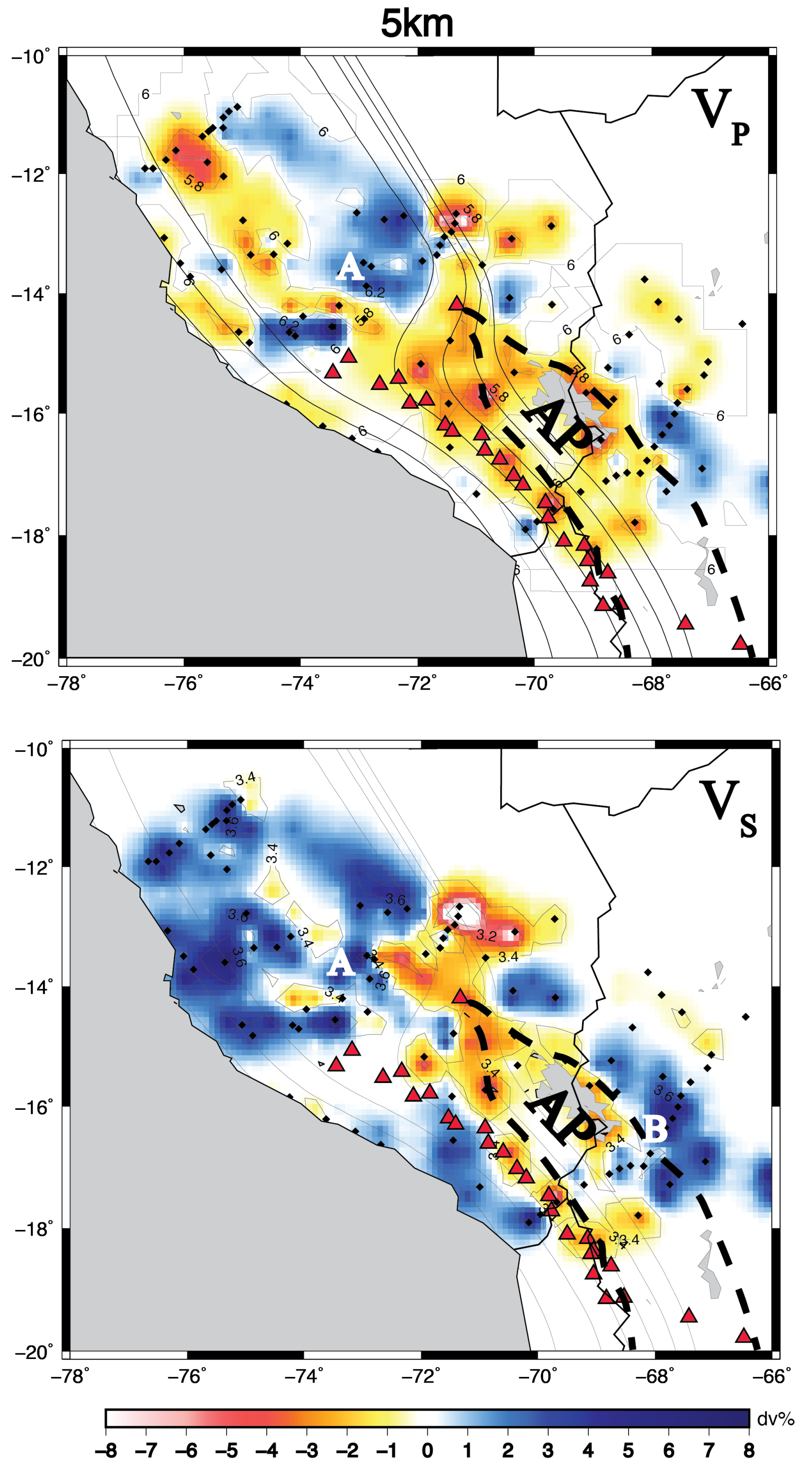

Figure 3.10- Map view results of tomographic inversion for V_P (top) and V_S (bottom) at 5 km depth. Anomalies A, B, and AP are labeled. Dashed line is approximate outline of the northern Altiplano (de Silva, 1989, Ward et al., 2013). Slab contours (thick black lines) are from Cahill and Isacks (1992), black diamonds are seismic stations, and red triangles are active volcanoes. Warm (reddish) and cool (bluish) colors are percent velocity deviations in V_P and V_S. Numbers on the contours indicate absolute velocity in km/s. V_P and V_S contours are in 0.2 km/s increments.

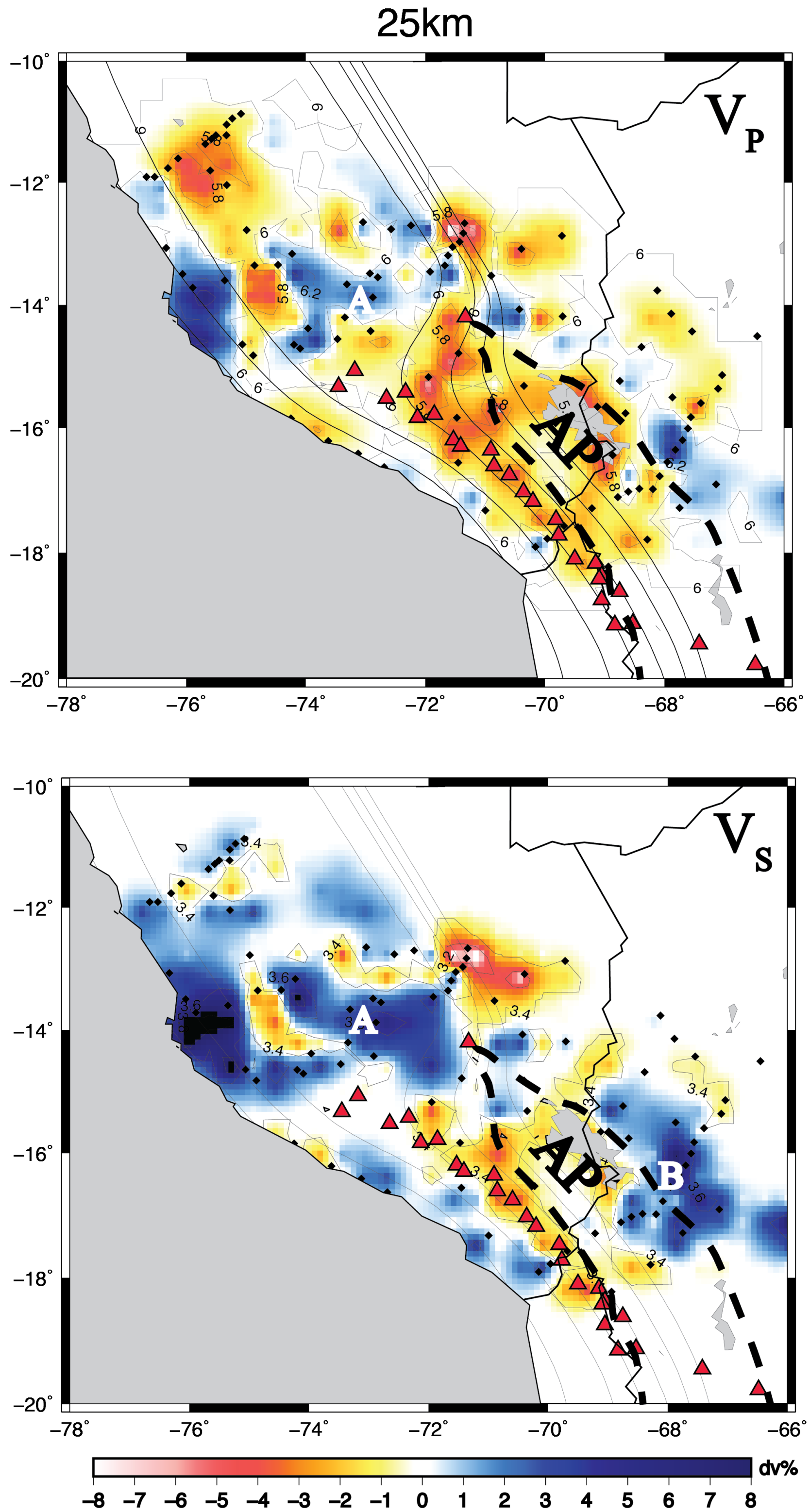

Figure 3.11- Map view results of tomographic inversion for V_P (top) and V_S (bottom) at 25 km depth. Anomalies A, B, and AP are labeled. Warm (reddish) and cool (bluish) colors are percent velocity deviations in V_P and V_S. Numbers on the contours indicate absolute velocity in km/s. V_P and V_S contours are in 0.2 km/s increments. Other symbols as in Figure 3.10.

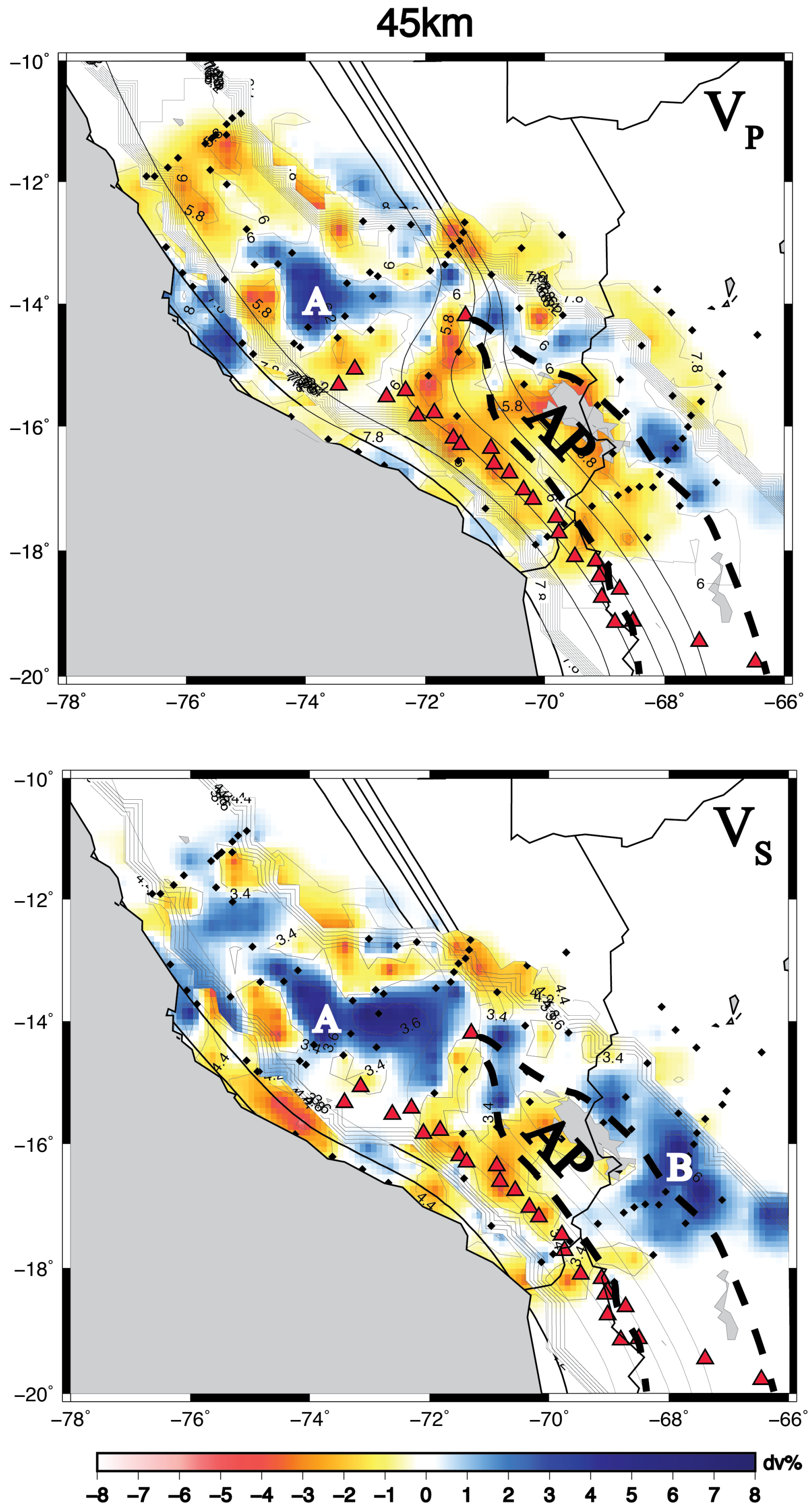

Figure 3.12- Map view results of tomographic inversion for V_P (top) and V_S (bottom) at 45 km depth. Anomalies A, B, and AP are labeled. Warm (reddish) and cool (bluish) colors are percent velocity deviations in V_P and V_S. Numbers on the contours indicate absolute velocity in km/s. V_P and V_S contours are in 0.2 km/s increments. Other symbols as in Figure 3.10.

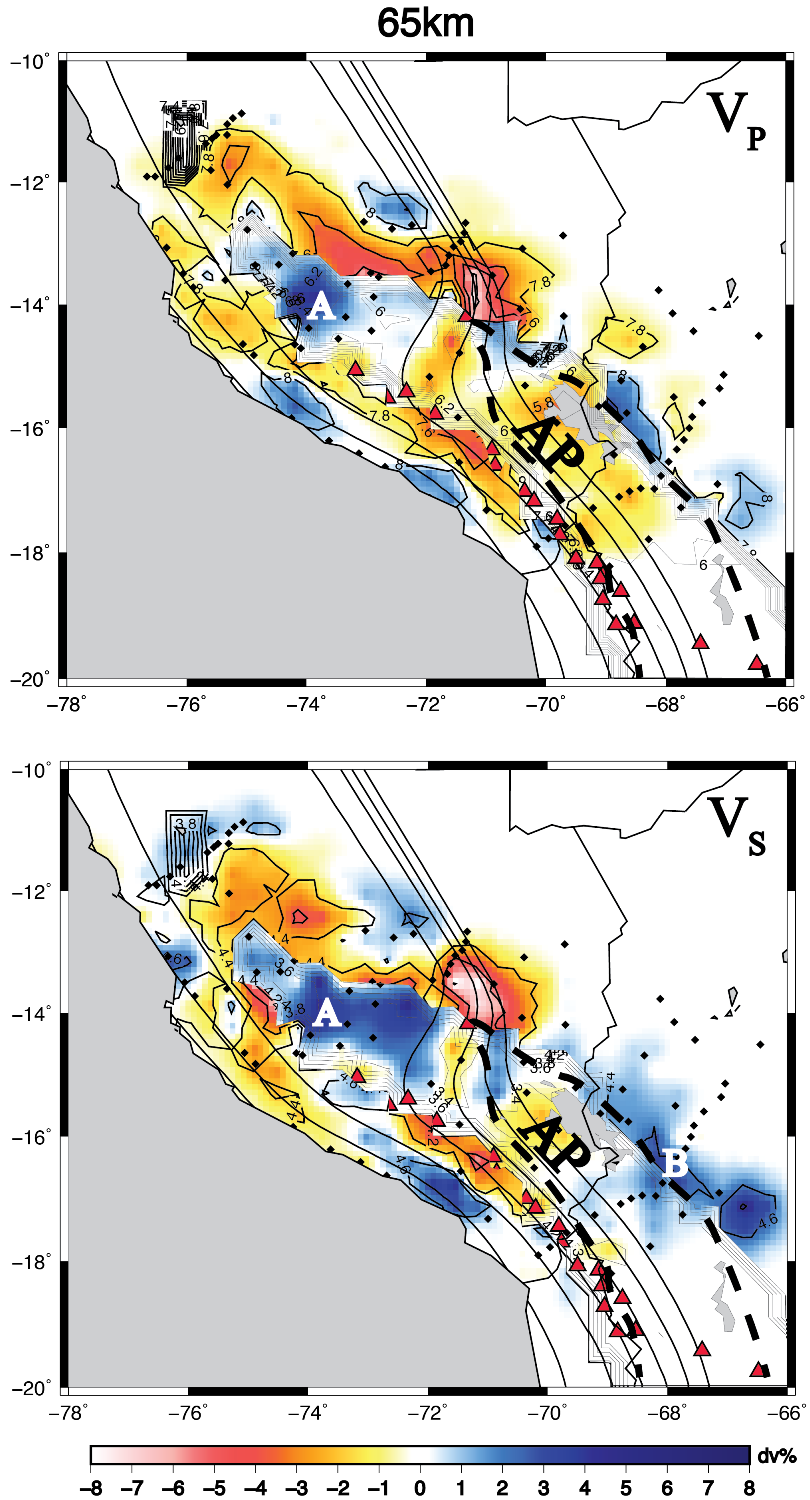

Figure 3.13- Map view results of tomographic inversion for V_P (top) and V_S (bottom) at 65 km depth. Anomalies A, B, and AP are labeled. Warm (reddish) and cool (bluish) colors are percent velocity deviations in V_P and V_S. Numbers on the contours indicate absolute velocity in km/s. V_P and V_S contours are in 0.2 km/s increments. The multiple close contours show the location of the Moho. Other symbols as in Figure 3.10.

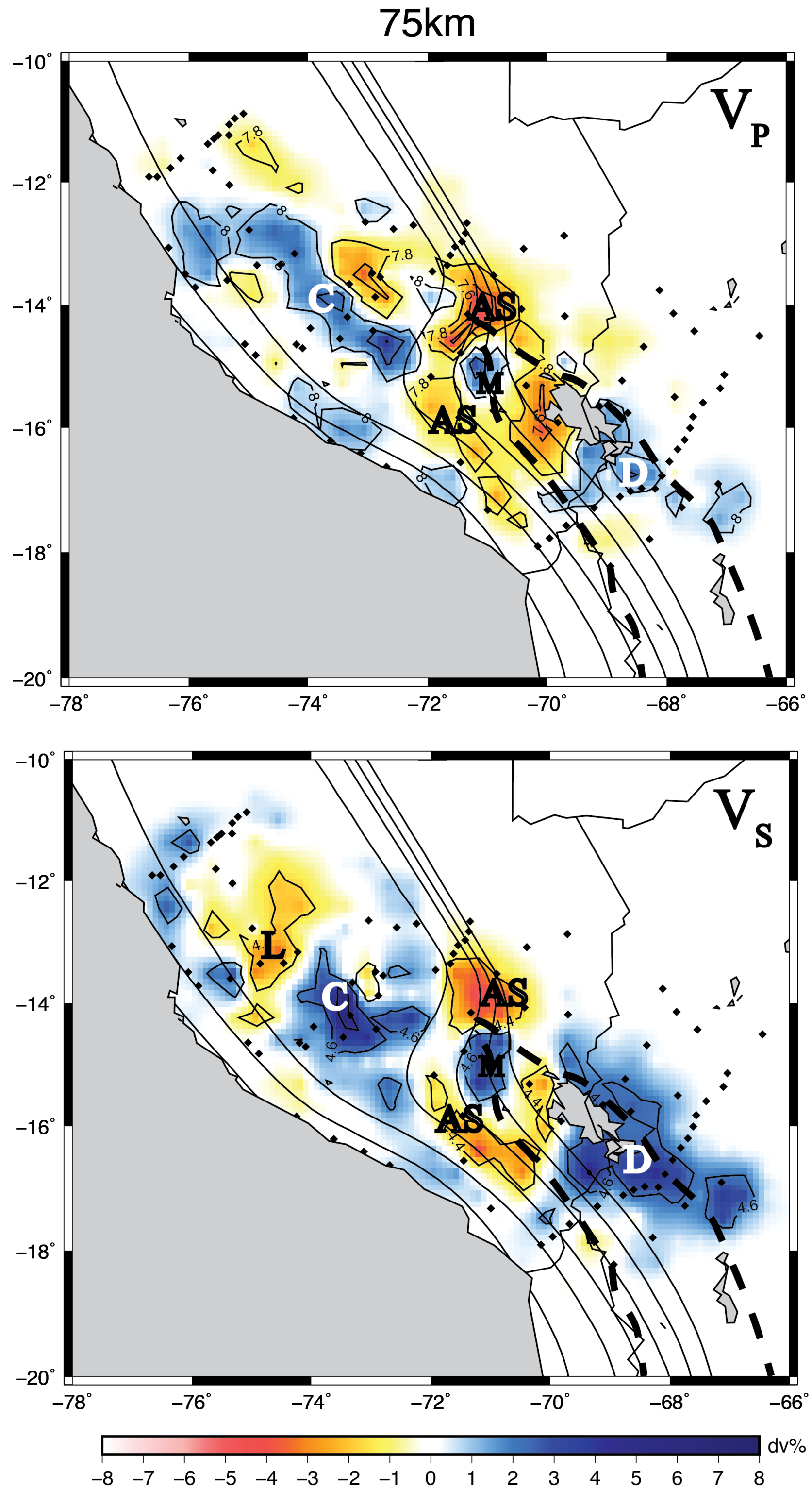

Figure 3.14- Map view results of tomographic inversion for V_P (top) and V_S (bottom) at 75 km depth. Anomalies C, D, L, AS, and M are labeled. Warm (reddish) and cool (bluish) colors are percent velocity deviations in V_P and V_S. Numbers on the contours indicate absolute velocity in km/s. V_P and V_S contours are in 0.2 km/s increments. Other symbols as in Figure 3.10.

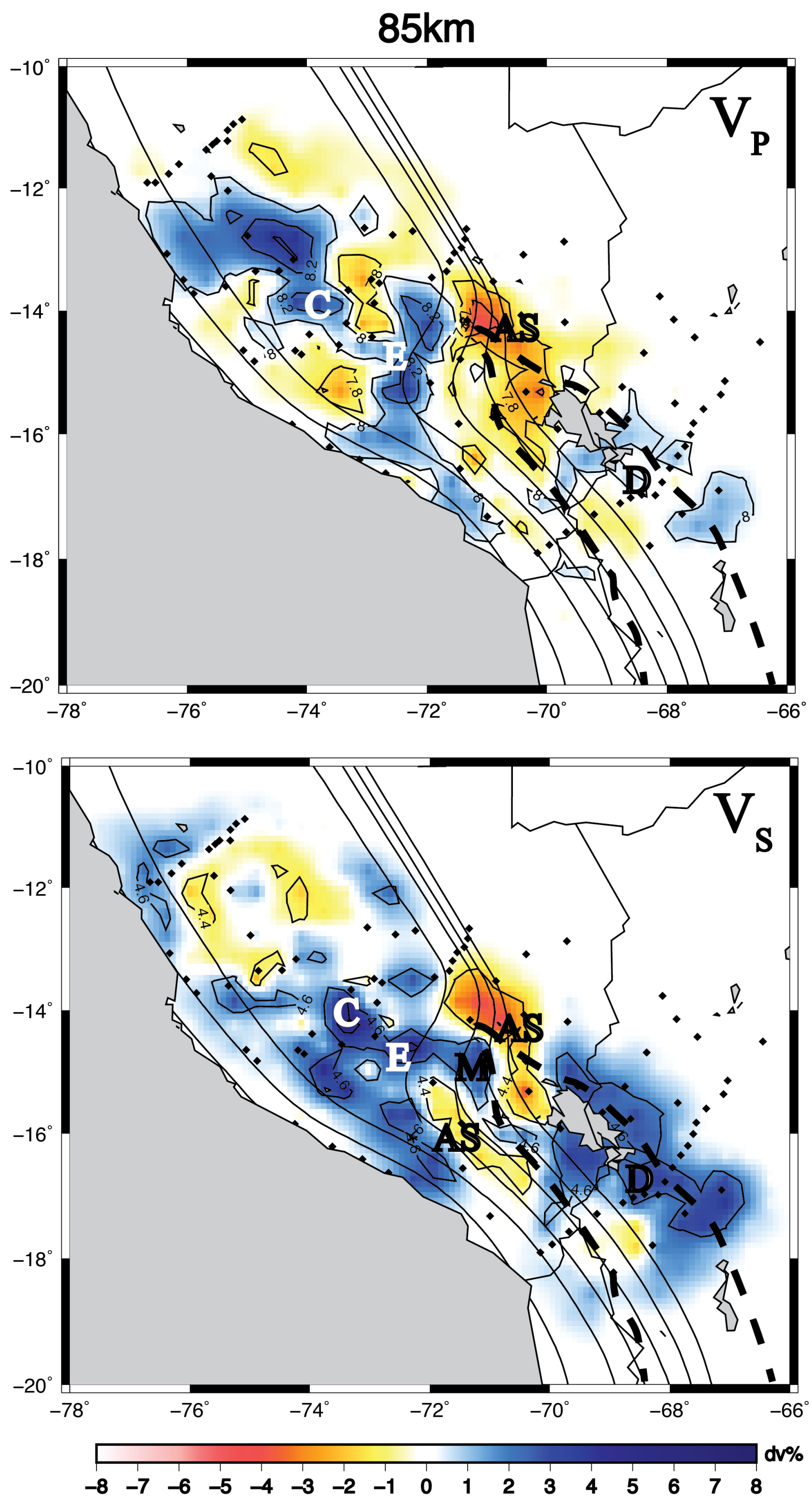

Figure 3.15- Map view results of tomographic inversion for V_P (top) and V_S (bottom) at 85 km depth. Anomalies C, D, E, AS and M are labeled. Warm (reddish) and cool (bluish) colors are percent velocity deviations in V_P and V_S. Numbers on the contours indicate absolute velocity in km/s. V_P and V_S contours are in 0.2 km/s increments. Other symbols as in Figure 3.10.

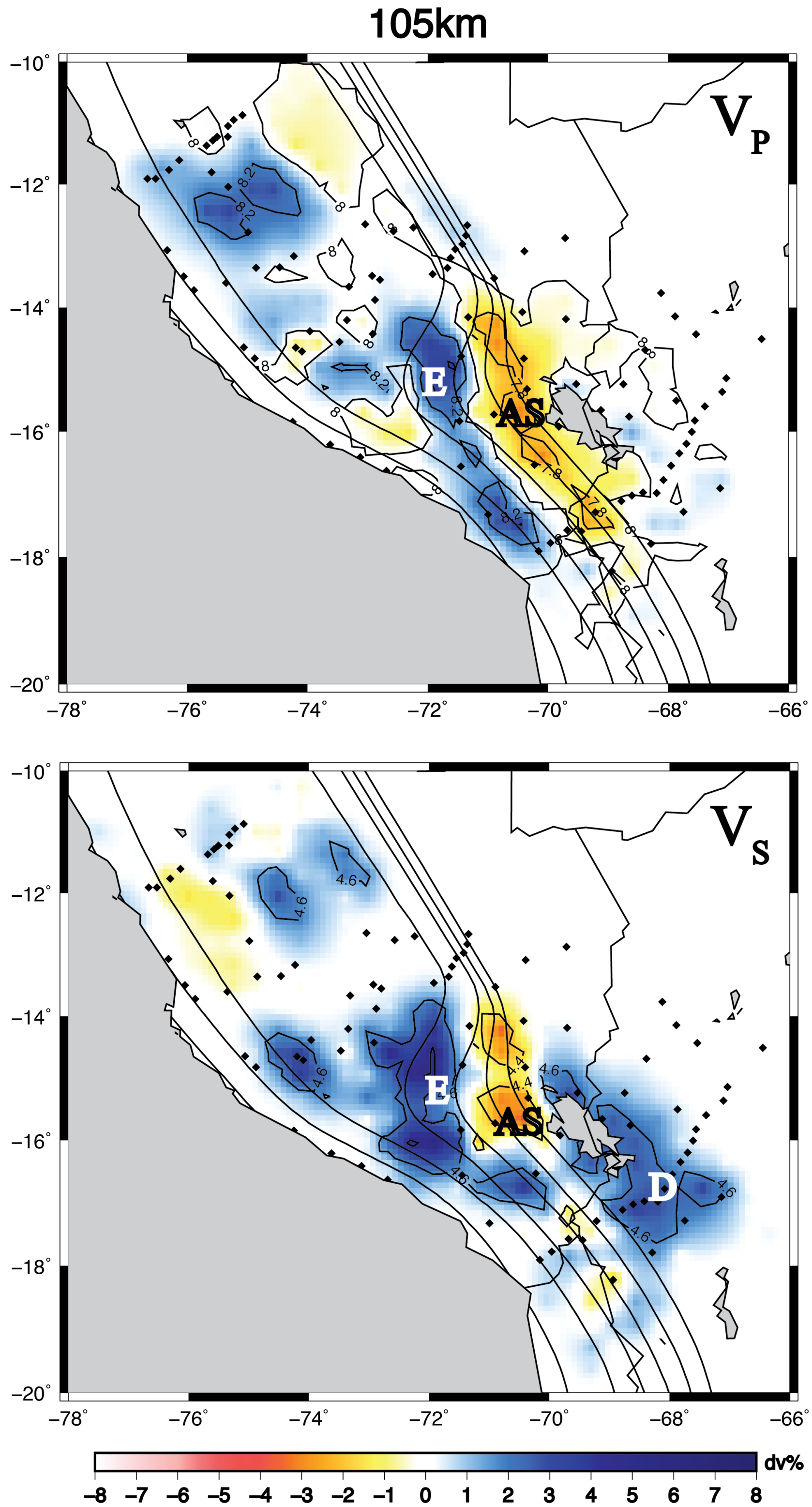

Figure 3.16- Map view results of tomographic inversion for V_P (top) and V_S (bottom) at 105 km depth. Anomalies D, E, and AS are labeled. Warm (reddish) and cool (bluish) colors are percent velocity deviations in V_P and V_S. Numbers on the contours indicate absolute velocity in km/s. V_P and V_S contours are in 0.2 km/s increments. Other symbols as in Figure 3.10.

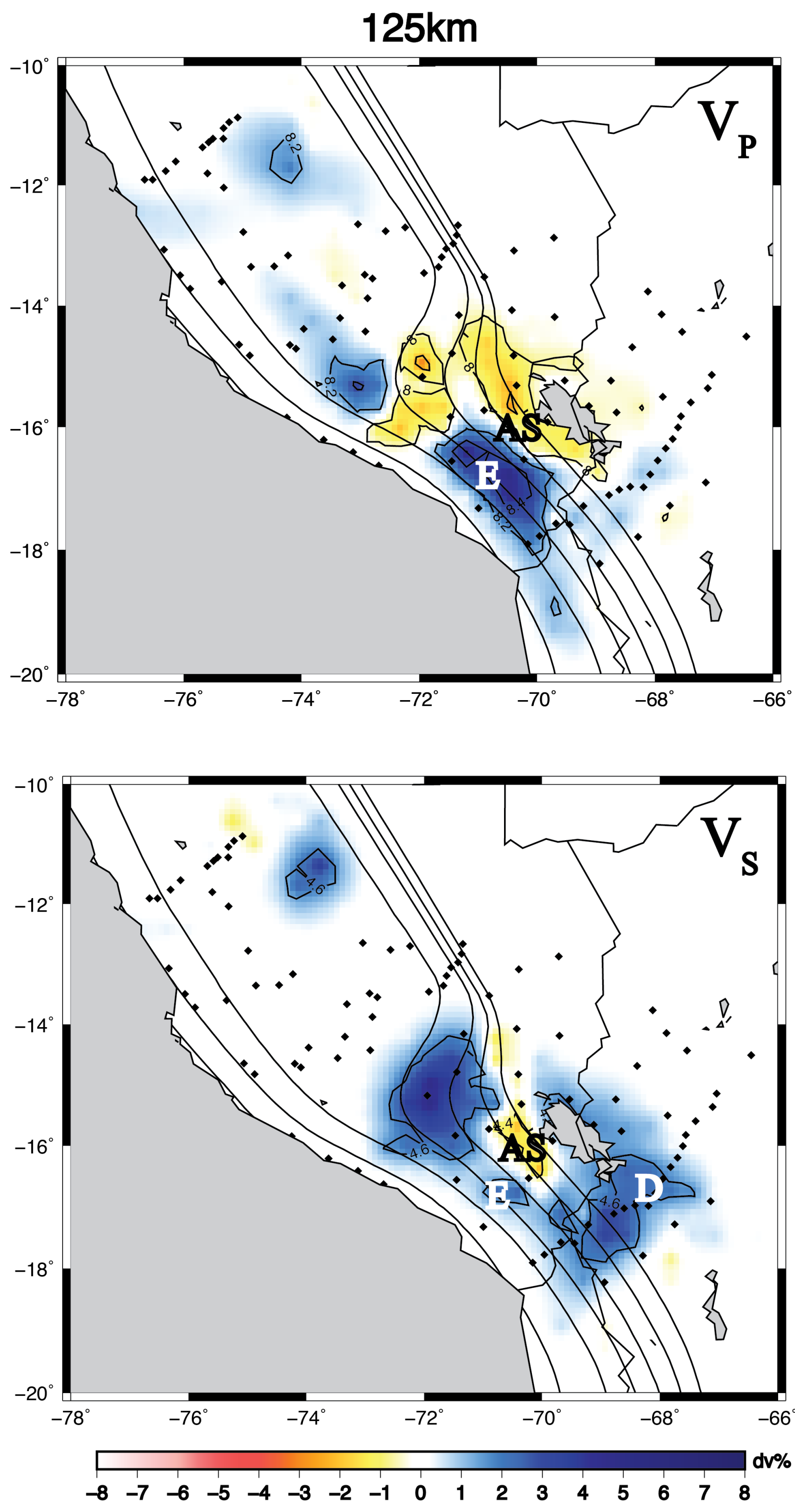

Figure 3.17- Map view results of tomographic inversion for V_P (top) and V_S (bottom) at 125 km depth. Anomalies D, E, and AS are labeled. Warm (reddish) and cool (bluish) colors are percent velocity deviations in V_P and V_S. Numbers on the contours indicate absolute velocity in km/s. V_P and V_S contours are in 0.2 km/s increments. Other symbols as in Figure 10.

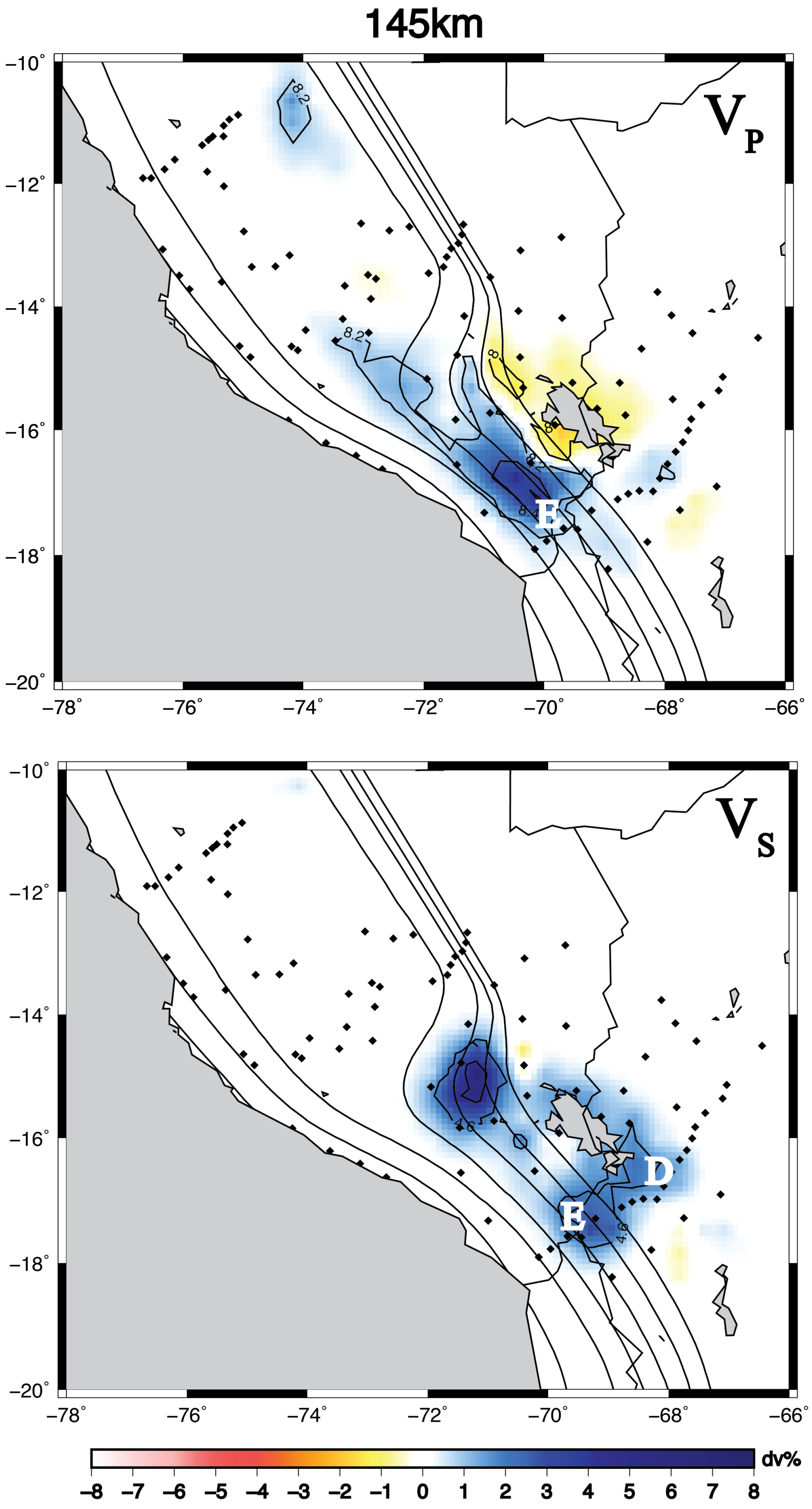

Figure 3.18- Map view results of tomographic inversion for V_P (top) and V_S (bottom) at 145 km depth. Anomalies D and E are labeled. Warm (reddish) and cool (bluish) colors are percent velocity deviations in V_P and V_S. Numbers on the contours indicate absolute velocity in km/s. V_P and V_S contours are in 0.2 km/s increments. Other symbols as in Figure 3.10.

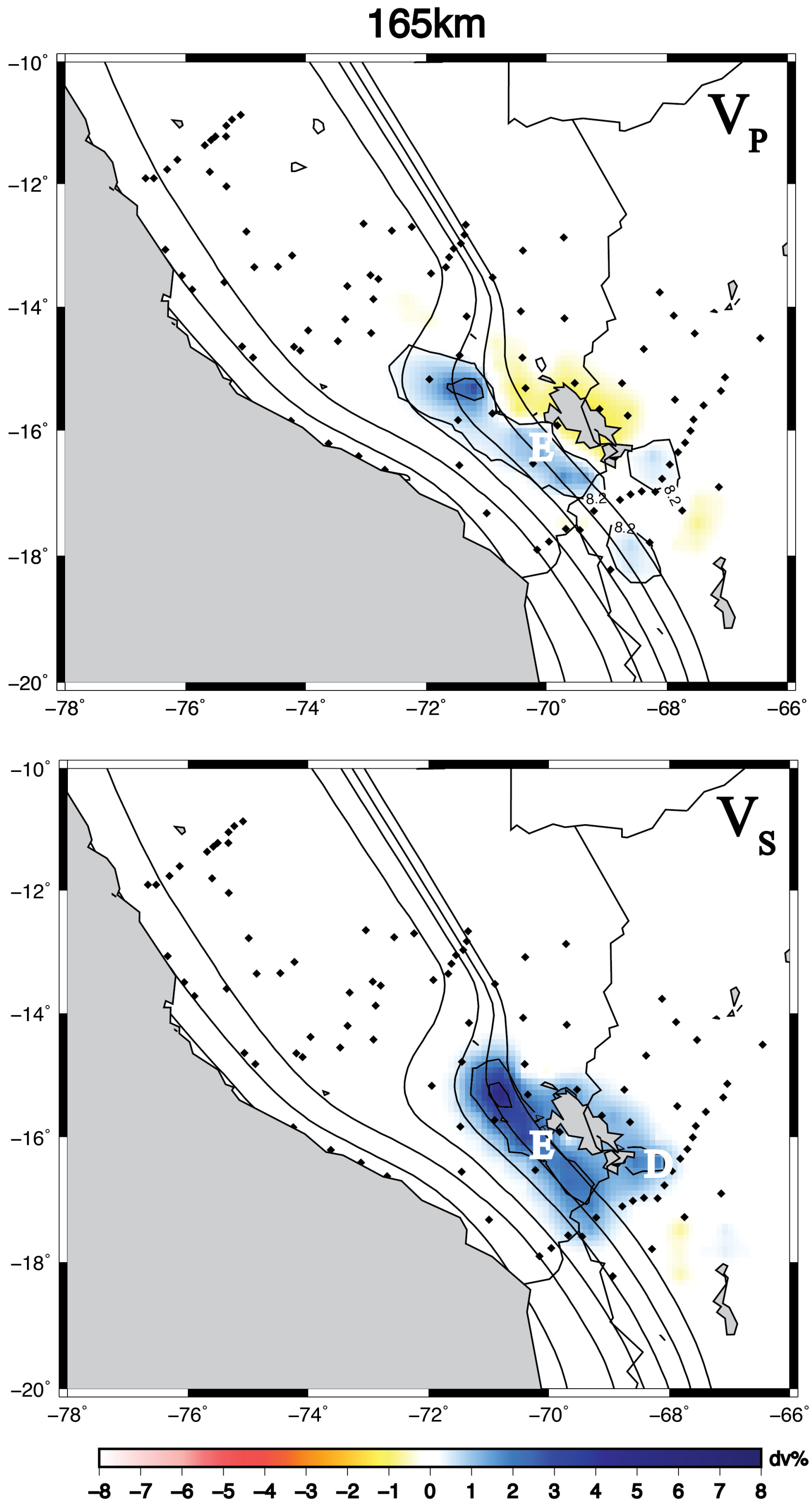

Figure 3.19- Map view results of tomographic inversion for V_P (top) and V_S (bottom) at 165 km depth. Anomalies D and E are labeled. Warm (reddish) and cool (bluish) colors are percent velocity deviations in V_P and V_S. Numbers on the contours indicate absolute velocity in km/s. V_P and V_S contours are in 0.2 km/s increments. Other symbols as in Figure 10.

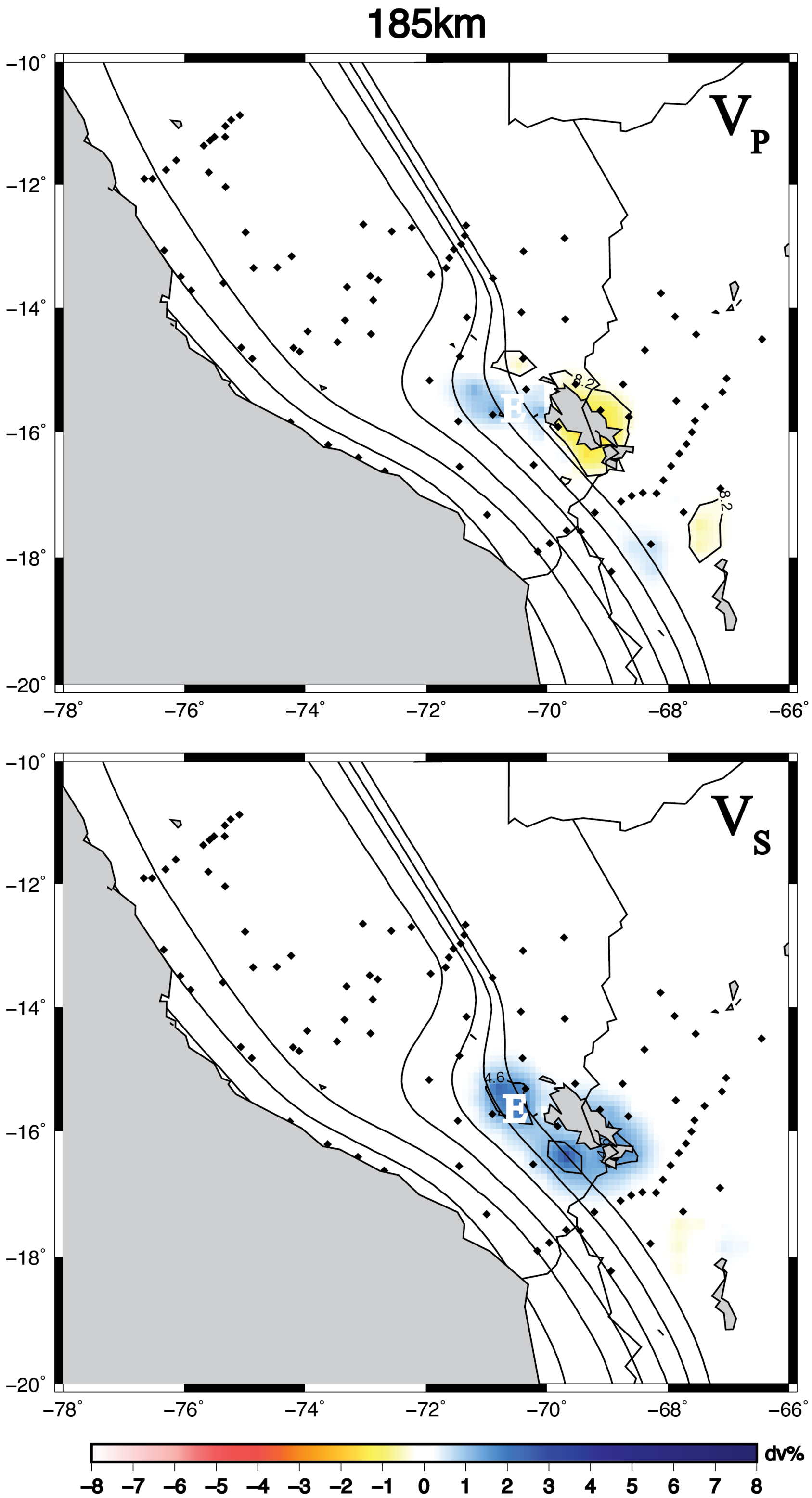

Figure 3.20- Map view results of tomographic inversion for V_P (top) and V_S (bottom) at 185 km depth. Anomaly E is labeled. Warm (reddish) and cool (bluish) colors are percent velocity deviations in V_P and V_S. Numbers on the contours indicate absolute velocity in km/s. V_P and V_S contours are in 0.2 km/s increments. Other symbols as in Figure 10.

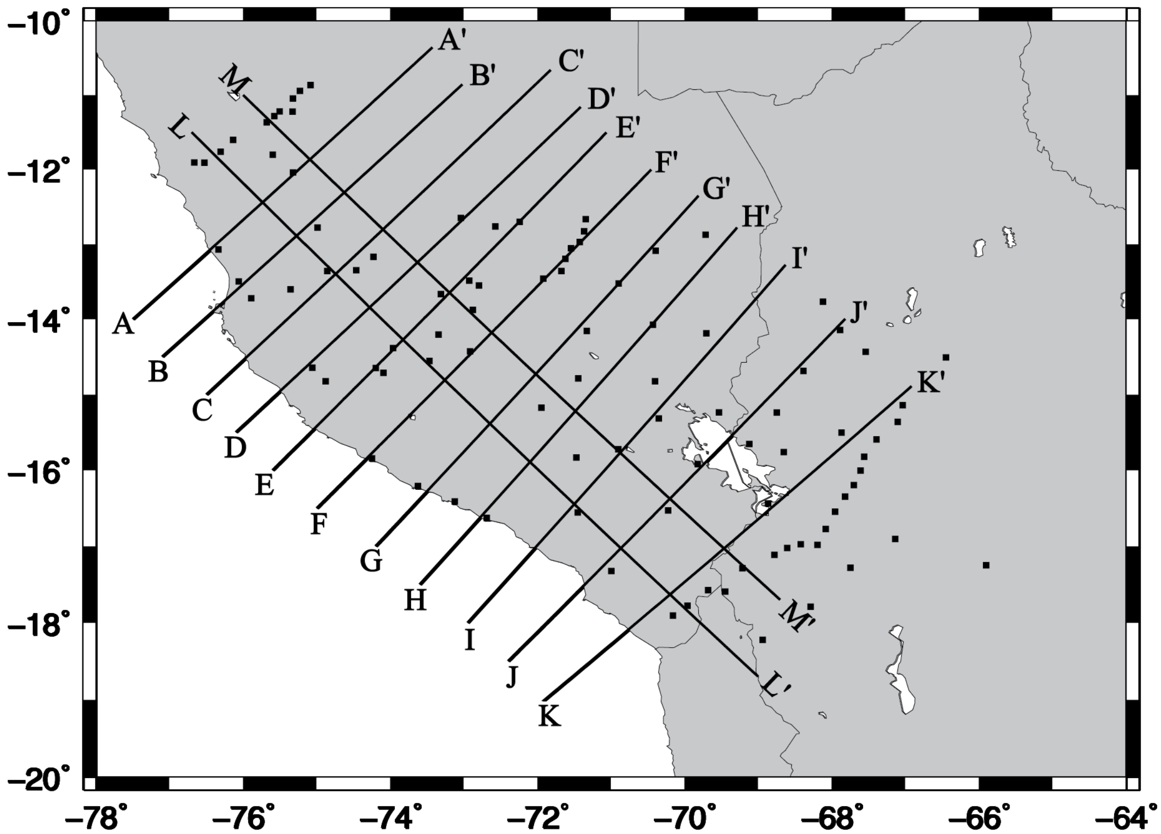

Figure 3.21: Map showing locations of the trench perpendicular and trench parallel cross sections shown in Figure 3.22-3.34.

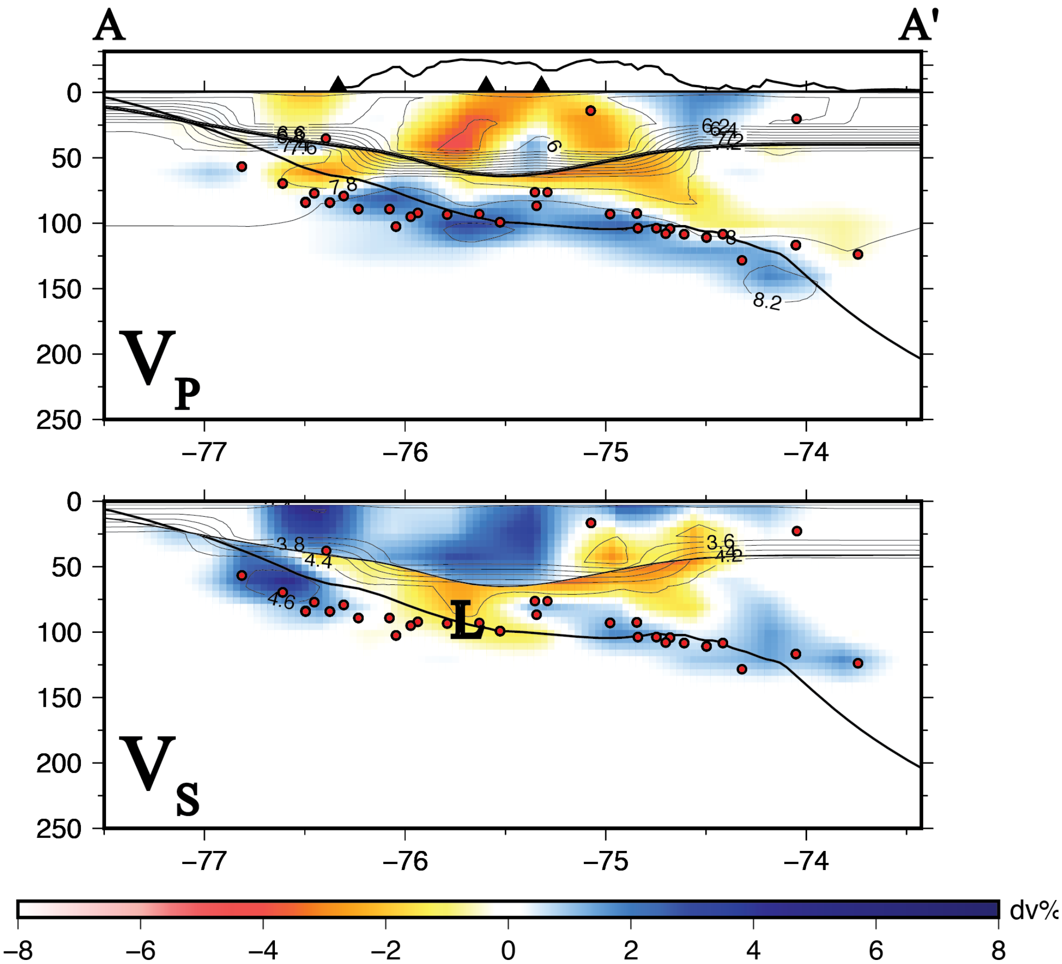

Figure 3.22- Results for V_P and V_S along cross section AA′, located north of the Nazca Ridge. The Moho is from density measurements of Tassara et al. (2006). The slab contours are from local seismicity study (Kumar et al., 2015) and the red dots indicate event locations. Anomaly L is labeled. Warm (reddish) and cool (bluish) colors are percent velocity deviations in V_P and V_S. Numbers on the contours indicate absolute velocity in km/s. V_P and V_S contours are in 0.2 km/s increments. Black triangles show the location of seismic stations along the AA′ transect.

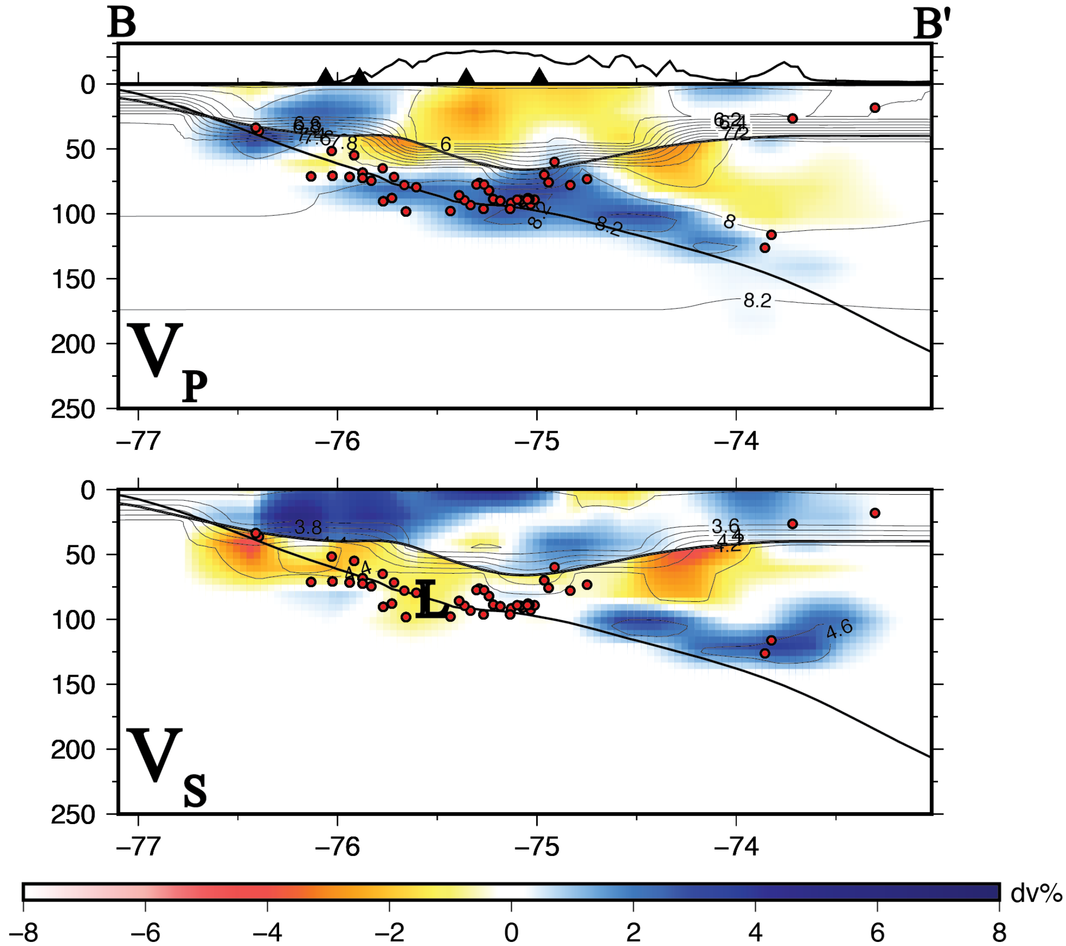

Figure 3.23- Results for V_P and V_S along cross section BB′, located north of the Nazca Ridge. Anomaly L is labeled. Warm (reddish) and cool (bluish) colors are percent velocity deviations in V_P and V_S. Numbers on the contours indicate absolute velocity in km/s. V_P and V_S contours are in 0.2 km/s increments. Other symbols as in Figure 3.22.

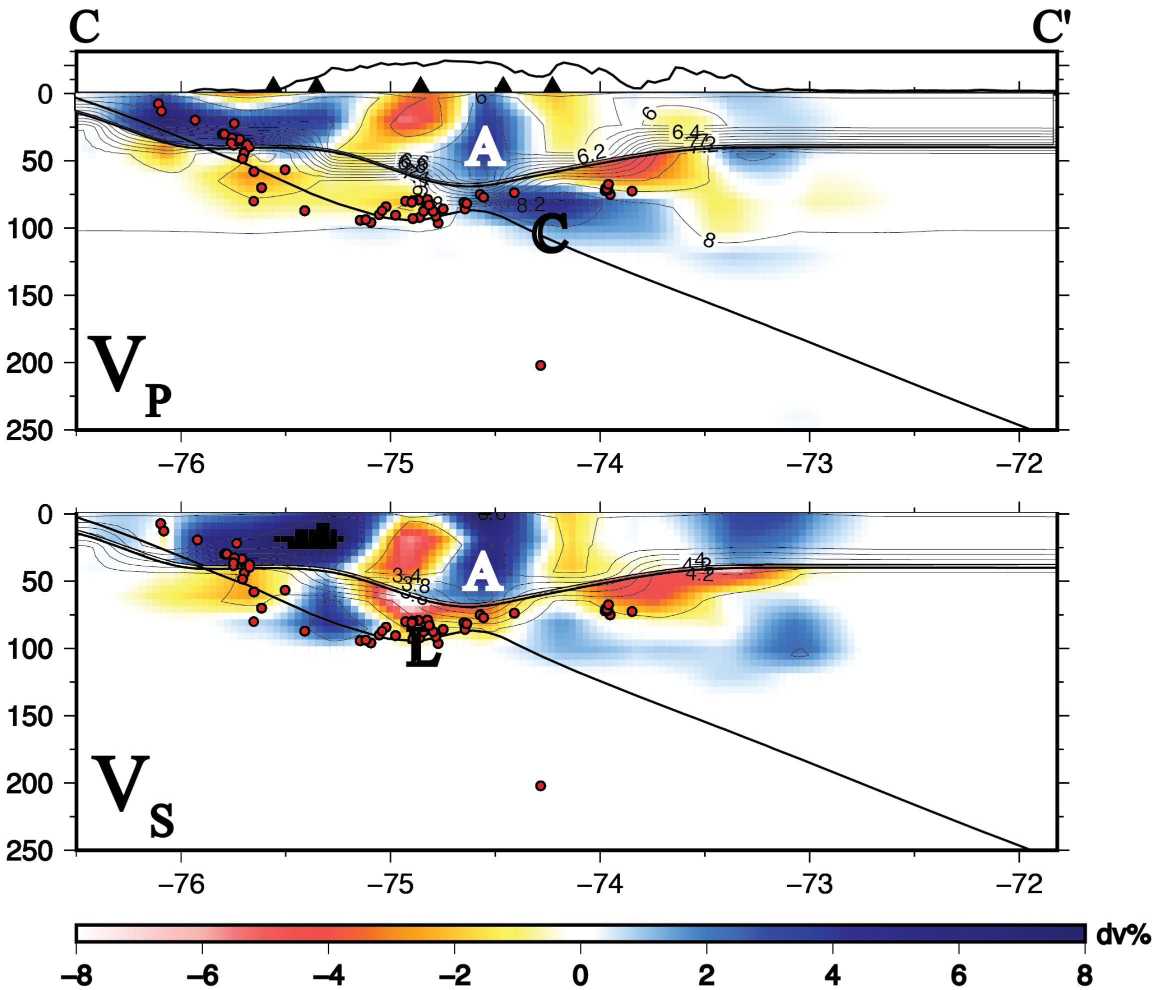

Figure 3.24- Results for V_P and V_S along cross section CC′. Anomalies A, C and L are labeled. Warm (reddish) and cool (bluish) colors are percent velocity deviations in V_P and V_S. Numbers on the contours indicate absolute velocity in km/s. V_P and V_S contours are in 0.2 km/s increments. Other symbols as in Figure 3.22.

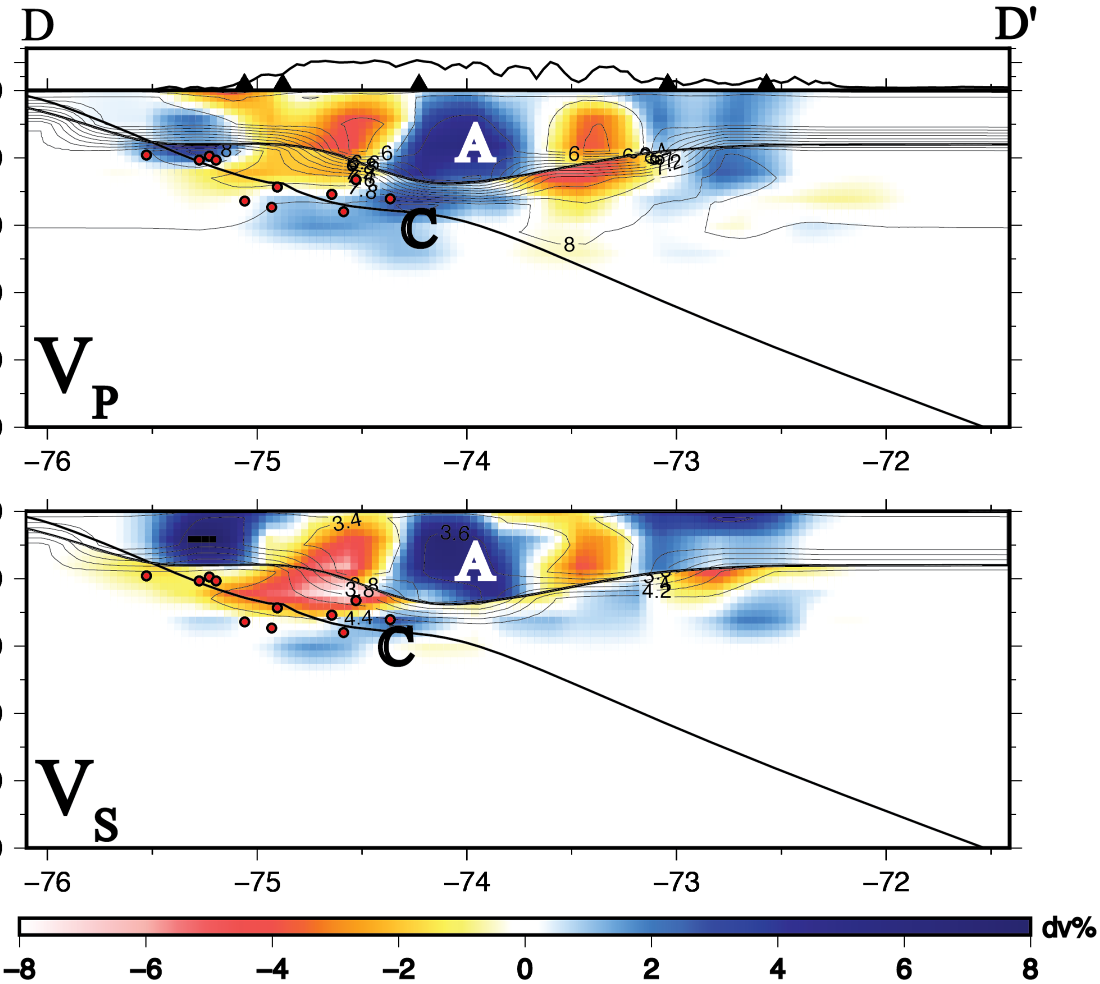

Figure 3.25- Results for V_P and V_S along cross section DD′, located along the Nazca Ridge. Anomalies A and C are labeled. Warm (reddish) and cool (bluish) colors are percent velocity deviations in V_P and V_S. Numbers on the contours indicate absolute velocity in km/s. V_P and V_S contours are in 0.2 km/s increments. Other symbols as in Figure 3.22.

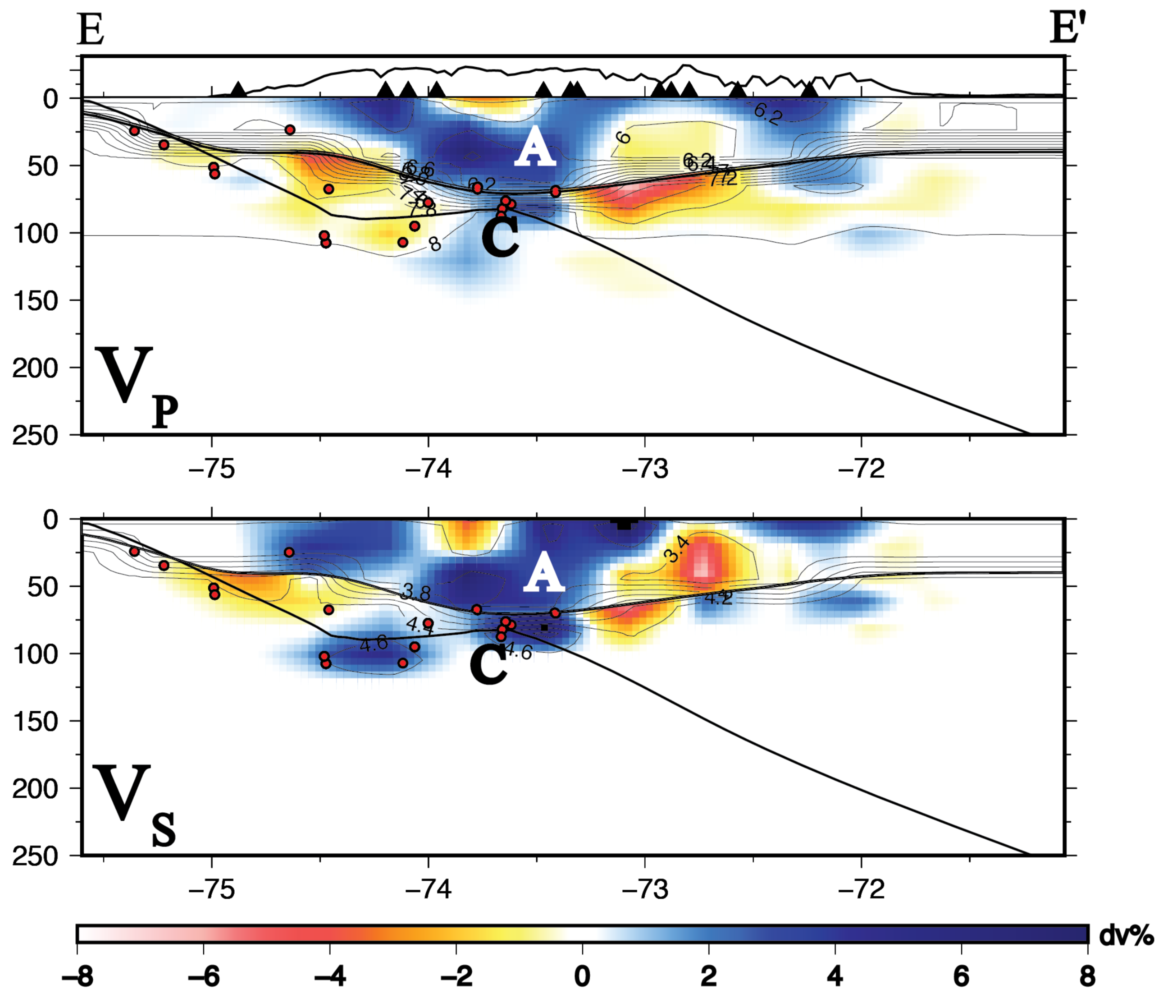

Figure 3.26- Results for V_P and V_S along cross section EE′, located along the southern margin of the Nazca Ridge. Anomalies A and C are labeled. Warm (reddish) and cool (bluish) colors are percent velocity deviations in V_P and V_S. Numbers on the contours indicate absolute velocity in km/s. V_P and V_S contours are in 0.2 km/s increments. Other symbols as in Figure 3.22.

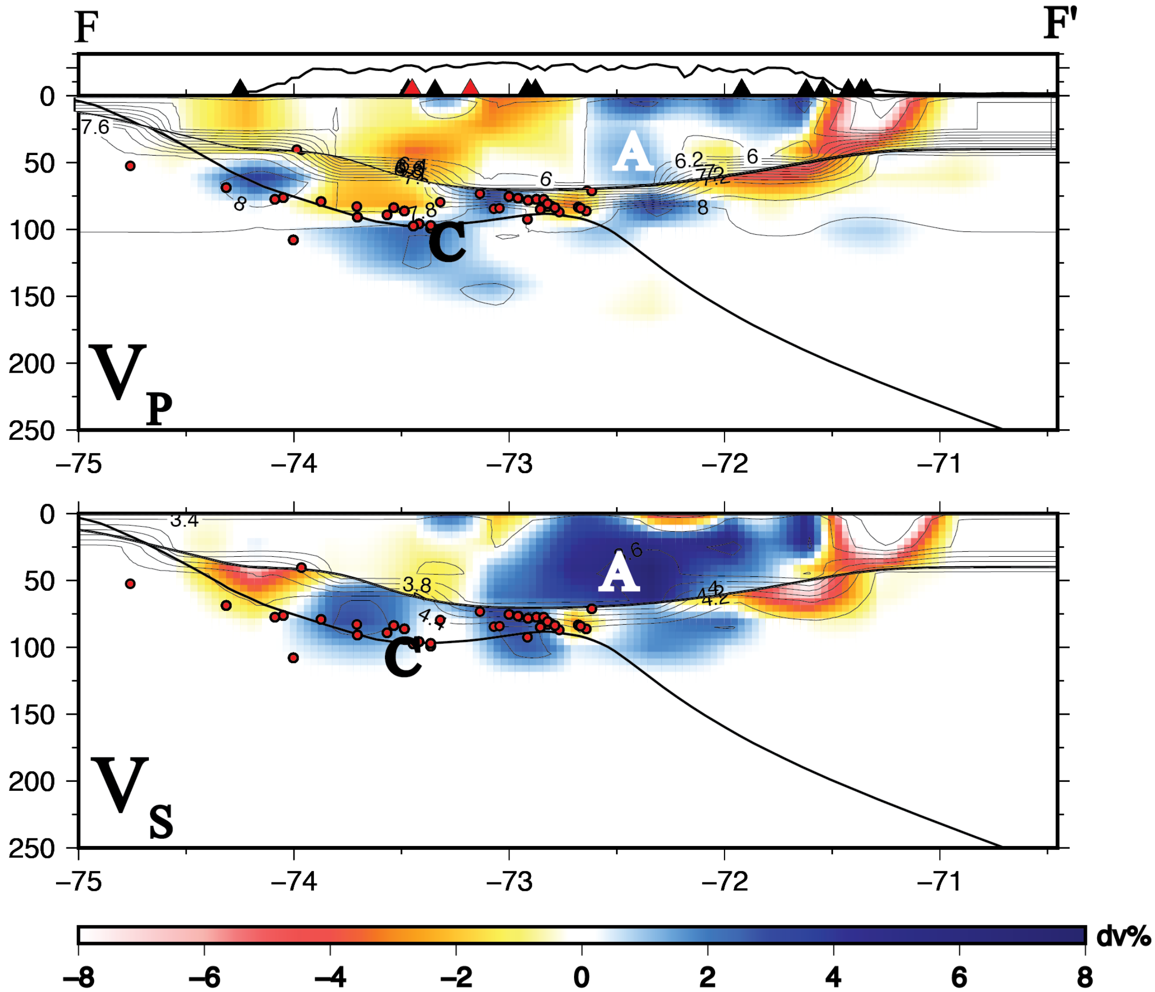

Figure 3.27- Results for V_P and V_S along cross section FF′, located along the southern margin of the Nazca Ridge. Anomalies A and C are labeled. Warm (reddish) and cool (bluish) colors are percent velocity deviations in V_P and V_S. Numbers on the contours indicate absolute velocity in km/s. V_P and V_S contours are in 0.2 km/s increments. The red triangles indicate the locations of active volcanism. Other symbols as in Figure 3.22.

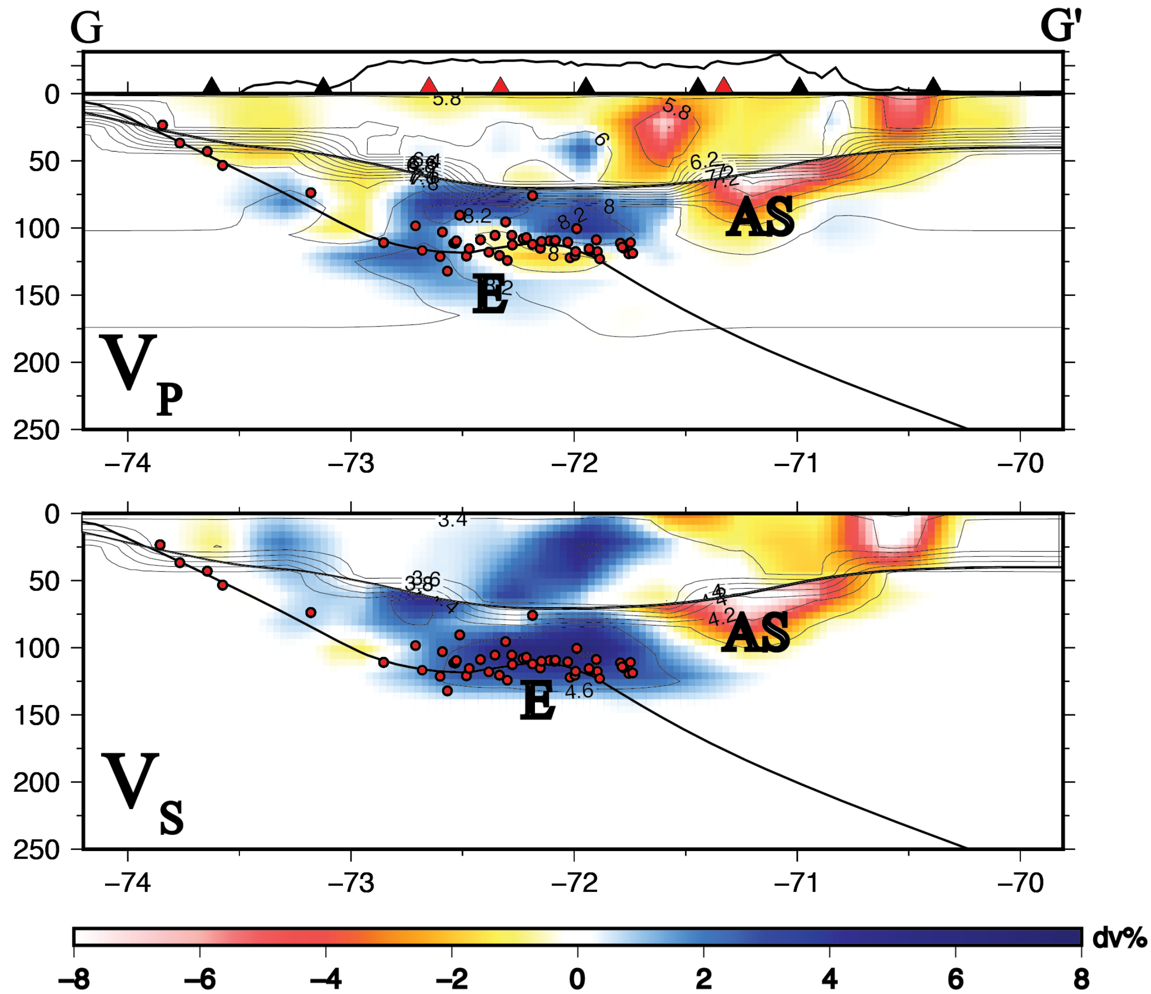

Figure 3.28- Results for V_P and V_S along cross section GG′, located immediately south of the Nazca Ridge. Anomalies E and AS are labeled. Warm (reddish) and cool (bluish) colors are percent velocity deviations in V_P and V_S. Numbers on the contours indicate absolute velocity in km/s. V_P and V_S contours are in 0.2 km/s increments. The red triangles indicate the locations of active volcanism. Other symbols as in Figure 3.22.

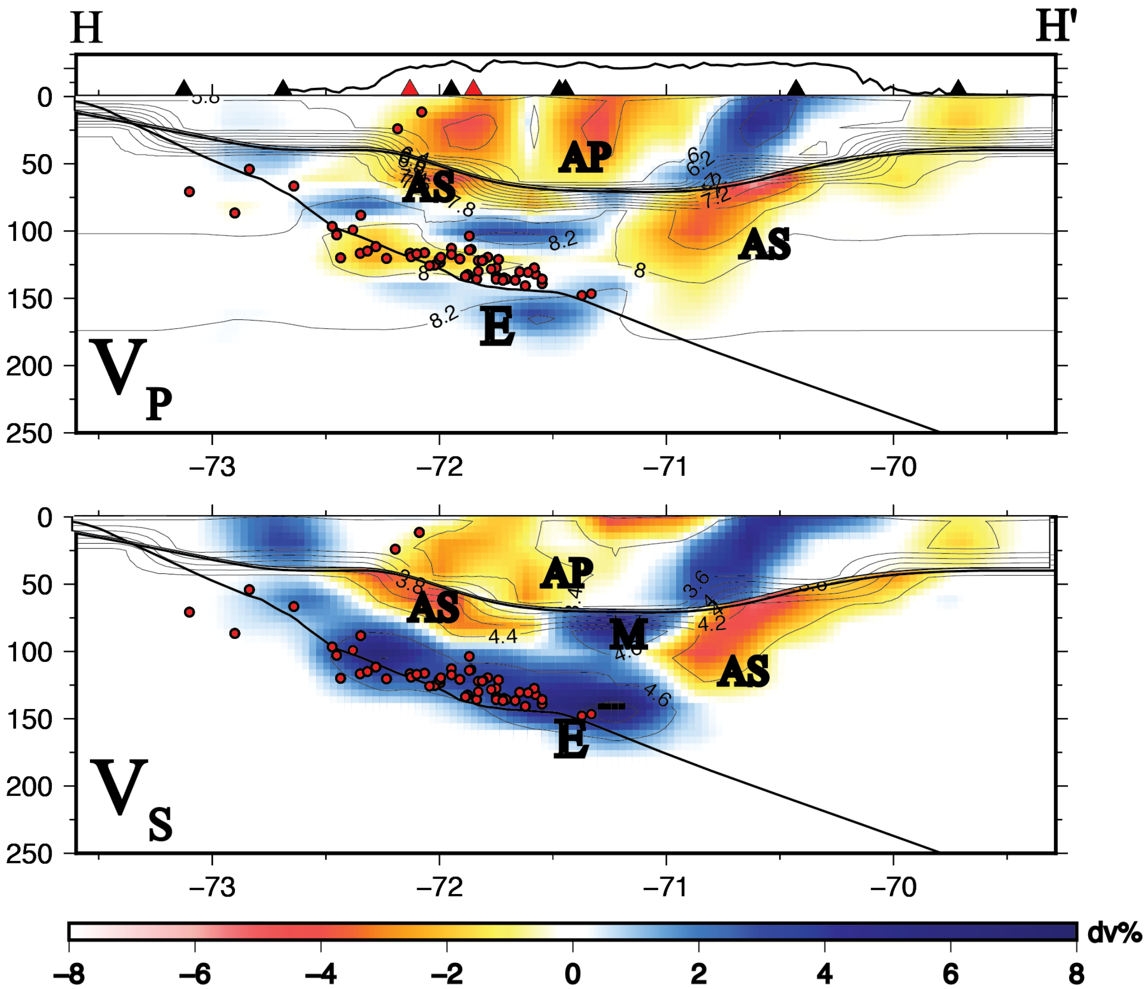

Figure 3.29- Results for V_P and V_S along cross section HH′, located south of the Nazca Ridge and passing through the northernmost edge of the northern Altiplano. Anomalies E, M, AS, and AP are labeled. Warm (reddish) and cool (bluish) colors are percent velocity deviations in V_P and V_S. Numbers on the contours indicate absolute velocity in km/s. V_P and V_S contours are in 0.2 km/s increments. The red triangles indicate the locations of active volcanism. Other symbols as in Figure 3.22.

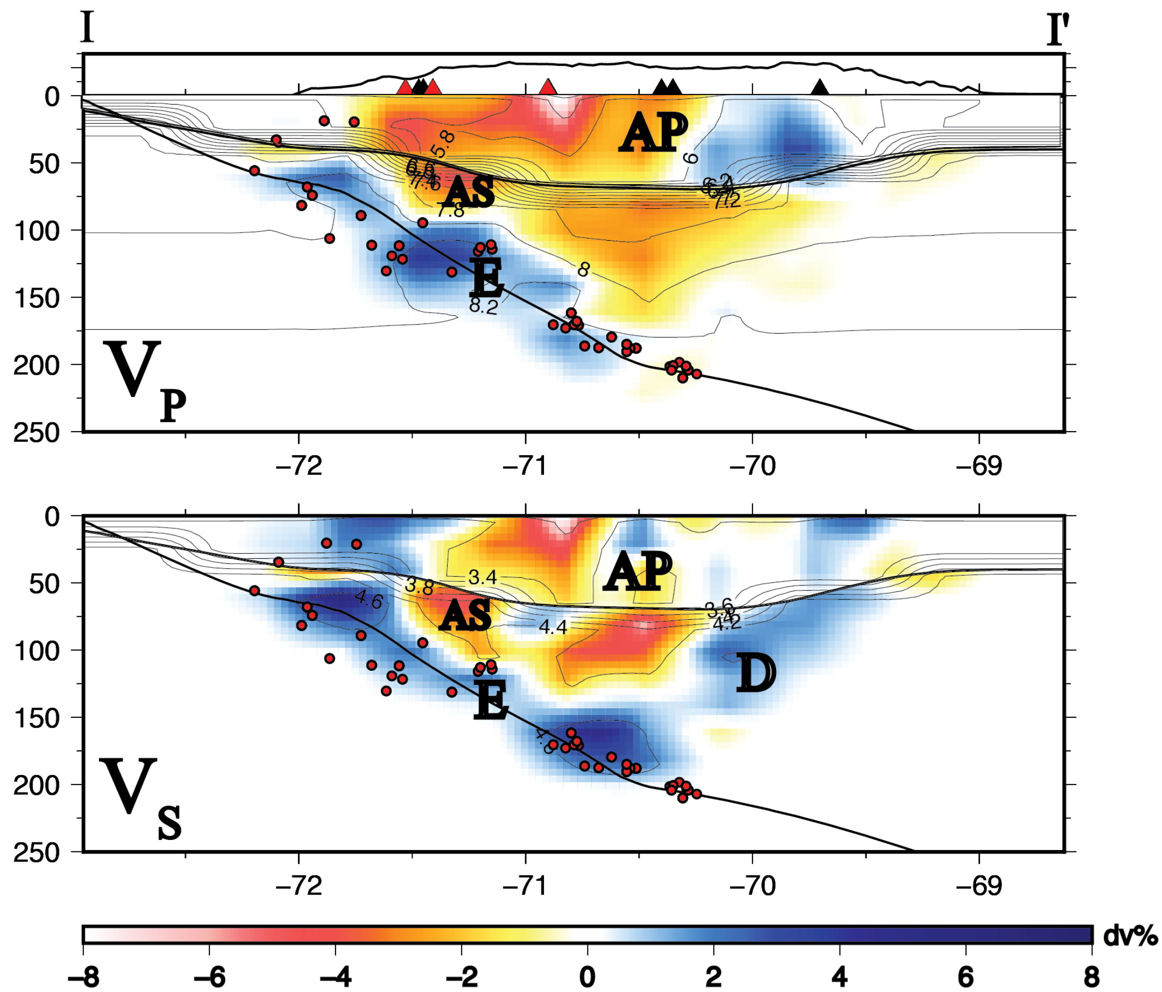

Figure 3.30: Results for V_P and V_S along cross section II′, located in the region of normal subduction in southern Peru and passing through the northern Altiplano. Anomalies D, E, AS, and AP are labeled. Warm (reddish) and cool (bluish) colors are percent velocity deviations in V_P and V_S. Numbers on the contours indicate absolute velocity in km/s. V_P and V_S contours are in 0.2 km/s increments. The red triangles indicate the locations of active volcanism. Other symbols as in Figure 3.22.

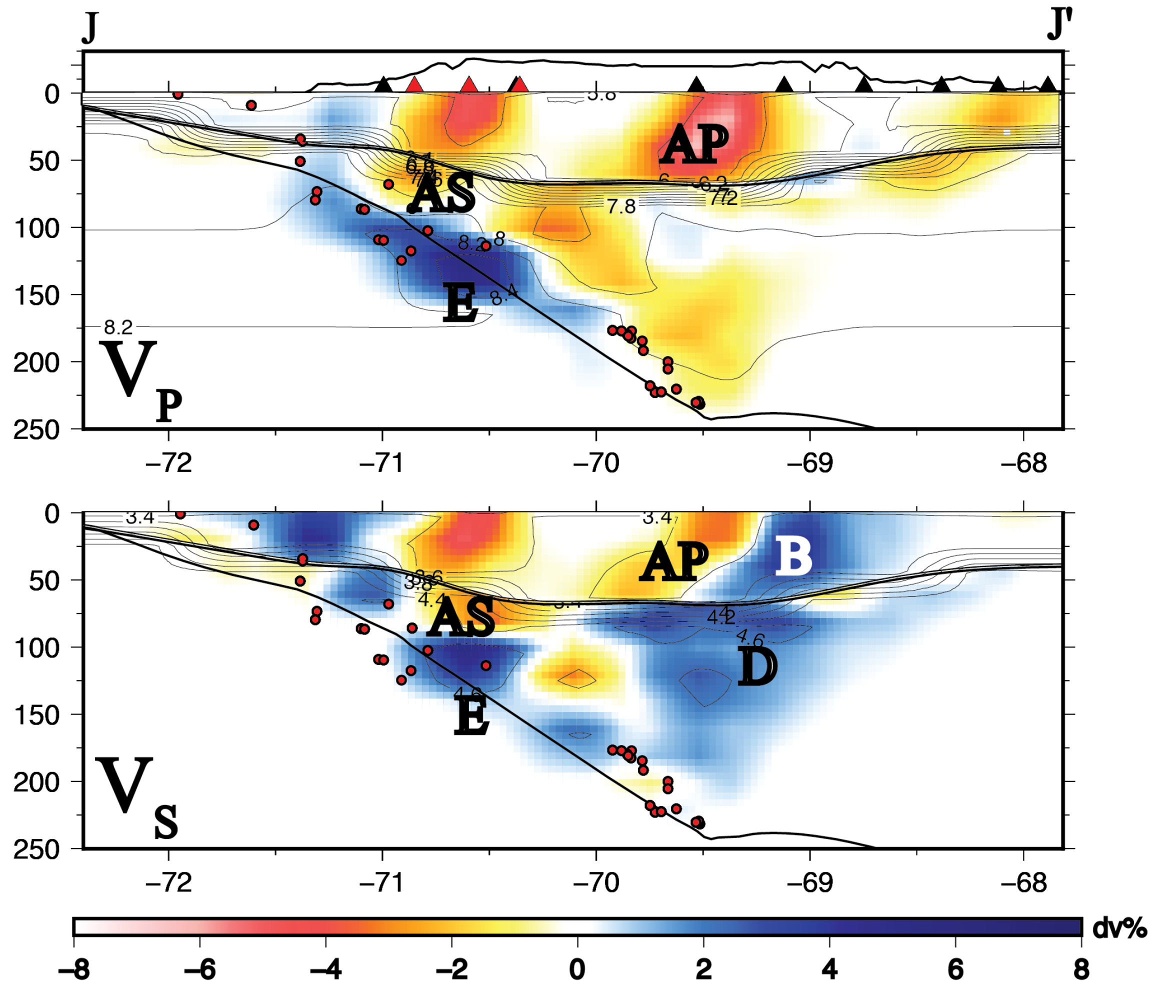

Figure 3.31- Results for V_P and V_S along cross section JJ′, located in the region of normal subduction in southern Peru and passing through the northern Altiplano. Anomalies B, D, E, and AP are labeled. Warm (reddish) and cool (bluish) colors are percent velocity deviations in V_P and V_S. Numbers on the contours indicate absolute velocity in km/s. V_P and V_S contours are in 0.2 km/s increments. The red triangles indicate the locations of active volcanism. Other symbols as in Figure 3.22.

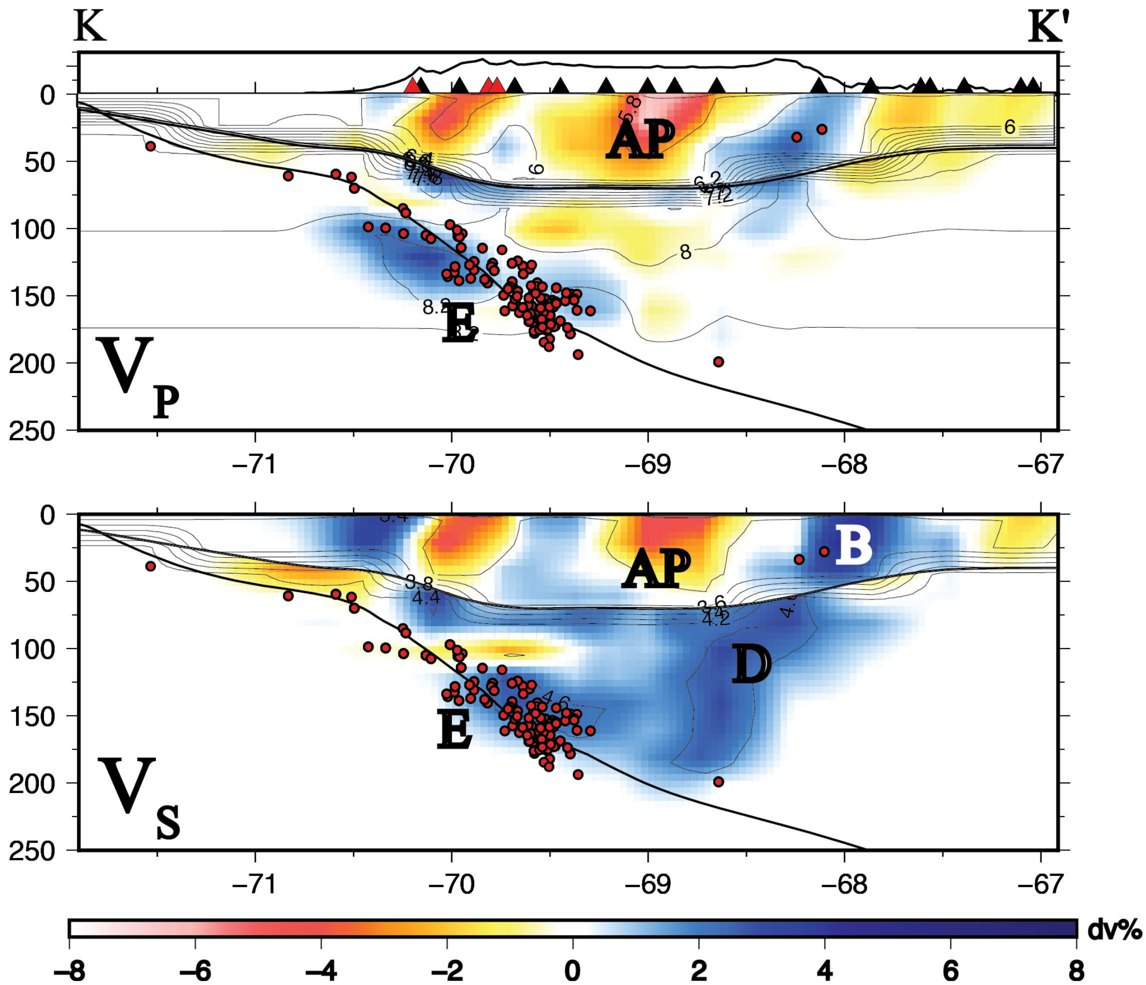

Figure 3.32: Results for V_P and V_S along cross section KK′, located in the region of normal subduction in southern Peru and passing through the northern Altiplano. Anomalies B, D, E, and AP are labeled. Warm (reddish) and cool (bluish) colors are percent velocity deviations in V_P and V_S. Numbers on the contours indicate absolute velocity in km/s. V_P and V_S contours are in 0.2 km/s increments. The red triangles indicate the locations of active volcanism. Other symbols as in Figure 3.22.

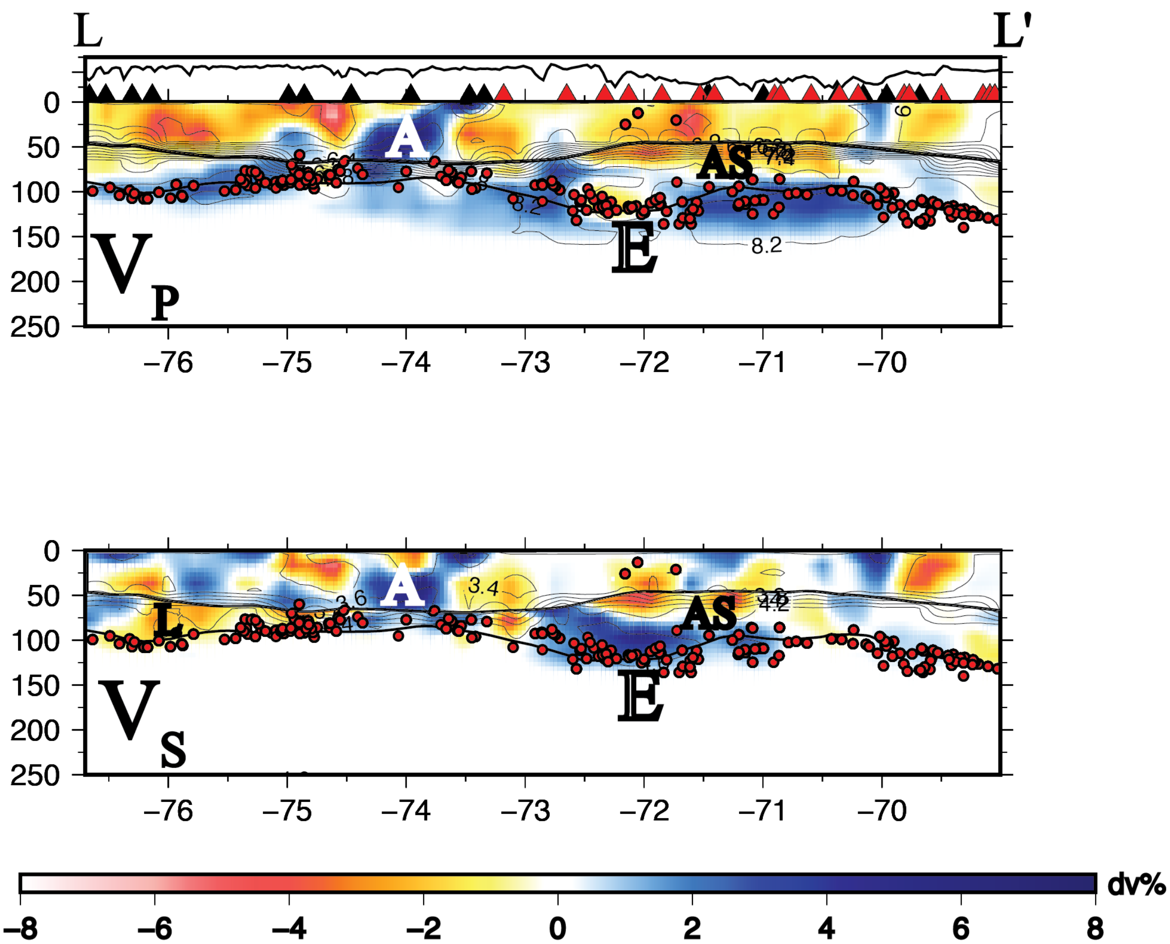

Figure 3.33- Results for V_P and V_S along cross section LL′, parallel to the trench. Warm (reddish) and cool (bluish) colors are percent velocity deviations in V_P and V_S. Numbers on the contours indicate absolute velocity in km/s. V_P and V_S contours are in 0.2 km/s increments. The red triangles indicate the locations of active volcanism. Other symbols as in Figure 3.22.

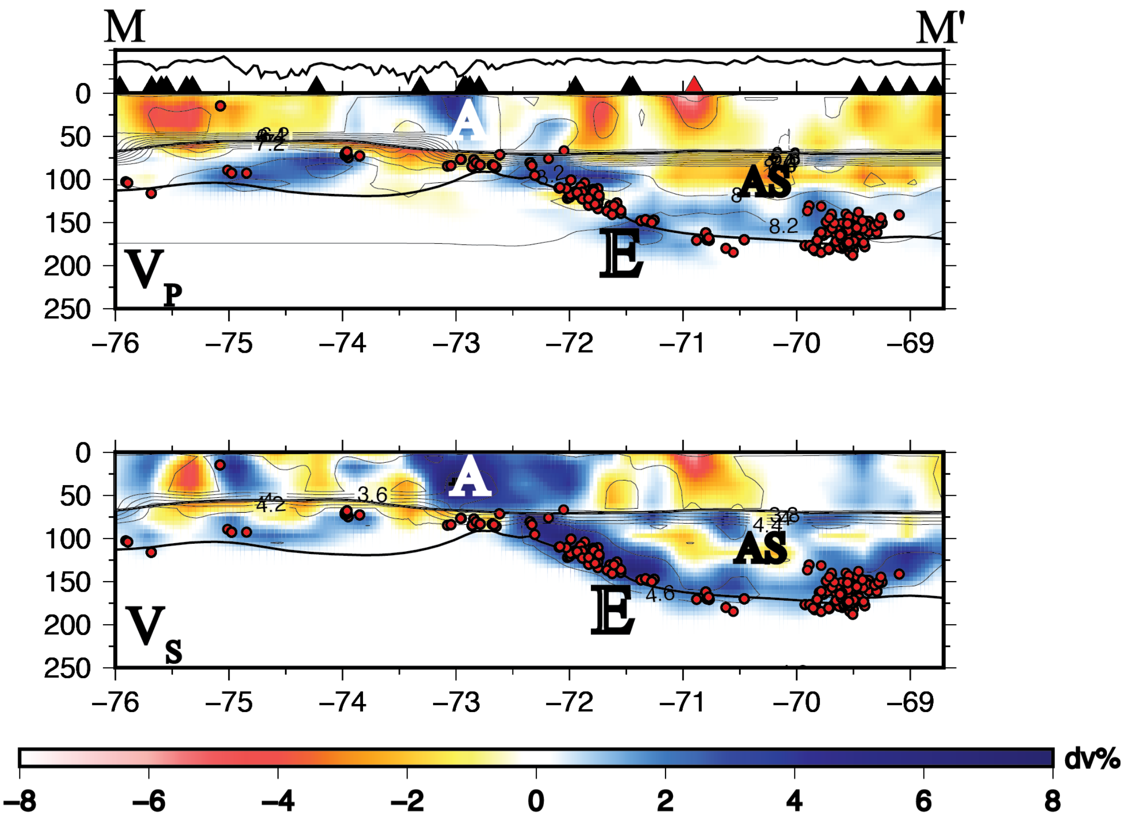

Figure 3.34- Results for V_P and V_S along cross section MM′, parallel to the trench. Warm (reddish) and cool (bluish) colors are percent velocity deviations in V_P and V_S. Numbers on the contours indicate absolute velocity in km/s. V_P and V_S contours are in 0.2 km/s increments. The red triangles indicate the locations of active volcanism. Other symbols as in Figure 3.22.

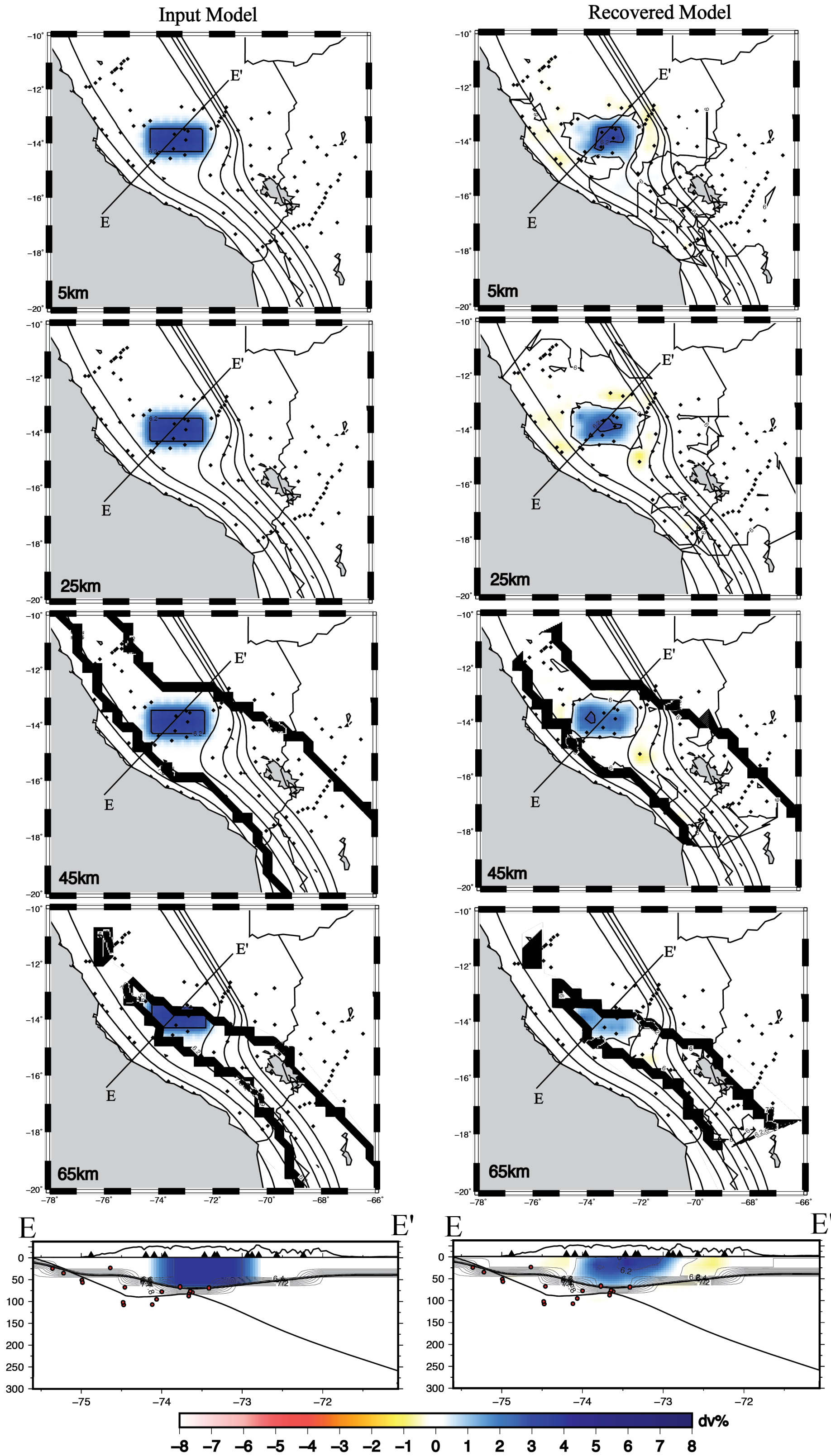

Figure 3.35- Results showing the recovery of high-V_P anomaly A (Test 1). Black dots indicate the locations of seismic stations. The multiple close contours show the location of the Moho. Location of the cross section EE′ is shown in map view.

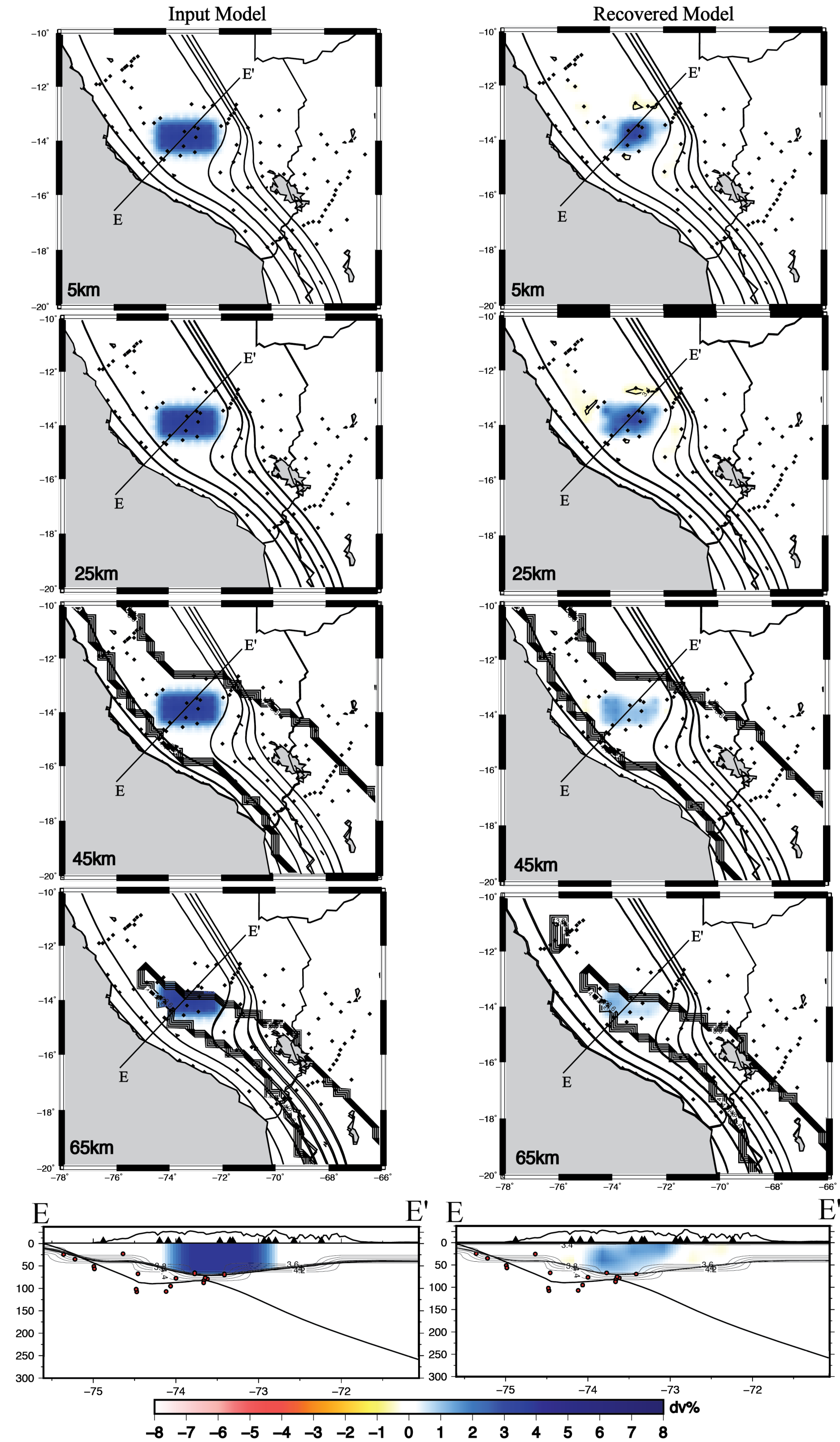

Figure 3.36- Results showing the recovery of high-V_S anomaly A (Test 2). Black dots indicate the locations of seismic stations. The multiple close contours show the location of the Moho. Location of the cross section EE′ is shown in map view.

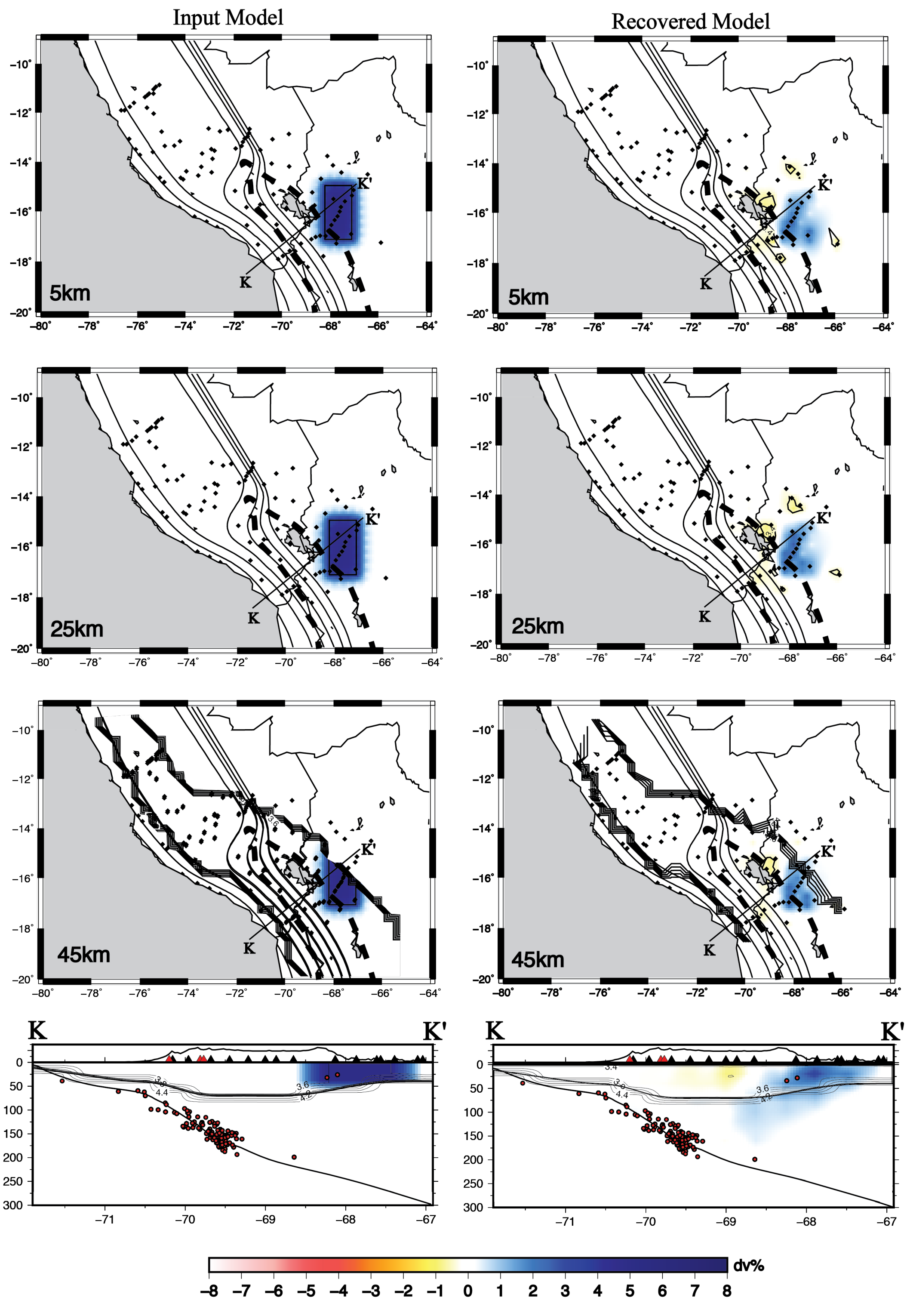

Figure 3.37- Results showing the recovery of high-V_S anomaly B (Test 3). Black dots indicate the locations of seismic stations and the multiple close contours show the location of the Moho in map view. In the cross section, the red and black triangles indicate the locations of active volcanism and seismic stations respectively. Location of the cross section KK′ is shown in map view.

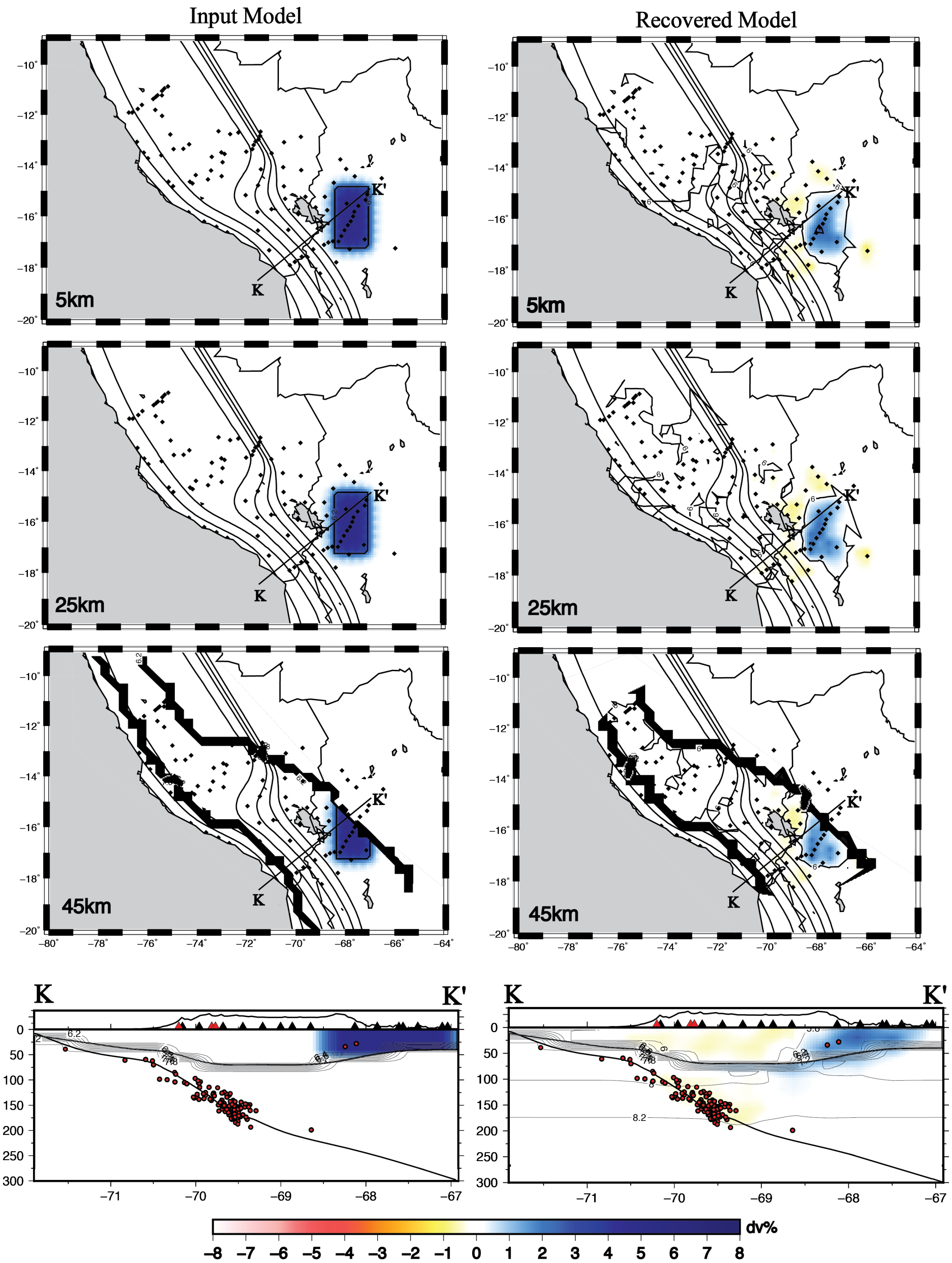

Figure 3.38- Results showing the recovery of high-V_P anomaly (Test4), roughly coinciding with the location of anomaly B. Black dots indicate the locations of seismic stations and the multiple close contours show the location of the Moho in map view. In the cross section, the red and black triangles indicate the locations of active volcanism and seismic stations respectively. Location of the cross section KK′ is shown in map view.

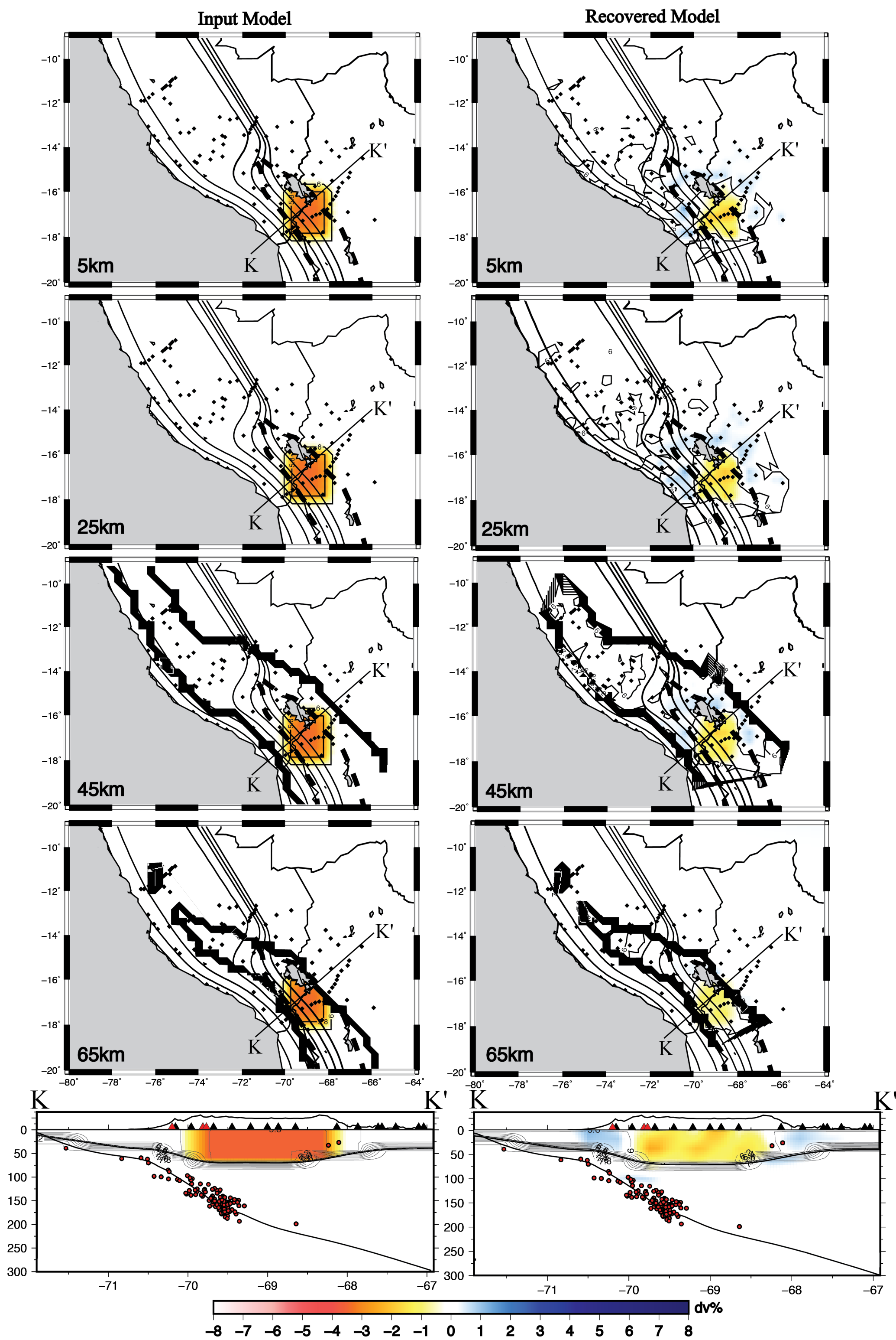

Figure 3.39- Results showing the recovery of low-V_P anomaly AP under the northern Altiplano crust (Test 5). Dashed line is approximate outline of northern Altiplano. The multiple close contours show the location of the Moho. Black dots indicate the location of seismic stations. Solid lines represent the slab contour from Cahill & Isacks (1992). Location of the cross section KK′ is shown in map view.

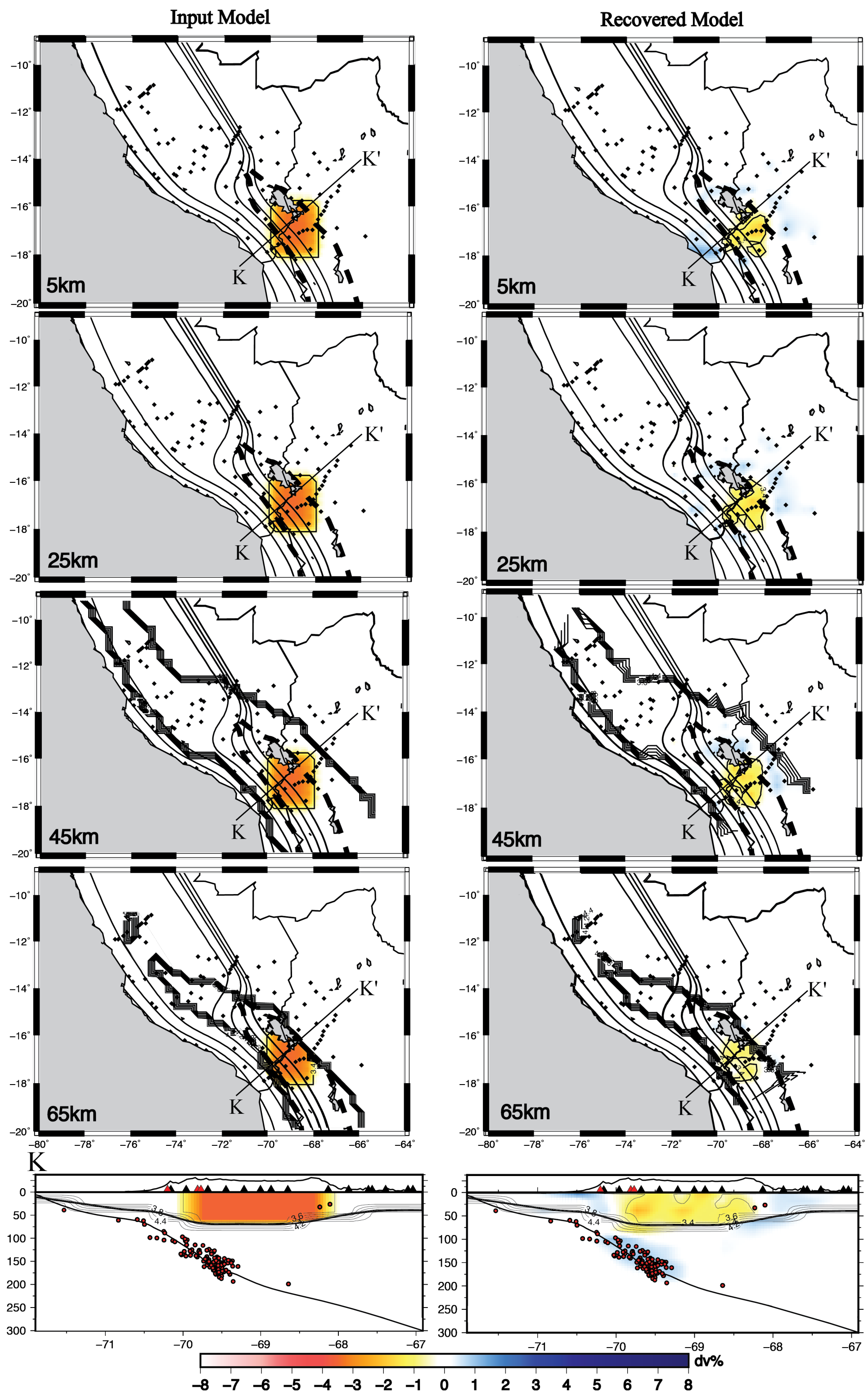

Figure 3.40- Results showing the recovery of low-V_S anomaly AP under the northern Altiplano crust (Test 6). Dashed line is approximate outline of northern Altiplano. The multiple close contours show the location of the Moho. Black dots indicate the location of seismic stations. Solid lines represent the slab contour from Cahill & Isacks (1992). Location of the cross section KK′ is shown in map view.

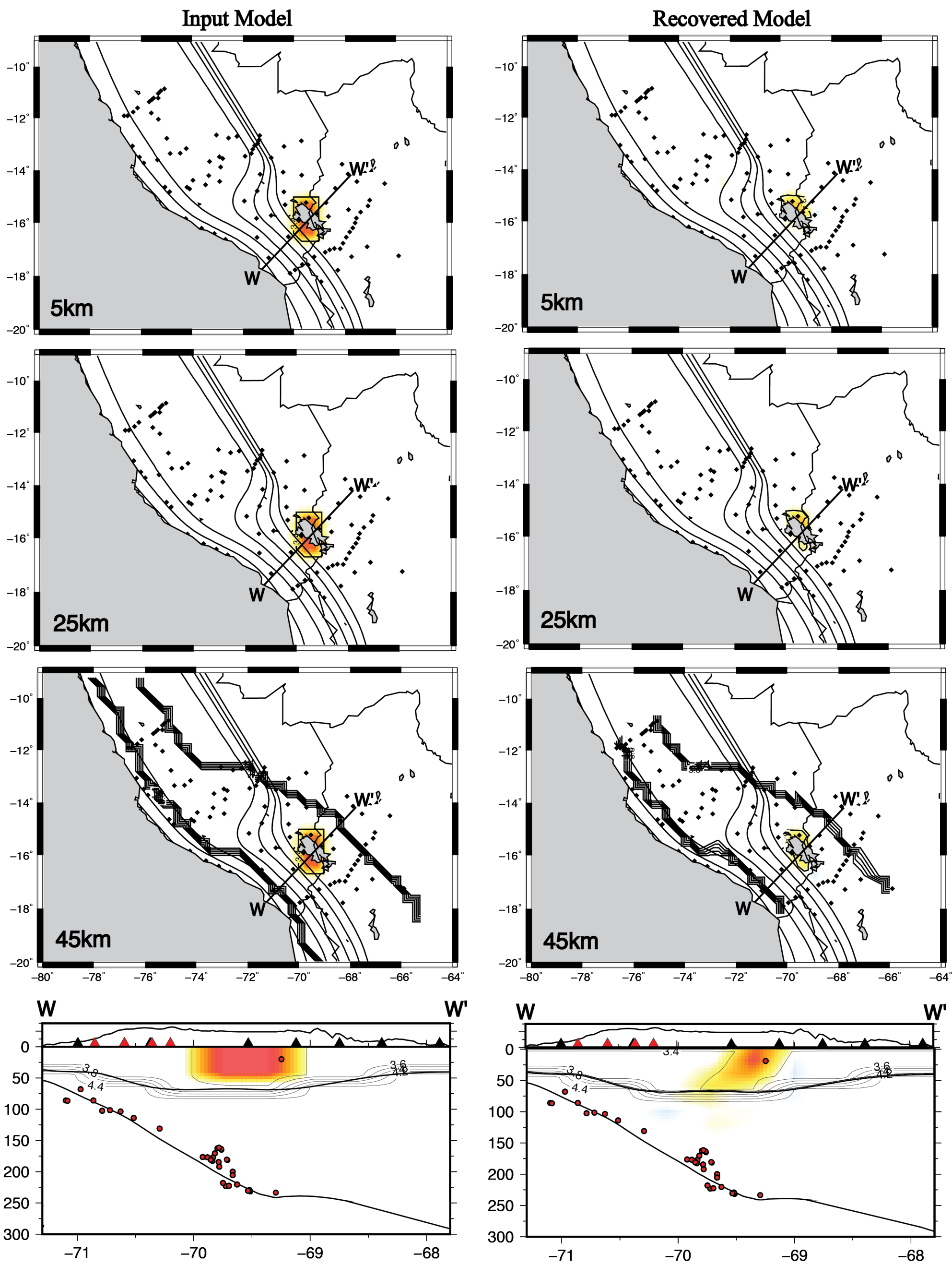

Figure 3.41- Results showing the recovery of low V_S anomaly under the northern Altiplano crust (Test 7). Location of the cross section is shown in the map (solid black line) and same as AA′ transect of Ward et al. (2013). Other symbols as in Figure 3.37.

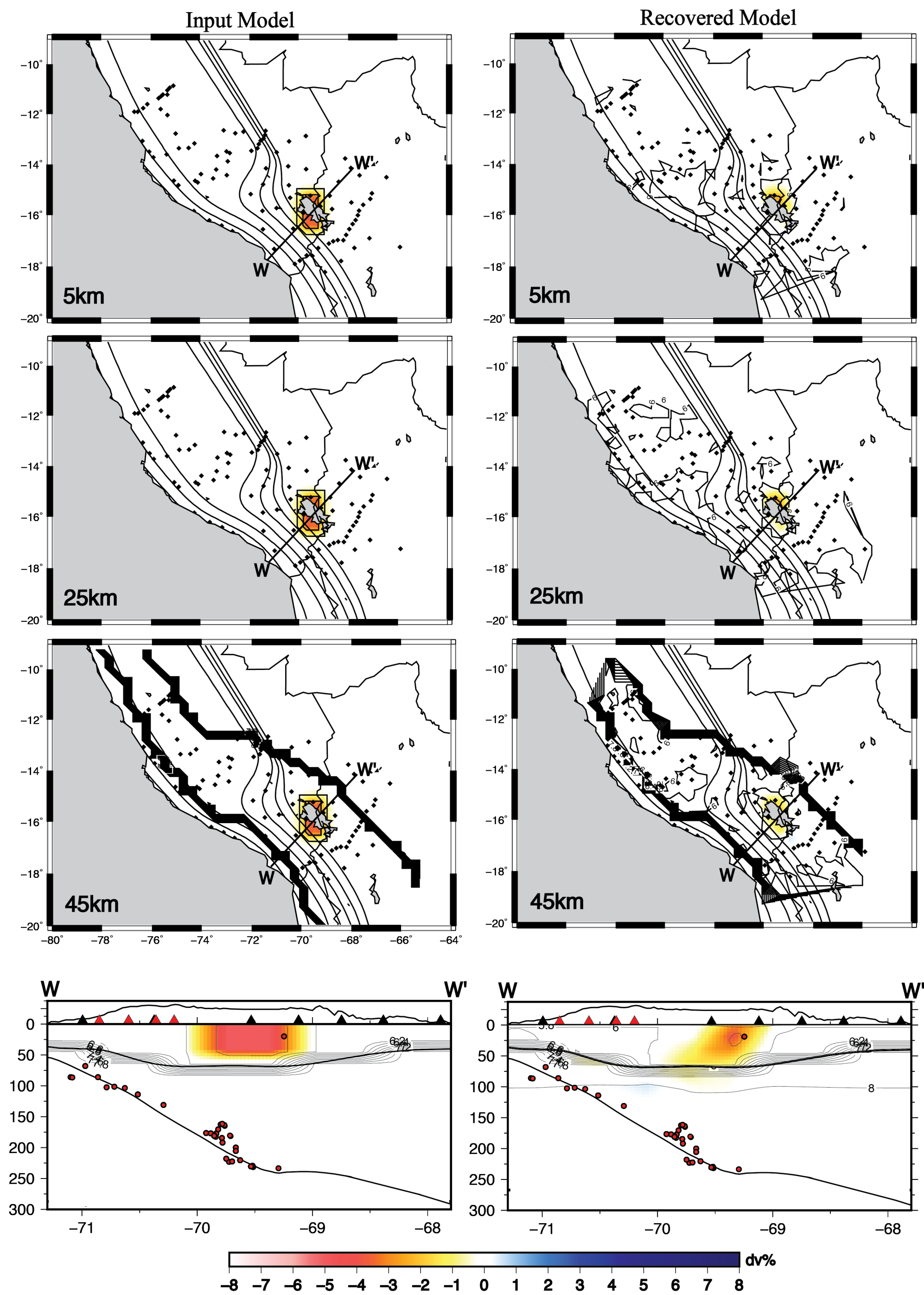

Figure 3.42- Results showing the recovery of low V_P anomaly under the northern Altiplano crust (Test 8). Location of the cross section is shown in the map (solid black line) and same as AA′ transect of Ward et al. (2013). Other symbols as in Figure 3.37.

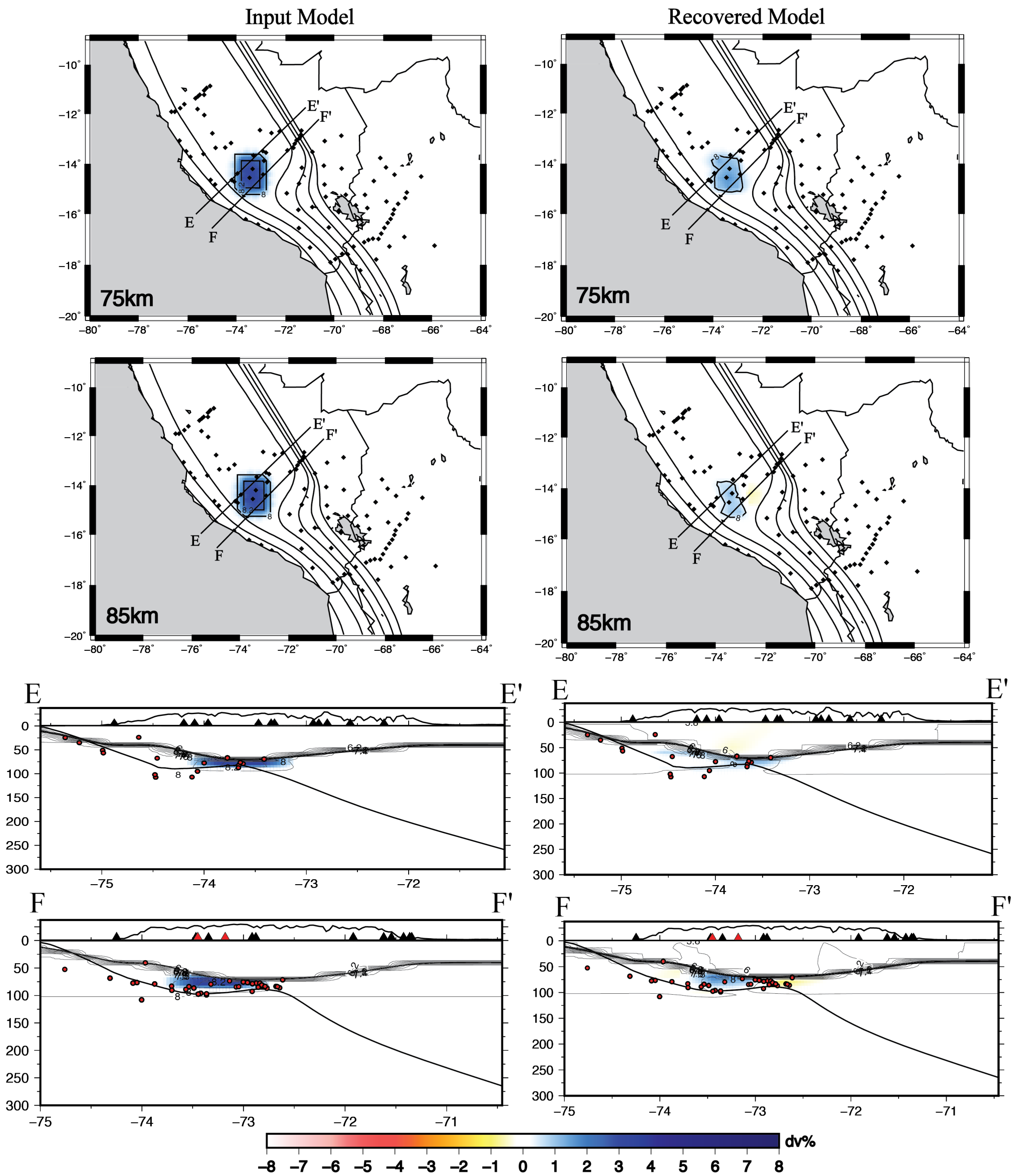

Figure 3.43- Results showing the recovery of high-V_P anomaly C (Test 9). Black dots indicate the location of seismic stations. Solid lines represent the slab contour from Cahill & Isacks (1992). Location of the cross sections EE′ and FF′ are shown in map view.

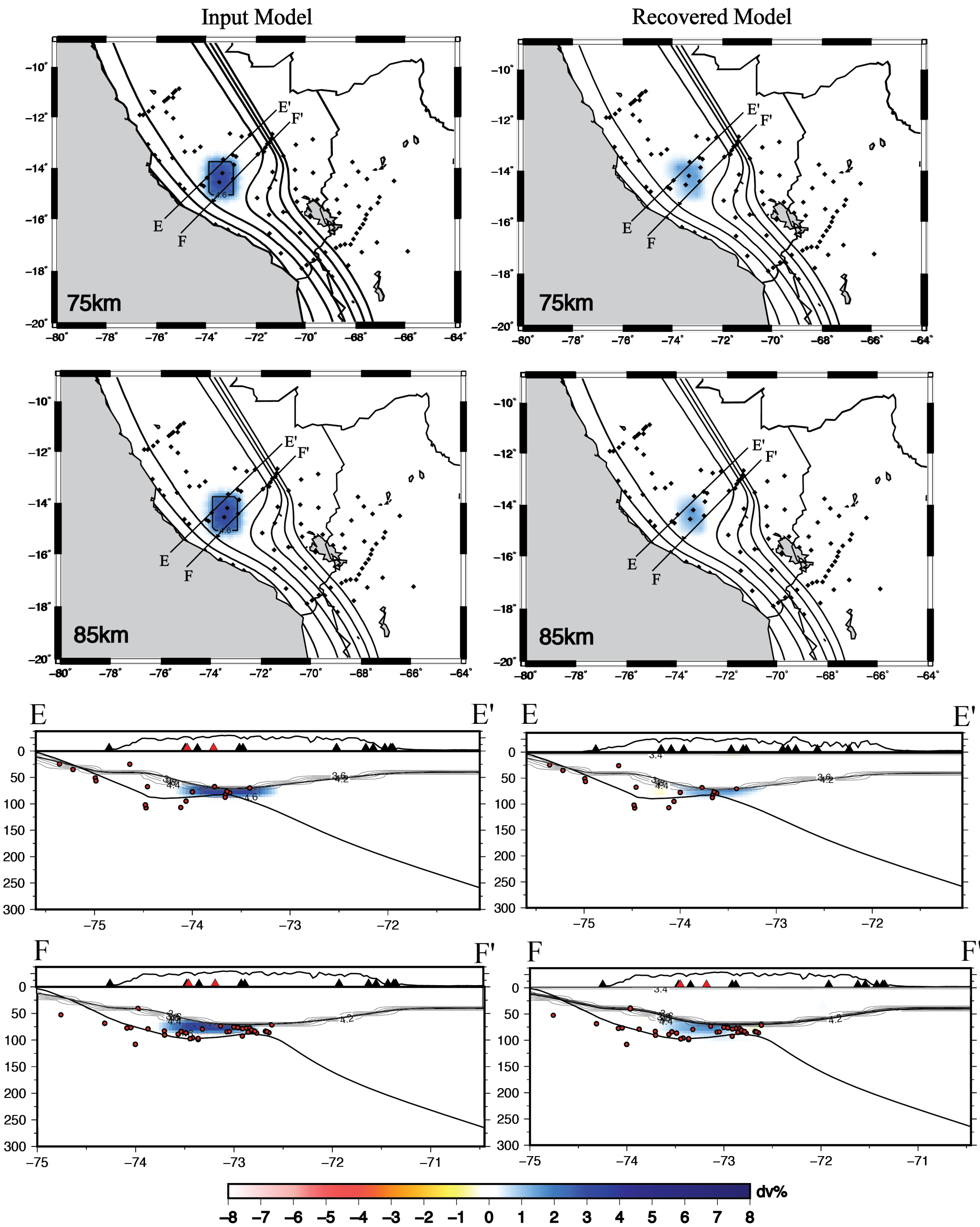

Figure 3.44- Results showing the recovery of high-V_S anomaly C (Test 10). Black dots indicate the location of seismic stations. Solid lines represent the slab contour from Cahill & Isacks (1992). Location of the cross sections EE′ and FF′ are shown in map view.

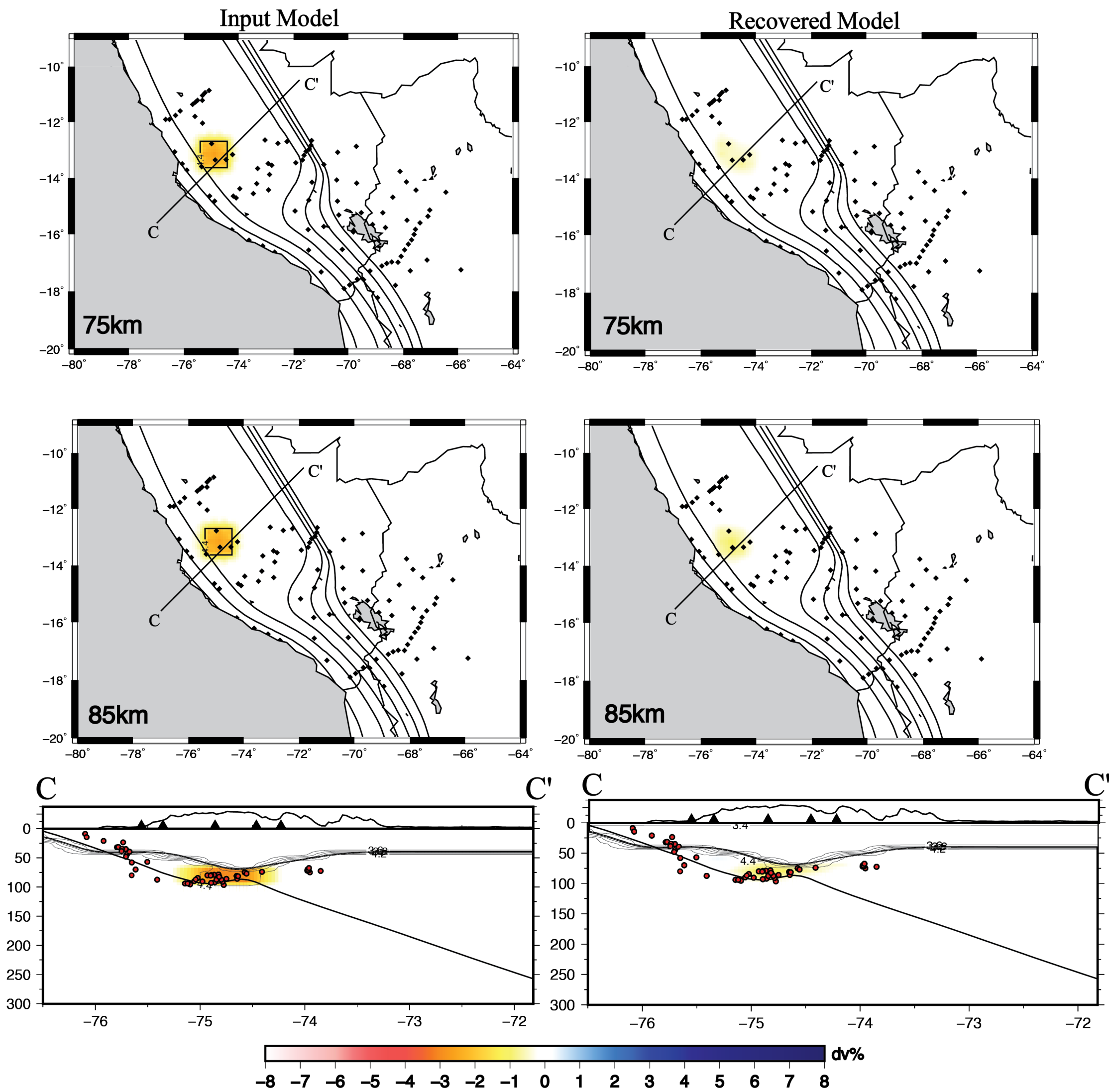

Figure 3.45- Results showing the recovery of low-V_S anomaly L (Test 11). Black dots indicate the location of seismic stations. Solid lines represent the slab contour from Cahill & Isacks (1992). Location of the cross section CC′ is shown in map view.

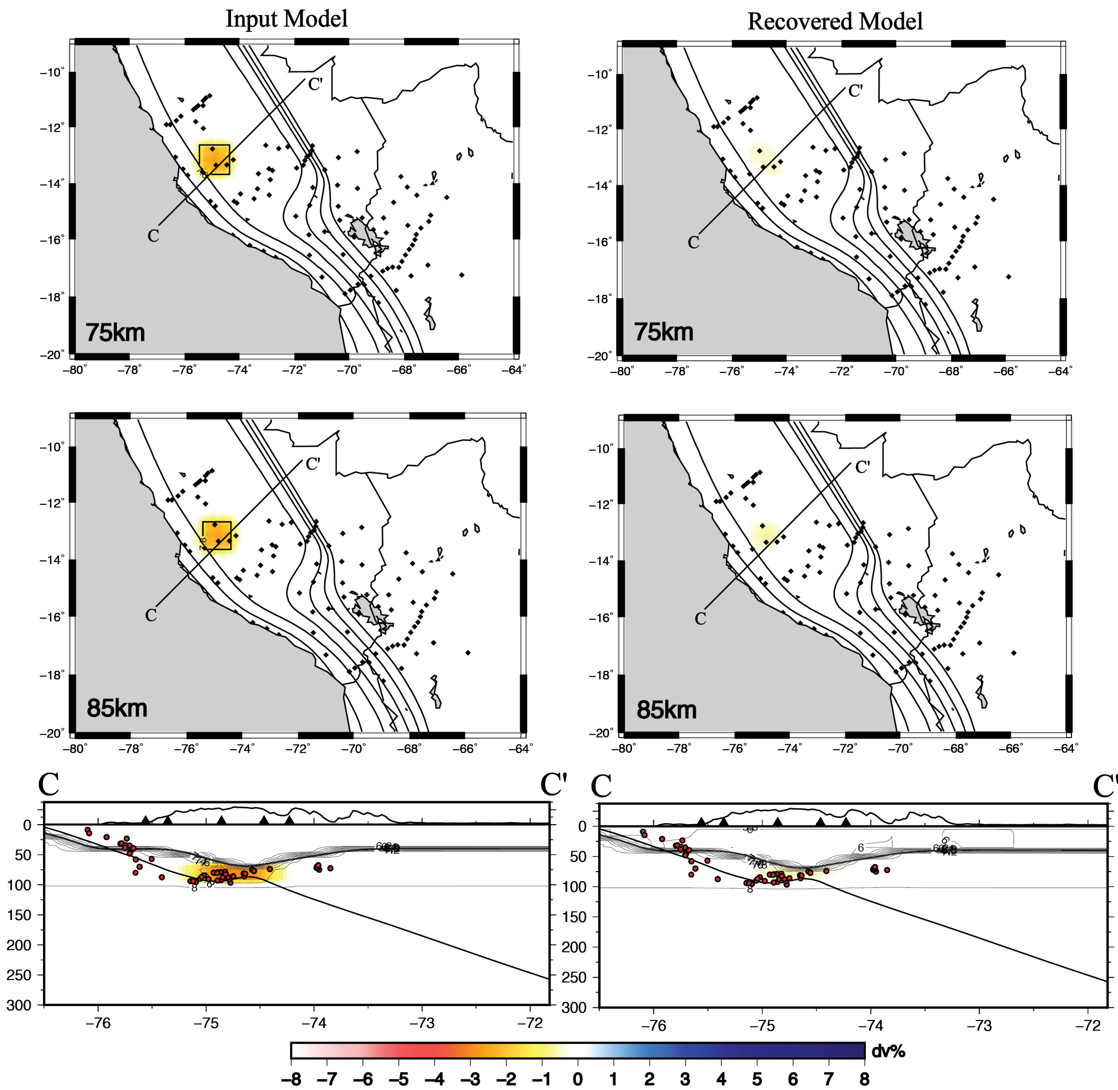

Figure 3.46- Results showing the recovery of low-V_P anomaly (Test12), roughly coinciding with the location of low-V_S anomaly L. Black dots indicate the location of seismic stations. Solid lines represent the slab contour from Cahill & Isacks (1992). Location of the cross section CC′ is shown in map view.

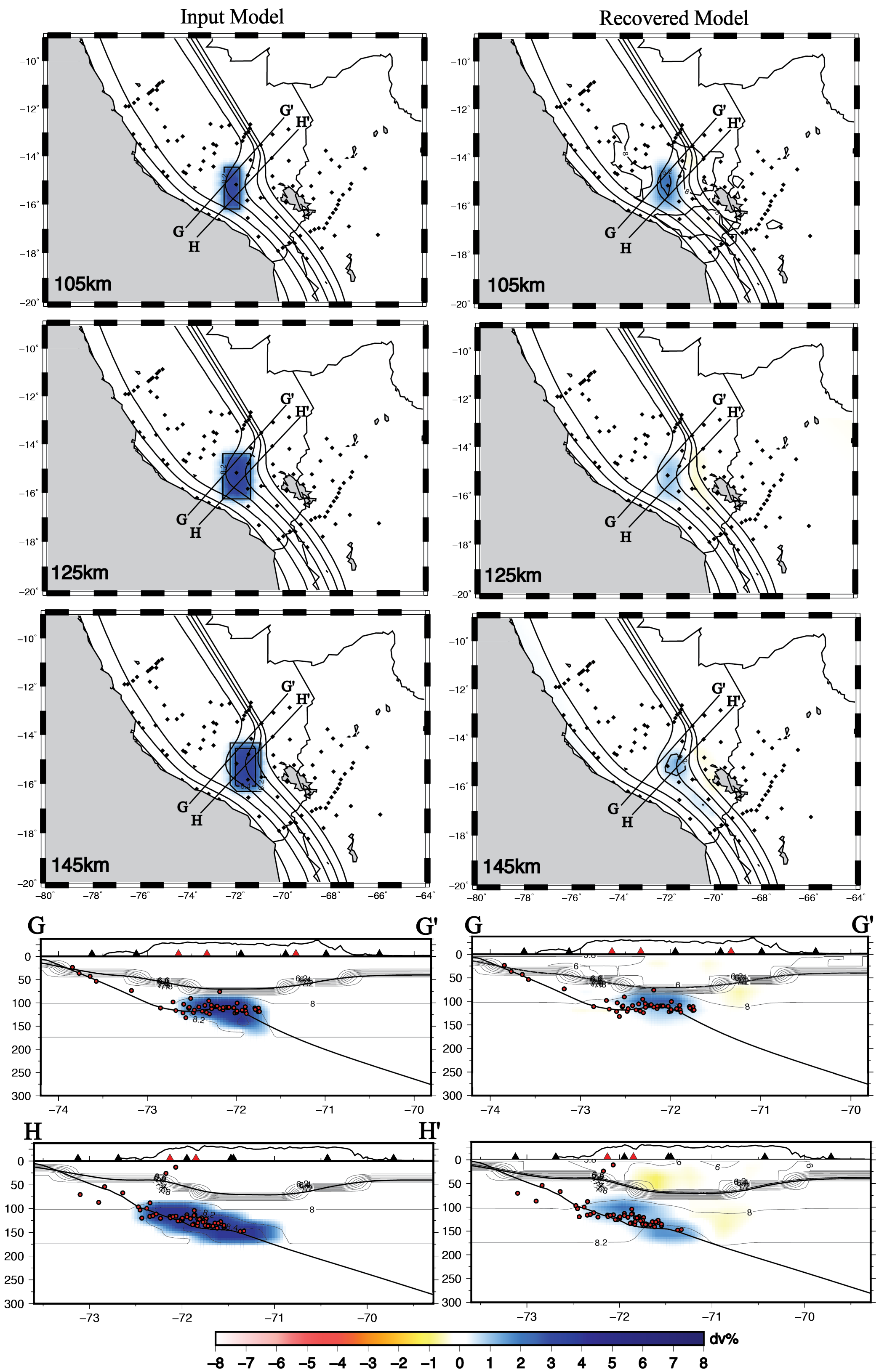

Figure 3.47- Results showing the recovery of high-V_P anomaly E (Test 13). Location of the cross sections GG′ and HH′ are shown in map view. Other symbols as in Figure 3.37.

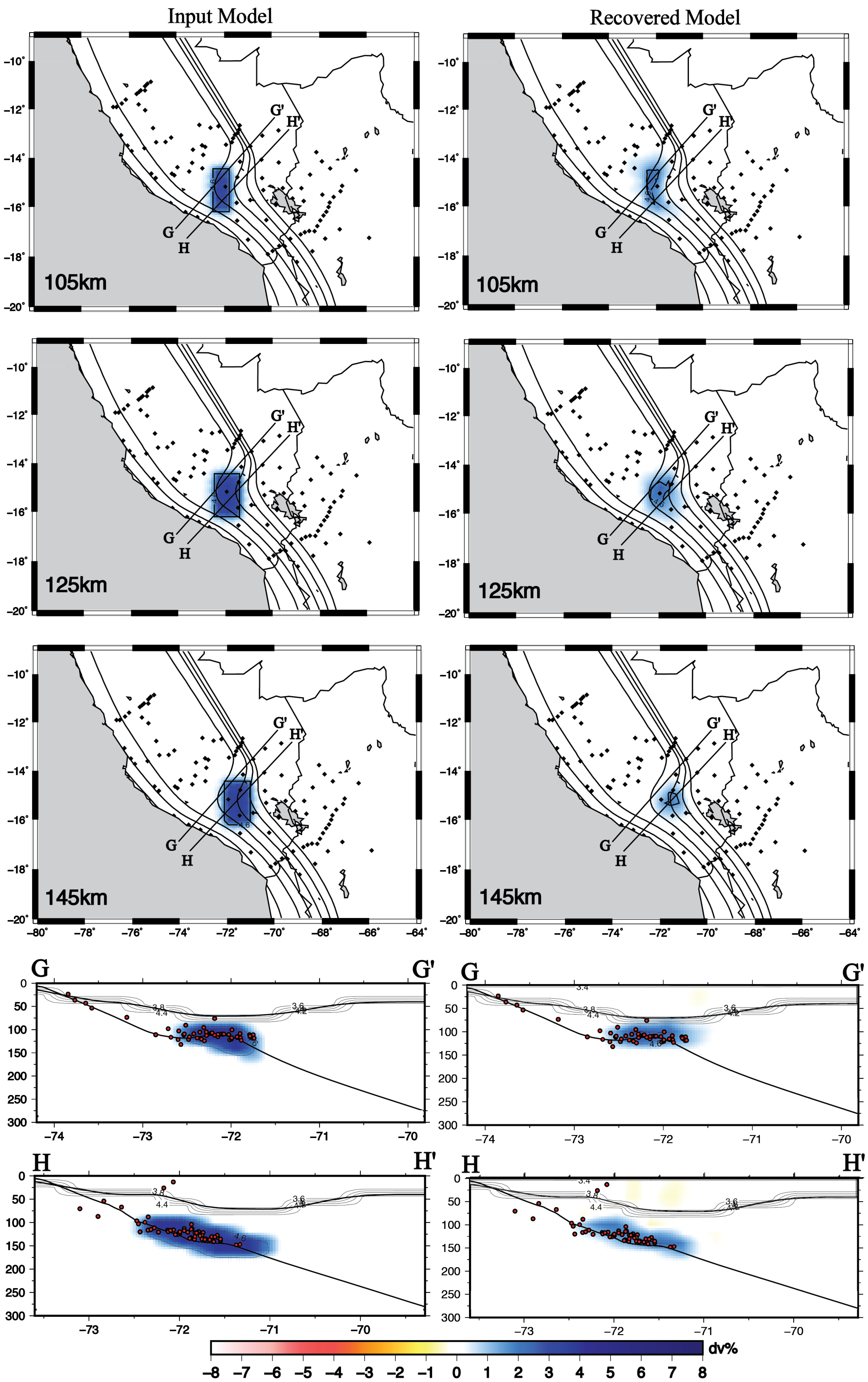

Figure 3.48- Results showing the recovery of high-V_S anomaly E (Test 14). Location of the cross sections GG′ and HH′ are shown in map view. Other symbols as in Figure 3.37.

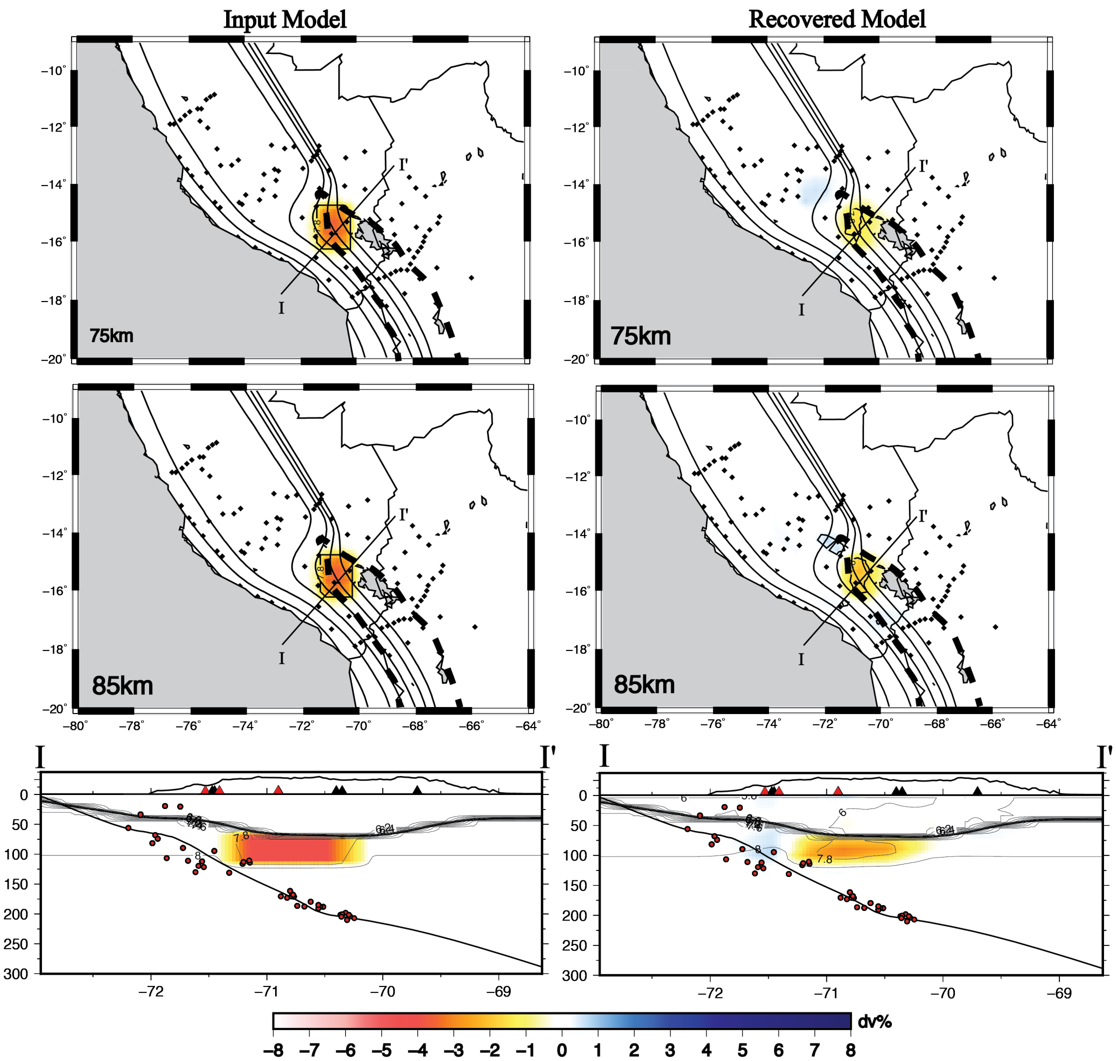

Figure 3.49- Results showing the recovery of low-V_P anomaly AS (Test 15). Dashed line is approximate outline of the northern Altiplano. Black diamonds indicate the location of seismic stations. Solid lines represent the slab contour from Cahill & Isacks (1992). Location of the cross sections II′ is shown in map view.

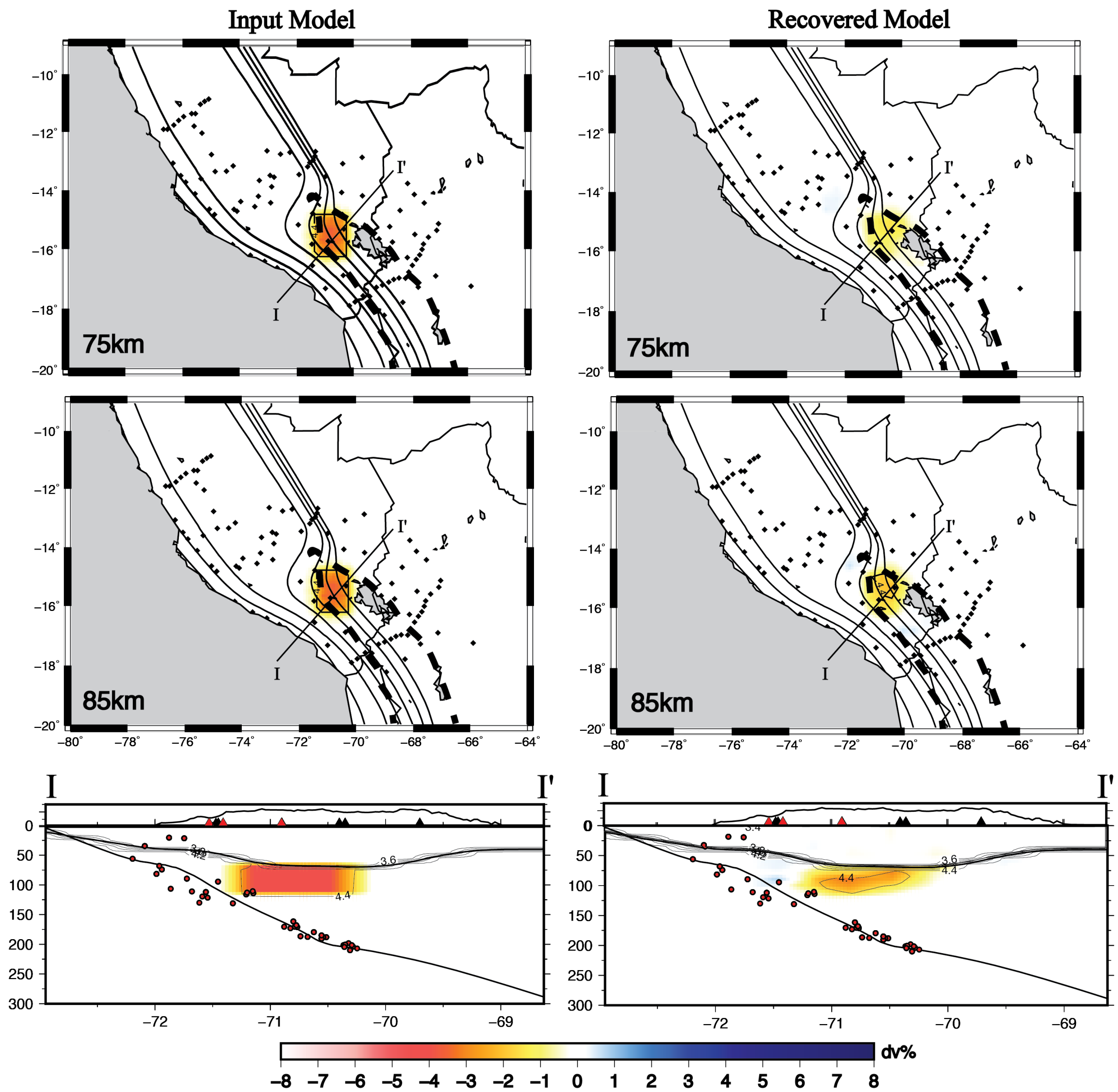

Figure 3.50- Results showing the recovery of low-V_S anomaly AS (Test 16). Dashed line is approximate outline of the northern Altiplano. Black diamonds indicate the location of seismic stations. Solid lines represent the slab contour from Cahill & Isacks (1992). Location of the cross sections II′ is shown in map view.

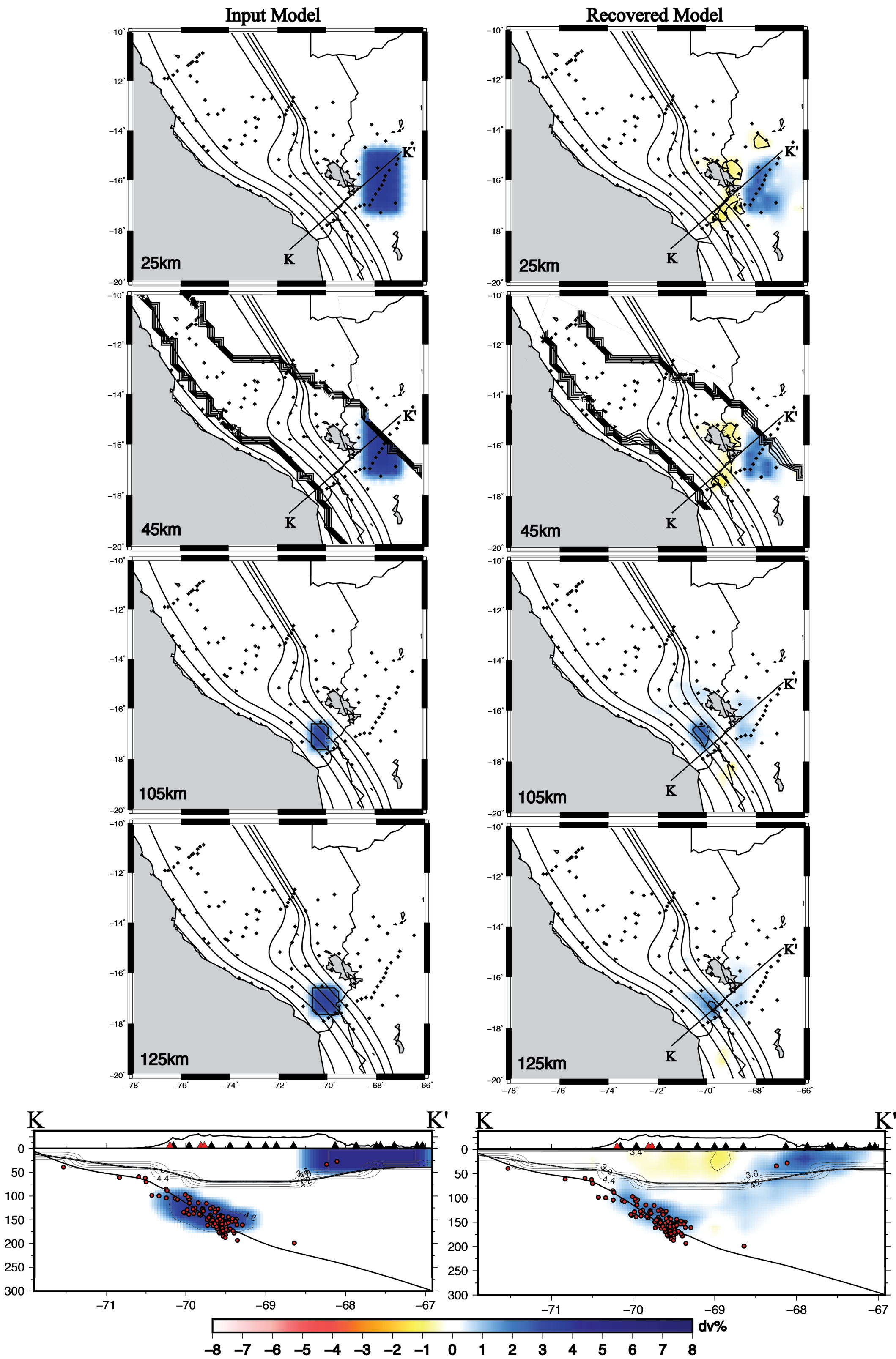

Figure 3.51- Results showing the recovery of high-V_S anomaly in the crust beneath the Eastern Cordillera and along the Wadati-Benioff Zone (Test 17). Location of the cross section KK′ is shown in map view.

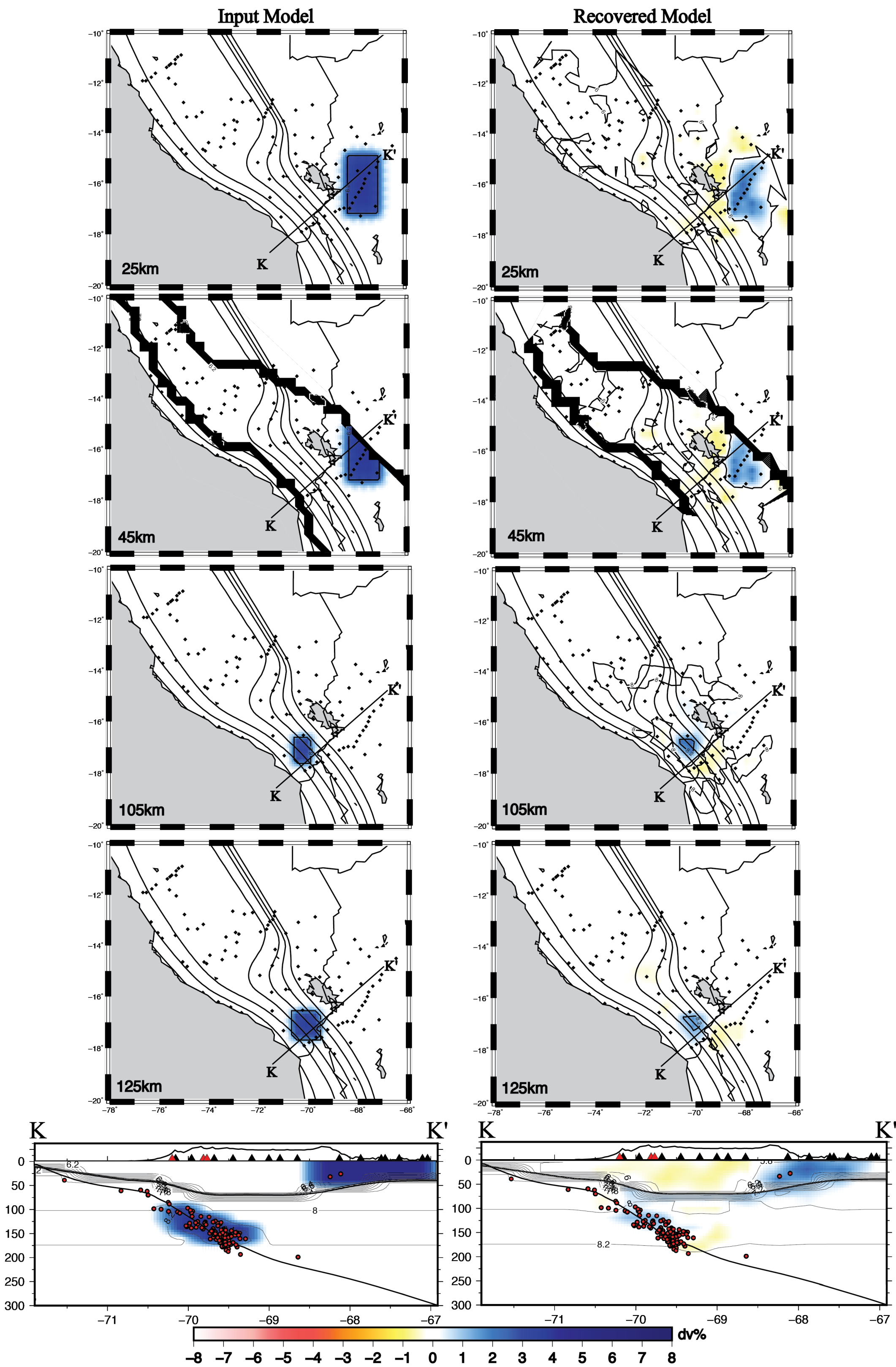

Figure 3.52- Results showing the recovery of high-V_P anomaly in the crust beneath the Eastern Cordillera and along the Wadati-Benioff Zone (Test 18). Location of the cross section KK′ is shown in map view.

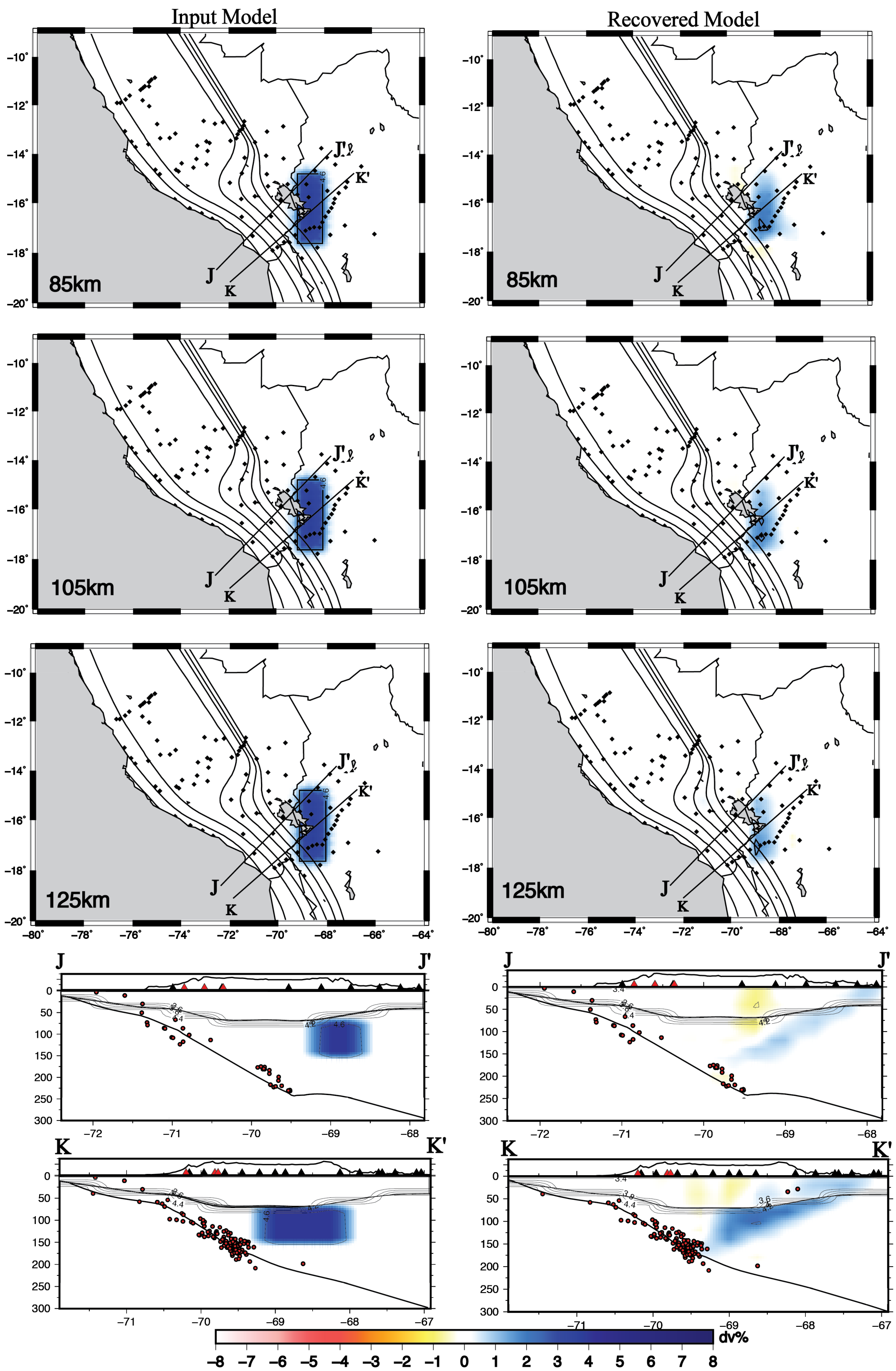

Figure 3.53- Results showing the recovery of high-V_S anomaly D (Test 19). Location of the cross sections JJ′ and KK′ are shown in map view. Other symbols as in Figure 3.37.

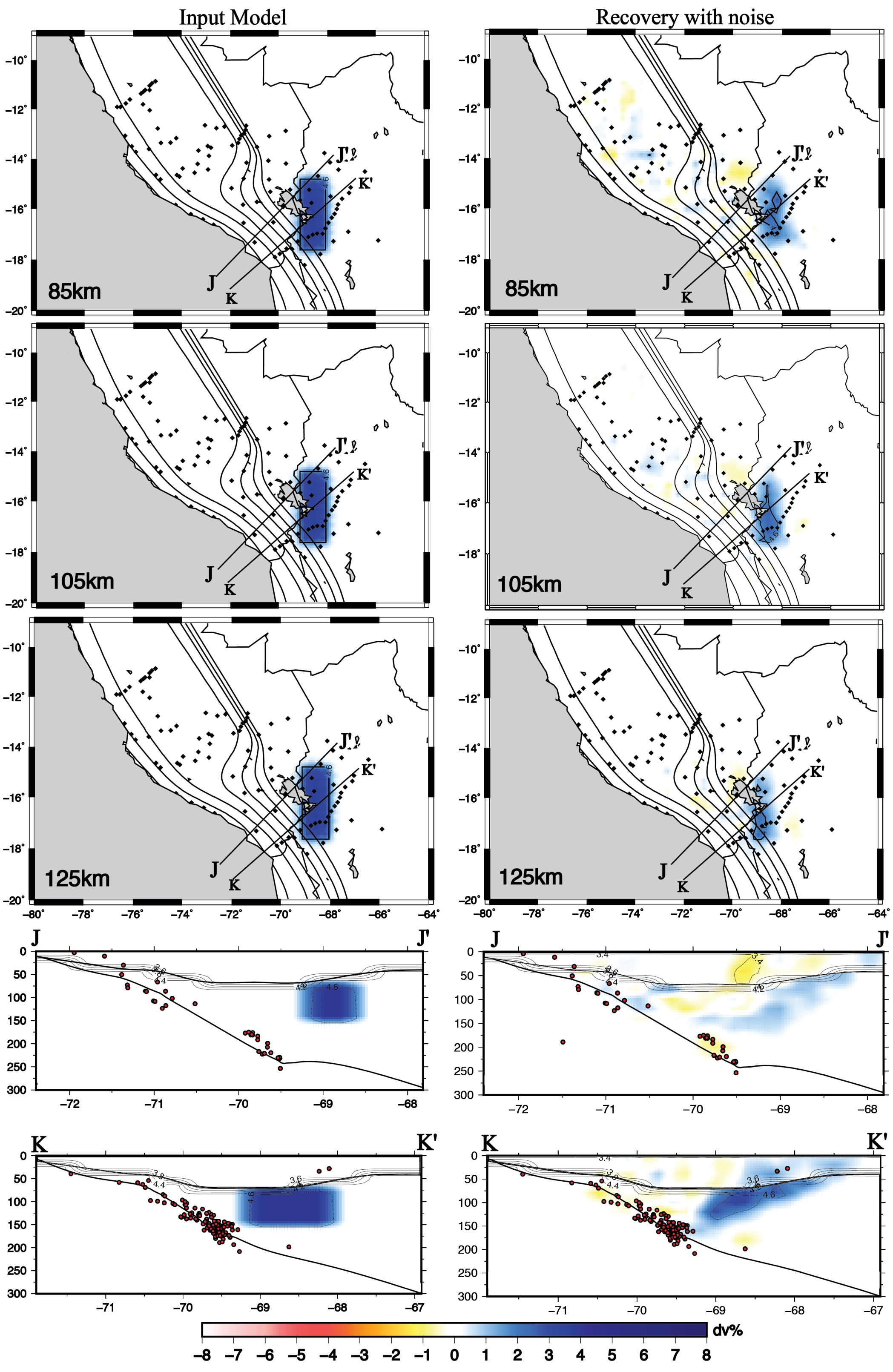

Figure 3.54- Results showing the recovery of high-V_S anomaly D, with random noise in the data (Test 20). Location of the cross sections JJ′ and KK′ are shown in map view. Other symbols as in Figure 3.37.

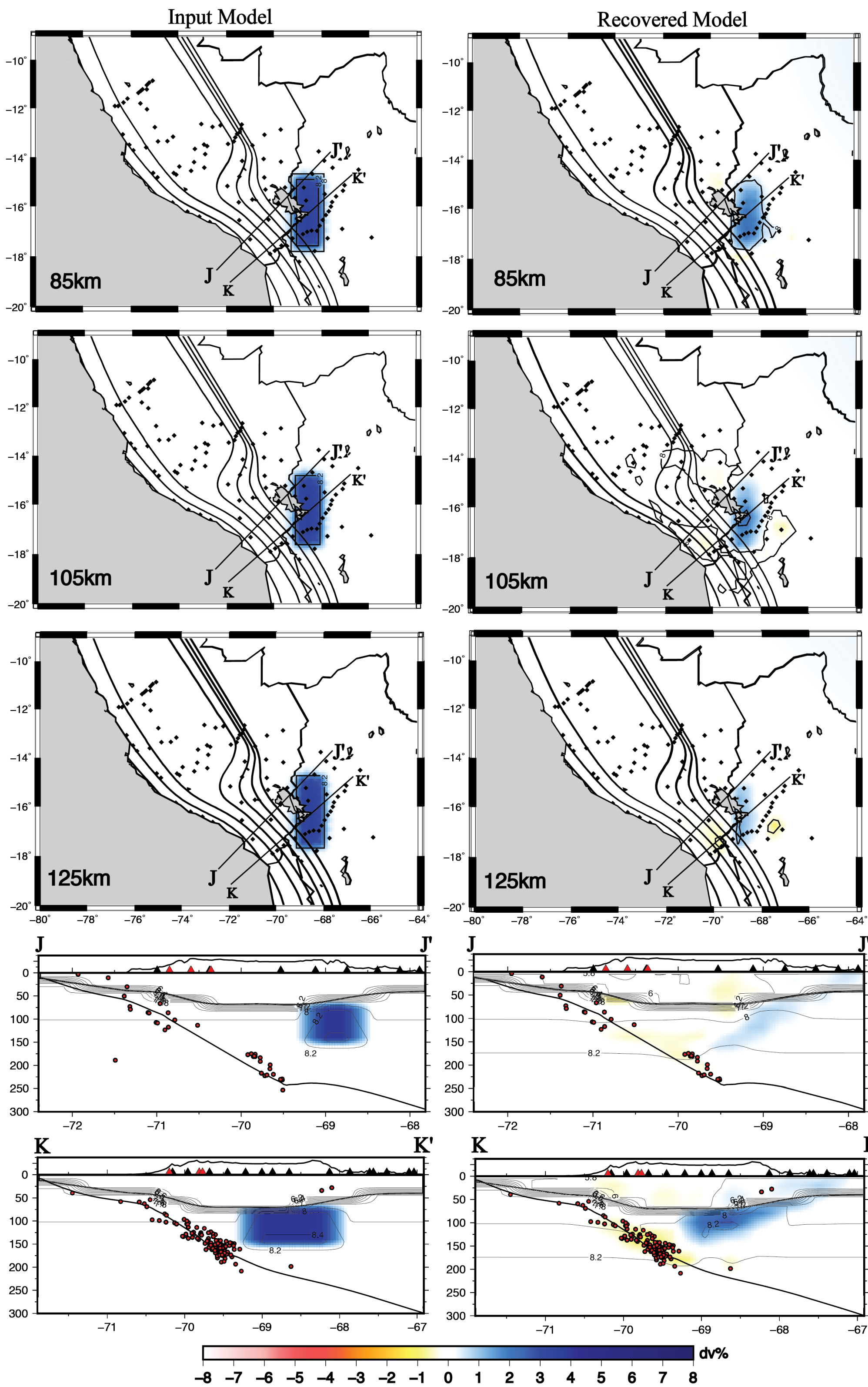

Figure 3.55- Results showing the recovery of moderately high-V_P anomaly D (Test21). Location of the cross sections JJ′ and KK′ are shown in map view. Other symbols as in Figure 3.37.

REFERENCES

Aitcheson, S., Harmon, R., Moorbath, S., Schneider, A., Soler, P., Soria- Escalante, E., Steele, G. &Swainbank, I., 1995. Pb isotopes define basement domains of the Altiplano, central Andes, *Geology*, **23**, 555–558.

Allmendinger, R.W., Jordan, T.E., Kay, S.M. & Isacks, B.L., 1997. The evolution of the Altiplano–Puna Plateau of the central Andes. *Ann. Rev. Earth Planet. Sci*., **25**, 139–174.

Barnes, J.B., Ehlers, T.A., McQuarrie, N., O'Sullivan, P.B., Pelletier, J.D., 2006. Variations in Eocene to recent erosion across the central Andean fold–thrust belt, northern Bolivia: implications for plateau evolution. *Earth Planet. Sci. Lett*., 248, 118–133.

Barnes, J. B. & Ehlers, T. A., 2009, End member models for Andean Plateau uplift, *Earth Sci. Rev*., **97**, 105–132, doi:10.1016/j.earscirev.2009.08.003

Baumont, D., Paul, A., Zandt, G., Beck, S. & Pedersen, H., 2002. Lithospheric structure of the central Andes based on surface wave dispersion, *J. Geophys. Res*., **107**(B7), 2133, doi:10.1029/2001JB000252.

Beck, S. L. & Zandt, G., 2002. The nature of orogenic crust in the Central Andes, *J. Geophys. Res*. **107**

Bird, P., 1979. Continental delamination and the Colorado Plateau. *J. Geophys. Res*., **84**, 7561-7571.

Bishop, B., Beck, S. L., Zandt, G., Scire, A., Wagner, L. S., Long, M.D. & Tavera, H., 2014. Peruvian Trench to Andean Thrust Front: Evidence for Coupling of the Peruvian Flat Slab to the Over-riding South American Plate, *AGU Fall Meeting*, San Francisco, California.

Cahill T. & Isacks B.L., 1992. Seismicity and shape of the subducted Nazca plate, *J. Geophys. Res.,* **97**, 17,503–17,529.

Carrapa, B., Adelmann, D., Hilley, G.E., Mortimer, E., Sobel, E.R., Strecker, M.R., 2005. Oligocene range uplift and development of plateau morphology in the southern central Andes. *Tectonics* 24, TC40

Christensen, N.I., 1996. Poisson's ratio and crustal seismology, *J. Geophys Res*., **101**, 3139-3156.

Coughlin, T.J., O'Sullivan, P.B., Kohn, B.P., Holcombe, R.J., 1998. Apatite fissiontrack thermochronology of the Sierras Pampeanas, central western Argentina: implications for the mechanism of plateau uplift in the Andes. *Geology* **26**, 999–1002.

Cunningham, P. S., Roecker, S. W. & Hatzfeld, D., 1986. Three-dimensional P and S wave velocity structures of southern Peru and their tectonic implications, *J. Geophys. Res*., **91**, 9517-9532.

Davidson, J.P. & de Silva, S.L., 1995. Late Cenozoic magmatism of the Bolivian Altiplano. *Contributions to Mineralogy and Petrology* **119**, 387–408.

Dorbath, C., Granet, M., Poupinet, G. & Martinez, C., 1993. A teleseismic study of the Altiplano and the Eastern Cordillera in northern Bolivia: New constraints on a lithospheric model*, J. Geophys. Res*., **98**, 9825– 9844.

Dorbath, C. & Granet, M., 1996. Local earthquake tomography of the Altiplano and Eastern Cordillera of northern Bolivia, *Tectonophysics*, **259**, 117–136.

Eberhart-Phillips, D., 1986. Three-dimensional velocity structure in northern California Coast Ranges from inversion of local earthquake arrival times, *Bull. Seismol. Soc. Am*., **76**, 1025–1052.

Ehlers, T.A. & Poulsen, C.J., 2009. Influence of Andean uplift on climate and paleoaltimetry estimates, *Earth planet. Sci. Lett*., **281**, 238–248.

English J.M., Johnston S.T., Wang K., 2003. Thermal modelling of the Laramide Orogeny: testing the flat-slab subduction hypothesis, *Earth planet. Sci. Lett*., **214**, 619–632, doi:10.1016/S0012-821X(03)00399-6.

Garzione, C.N., Molnar, P., Libarkin, J., MacFadden, B., 2006. Rapid late Miocene rise of the Bolivian Altiplano: evidence for removal of mantle lithosphere, *Earth planet. Sci. Lett.,* **241***,* 543–556.

Garzione, C.N., Hoke, G.D., Libarkin, J.C., Withers, S., MacFadden, B., Eiler, J., Ghosh, P., Mulch, A., 2008. Rise of the Andes. Science **320**, 1304–1307.

Ghosh, P., Garzione, C.N., Eiler, J.M., 2006. Rapid uplift of the Altiplano revealed through ^{13}C–^{18}O bonds in paleosol carbonates, *Science,* **311**, 511–515.

Giese,P ., 1996. The problem of crustal thickening and nature of Moho in the central Andes (abstract), Eos Trans. AGU, 77 (46), Fall Meet. Suppl., F646-F647.

Graeber, F.M. & Asch, G., 1999. Three-dimensional models of P wave velocity and P-to-S velocity ratio in the southern central Andes by simultaneous inversion of local earthquake data. *J. Geophys. Res*., **104**, 20237–20256.

Gregory-Wodzicki, K.M., McIntosh, W.C., Velasquez, K., 1998. Climatic and tectonic implications of the late Miocene Jakokkota Flora, Bolivian Altiplano. *J. S. Am. Earth Sci.,* **11**, 533–560.

Gutscher M.A., Spakman W., Bijwaard H. & Engdahl E.R., 2000. Geodynamics of flat subduction: seismicity and tomographic constraints from the Andean margin, *Tectonics,* **19***,* 814–833.

Gutscher, M. A. & Peacock, S. M., 2003. Thermal models of flat subduction and the rupture zone of great subduction earthquakes, *J. Geophys. Res*. **108**.

Hacker, B. R., Peacock, S. M., Abers, G. A. & Holloway, S. D., 2003. Subduction factory-2. Are intermediate-depth earthquakes in subducting slabs linked to metamorphic dehydration reactions? *J. Geophys. Res*., **108**.

Hasegawa, A., Umino, N., Takagi, A., Suzuki, S., Motoya, Y., Kameda, S., Tanaka, K. & Sawada, Y., 1983. Spatial distribution of earthquakes beneath Hokkaido and northern Honshu, Japan (in Japanese with English abstract), *J. Seisrnol. Soc. Jpn*., **39**, 381-395.

Havskov, J. & Ottemoller, L., 1999. SeisAn Earthquake Analysis Software, *Seis. Res. Lett*.,**70**, 532-534, doi:10.1785/gssrl.70.5.532.

Hayes, G. P., Wald, D. J. & Johnson, R. L., 2012. Slab1.0: A new three-dimensional model of global subduction interface geometry, *J. Geophys. Res.*, **117***,* B01302, doi:10.1029/2011JB008524.

Henry, S.G. & Pollack, H.N., 1988. Terrestrial heat flow above the Andean subduction zone in Bolivia and Peru. *J. Geophys Res*. **93**, 15153–15162.

Hoke, G.D. & Garzione, C.N., 2008. Paleosurfaces, paleoelevation, and the mechanisms for the late Miocene topographic development of the Altiplano plateau. *Earth planet. Sci. Lett.,* **271**, 192–201.

Hoke, L. & Lamb, S., 2007. Cenozoic behind-arc volcanism in the Bolivian Andes, South America: implications for mantle melt generation and lithospheric structure. *J. Geol. Soc. London* **164**, 795–814.

Horton, B.K. & DeCelles, P.G., 1997. The modern foreland basin system adjacent to the Central Andes: *Geology*, **25**, 895–898.

Houseman, G., McKenzie. D. and Molnar, P., 1981. Convective instability of a thickened boundary layer and its relevance for the thermal evolution of continental convergent belts. *J. Geophys. Res*., **86**, 6115-6132.

Inoue, H., Fukao, Y., Tanabe, K. & Ogata, Y., 1990. Whole mantle P-wave travel time tomography, *Phys. Earth Planet. Inter*., **59**, 294-328.

Isacks, B.L., 1988. Uplift of the Central Andean Plateau and bending of the Bolivian Orocline. *J. Geophys. Res*., **93**, 3211–3231.

Jiao, W., Silver, P. G., Fei, Y. & Prewitt, C. T., 2000. Do intermediate- and deep-focus earthquakes occur on preexisting weak zones? An examination of the Tonga subduction zone, *J. Geophys. Res*., 105, 18,138–28,125.

Jordan, T.E., Reynolds III, J.H., Erikson, J.P., 1997. Variability in age of initial shortening and uplift in the Central Andes. In: Ruddiman, W.F. (Ed.), Tectonic Uplift and Climate Change. Plenum Press, New York, 41–61.

Kay, R.W., Mahlburg Kay, S., 1993. Delamination and delamination magmatism. *Tectonophysics,* **219**, 177–189.

Kennett, B. L. N. & Engdahl, E. R., 1991. Travel times for global earthquake location and phase identification, *Geophys. J. Int.,* **105**, 429-465.

Kern, H., 1978. The effect of high temperature and high confining pressure on compressional wave velocities in quartz-bearing and quartz free igneous and metamorphic rocks, *Tectonophysics*, **44** , 185- 203.

Kirby, S.H., Okal, E.A. & Engdahl, E.R., 1995. The 9 June 94 Bolivian deep earthquake: an exceptional event in an extraordinary subduction zone, *Geophys. Res. Lett*. **22**, 2233–2236.

Kirby, S., Engdahl, E. R. & Denlinger, R., 1996. Intermediate-depth intraslab earthquakes and arc volcanism as physical expressions of crustal and uppermost mantle metamorphism in subducting slabs, *Subduction Top to Bottom, Geophys. Monogr. Ser*., vol. 96, edited by G. E. Bebout et al., AGU, Washington, D.C., 195-214.

Kley, J., Monaldi, C.R., Salfity, J.A., 1999. Along-strike segmentation of the Andean foreland: causes and consequences. *Tectonophysics,* **301**, 75–94.

Knezevic, S. K., Wagner, L. S., Kumar, A., Beck, S. l., Long, M. D., Zandt, G., Tavera, H. & Condori, C., 2015. The Role of Slab Buoyancy in the Formation of Flat Slabs, *Nature,* in review.

Lamb, S. & Hoke, L., 1997. Origin of the high plateau in the central Andes, Bolivia, South America. *Tectonics,* **16**, 623–649.

Lenters, J.D. & Cook, K.H., 1995. Simulation and diagnosis of the regional summertime precipitation climatology of South America. *Journal of Climate,* **8**, 2988–3005.

Masek, J.G., Isacks, B.L., Gubbels, T.L., Fielding, E.J., 1994. Erosion and tectonics at the margins of continental plateaus. *J. Geophys. Res*., **99**, 13941–13956.

Matsubara, M., Obara, K. & Kasahara, K., 2009, Three-dimensional P- and S-wave velocity structures beneath the Japan Islands obtained by high-density seismic stations by seismic tomography, *Tectonophysics,* **472**, 6–17.

McQuarrie, N., Horton, B.K., Zandt, G., Beck, S., DeCelles, P.G., 2005. Lithospheric evolution of the Andean fold–thrust belt, Bolivia, and the origin of the central Andean plateau. *Tectonophysics,* **399**, 15–37.

McQuarrie, N., Barnes, J.B., Ehlers, T.A., 2008. Geometric, kinematic, and erosional history of the central Andean Plateau, Bolivia (15–17°S). *Tectonics,* **27**, TC3007.

Menke, W. 1984*,* The resolving power of cross-borehole tomography*, Geophys. Res. Lett.*, 11(2)*,* 105–108.

Molnar, P. & Lyon-Caen, H., 1988. Some simple physical aspects of the support, structure, and evolution of mountain belts, in: S.P. Clark, B.C. Burchfiel, J. Suppe (Eds.), Processes in Continental Lithospheric Deformation, *Geol. Soc. Amer. Spec. Pap*., **218**, 179– 207.

Molnar, P. & Garzione, C.N., 2007. Bounds on the viscosity coefficient of continental lithosphere from removal of mantle lithosphere beneath the Altiplano and Eastern Cordillera. *Tectonics* 26, TC2013.

Myers, S., Beck, S., Zandt, G. & Wallace, T., 1998. Lithospheric-scale structure across the Bolivian Andes from tomographic images of velocity and attenuation for P and S waves, *J. Geophys. Res*., **103**, 21,233–21,252.

Nakajima, J., Matsuzawa, T. & Hasegawa. A., 2001. Three-dimensional structure of V_P, V_S, and V_P/V_S beneath northeastern Japan: Implications for arc magmatism and fluids, *J. Geophys. Res.*, **106**, 21,843– 21,857.

O'Connell, R. J. & Budiansky, B., 1974. Seismic velocities in dry and saturated cracked solids, *J. Geophys. Res*., **79**, 5412-5426.

Oncken, O., Chong, G., Franz, G., Giese, P., Gotze, H.J., Ramos, V.A., Strecker, M.R., Wigger, P. (Eds.), 2006. The Andes: Active Subduction Orogeny. Frontiers in Earth Sciences. Springer-Verlag, Berlin. 569 pp.

Ottemöller, L., Voss, P. & Havskov, J., 2011. SEISAN: the Earthquake Analysis Software for Windows, Solaris, LINUX, and MACOSX, version 9.0.1, University of Bergen, pp. 361.

Paige, C. & Saunders, M., 1982, LSQR: An algorithm for sparse linear equations and sparse least squares, Assoc. Comput. Mach. Trans. Math. Software, **5**, 43– 71.

Polet, J., Silver, P., Zandt, G., Ruppert, S., Bock, G., Kind, R., Reudloff, A., Asch, G., Beck, S. & Wallace, T., 2000. Shear wave anisotropy beneath the Andes from the BANJO, SEDA, and PISCO experiments, *J. Geophys. Res*., **105**, 6287–6304.

Pope, D. C. & Willett, S. D., 1998*,* Thermal-mechanical model for crustal thickening in the central Andes driven by ablative subduction, *Geology,* **26**, 511–514.

Raleigh, C. B. & Paterson, M. S., 1965. Experimental deformation of serpentinite and its tectonic implications, *J. Geophys. Res*., 70, 3965–3985.

Ranero, C. R., Villasen˜or, A., Phipps Morgan, J. & Weinrebe, W., 2005. Relationship between bend-faulting at trenches and intermediate-depth seismicity, *Geochem. Geophys. Geosyst*., 6, Q12002, doi:10.1029/ 2005GC000997.

Rech, J.A., Currie, B.S., Michalski, G., Cowan, A.M., 2006. Neogene climate change and uplift in the Atacama Desert, Chile. *Geology,* **34**, 761–764.

Rudnick, R.L. & Fountain, D. M., 1995 Nature and composition of the continental crust: A lower crustal perspective, *Rev. Geophys*., **33**, 267-309.

Sato, H., Muro, K. & Hasegawa, A., 1998. Three-dimensional mapping of magma source and transport regions from seismic data: The mantle wedge beneath northeastern Japan, *Pure Appl. Geophys*., **153**, 377–398.

Schmitz, M., Heinsohn, W. D. & Schilling, F. R., 1996. Seismic, gravity and petrological evidence for partial melt beneath the thickened central Andean crust (21-23°S), *Tectonophysics*, **259**, 313-326.

Seibert, L. & Simkin, T., 2002. Volcanoes of the World: an Illustrated Catalog of Holocene Volcanoes and their Eruptions, Smithsonian Institution, Global Volcanism Program Digital Information Series, GVP-3. Available at: http://www.volcano.si.edu/world/

Somoza, R., 1998. Updated Nazca (Farallon)-South America relative motions during the last 40 My: Implications for mountain building in the central Andean region, *J. S. Am. Earth Sci.,* **11**, 211–215.

Swenson, J., Beck, S. & Zandt, G., 2000. Crustal structure of the Altiplano from broadband regional waveform modeling: Implications for the composition of thick continental crust, *J. Geophys. Res*., **105**, 607 – 621.

Tao, W. C. & O'Connell, R. J., 1992. Ablative subduction: A two-sided alternative to the conventional subduction model: Journal of Geophysical Research, **97**, 8877–8904.

Thurber, C. H., 1981. Earth structure and earthquake locations in the Coyote Lake area, central California, *Ph.D. Thesis*, Massachusetts Institute of Technology, Cambridge, Massachusetts, 332 pp.

Thurber, C. & Ritsema, J., 2007. Theory and observations—seismic tomography and inverse methods. In: Schubert, G. (Ed.), Seismology and the Structure of the Earth. Treatise on Geophysics, vol. 1. Elsevier, pp. 323–360.

Trumbull, R. B., Riller, U., Oncken, O., Scheuber, E., Munier, K. & Hongn, F., 2006. The time-space distribution of Cenozoic volcanism in south-central Andes: a new data compilation and some tectonic implications, In Oncken, O., Chong, G., Franz, G., Giese, P., Gotze, H.-J., Ramos, V.A., Strecker, M.R., Wigger, P. (Eds.), The Andes: Active Subduction Orogeny. Springer-Verlag, Berlin, pp. 29-43.

Um, J. & Thurber, C., 1987, A fast algorithm for two-point seismic ray tracing, Bull. Seismol. Soc. Am., **77**, 972–986.

Ward, K.M., Porter, R.C., Zandt, G., Beck, S.L., Wagner, L.S., Minaya, E. & Tavera, H., 2013. Ambient noise tomography across the Central Andes, *Geophys. J. Int*., **194**, 1559–1573.

Watts, A., Lamb, S., Fairhead, J. & Dewey, J., 1995. Lithospheric flexure and bending of the central Andes, Earth Planet. Sci. Lett., **134**, 9– 21.

Whitman, D., Isacks, B. L., Chatelain, J. L., Chiu, J. M. & Perez, A., 1992. Attenuation of high-frequency seismic waves beneath the central Andean plateau, *J. Geophys. Res*., **97**, 19,929-19,947.

Wigger, P.J., Schmitz, M., Araneda, M., Asch, G., Baldzuhn, S., Giese, P., Heinsohn, W.-D., Martinez, E., Ricaldi, E., Roewer, P., Viramonte, J., 1994. Variation in the crustal structure of the southern central Andes deduced from seismic refraction investigations. In: Reutter, K.J., Scheuber, E., Wigger, P.J. (Eds.), *Tectonics of the Southern Central Andes*. Springer-Verlag, Berlin, pp. 23–48.

Yuan, X., Sobolev, S.V., Kind, R., 2002. Moho topography in the central Andes and its geodynamic implications. *Earth planet. Sci. Lett.,* **199**, 389–402.

Zhao, D., Horiuchi, S. & Hasegawa, A., 1990. 3-D seismic velocity structure of the crust and the uppermost mantle in the northeastern Japan arc, *Tectonophysics,* **181**, 135-149.

Zhao, D., Hasegawa, A. & Horiuchi, S., 1992, Tomographic Imaging of P and S wave velocity structure beneath northeastern Japan, *J. Geophys. Res*., **97**, 19,909– 19,928

Zhang, H., & Thurber, C.H., 2007. Estimating the model resolution matrix for large seismic tomography problems based on Lanczos bidiagonalization with partial reorthogonalization, *Geophs. J. Int.,* **170**, 337-345.